Pulse-Resolved Dosimetry Using CVD Diamond Detectors and Applications in Advanced Radiotherapy Treatment

MOHD ARIFF MOHAMED HANIFA

Swansea University
Prifysgol Abertawe

Submitted to Swansea University in fulfilment of the requirements for the Degree of Doctor of Philosophy

School of Medicine
Swansea University
2020

Supervisors: Dr R.P.Hugtenburg

Dr I. Al-Affan

Abstract

A pulse-by-pulse dosimetry system based on diamond material was developed for the purpose of point dose measurements that require high spatial and temporal dose resolutions during VMAT technique delivery. In collaboration with the University of Bristol, a front-end electrometer with a high sample-rate was developed to measure individual pulses generated from the therapeutic linear accelerator (LINAC).

One of the main drawbacks of using diamond detectors in the dosimetry field is the non-linear characteristic of the diamond response against the radiation dose-rate (Δ). The dose-rate dependency of several diamond detectors was investigated, including the commercial diamond detector known as microDiamond and a purchased prototype diamond detector known as DD4. Two methods were employed in varying the dose-rate, either by varying the pulse-rate of the LINAC or varying the distance between the radiation source and the detector. The Δ values obtained for the microDiamond detector were 0.9985 ± 0.0005 and 0.9870 ± 0.0024 based on the first and second method, respectively. For the DD4 detector, the Δ value obtained based on the second method was 0.996 ± 0.025, which was close to the value of 0.99 ± 0.03 reported in previous work for DD4.

The dosimetry system based on LINAC has successfully measured the dose for each pulse up to the rate of 400 Hz. The signal response from the DD4 detector was analysed and the models of the dose deposited were reconstructed based on the data obtained from the treatment planning system (TPS) and the LINAC logfile. Both models indicate dose differences of less than 0.5 % compared to the measurement. Cumulative dose as a function of time and gantry angle-to-agreement ($\Delta t/\Delta g$) were evaluated using a gamma-like analysis to determine the percentage of gamma passing rates (%GP). The %GP for cumulative dose evaluation against the time of 5%/1s was 100 % for both TPS and LINAC logfile compared to the measurement, and above 95 % with 3 %/1s criterion for both evaluated parameters. The %GP for cumulative dose evaluation against the gantry angle with 5 %/4^0 and 3 %/4^0 achieved above 95 % for both comparisons. The evaluation was also conducted for the instantaneous dose but with a high failure in %GP.

With improvements in the front-end and using a newly installed Elekta Agility, a treatment plan was created for an anonymised prostate cancer patient using VMAT technique delivery in a phantom. The signal response from the DD4 detector was analysed using a more sophisticated method where the signal response was separated from the background (BG) signal for individual pulses. The result of the investigation shows the change in BG as a function of the pulse repetition frequency (PRF). The analysis also revealed that the average dose per pulse increases at higher PRF. A comparison of the cumulative dose measured by the DD4 detector and the commercial independent dose calculation tool known as RadCalc reveals the dose per control point (CP). Gamma-like analysis showed that there was an excellent agreement between the measured and intended cumulative dose delivered with %GP, was 100 % for a 1 %/2s criterion.

DEDICATION

To my eight wonderful children, you are all the main reason and purpose of any of my accomplishments and I hope you are proud of your ayah!

Abu Bakar Siddiq

Mariah Qistina

Umar Farooq

Uthman Ghanie

Rowdha Safiyyah

Habeebah Illahi

Ali Muhsin

Kalsoom Illyeen

DECLARATION

I declare that this thesis is an original work of my research and has not previously been accepted for any degree. The experimental tasks are entirely my work, and the collaborative contributions have been indicated clearly and acknowledged. The work was done under the guidance of Dr. R. P. Hugtenburg and Dr. I. Al-Affan at Swansea University.

I, with this, give consent for my thesis, if accepted to be available for photocopy and inter-library loan and for the title and summary to be made available to outside organisations.

MOHD ARIFF MOHAMED HANIFA

Swansea, 19/03/2021

CONTENTS

ACKNOWLEDGEMENTS

In the name of Allah, the Most Gracious and the Most Merciful

Alhamdulillah, all praise to Allah, for providing me the strength, guidance, courage and patience to complete my PhD thesis. Peace and blessing be upon prophet Muhammad, from whom I learned the value of patience and the love of knowledge.

My PhD journey would not have been possible without the guidance and support that I received from many people. Firstly, my gratitude to Dr Hugtenburg for his mentorship and support, who encouraged me to pursue my doctoral studies at Swansea University, ten years after completing my master's degree. Thank you to Dr Affan for his encouragement and weekly visit to the student office.

Thank you to everyone in the Department of Medical Physics & Clinical Engineering for the support I received in completing my research: Radiotherapy Physics LINAC & QA; Dr Walter Thomas who helped me at night during the measurements and Mark Edwards, Radiotherapy Physics Planning, James Williams and Adam Selby, Radiotherapy Physics Clinical IT, Ian Davies and from the Radiotherapy Electronic Team: G. Lewis, G. Masom and Collin for helping me during the study related to the LINAC. Also thanks to my Ph.D. colleagues, Mohd Qutub and Sumaira Nazir, who are helping me through discussion and completing this study.

Thank you to the Ministry of Health Malaysia for sponsoring my masters and doctoral studies. Sincere thanks to all my friends at the Sabah Women and Children Hospital for their help and for inspiring me to complete my study.

Last but not least, thanks to my parents and siblings for their prayers and supporting me to complete my thesis. Special thanks to my eight dumplings, for their love, understanding and help in encouraging me to complete my PhD journey.

Table of Figures

List of Tables

ACRONYMS

CPE	Charge Particle Equilibrium
EBRT	External Beams Radiotherapy
EPID	Electronic Portal Imaging Device
IMRT	Intensity Modulation Radiation Therapy
LINAC	Linear Accelerator
MLC	Multileaf Collimator
MU	Monitor Unit
OAR	Organ At Risk
ODI	Optical Distance Indicator
PRF	Pulse Repetition Frequency
SAD	Source-to-Axis Distance
SRS	Stereotactic radiosurgery
SSD	Source-to-Surface Distance
VMAT	Volumetric Modulation Arc Therapy

1

Introduction

1.1 *Introduction*

The International Agency for Research on Cancer (IARC), a subsidiary of the World Health Organization (WHO), reported that the global burden of cancer has risen to 18.1 million new cases and 9.6 million of deaths in 2018 [1]. One in five men and one in six women will develop cancer while one in eight men and one in eleven women will die from the disease. It is estimated that by 2050, the number of deaths and new cancer cases will increase dramatically due to population growth and aging. According to the report, lung cancer is on top of the list causing death for both men and women, followed by breast, colorectal, prostate and stomach cancer. One of the main factors for the increase in global cancer is due to poor prognosis [1]. Therefore, prevention, early detection and proper treatments are important in controlling cancer cases. In general, treatment for a cancer patient can be either by surgery, chemotherapy, radiation or by a combination of these.

Radiation therapy has been used in treating cancer patients since the publication of Marie Curie's "Theory of Radioactivity" in 1912, which suggested the usefulness of X-ray for therapy. Dynamic radiotherapy treatments such as intensity-modulated radiation therapy (IMRT), volumetric-modulated arc therapy (VMAT) and stereotactic radiosurgery (SRS), are among the latest technology delivered by the therapeutic medical linear accelerator (LINAC). Unlike conventional radiotherapy which is used for large field-size, the aforementioned complex techniques are used for small field dimension. The use of small fields during treatment results in substantial uncertainty in the accuracy of dose measurements due to non-equilibrium conditions in the detector. For this reason, the radiation detectors used in measuring complex techniques need to be small relative to the treatment field. The Institute of Physics and Engineering in Medicine (IPEM)[2] defined small field to be smaller than 40×40 mm^2 . There are significant differences between the dose measured by a conventional radiation detector with a sensitive volume of 0.6 cm^3 and a small detector for complex technique delivery with a sensitive volume of 0.015 cm^3.

Besides the size of the detector used during beam delivery, the dose-rate dependency of the detector is another important characteristic that needs to be considered during dose delivery measurement. The instantaneous dose-rate changes drastically in dynamic radiotherapy delivery. It can deliver 500 cGy/min for standard delivery and 1000 cGy/min for flattening-filter-free (FFF) delivery which makes it impossible for a conventional detector to capture the whole event of the dose delivery. The continuous change of the shape and intensity of the beams cause the dose distributions to have a steep dose gradient. To overcome this problem, a suitable radiation detector should have a high spatial resolution that can respond within 2 ms in order to capture the pulse generated by the LINAC is within 2.0 -2.5 ms.

There are various types of commercial radiation detectors available. They include air and liquid ionization chambers, solid-state detectors, diodes, scintillators, and thermoluminescent dosimeters and they are available in a range of sensitive volumes from mm^3 to cm^3. Some of these detectors have undergone improvement for more accurate dose measurements especially for complex beam delivery.

Besides the size of the detector, energy independence as well as tissue equivalence are equally important requirements for radiation dosimeters [3]. A promising material that can fulfil the above conditions is diamond [4] which has the following distinctive characteristics compared to other materials: highly radiation-resistant, non-toxic, chemically inert and excellent spatial resolution with near tissue-equivalence. Due to its density, it is possible for diamond to have a small active volume and a high spatial resolution compared to the conventional ionization chamber [5]. The use of natural diamond as a radiation detector was first considered by Cotty in 1956 [6] but investigation on the use of natural diamond detector for medical applications was only conducted in the late 1970s by Planskoy [4] and Burgemeister [7]. However, the cost and variability in the quality of natural diamond has made it impractical for commercial use and it was superseded by silicon diodes. Interest in investigating diamond detectors only resumed following the development of synthetic diamond. The main advantage of synthetic diamond is that its specific properties may be controlled and reproduced at a relatively low cost [8]. The potential of the synthetic diamond detector for clinical use has been investigated by several researchers [9-11]. Single-crystal synthetic diamond has been found to have much higher sensitivity compared to

the polycrystalline synthetic diamond, and therefore it has been explored for application in radiation dosemeters [12]. There are a number of custom-made prototype synthetic single-crystal chemical vapour deposition (SC CVD) diamond detectors fabricated at individual centres and studies have been conducted on their specific characteristics. This includes the prototype diamond detectors used by Piliero [13] which were purchased from the Diamond Detectors Ltd (Poole, U.K.). One of the prototype diamond detectors used by Piliero [13] known as DD4, will be used in this study.

1.2 *Motivation*

VMAT technique is considered a complex technique in therapeutic dose delivery and requires comprehensive quality assurance (QA) verification to ensure the dose delivered to the patient is as planned before the actual treatment. There is an increasing trend towards the use of higher doses and it is vital to detect any errors that may occur during the procedure to ensure effective treatment. There is a demand to have dose verification for the VMAT technique in real-time dosimetry. Stefano and Derek. [14], Elbalaa et al. [15] and Woodruff et al. [16] have investigated the use of electronic portal imaging device (EPID) for dose verification during treatments. But there are several challengers when using EPIDs as dosimeter during VMAT technique delivery such as i) pixel sensitivity variation within ± 5 % [17], ii) beam fluence shape which "flattens" the nonuniform of the beam fluence which as a result will modified the response of the device [18], iii) EPID signal underresponsed at small dose due to short irradiation times [19-20] and iv) issue of "image lag" and "image ghosting" due to the photodiodes known to exhibit temporal artefact [21]. Although SC CVD diamond detectors have been investigated extensively for clinical application, no studies have been conducted on dose verification for the VMAT technique at pulse-resolved dosimetry. The primary obstacle for using diamond as a radiation detector, as described by Fowler [22], is due to its dose-rate dependency. The majority of studies on synthetic diamond detector focused on testing and demonstrating the non-linearity characteristic of the detectors. However, a recent study has evaluated the improved synthetic diamond detectors using pulse-resolved and found them to have excellent linearity with the dose-rate [23].

A novel approach in determining the dose delivery during a VMAT treatment is by measuring the pulses generated from the LINAC. In this approach, an understanding of the production of radiation beams from the LINAC and the use of a suitable radiation detector to measure the doses, are required. Furthermore, each LINAC produces photons differently depending on the waveguide design. Therefore, pulse-resolved dosimetry will arguably provide physical insight into modern radiotherapy beam delivery.

Given the excellent characteristics of diamond, especially its high sensitivity, makes it a good candidate for dose measurement with pulse-resolved dosimetry. Since the LINAC generates pulses at the maximum rate of 400 Hz, a high-count rate system (front-end) has been developed in collaboration with the University of Bristol. The DD4 detector was connected to the front-end system to better understand the pulses delivered by the LINAC during VMAT delivery. The primary objective of the pulse-resolved dosimetry system is to reconstruct doses for each pulse distinctively. The benefit of pulse-resolved dosimetry over accumulated dose measurements lies in the possibility of separating errors due to, for example, MLC motion, gantry motion and the interplay effects.

1.3 *Outline*

This chapter presents the motivation and objectives of the study. The overall aim of this study is to investigate the applicability of a prototype diamond detector known as DD4 in pulse-by-pulse dosimetry for the purpose of complex radiotherapy delivery and it focuses on prostate cancer radiotherapy delivered with the VMAT technique.

Chapter 2 describes the basics of diamond as a semiconductor material and the fabrication methods used for synthetic diamond. The chapter further explains the principles of the diamond as a radiation detector including a new commercial synthetic diamond based on the Schottky-diode known as the microDiamond detector. As the primary radiation source for external beam radiotherapy (EBRT), details are provided on how the LINAC generates photon beams. A timeline of the development and implementation of the treatment planning system (TPS) from two dimensional (2D) to three dimensional (3D), is also discussed. The aim of radiotherapy delivery is to ensure that the prescribed dose to the target and surrounding tissues are delivered as intended.

For this purpose, a brief discussion on the importance of in-vivo dosimetry is presented.

In Chapter 3, findings of the investigation on the characteristics of the microDiamond detector from PTW is presented. The chapter also presents the principles of fabrication of the microDiamond detector as well as the results of the investigation on the pre-irradiation dose required, signal-to-noise ratio, repeatability, angular dependency and dose dependency.

Chapter 4 discusses the findings on dose-rate dependency for the microDiamond and DD4 detectors. The chapter also describes the collaboration work undertaken with the University of Bristol in developing the high-count rate system to be connected to the DD4 detector. Two methods are used in varying the dose-rate: varying the pulse-rate available within the LINAC and by changing the distance between the radiation source and the detector. The results of the responses from the detectors using the relationship described by Fowler are also presented. Lastly, the chapter presents the findings on the relationship between the pulse height and the pulse-rate measured by DD4 detector.

Chapter 5 presents the preliminary results of the dosimetry measurements for the VMAT technique delivery for both the microDiamond and DD4 detectors. The details of beam delivery from the TPS were analysed using MatLab to retrieve information of the dose per control point (MU/CP) and the MLC positions. The information on the position of MLC during beam delivery from the LINAC logfile was retrieved from the LINAC control console to enable comparison with the TPS. The dose deposition models were reconstructed based on the information obtained from the TPS and the LINAC logfile. The measurements of pulse were determined by utilizing the "ROOT" package with an appropriate threshold value. The measurements with DD4 detector were based on pulse per volt (pulse/V). A cross-calibration between DD4, microDiamond and Farmer chamber was conducted to find the correction factors from the unit of (pulse/V) to (pulse/gray). The dose deposition models were compared using a gamma-like analysis for the point dose verification with the developed in-house script in MatLab.

In Chapter 6, treatment planning versus delivery of a prostate cancer treatment with the VMAT technique, was further investigated. An improvement in the high-count rate system with a newly installed LINAC which has a 0.5 cm MLC leaf width, offers new challenges in pulse-by-pulse dosimetry. In this chapter, an optimum voltage applied to the analogue front-end (AFE) was also evaluated. An investigation on the priming dose requirement for the DD4 detector was conducted and the result was compared with those reported by Piliero. Lastly, the dose-rate dependency for the microDiamond and DD4 detectors were investigated with cubical and spherical phantoms. A treatment plan was created from a new TPS for a VMAT prostate cancer. Unlike the previous chapter, the spherical phantom with both detectors were CT scanned and the planned dose was calculated by the TPS for both detectors in order to get accurate comparison later for the measurement. The spherical phantom was set up at the isocentre of the beams and the pulse-by-pulse dosimetry was then performed. The details on the parameters of the delivery were sent to RadCalc, an independent dose calculation tool for point dose comparison between the measurement and the RadCal. Lastly, a gamma-like analysis was again used for comparison purposes.

The conclusions of the whole study and suggestions for future work are presented in Chapter 7.

In addition to the work described above, I also provided support to the study on performance of the microDiamond detector in measuring the dose from the microCT scan by Sarah Aldrige [24]. The measurements were conducted at the College of Engineering, Swansea University, Bay Campus. The aim of this study is to find the relationship between the charge (measured by the microDiamond detector) and the dose received by the bone during the scanning process. The microDiamond was placed 203 mm from the target and irradiated for 30 s. The output reading from the microDiamond detector is in the form of charge (C). By applying the nominal sensitivity of microDiamond detector provided by the manufacturer, the relationship between the dose-rate and distance can be obtained.

I also had the opportunity to investigate the performance of the microDiamond and DD4 detectors under the influence of the magnetic-field. The investigation was part of a research by Gavin Morgan [25] for his MSc dissertation. The investigation was conducted at the National Physics Laboratory in Teddington, London. An Elekta

Agility LINAC was used to irradiate both detectors. The detector was placed at a distance of 3 m from the LINAC head. The magnetic-field used in this study ranged from 0.1 to 1.1 tesla (T). The result of the study indicates that with the DD4 detector, the total dose measured is inversely related to the magnetic-field and the relationship is linear. Result further shows that the average pulse height is inversely dependent of the magnetic-field which means, the dose per pulse decreases with increasing magnetic-field. Likewise, for the DD4 detector, the total dose measured decreases with increases in the magnetic-field but the relationship is poorer compared to the DD4 detector. This makes the DD4 detector suitable to be used as a detector in the presence of magnetic-field.

The first finding in measuring pulse-by-pulse dosimetry for VMAT delivery with DD4 detector has been presented at the 3rd International Conference on Dosimetry and its Applications (ICDA-3) in Lisbon in 2019 [26]. The paper for this study will be published soon.

2

Background

2.1 *Introduction*

In this chapter, a review of the properties of diamond, including what cause diamonds to have various colour, the fabrication methods of synthetic diamonds by either high temperature high pressure (HTHP) or chemical vapour deposited (CVD) and the basic operation of diamonds as radiation detector, are presented.

An overview is also provided of the medical linear accelerator (LINAC), a device commonly used for external beam radiotherapy (EBRT) treatments for patients with cancer, and the development of the LINAC technology in delivering beams for complex techniques, such as the intensity-modulation radiation therapy (IMRT) and the volumetric-modulation arc therapy (VMAT).

The developments of the treatment planning system (TPS) used in the radiotherapy process before the treatment is being delivered is discussed. This includes implementation from two dimensional (2D) to three dimensional (3D) for the inverse planning method. In the inverse planning method, a planner (Oncologist and Dosimetrist) defines a patient's critical organ, tumour and their dose tolerance, after which an optimisation program in TPS is run to find the best treatment plan which matches all the input criteria with the LINAC capacity. A complex algorithm for dose distribution calculation is used for the VMAT techniques.

Lastly, a discussion on the importance of in-vivo dosimetry (IVD) for advance beam delivery is presented. It is critical to understand this aspect as the dose delivered with the VMAT technique is used for small field dimensions, at various dose-rates, variable gantry rotation speeds and variable MLC positioning speeds.

2.2 Basic knowledge on semiconductor

Diamond is derived from an ancient Greek word meaning "unbreakable". This is not surprising because diamond is known to be the hardest natural material and has been used for cutting other hard materials. Besides being appreciated as a gemstone, humans

have for long used it as an engraving tool. Diamonds are formed by millions of years of geological pressure and must be extracted from mines deep in the earth. Diamond is also recognised today for its vital contribution to technology development in various fields such as high-energy particle detector, quantum computing, biotechnology and micro-electromechanical system.

In the diamond structure, each atom shares four electrons with its four neighbours. In crystallography, a crystal is made up of a periodic arrangement of one or more atoms repeated at each lattice point. The diamond cubic structure is FCC (face-centred cubic) which makes it very stable and rigid (see Figure 2.1). This structure makes diamonds to be very hard and have a high melting point.

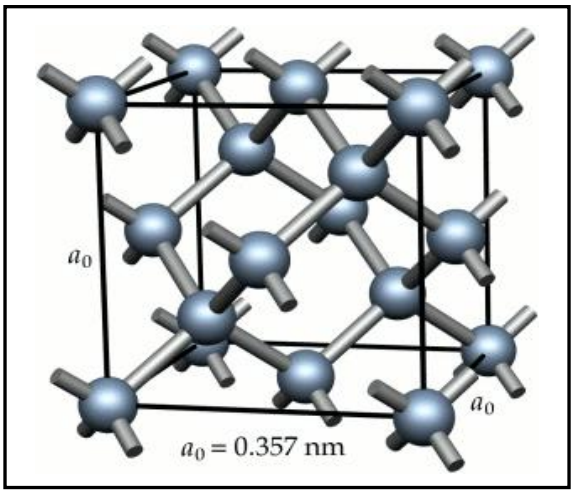

Figure 2.1: Diamond structure in a tetrahedral arrangement [27]
The schematic diagram shows the diamond with four electron valence sharing with another atoms

Natural diamond and silicon are known to be good semiconductor materials and both belong to the group four element in the periodic table. Table 2.1 presents a comparison of the properties between diamond and silicon. Semiconductor material triggers an electrical conductivity between the conductor and insulator at a specific temperature. For example, a diamond's resistance decreases when its temperature increases and this allows the current to flow.

Property	Diamond	Silicon
Density (gcm^{-3})	3.52	2.33
Bandgap (eV)	5.47	1.12
Electrical Resistivity (Ω m)	10^{11} to 10^{18}	2.5 x 10^{5}
Electron mobility ($V^{-1}cm^2s^{-1}$)	2400	1350
Hole mobility ($V^{-1}cm^2s^{-1}$)	2100	480
Energy to form e-h pair (eV)	13	3.6
Thermal conductivity ($W\ m^{-1}\ K^{-1}$)	2000	150
Dielectric constant	5.6	11.7

Table 2.1: Comparison between diamond and silicon properties at 293K [28-29]

The arrangement of electrons configuration for carbon is $1s^2, 2s^2, 2p^2$. The outermost layer of the electron shell is called the "valence band" and an electron in this layer forms bonds with the neighbouring atom. The electrons are able to move around within the valence band. Above the valence band is the conduction band, and in the case of metal, the electrons are able to move freely giving rise to electrical conductivity. Between the valence band and conduction band is the bandgap. A larger bandgap means more energy is required to excite the electron from the valence band to the conduction band. Conversely, when the valence band and conduction band overlaps, which is often the case for metals, electrons will jump between those two bands. This is the cause for the difference between a conductor, a semiconductor and an insulator (see Figure 2.2).

Fermi energy level is defined as the highest energy state occupied by the electrons at absolute zero temperature (0 K). In the case of diamond (a semiconductor), it acts as an electrical insulator at room temperature. However, by increasing the temperature, the electrons at the valence band can be excited to move to the conduction band due to the absorption of the energy and leaving behind an electron deficiency known as "hole", which behaves like a positive charge. When a voltage is applied to the material, the electron will move towards the positive terminal while the hole moves towards the negative terminal and as a result, a small current flow through the material.

Semiconductor materials can be divided into two types: intrinsic semiconductor and extrinsic semiconductor.

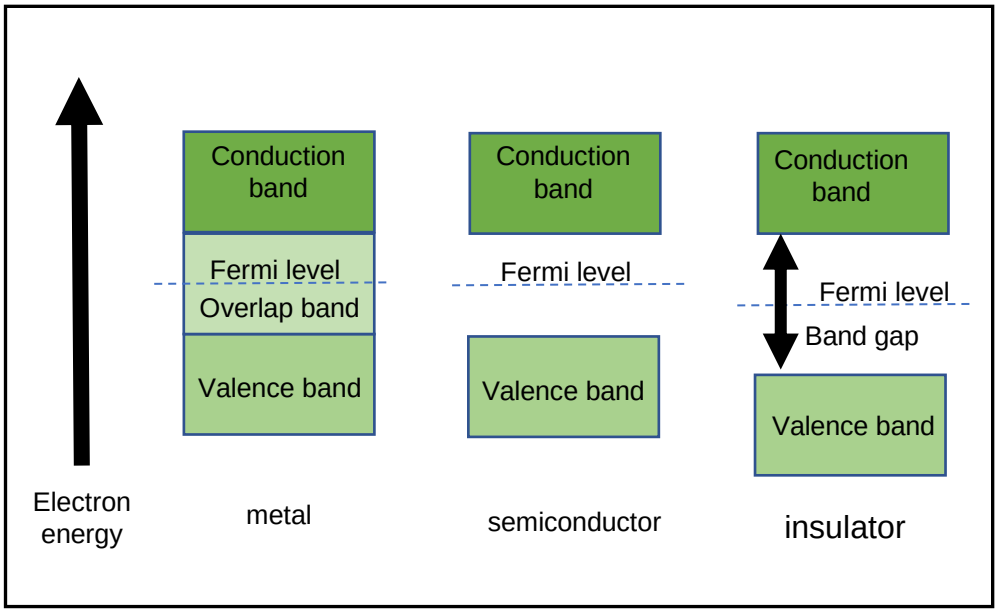

Figure 2.2: Differences between metal, semiconductor and insulator materials. The Fermi level is the highest energy level where the outermost electron orbital is at a temperature of zero (0 K)

An intrinsic semiconductor is theoretically a pure semiconductor without any impurities present. Hence, the number of electrons in the conduction band is equal to the number of holes in the valence band. Likewise, a natural diamond that is chemically pure and structurally perfect, will be absolutely transparent. However, in reality, it is rare to find natural diamond that is absolutely perfect. The colour of natural diamond may be affected by chemical impurities and/or structural defects in the crystal lattice. As presented in Table 2.2, natural diamonds are generally classified into two types based on amount of nitrogen content and sub-types according to the amount of impurities that will affect light absorption. In the early 1950s, investigations were conducted on natural diamonds to support nuclear physics in the development of radiation detector [30]. Unfortunately, natural diamond is too costly for research purposes as the selected samples of natural diamonds were often of very high quality and tend to vary in terms of electrical properties. Due to this, natural diamonds were not commercially available for electronic application.

Diamond type		Description
I	*Containing a measurable amount of nitrogen*	
	Ia: 500-3000 ppm	Diamond colour of pale yellow
	Ib: less than 500 ppm	Diamond appears yellow-to-brown
II	*Containing a very low amount of nitrogen*	
	IIa: diamond almost pure without any impurities	Diamond is transparent and colourless
	IIb: contain boron and nitrogen	Diamond appears light blue or grey

Table 2.2: Classification of diamonds [31] based on impurities present

An extrinsic semiconductor is a semiconductor material (diamond) with a foreign atom present, known as a doping agent. Depending on the impurities present, the extrinsic semiconductor can be categorised into two types: n-type or p-type semiconductor. The process of deliberately introducing other impurities to the crystal is known as doping. When a pentavalent such as nitrogen (N) is present in the diamond, it is called an n-type semiconductor. Since nitrogen has five valence electrons and diamond has four valence electrons, there is an extra electron from nitrogen called "free electron" (see Figure 2.3a). In the n-type semiconductor, there are more free electrons than the holes and they act as majority carriers. When a voltage is applied to the n-type diamond, the free electrons move towards the positive terminal and carries an electric current while the holes move towards the negative terminal (Figure 2.3b). The small number of holes also carries an electrical current but it is practically negligible due to the low amount present. Fermi energy level for this type of semiconductor is close to the conductor band rather than the valence band. The colour of this type of diamond depends on the amount of nitrogen present; if less than 500 ppm, the diamond tends to be yellow-brown and if nitrogen amount is more than 500 ppm, this will make the diamond yellow in colour (see Table 2.2).

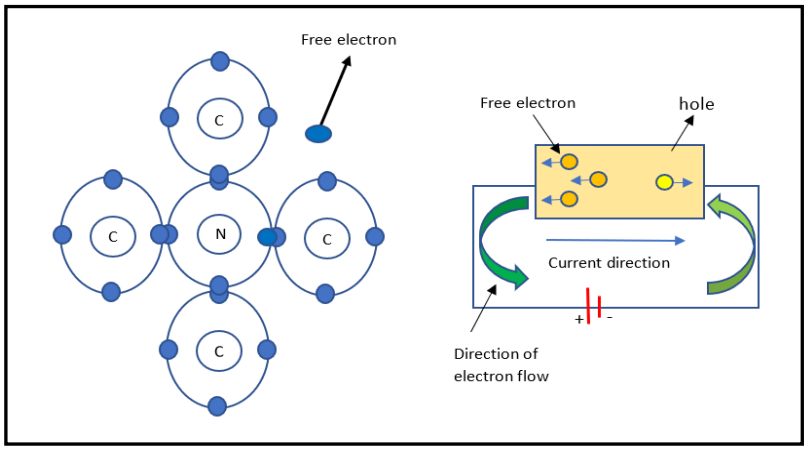

Figure 2.3: Schematic diagram of n-type diamond with nitrogen as a doping agent (a) and direction of current flow from the electron and current flow from the moving holes (b)

If the trivalent impurities such as boron (B) are present together with the diamond, then it is called a p-type semiconductor. The boron atom has three valence electrons while diamond has four valence electrons. This creates a three covalence bond with the fourth covalent bond being incomplete, known as a hole (positive). Similar to the n-type semiconductor, the p-type semiconductor contains more holes compared to electrons, causing the holes to act as a majority carrier (see Figure 2.4a). Fermi level for p-type diamond lies close to the valence band. When voltage is applied to the p-type semiconductor, the current conduction is mainly due to the holes (Figure 2.4b).

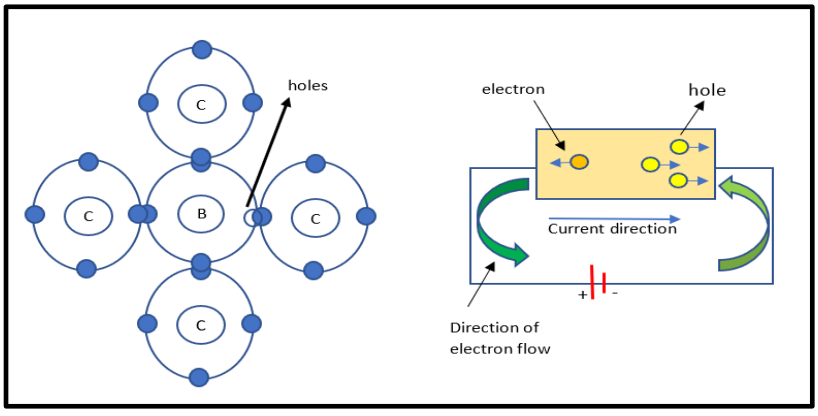

Figure 2.4: Schematic diagram of p-type diamond with boron as doping agent (a) and direction of current flow from the electron and current flow from the moving holes (b)

2.3 *Why Diamond ?*

Diamonds, as discussed in the previous section, are known for its high endurance and refractive index. In general, the price of a diamond is determined by its weight (size), colour and clarity. The colour of the diamond depends on the amount of impurities dissolved in the carbon structure and the classification of the diamond is according to the nitrogen content and amount of impurities (see Table 2.2). Due to their atom arrangement, diamonds are extremely hard and tough. Hardness refers to resistance to scratch while toughness relates to the ability to resist breaking from falls or an impact. With its high-density value, a diamond can be produced in a small volume for highly sensitive measurement.

Thermal conductivity is the ability of the diamond to conduct heat. Materials with low thermal conductivity property are often used as insulators. Thermal conductivity for a natural diamond at room temperature is several times higher than metal due to the strong covalent bonds between the carbon atoms. Despite diamond having high thermal conductivity, it is also an excellent electrical insulator at room temperature. Having a wide-bandgap in the diamond permits it to operate at much higher voltage, frequency and temperature than silicon.

Diamond has a low dielectric constant compared to silicon. Dielectric constant describes the ability of the material plates to hold an electric charge for a longer time or to hold large quantities of charges and as the result diamond detector inherently low leakage current [28]. Thus, a lower value of the dielectric constant is better. The atomic arrangement in a diamond enables it to stand high doses of radiation. Diamond is also known as a material that is chemically unreactive or chemical inert to most acids and alkalis [29].

Electron and hole mobility is characterised by how quickly the electron and hole can move through the semiconductor material when a voltage is applied to it. The principle of detecting radiation using a diamond detector relies on the creation of electron-hole pairs within the diamond. The energy required to form a pair of electron-hole is described as the energy to excite an electron from the valence band to the conduction band. When the electron loses energy, it will fall back (recombination) to the hole in the valence band through one or multiple steps. The location where this

takes place is known as the recombination centre. Electrons and holes are able to capture (recombined) and annihilate each other. The presence of impurities or structural defects in the diamond can cause an electron or hole to fall into a "trap," which is the energy level within the bandgap. The trap will capture and immobilise an electron or hole and prevent it from being recombined. An electron or hole can be released from the traps by additional energy. This trap can only accept one electron at a time and if the electron has enough energy, it will fall back into an empty state in the valence band as a second step in completing the recombination process. Shallow impurities are those that require less energy to fall back into the valence band while deep impurities require a large amount of energy to remove an electron or hole from the trap to the valence band. Therefore, theoretically, the diamond detector needs to undergo pre-irradiation before it can be used for measurement in emptying the traps. For a pure diamond where no impurities exist, the recombination rate is proportional to the square root of the induced radiation dose-rate. Therefore, the charge collection efficiency will decrease with increase in the radiation dose-rate and a non-linear relationship is observed between the induced radiation and the output signal [32].

Since diamond is almost equivalent to the effective atomic number of a soft tissue, the signal from the diamond detector is proportional to the absorbed dose to the tissue. Therefore, the dosimetry measurement with a diamond detector can be used without any correction [33-34]. The ratio of carbon to tissue is almost constant over the range of energies for the electron mass stopping power and photon mass energy absorption coefficient. This makes diamond to be energy independent compared to other detectors.

2.4 *Fabrication of synthetic diamond*

The use of synthetic diamond over natural diamond is due to the high cost and difficulty in obtaining and reproducing the required diamond grade [29]. The significant use of diamond in the industrial field prompted extensive research being conducted as early as the 1950s in producing synthetic diamond. If the synthetic diamond can be produced in the laboratory with high reproducibility through the controlled process, then the cost of synthetic diamond can be reduced. The first publication on synthetic diamond research was by Bundy et al. in 1955 [35] from the Research Laboratory of the General Electric Company, New York. They claimed that

synthetic diamond can be produced via a high-temperature high-pressure (HTHP) process. The use of atomic hydrogen to increase its growth rates during the growth period was suggested by a Soviet group of researchers [36]. Another method of producing synthetic diamond is through chemical vapour deposition (CVD), an area intensively explored by Butler et al. [37-38]. The various successes with synthetic diamond have made it relatively inexpensive and can be tailored for application in electronic devices.

2.4.1 High-Temperature High-Pressure (HTHP)

The Tracy Hall's group at the General Electric Company invented this method of producing synthetic diamond in 1954. The HTHP method simulates or mimics the growth condition of the natural diamond by applying high temperature and high pressure alongside a metal catalyst to dissolve carbon atom into a diamond seed. The initial attempts through this method were unsuccessful but after comprehensive investigation and the use of catalysts to lower the temperature and pressure conditions have made it possible to grow the diamond. The temperature used was in excess of 3000^0 C with the pressure easily reaching 18 GPa [35].

HTHP method starts with a tiny diamond seed being placed at the bottom of the cylindrical capsule. Principally, this method involves compressing and heating a carbon sample placed in between two heavy anvils (see Figure 2.5). The sample is placed in a soft solid shell such as pyrophyllite that acts as a pressure transmitting medium. The sample can be a melting graphite mixed with other metals such as iron, nickel or cobalt. The heavy anvils also act as electrodes through which the high voltage is passed to heat up the sample. Once the temperature and pressure reached an ideal condition, carbon from the melting graphite at the top of the capsule dissolves in the metal and is drawn to the bottom of the capsule where the diamond seed is located. It is here that the synthetic diamond starts to grow, molecule by molecule, layer by layer, emulating nature's process.

Following the success in producing the first synthetic diamond, many modifications and improvements in the process have been made in order to meet the demand for synthetic diamond.

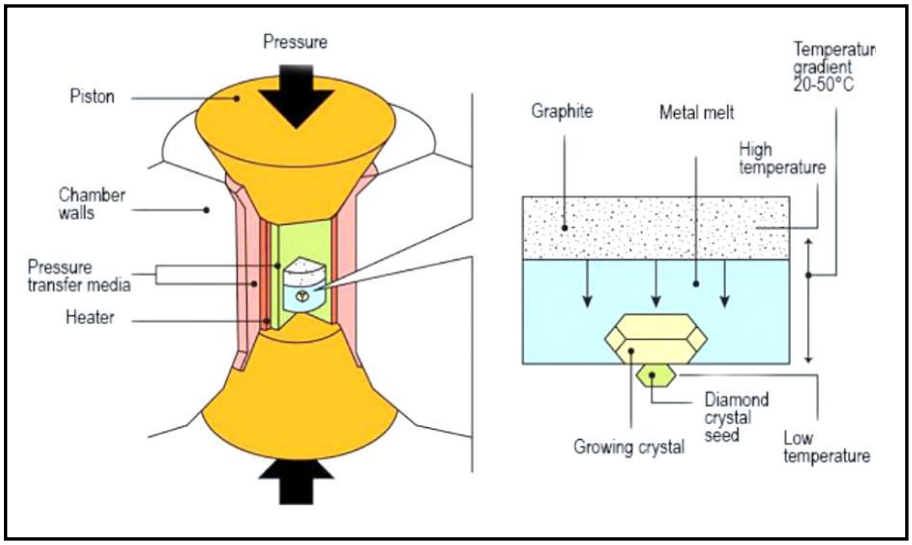

Figure 2.5: The HTHP method of producing synthetic diamond [39]

2.4.2 Chemical vapor deposition (CVD)

Before the advent of the single-crystal diamond synthesized by the CVD method, the natural diamond to be used as an electronic device had to be carefully selected from type IIa as it is very rare to find it naturally with a low level of nitrogen. The principle of producing synthetic diamond using the CVD method is entirely different from the other methods. Compared to the HTHP method, the CVD method used low pressure and smaller machines. This method is suitable for small scale research purposes since its production can be controlled. The vacuum chamber is filled with hydrogen gas (H) which acts as a scavenging agent and methane (CH_4) acting as the source of carbon. The diamond seed is placed at the bottom of the vacuum, acting as the template for the cyclic repetition of the seed structure. The heating device within the chamber is heated up to ionize the gas mixture (see Figure 2.6). When the gas turned into a plasma (electrically charged) at extremely high temperatures, the microwave will energize the plasma by breaking the atoms apart to allow the carbon ion to attach to the diamond seed. The advantages of this method is that a large surface area can be coated at a time and it is inexpensive. Synthetic diamond produced based on this technique can be used for the production of either the single crystal or polycrystal diamond.

The synthetic single-crystal diamond or homoepitaxial diamond has the same lattice structure and orientation as the original seed. The advantage of this method is that the required quality of the synthetic diamond can be controlled. Most CVD

diamonds used type IIa natural diamond seeds [29] as they have the lowest levels of nitrogen impurity. As a result, the CVD produced has high electrons and holes mobilities of 4500 and 3800 $cm^2V^{-1}s^{-1}$, respectively, at room temperature [29]. On the other hand, Tranchant et al. [40], reported the value of electrons and holes mobilities to be 2500 and 3200 $cm^2V^{-1}s^{-1}$, respectively for natural diamond detector type IIa commercialised by PTW. Electrons and holes mobilities determine how quickly they can move through the diamond and increase the sensitivity of the material. The development of the CVD synthesis technology has enabled the growth of intrinsic single-crystal and B-doped diamond by controlling the amount of impurities to process thin layers and structure of the synthetic diamond.

Parameter	**CVD diamond**	**Natural diamond**
Electron carrier mobility ($cm^2V^{-1}s^{-1}$)	4500	2400
Hole carrier mobility ($cm^2V^{-1}s^{-1}$)	3800	2100
Saturation velocity	0.8	0.8
Dielectric breakdown field ($MVcm^{-1}$)	5-10	5-10
Thermal properties ($W\ m^{-1}\ K^{-1}$)	2400	2000-2200

Table 2.3: Comparison between CVD and natural diamond [29]

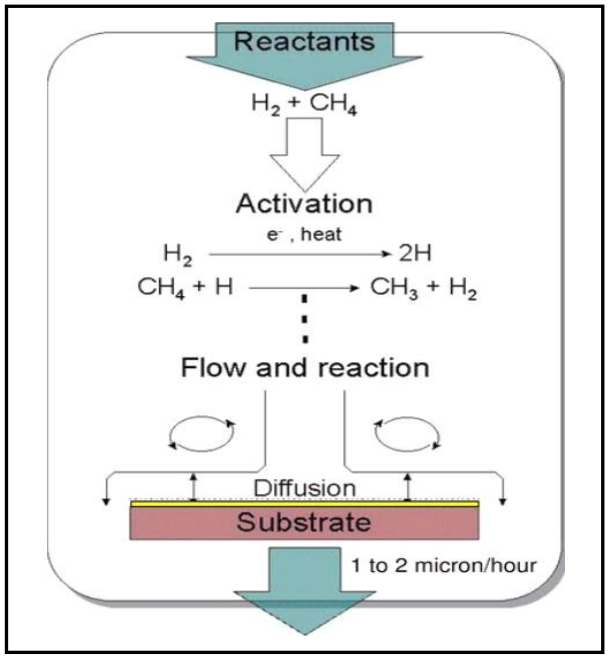

Figure 2.6: Schematic diagram showing the process of developing synthetic diamond with the CVD method [41]

2.5 *Diamond as a radiation detector*

In the early 1950s, research on natural diamond was conducted to produce a solid-state "crystal counter" to replace the gas counter in order to support nuclear physics researchers. In the late 1970s, natural diamond dosimeters were first fabricated and tested for clinical application by Planskoy and Burgemeister [4,7]. Since then, various investigators have exploited the natural diamond with a lower nitrogen content for radiation dosimetry, with some being commercialised by PTW [33,42-43]. The invention of synthetic diamond by high-temperature high-pressure (HTHP) and chemical vapour deposition (CVD) methods have made it possible for use in radiotherapy dose measurement at a lower cost.

In principle, the diamond detector relies on the creation of electron-hole pairs within the diamond when the interaction of incident radiation happens [44-46]. When it is exposed to ionising radiation, atoms in the crystal lattice sites will become ionized causing the electrons to move into the conduction band and leaving holes in the valence band. From the applied electric field, the charges drift across the diamond producing a signal that can be measured by an appropriate apparatus. Figure 2.7 shows the schematic principle of a diamond detector.

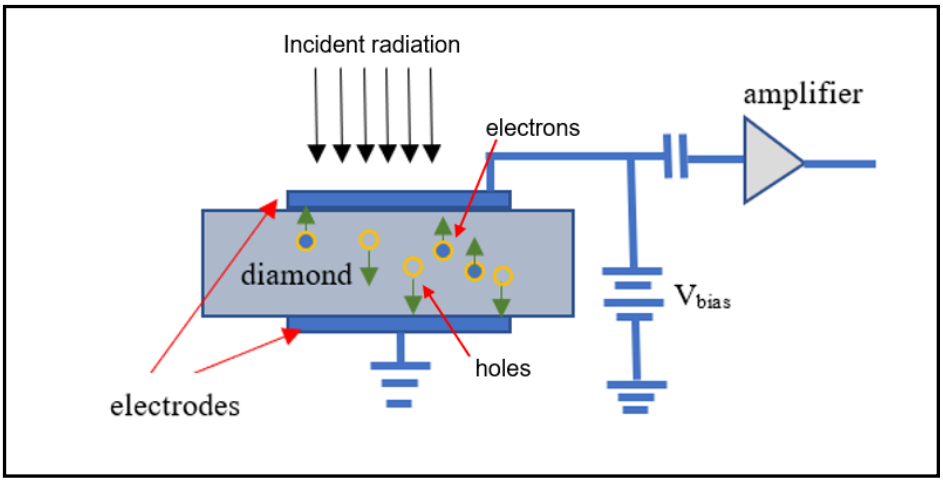

Figure 2.7: Schematic diagram of the diamond detector working as a radiation detector

With recent development in CVD technology, a group at the Industrial Engineering Department of Rome Tor Vergata University invented another structure of diamond detector . It is a metal/intrinsic/p-type layered structure that has been tested

for radiotherapy application [47]. This new structure of diamond detector is known as a Schottky-diode where the electrodes were made of metal and it doesn't require any bias voltage to be passed due to the existence of a build-in voltage. The intrinsic diamond (undoped) is connected to the metals forming an ohmic contact, and no p- or n-type junction is required. This diamond detector is an active detector which produces a signal in the presence of ionizing radiation in real-time. PTW has been commercialised as a single-crystal Schottky diode diamond known as microDiamond (600019) detector and has proven to have good dose-rate linearity [48-50]. Further discussion on this detector will be presented in Chapter 3.

There are two methods of measuring the signal from the diamond detector: pulse-counting mode and current mode depending on the display of the output device. When the diamond detector is exposed to ionizing radiation, this caused the electrons to move into the conduction band and leaving holes in the valence band. The generation of mobile charges (electron-hole pairs) is proportional to the intensity of the incident radiation. Since the electrons from the LINAC are generated in pulses (a bunch of electrons), the response on the generation of mobile charges can be identified as the signal and will be processed by the customised front-end followed by a two-stage shaper that results in a semi-Gaussian voltage output. By increasing the number of pulses or dose-rate will cause the rate of generation of mobile charges to be proportional to the intensity of the absorbed radiation pulses divided by the average energy to form a mobile electron-hole pair (13 eV). The details on the generation of pulses from the LINAC will be presented in the next section.

On the other hand, if the output device measures the signal in terms of current, then the reading obtained will be in Ampere (A). Only the method of pulse display will be discussed in this investigation. The details of measurement apparatus will be presented in Chapter 4. The pulse mode measurement which is reflected to the dose delivered by the LINAC can be evaluated based on either cumulative pulses (cumulative dose) or instantaneous pulse-rate (instantaneous dose). When the measurement apparatus is operating in the integrated current, the measured current represents its proportion to the intensity of radiation.

2.6 *Medical Linear Accelerator (LINAC)*

The aim of a medical linear accelerator (LINAC) is to produce electrons with high kinetic energies in the range of 4-25 MeV. Figure 2.8 illustrates the basic components in a LINAC. Once the filament (cathode) of the electron gun is turned-on (heated up), it releases electrons from the filament surface. These electrons will then get attracted to the grid (anode) due to different electrical potential created between the cathode and anode by the high voltage generator. The control unit and pulsed modulator are devices that control the generation of the electrons in pulses. The duration taken for the electron gun to operate is around 5 μs and the time between pulses depends on the requested pulse repetition frequency (PRF) [51]. The doughnut-like shape anode creates an electromagnetic field that guides the electron through the hole into the next phase of an accelerator known as the buncher. As electrons come out of the filament, it is the task of the buncher or accelerating waveguide to pack them into bunches. The function of the waveguide system is to generate microwave pulses of several microseconds (μs) duration and with a repetition-rate of several hundred pulses per second. In order to do this, a bunch of electrons receives microwave radiation from the magnetron (Elekta) or klystron (Varian) in the same way as surfers are carried along by the sea wave. When the electron gained more energy from the microwave, its acceleration speed will depend on how near the bunch of electrons are to the crest of the wave. The electrons riding higher on the wave will catch up with the slower ones riding lower on the wave, thus causing them to stay within the accelerating waveguide. The electrons are not continuously accelerated due to thermal and other constraints but the beams are generated in a short repetitive period.

The typical PRF used in clinical practices is between 400-500 Hz (2.5-2.0 ms), with 400 pulses produced in one second for a maximum dose-rate. By adjusting the PRF and high voltage in the magnetron, the dose-rate can be selected as in the case for IMRT and VMAT, where the magnetron is equipped with an electronic tuning device allowing instantaneous dose-rate changes while the beam is still on.

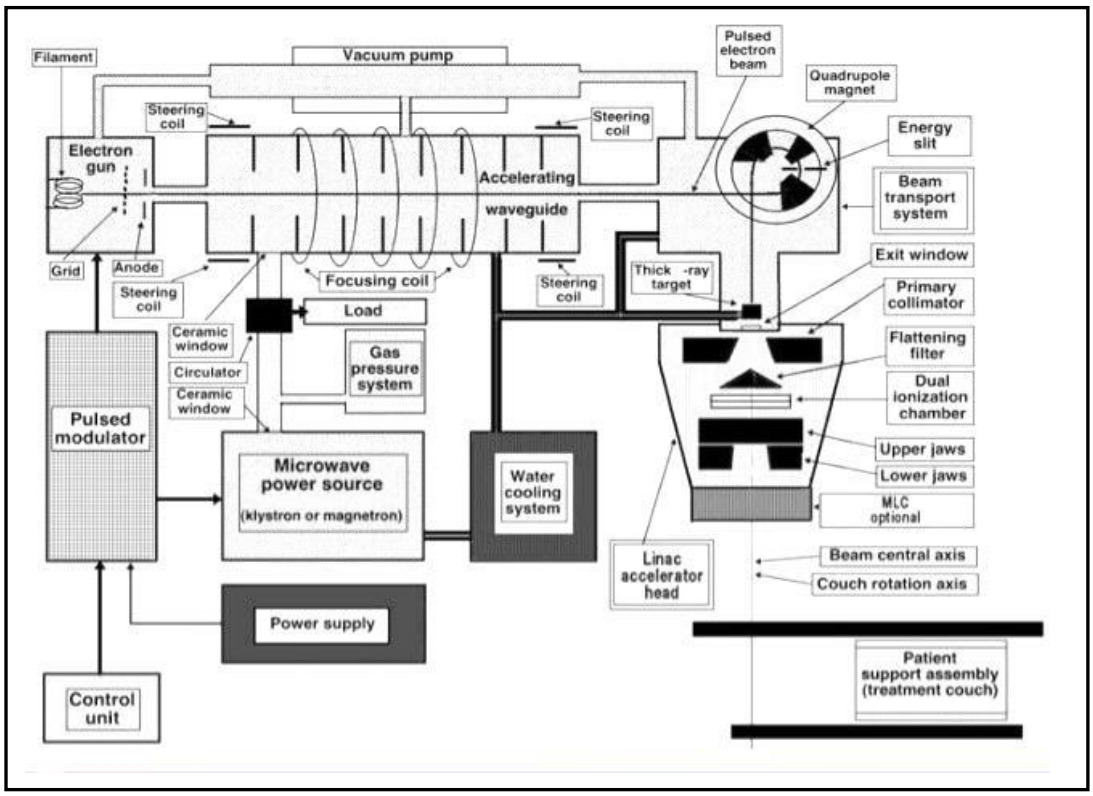

Figure 2.8: Schematic diagram of the basic components of the medical linear accelerator [52]

Once the pulsed (bunches) electron beam exit the accelerating waveguide, a bending magnet will bend it down towards the target or patient. In the electron mode of LINAC operation, the pulsed electron beams are made to strike the scattering foil to spread the beams as well as to give the beams a uniform electron fluence. Normally, the scattering foils are made of aluminium or copper. If photon mode is required for the treatment, the pulsed electron beams will strike the target to create pulsed photon beams. The generated pulsed photon beams will then go through the flattening filter to flatten the beams for uniformity and symmetry. The pulsed radiation that leaves the scattering foils or flattening filter will pass through a dual ionization chambers that monitor the integrated dose, the dose-rate and the field symmetry.

As an example, if photon mode is required, the filament will get heated up after a few seconds before a bunch of electrons enters the waveguide to be accelerated by the magnetron. The pulsed electron beams will then be bent to collide with the target to produce an X-ray pulse. This process will take a few moments to allow the pulsed electron beams to adjust to the right energy during the bending. Therefore, the

amplitude of pulse produced keeps increasing for some period before it is stabilised, as will be discussed further in Chapter 4.

With the development of the LINAC technology, more complex techniques have been invented for beams delivery in order to spare healthy tissue. Intensity-modulated radiation therapy (IMRT) and volumetric-modulated arc therapy (VMAT) are examples of advanced techniques using the modulation of the beam. These techniques, which involve high dose gradient and fast dose-rate changes during the beam delivery, require radiation dosimeter with a small active dimension that is able to respond fast enough to accommodate the change in the dose-rate. Diamond has high potential for use in the advanced technique application in radiation dosimetry. Throughout this thesis, only radiation with the energy of 6 MV from the medical linear accelerator (LINAC) is used.

2.7 *Volumetric Modulated Arc Therapy (VMAT)*

In the early 1980s, two-dimensional (2D) external-beam radiation treatment was considered as the standard for external beam radiotherapy (EBRT) delivery. It relies heavily on the radiographs and anatomical knowledge in determining the best position for the entrance of radiation beams to adequately treat the tumour. Figure 2.9 shows an example of the image of the anatomical pelvis with the simulator. The advent of computed tomography (CT) for radiotherapy in the mid-1980s has revolutionised the way of external-beam delivery. The treatment planning has moved from two-dimensional (2D) to three-dimensional (3D) as shown in Figure 2.10, allowing for the images of the tumour, healthy tissue and dose distribution to be constructed [53]. In the late 1980s, the medical linear accelerator (LINAC) has been improved for external beam delivery following the invention of the multileaf collimator (MLC) which allowed for the dose distribution to be conformal. In the early 1990s [54], intensity-modulated radiation therapy (IMRT) was introduced. This technique divides each large beam into a number of small beams known as beamlets and each beamlet has a different radiation intensity or fluence as shown in Figure 2.11. In this technique, the user will introduce the maximum dose tolerance for the tumour and organ at risk (OAR) and the treatment planning system (TPS) will calculate each beamlet in order to fulfil the condition set by the user. This is known as the inverse planning method where the user puts the condition in the TPS rather than the conventional method where

the TPS will calculate the dose distribution without considering the dose received by the tumour or healthy tissues. IMRT technique has made it possible to achieve complex dose distribution and to spare the healthy tissue. Similar to the 3D technique, IMRT delivers fixed beams at certain gantry angle but with no radiation being produced during the gantry rotation.

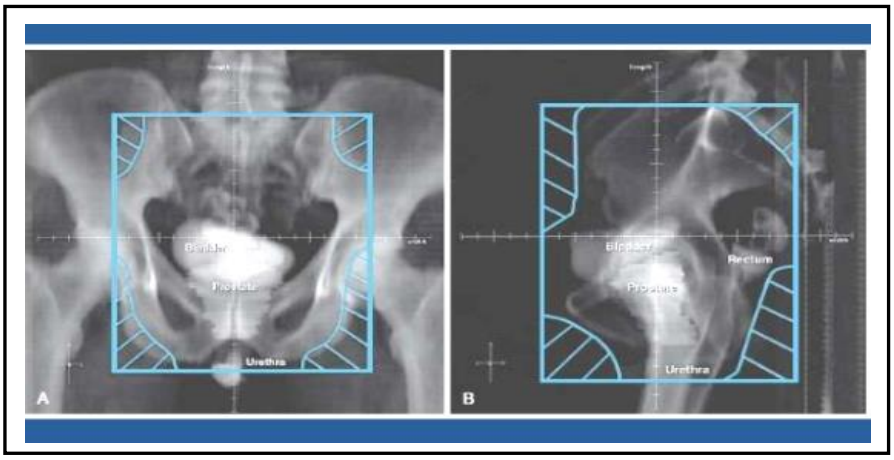

Figure 2.9: An example of two-dimensional (2D) images from an X-ray simulator for prostate treatment planning [55]. The anatomical knowledge is essential in order to delineate the treatment area

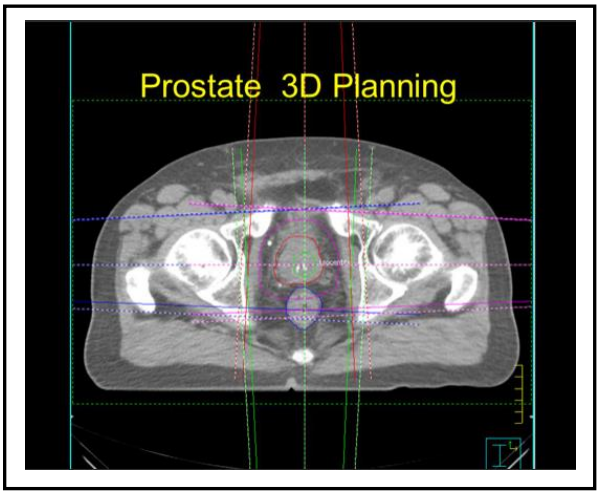

Figure 2.10: An example of one slice of computed tomography (CT) image for 3D planning of prostate cancer treatment [56]. The beams are conformal with the use of jaws alone but the tumour, healthy tissue and other organ can be clearly seen with the CT images

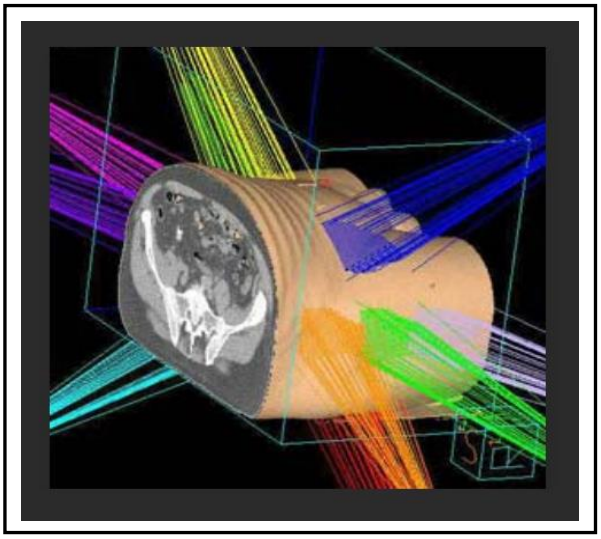

Figure 2.11: An example of the IMRT technique treatment planning system. Each large beam is divided into small beams known as beamlets and each beamlet has different radiation intensity [57]

Although IMRT is a complex technique that has been proven to be capable of achieving conformal dose distribution, especially involving vital OAR, this technique also has its disadvantages. IMRT delivery takes longer time due to the given higher monitor unit (MU) [58]. This will cause the patient to spend a longer time on the treatment table which will have an impact on the patient's interplay during the treatment. This will also impact on the workload of the LINAC and the number of patients that can be treated. Wang et al. [59] highlighted that the increase in treatment time will also increase the time-to-repair the tumour cell. Therefore, the length of treatment time is an important aspect that needs to be considered when treating patients.

In 1995, Yu [60] developed a new technique called intensity-modulated arc therapy (IMAT) where the intensity-modulated beams are continuously delivered while the gantry is rotating (see Figure 2.12). It is an alternative to TomoTherapy which shows that the more modulated beams orientations being employed during the beams delivery can help achieve greater tumour control probability (TCP) [61]. There was no progress in the technique until 2008. Otto [62] described the volumetric-modulated arc therapy (VMAT) as an extension of IMAT. VMAT is considered as a complex technique in dose delivery that involves three parameters that vary during the beams delivery: MLC speed, dose-rate and gantry rotation speed. As suggested by Yu

[60], arc radiation delivery is analogous to the TomoTherapy but the use of conventional LINAC allows for the whole volume to be treated instead of slices as in TomoTherapy delivery.

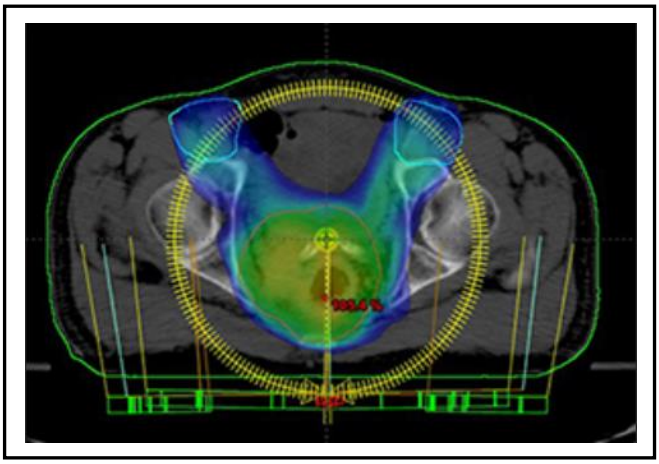

Figure 2.12: An example of the VMAT technique beam delivery. The beam is "on" while the gantry is rotating, thus reducing the treatment time compared to IMRT [63]

The major difference between VMAT and other techniques is in terms of treatment time. VMAT technique speeds up the treatment time. As discussed earlier, reducing the treatment time can increase the number of patients that can be treated and also help reduce the patients' intra-fraction movement [64]. The description of VMAT technique delivery will be further discussed in Chapter 4.

2.8 *In-vivo dosimetry*

The aim of radiotherapy delivery is to ensure that the prescribed dose to the target and surrounding tissues are delivered as intended. For this purpose, it is vital for every radiotherapy department to undergo a comprehensive quality assurance (QA) exercise of the plan calculated by the treatment planning system (TPS) and dose distribution in the phantom before delivering the treatment. Any errors during the pre-treatment evaluation can be analysed and corrected if required. A number of radiation incidents at the radiotherapy department have recently been reported [65-66]. While therapeutic radiation incidents are caused mainly by human error, suboptimal patient treatments

might happen due to a systematic error in one of the parameters involved in the patient's irradiation [67].

Given the new development in therapeutic radiation delivery, Holmberg et al. [68] emphasised on the importance for the department to increase the level of alertness in verifying that the prescribed dose delivered is safe and accurate. Hence, the department is encouraged to have a comprehensive QA programme to verify the correct functioning of all components in the radiotherapy chain, from the TPS to treatment delivery. Besides treatment delivery, a separate component in the pre-treatment verification involves checks on the specific patient. This can be achieved by using either an independent dose or based on monitor unit (MU) calculation while the dose delivery verification is conducted using QA devices such as the ionization chamber or diode arrays.

With recent development on the LINAC technology, the demand for in-vivo dosimetry has increased. The new techniques of delivery, such as IMRT, VMAT and stereotactic radiosurgery (SRS), allows for various dose-rates to be prescribed. Stereotactic radiosurgery (SRS) is another technique of varying the intensity of radiation beams delivery for brain tumour treatment without any surgery. This technique uses 3D imaging to deliver high radiation dose to the tumour with minimal dose on the surrounding brain tissue. In-vivo dosimetry (IVD) is generally performed by placing the detector on the patient's skin or close to the interested part of the patient's anatomy where the specific dose has to be measured. The detector response can be correlated with the dose either by measuring the dose directly on the patient or measuring inside the patient based on the dose depth of the interested location. Stefano et al. [15] claimed that with the use of IVD, radiotherapy errors which can lead to serious patient injury or death could be avoided.

Currently, the in-vivo dosimetry methods available are either the thermoluminescent (TLD) dosimeter or diodes. The detector used in IVD requires a comparison of the calibration obtained from the response against a calibrated ionization chamber (IC). The detectors are mostly dependent on the dose-rate and energy and they need to be adjusted based on the response in order to account for changes in the actual radiation conditions compared to the calibration condition. Correction factors such as field-size, SSD, temperature, pressure, and detector

orientation also need to be included in the calculation of the absolute dose delivered in the readout device.

Real-time IVD is another method of measuring the total dose delivery during a treatment session. It is not only capable of measuring time-resolved of the intrafraction dose delivery but can also provide additional information on dose deposited, such as the patient's interplay, the MLC position and the setup error. There are several real-time detectors available in the market and they include silicon diodes, MOSFET, plastic scintillation detectors and more recently, EPID.

The latest method of IVD is the use of an electronic portal imaging detector (EPID) to measure dose distribution during the treatment delivery. It does not require the detector to be on the skin or inside the patient. Dose distribution can be displayed either in 2D or 3D for beams delivery, thus enabling for dose verification of complex planning and delivery procedures such as VMAT. There is a proliferation of EPID dosimetry for dose verification since it is independent of the dose-rate and is linear to the cumulative dose [69]. However, the disadvantages of EPID dosimetry are its over sensitive nature to a photon of lower energy and its dependence on the off-axis position of a specific pixel due to the beam hardening [70].

The recent development of the synthetic diamond detector has made it a good candidate for IVD. Since it has high resolution characteristic and is almost linear to the dose-rate, this has made it possible to measure the dose delivered with the time-resolved. This is important with time resolution as any errors can be identified before the treatment is completed. The evaluation during the pre-treatment can be used as a guide during the real-time measurement. The gamma-like analysis can also be used for the evaluation of dose distribution depending on the criteria set by the user. The next two chapters will discuss the potential of the single-crystal CVD diamond detector in measuring the dose using the VMAT technique in treating prostate cancer.

2.9 *Conclusion*

The last decade has seen developments in the way cancer patients are being treated using the LINAC, TPS and also in meeting the demands for more accurate dose verification. This chapter discussed the basics regarding the diamond structure, the fabrication methods of synthetic diamond, the use of diamond as a radiation detector,

and the development of a treatment planning system, which enables for the maximum dose to be delivered to the target while sparing the normal tissues. The inverse treatment planning has revolutionised the delivery of radiation beam. By providing the dose tolerance to the target and the organ at risk to the TPS will enable it to calculate the best optimization beams delivery within the various range of tolerance.

Then the discussion turns to the developments of the LINAC technology and delivery of radiation pulse with the use of MLC. VMAT technique is currently considered as the best option for radiation beams delivery due to less monitor unit (MU) and time employed during the treatment compared to the IMRT. The modern conventional LINAC allows a whole volume to be treated compared to the TomoTherapy which only treats on a slice-by-slice basis. Due to the complex technique employed in VMAT delivery, an accurate and appropriate detector is required. Diamond detectors are considered to be a good candidate in measuring small fields and for high dose gradient. The next chapter will discuss further the characteristics of the microDiamond as a radiation detector.

The last section of this chapter discussed the importance of in-vivo dosimetry (IVD), especially as an advanced technique in radiotherapy beam delivery. Real-time dosimetry is useful as any small error can be determined earlier. The main investigation in the following chapters is regarding the measurement of the radiation beams at a pulse-rate from the LINAC using the prototype diamond detector. The pulse-by-pulse dosimetry measured by the prototype diamond detector will reveal new knowledge on how the LINAC delivers the dose.

3

microDiamond Detector Evaluation

3.1 *Introduction*

LINAC developments in recent years have enabled more effective and curative radiotherapy techniques to be employed by manipulating the intensity of the beam delivered by overlapping small fields with the use of multileaf collimator (MLC). The success of the intended beam delivery relies on accurate dosimetry of the absorbed dose and patient positioning. Accuracy in patient positioning is improved by employing patient immobilization and utilizing advanced imaging modalities such as electronic portal imaging device (EPID). Unfortunately, the accuracy of absorbed dose is reduced using advanced techniques such as IMRT and VMAT. The use of conventional ionization chambers is no longer valid for small field dimension due to the following factors:

a) lack of charge particle equilibrium (CPE);
b) partially occlusion of the primary radiation beam source; and
c) large detector sizes [71].

The use of advanced therapeutic dosimetry requires a detector to be small in size and has linear dependence on the absorbed dose, dose-rate, energy and the detector's angular independent. Besides being small in size, the detector must also not introduce perturbations of the incident radiation and must have an excellent spatial resolution [9]. Amongst the detectors that fulfil those requirements is the silicon-based detector. It is known to be more efficient for dose measurement as it provides more homogeneous signal response, is cheaper and also readily available in the market. However, silicon-based detector has limitations in terms of spatial resolution for fast response and also is energy dependence [72-75].

A competitor to the silicon detector is the diamond detector. The potential of natural diamond as a radiation detector was discovered as early as the 1940s for the detection of nuclear particles [30]. Due to the scarcity of and variability in the quality of natural diamonds, it is no longer available commercially. In addition, it is costly and takes longer time for delivery [74-76].

A diamond may have the same advantages as silicon but the most distinguishing property of the diamond detector compared to other detectors is that it has nearly tissue-equivalence [33]. Diamond has an atomic number (Z) of 6, which is very close to the mean atomic number of 6.5 and 6.6 for human soft-tissue and water, respectively. The ratio of diamond to tissue is almost constant over the range of energies for the electron mass stopping powers (- dE/dx) and photon mass energy absorption coefficient (μ/ρ). This makes the diamond detector to be energy independent [77]. The high density in diamond, which is attributed to the number of carbon atoms per unit volume, allows it to have a small active volume for high spatial resolution. This also makes it possible for a diamond to have a high signal-to-noise ratio (S/N) and a high resistivity to the radiation.

With the advancement in the manufacturing process, the production of the synthetic diamond can be fabricated by either the chemical vapour deposition (CVD) or high-temperature high-pressure (HTHP) methods. However, the CVD method is preferable since the specific properties of desired diamond material can be controlled and reproduced at a low cost [78]. Many authors have extensively investigated either the monocrystalline or polycrystalline CVD diamond [40, 79-82] for radiotherapy dosimetry applications. However, Tromson et al. [34] reported that polycrystalline CVD has a slow response time compared to the single crystal (SC) CVD. Since fast response time is essential for the purpose of this study, therefore a single crystal CVD diamond is preferable than the polycrystalline CVD to be used as the radiation detector in this study.

Most recently, PTW (Freiburg, Germany) has commercialised a single crystal chemical vapor deposition (SC CVD) diamond detector known as microDiamond (PTW-60019) detector for use in small field dose measurements in radiotherapy. This device is a diamond-based Schottky-diode operating with a zero-bias voltage. It was invented by a group of researchers at the Industrial Engineering Department of Rome Tor Vergata University in Italy [48, 83]. Many researchers have since investigated the characteristics and suitability of the microDiamond detector for use in measuring the dose delivery of electrons, photons or protons [84-91].

In this chapter, an assessment of the characteristics of the microDiamond detector in relation to its pre-irradiation dose, dose linearity and angular dependency

are conducted. These characteristics are important for VMAT delivery when employing a high dose gradient. A comparative analysis on the results obtained in these investigations on the microDiamond detector and that of other researchers is carried out. Since the microDiamond detector is a reliable diamond detector, it will be used for cross-calibration with the prototype diamond detector in the following chapter.

3.2 *The microDiamond Detector*

In this study, the commercially available single-crystal diamond detector (SCDD), known as the microDiamond PTW-60019 (PTW, Freiburg, Germany), was evaluated. This device is a diamond-based Schottky-diode which operates with a zero-bias voltage. The Schottky-diode is constructed using a metal electrode bonded to an intrinsic semiconductor to form a metal-intrinsic junction. At this junction, no depletion region is formed and hence, can be classed as a unipolar device. The metal-intrinsic contact has reasonably low ohmic resistance value to allow more current to flow and to produce smaller forward voltage drop (V_f). The forward voltage in Schottky-diode can be many times smaller than that of a conventional pn-junction diode, depending on the metal electrode used [92]. The single-crystal diamond detector (SCDD) in a Schottky-diode configuration was initially developed at the laboratory of Rome Tor Vergata University [83], and the PTW has commercialized the work of this group. Almaviva et al. [83] provided the general fabrication of the device, as shown in Figure 3.1.

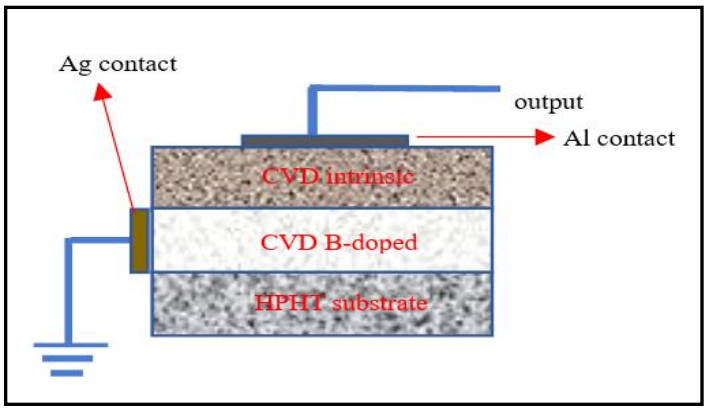

Figure 3.1: Schematic diagram of the SCDD Schottky-diode configuration developed at the Rome Tor Vergata University

The dosimeter is fabricated in a metal/intrinsic/p-type layered structure. The single-crystal diamond, highly doped with boron (B), is grown on a commercial HTHP IIb single-crystal substrate. Next, a layer of intrinsic diamond is deposited on top of the doped surface. An aluminium (Al) metal is made into an ohmic electrical contact on the top of the intrinsic diamond while a grounded contact is formed on the CVD boron-doped layer. The sensitive volume of the diamond that acts as the radiation detector is dependent on the CVD intrinsic volume and there is no contribution on the detector sensitivity from the HTHP substrate. The commercial PTW microDiamond detector has 0.004 mm^3 active volume with extremely small thickness of approximately 0.001 mm [93]. The detector elements are encapsulated in a disk-shape of 6.90 ± 0.02 mm diameter epoxy water-equivalent cylinder with 0.3 mm of RW3, 0.6 mm of epoxy and 0.01 mm of aluminium on the front face (see Figure 3.2) [93]. The effective point of measurement is 1.00 ± 0.15 mm below the top of the housing surface and is marked by a ring on the detector. The total length of the detector is 45.5 ± 0.4 mm [93]. Since the contact is made by the metal, the Schottky-diode radiation detector does not require an external bias voltage and the built-in potential is generated at the electrode-diamond interface.

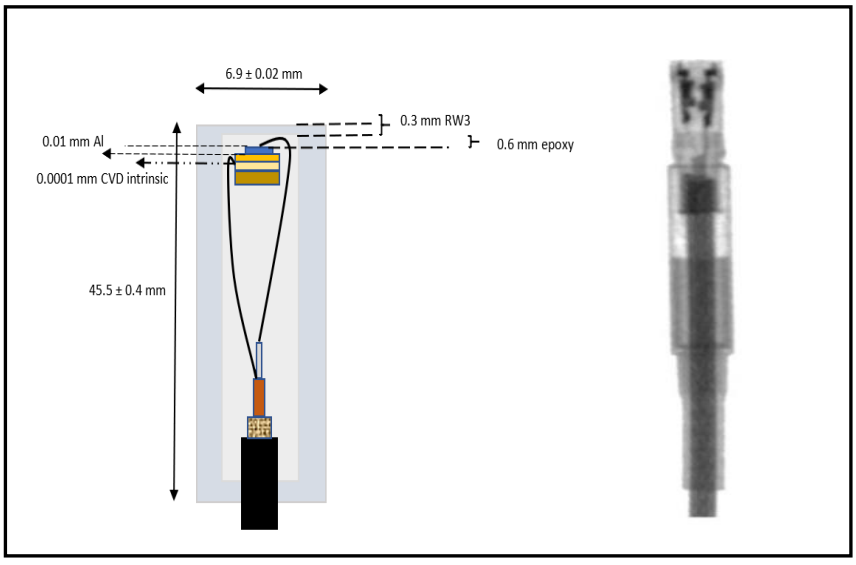

Figure 3.2: Schematic diagram and photograph of a microDiamond detector. Longitudinal cross-section with the details of the materials (a) and an X-ray image of the PTW microDiamond detector (b) [86]

3.3 *Materials and Methods*

3.3.1 Detector and electrometer

A microDiamond detector, type 60019 from PTW (SN:122760; Freiburg, Germany), was used in this study. According to the technical manual, the detector has a nominal response or sensitivity of 1nC/Gy, the pre-irradiation dose required is 5 Gy and it has a high spatial resolution of 4 mm^2 active measurement area. The microDiamond detector is connected to the dosemeter through a TNC cable.

Throughout the period of investigations, the detector is connected to the PTW UNIDOS Universal dosemeter (PTW, Freiburg, Germany) [94]. The dosemeter can display the reading in various radiological unit such as Gy, Gy/min, Sv, Sv/hr, R or R/min while the electrical unit is in coulomb (C) or ampere (A). The range of measurements for the charge and current are 2 pC to 65 mC and 200 fA to 1μA, respectively. The long-term stability is stated as less than ± 0.1 % annually. The device has leakage of less than ± 1 fA and can be operated either by battery or power supply. It has a comprehensive detector list library which makes it possible to store the calibration factor for the respective detector. The device also has an automatic leakage compensation button and a built-in system test [95].

3.3.2 Measurement setup

The measurements reported in this chapter were performed with an Elekta Synergy (Elekta, Stockholm, Sweden) known as LIN D located at the Department of Radiotherapy and Oncology, Singleton Hospital in Swansea, Wales. The LINAC is capable of delivering 6 and 10 MV X-rays, as well as 6, 9, 12, 15, and 20 MeV electron beams. However, only 6 MV X-ray beam was used for these evaluations. For the Elekta Synergy LINAC, a multileaf collimator (MLC) is located above the Y-jaw, as illustrated in Figure 3.3. The MLC leaves move in the Y-direction, which is parallel to the axis of gantry rotation. The Y-jaw acts as a back-up diaphragm or a secondary collimator with a thin jaw that can be set to follow the leaves if they are arranged together and set to the position of the outermost leaf if the leaves are of an irregular shape. X-jaw acts as a back-up collimator positioned beneath the Y-jaw.

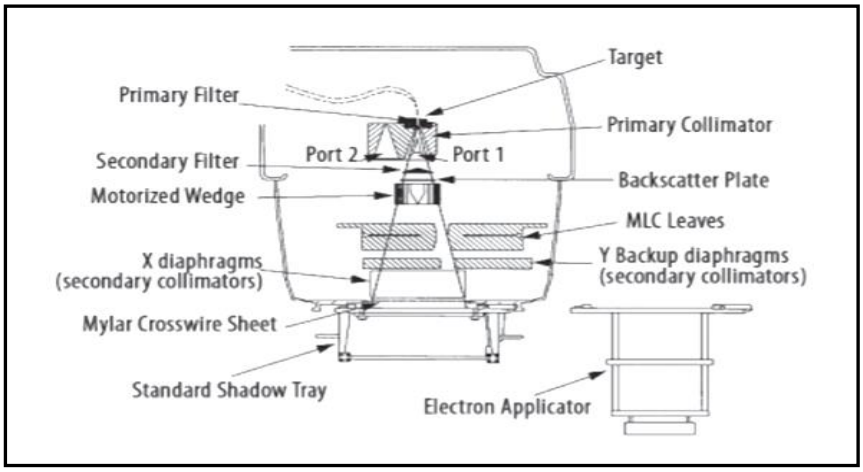

Figure 3.3: Schematic diagram depicting the location of MLC for Elekta Synergy LINAC. The location of MLC within the LINAC head depends on the manufacturer of the LINAC [96]

The radiation fields used in the investigations were defined by the MLC alone and not the Y-jaw. Throughout the investigations, the detector was mounted in a customised $8 \times 8 \times 8$ cm^3 PMMA cubical phantom surrounded with a multi-block plastic solid water-equivalent (WT1) phantom, as illustrated in Figure 3.4. The dimension of the total cross-section area for the phantom is 30×30 cm^2. The additional multi-block phantom has been purposely added to account for the effects of scattering during the irradiation. There is an additional 5 cm thickness of the slab phantom placed between the treatment table and the cubic phantom to avoid radiation scattering from the treatment table. The following characteristics of the microDiamond detector were investigated: measurements on leakage charge, pre-irradiation, repeatability, linearity with the dose, and angular dependence.

(a) **(b)**

Figure 3.4: Photographs of the measurement setup with the microDiamond detector used during the investigations. A cubical phantom is being surrounded by a multi-block water-equivalent phantom to minimize the scattering effect (a) and two slaps of solid-water phantom equal to 1.5 cm thick is attached on top of the detector for measurement at 1.5 cm depth at SSD of 100 cm (b)

3.3.3 Leakage measurement

The leakage current or dark current is defined as the current that flows in a device while it is in an "off" mode. It is important for the leakage current to be very low with respect to the radiation-induced current for a dosimeter if this is to be used in therapeutic dosimetry measurement.

The detector was positioned with its axis being parallel to the central beam axis (vertical orientation). The measurements were conducted at the depth of 1.5 cm as shown in Figure 3.4. A standard field-size of $10 \times 10\,\text{cm}^2$ (defined by the MLC position) at 100 ± 0.5 cm of SSD was employed. SSD was set by utilizing an optical distance indicator (ODI) that is available on the LINAC's head. The centre of the detector was positioned using the in-room laser which will act as the isocentre of the irradiation beams. The microDiamond detector was connected to the PTW UNIDOS Universal dosemeter with no bias voltage being supplied and the output readings were in terms of charge (C). The dosemeter has an automatic leakage compensation button which can subtract the output from the leakage (BG). However, the leakage measurements were calculated manually. In the absence of radiation, the leakage charge was initially measured for 60 seconds utilizing a built-in timekeeper on the dosemeter. Then the detector was irradiated for another 60 seconds for 200 MU at 207 MU/min. After completing the irradiation, the detector was allowed to rest for 60 seconds in order to stabilise it before measuring again the dark charge for 60 seconds. The method of obtaining the dark charge was repeated for five consecutive

measurements alternately with irradiation. Then an evaluation of the signal-to-noise ratio (S/N) of the detector was determined.

3.3.4 Pre-irradiation (priming irradiation)

At room temperature, the electrons completely occupy the valence band and the conduction band is devoid of electrons from the diamond. Since the electrons at the valence band are not free to move through the crystal, no electric signal can flow. Therefore, diamond acts as an insulator at room temperature.

When ionizing radiation interacts with the diamond, electron at the valence band acquires sufficient energy to be excited and becomes free to move to the conduction band via the hole created at the valence band. In other words, electron-hole pairs (charge carriers) were generated. An applied bias voltage secures the collection of charges by attracting them to the electrodes and enabling electrical signal to be measured. When the electron loses energy, it will fall back to the hole in the valence band (recombination) and the location where this takes place is known as the recombination centre.

By introducing impurities or defects in the diamond will create an electronic level in the bandgap which could alter the electrical performance of the material [78]. The impurities work as a trap for the electrons in obstructing them from recombining with the holes. But if high concentration of impurities is present, too many electrons will be at the traps causing the signal to be insufficient [97]. The electrons at the traps will create a depletion region that give rise to an electric field opposite to the applied bias voltage causing the collection efficiency to decrease and this is known as polarization [13, 98].

The traps can be either deep (lying in the middle of the bandgap) or shallow (lying at the edges of the bandgap). At the shallow traps, electrons may jump easily from the traps site to the conduction band. The material will show very unstable behaviour, e.g. giving signal, only when it is heated. In the case of deep traps, the energy required to remove an electron from the trap is much larger compared to the shallow trap. Therefore, during irradiation, the signal measured from the diamond detector will increase due to the filling of the deep traps which gradually increases the

detector's sensitivity until an equilibrium state is reached. This process is known as "pumping".

During the measurement with the diamond detector, both polarization and pumping events occur simultaneously and what determines whether the detector has a decreasing (due to polarization) or an increasing (pumping) signal depends on which process is more dominant [99]. The dose required to reach beyond the increasing or decreasing signal is called the priming dose. Therefore, a priming dose must be performed to stabilize the diamond detector's sensitivity before any other measurements can be conducted. However, Laub et al. [85] suggested that no priming irradiation is required for the microDiamond detector but this is contradictory to the recommendation by the manufacturer [93] which suggests that at least 5 Gy priming dose is needed before any measurement is being conducted.

As a routine, before taking any measurements, the detector will be irradiated to a certain amount of dose (or MU). The set up for the priming dose evaluation is the same as in the previous section (Figure 3.4). The microDiamond detector is positioned in a vertical orientation with the detector's main axis being parallel to the central beam axis. The pre-irradiation measurement was conducted on a field-size of 10×10 cm^2, depth of 1.5 cm for a maximum dose depth of 6 MV, with 100 cm of SSD and dose delivery of 100 MU at dose-rate of 419 MU/min . The LINAC was calibrated to give an output of 0.01 Gy/MU at the maximum depth in water following the IAEA TRS-398 dosimetry protocol [99]. The detector was irradiated with 100 MU repeatedly until a total of 2700 MU was delivered for the validation purpose, which equivalent to a total dose delivery of 27 Gy despite the manufacturer recommending only 5 Gy.

3.3.5 Repeatability

If a detector is to be used in dosimetry measurements, one of the main parameters that need to be considered is its repeatability. The International Atomic Energy Agency (IAEA) [97] recommends the repeatability characteristic of the detector to be less than 0.5%. Repeatability is defined as the ratio of the standard deviation (SD) of charge measured to the average charge measurement, as shown in equation (3.1) below.

$$\text{Repeatability (\%)} = \left(\frac{SD_{charge}}{average\ charge} \times 100\%\right) \quad \text{(3.1)}$$

With the same set up as in the previous section, the detector response for different dose-rates was investigated. Dose-rates of 419, 207, 25 and 5 MU/min were evaluated. The total monitor unit of 100 MU was delivered for dose-rates of 419 and 207 MU/min while only 10 MU was delivered for dose-rates of 25 and 5 MU/min due to LINAC stability and longer "beam-on". The repeatability of the detector was examined over five consecutive measurements with a constant dose-rate for the respective studies. The evaluations were based on the different dose-rates available from the LINAC.

3.3.6 Angular dependency

In the absence of an ideal spherical phantom, the investigation on the angular dependency of the microDiamond detector was evaluated using a PMMA cubic phantom surrounded with a water-equivalent phantom material (WT1). The detector orientation was positioned with its axis being parallel to the central beam axis (vertical orientation). The detector was set up based on the standard set up: 10×10 cm^2, a source-to-surface distance (SSD) of 100 cm, the depth of measurement is 1.5 cm for 6 MV, and a dose-rate of 419 MU/min is being delivered. A set of measurements was performed at different gantry angles based on an interval of 15^o steps. The angular dependency of radiation was tested by rotating the gantry between -90^o to + 90^o (see Figure 3.5). The position of the sensitive volume at the isocentre was positioned by utilizing the in-room lasers. The angle was varied by rotating the gantry but keeping the detector's position fixed. The performance of the microDiamond detector was assessed relatively on the normalised output at 0^o gantry angle.

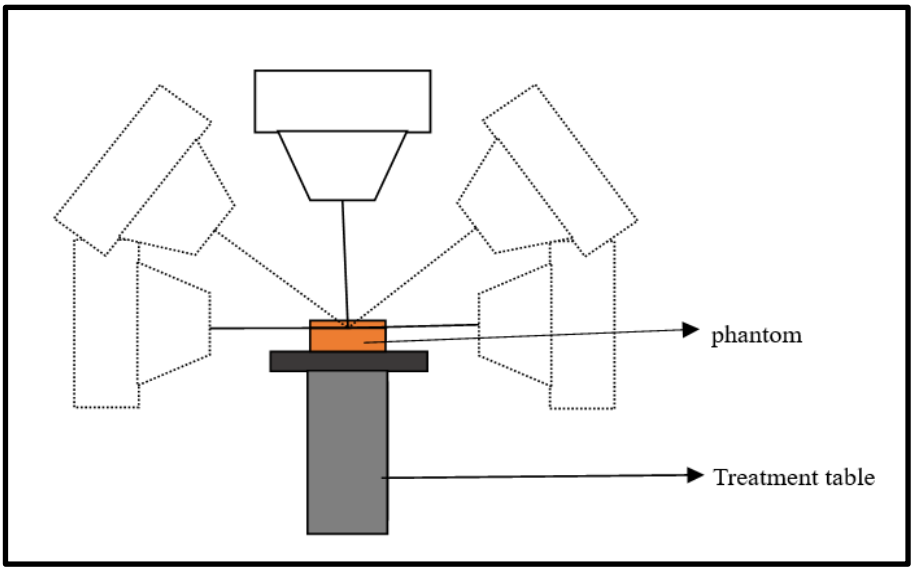

Figure 3.5: Schematic diagram showing the setup for angular dependency investigation for microDiamond detector measured at 1.5 cm depth

3.3.7 Dose dependence

Dose linearity of the microDiamond detector response to a fixed dose-rate was also investigated. Different doses, from 0.01 to 10 Gy (1-1000 MU), were delivered to the detector at a depth of 1.5 cm in the PMMA cubic phantom surrounded by solid water-equivalent multi-block phantom for a field-size of 10 × 10 cm^2 and at SSD of 100 cm with a fixed dose-rate of 419 MU/min. The objective of this investigation was to study the relationship between the measured charge (C) and the dose (Gy). Theoretically, the detector's sensitivity can be calculated manually as given below:

Diamond sensitive volume [93] = 4.0 mm^3 …… (3.2)

Density of diamond [100] = 3510 kg/m^3 with the assumption that the constant is known exactly,

$$\text{Mass of diamond detector} = (3510\ kg/m^3) \times (4.0 \times 10^{-12}\ m^3)$$

$$= 1.4 \times 10^{-8}\ kg \quad \ldots\ldots\ldots\ldots\ldots\ldots\ldots \quad (3.3)$$

1 Gy absorbed dose corresponds to a radiation energy absorption of 1 J/kg of material. Therefore;

$$1\ Gy = 1\ J/kg \quad \ldots\ldots\ldots\ldots\ldots\ldots\ldots \quad (3.4)$$

From the definition in equation (3.4), 1 Gy produces 1.4×10^{-8} J of absorbed energy of the mass of the diamond detector. By definition, 1eV is the amount of kinetic energy (1 J) gained or lost by a single electron as it traverses through a potential difference of one volt (1V) in a vacuum.

$$1 \text{ eV} = 1.602 \times 10^{-19} \text{ J} \quad \text{..... (3.5)}$$

Hence, the energy imparted onto the sensitive volume of diamond corresponds to 8.7×10^{10} eV. If 13 eV/ion pair is required to produce an ion pair in the diamond, thus 8.7×10^{10} eV will produce 6.7×10^{9} ion pairs. Assuming that no recombination event occurs and that the entire charges take part in the photoconduction event, then by multiplying 6.7×10^{9} of electrons pairs with the electron charge will give 1.1 nC. Therefore, the theoretical calculation of microDiamond detector sensitivity is given by;

$$\text{Sensitivity of microDiamond detector} = 1.1 \text{ nC/Gy} \quad \text{..... (3.6)}$$

A sensitivity of 1.1 nC/Gy for the microDiamond is a perfect theoretical calculation, but in the reality, recombination process may occur and some electrons may be trapped either at the shallow or deep trap due to the impurities or defects in the physical diamond.

3.4 *Results*

3.4.1 Leakage measurement

The result of the leakage measurements for the microDiamond detector is presented in Table 3.1. At room temperature, the diamond will be in the meta-stable state and acts as an insulator. The dark charge measured was due to the charge generated by the trapped electrons inside the diamond. Following the irradiation, the electrons that were trapped at shallow and deep energy levels were released. Therefore, as the detector continues to absorb the dose (radiation), the leakage charge increases as more of the electrons trapped were released until it reaches a stabilized state. By measuring the response from the detector alternately with and without radiation will disclose how fast the traps were being emptied before the next reading with the radiation being applied. The leakage charge stability was evaluated by performing measurements as a function of time after the irradiation.

Table 3.1 shows that the leakage current becomes stable after multiple irradiations. The uncertainty reading obtained in the absence of radiation was within 0.5 %, and it is in agreement with IAEA dosimetric requirement [97], where the threshold dosimeter for stability should be less than 0.5 %.

Measurements	Dark charge measurement (pC)	Period of measurement (s)
1	1.022	60 ± 1
2	1.025	60 ± 1
3	1.030	60 ± 1
4	1.032	60 ± 1
5	1.033	60 ± 1
Average	1.028	
SD	0.005	
% SD	0.5	

Table 3.1: The results of the dark charge measurement for 60 s before and after irradiation for 200 MU at 207 MU/min. The magnitude of dark charge increased as more electrons were released following the dose absorption

From Table 3.1, the average dark charge was found to be 1.03 x 10^{-12} C. From the following equation:

$$I = \frac{Q}{t} \qquad \text{..... (3.7)}$$

where Q is the charge measured, I is current, and t is the time of measurement obtained from the dosemeter, the dark current is found to be:

$$= 1.03 \times 10^{-12} \text{ C}/ 60 \text{ s}$$

$$= 17.1 \pm 0.4 \text{ fA} \quad \text{..... (3.8)}$$

The dark current obtained from the calculation above is in agreement with the manufacturer's claim of it being less than 20 fA [91]. Woodings et al. [101] reported the value of leakage current as 0.04 fA for 21 minutes measurement between the absence of radiation and after the irradiation. Laub et al. [85], on the other hand,

measured the leakage current for 300 seconds and obtained a value of 0.0025 fA but no further details were provided on the statistical measurement. In the current investigation, the period of leakage charge measurement is for 60 seconds in the absence of radiation and the other 60 seconds is in the presence of radiation. Five consecutive measurements were conducted to get better evaluation on the mean of the leakage current.

The signal-to-noise ratio evaluation is a straightforward comparison between the detector response with and without radiation for the same period of time. From the detector's response, the signal-to-noise ratio (S/N) is given by:

$$S/N = \left(\frac{detector\ response\ with\ radiation}{detector\ response\ without\ radiation}\right) \quad \ldots\ldots\ldots\ldots\ldots\ldots\ldots\ldots (3.9)$$

S/N ratio and response time from the detector are important in modulated beams intensity dosimetry since the small beam variations and sharp field edges are employed. Consequently, the volume of the detector needed is very small but requires a very high signal-to-noise ratio value.

Measurements	Periods of measurement (s)	Measured with radiation (nC)
1	60 ± 1	2.480
2	60 ± 1	2.480
3	60 ± 1	2.470
4	60 ± 1	2.470
5	60 ± 1	2.470
Average		2.480
SD		0.005
% SD		0.5

Table 3.2: The results of the irradiation measurement for 60 s with 200 MU at 207 MU/min for the signal-to-noise ratio measurement

It is found that at 207 MU/min, the signal-to-noise ratio (S/N) for the microDiamond detector is 2406 while according to the recommendation by IAEA [97], the signal-to-noise ratio should be at least more than 200:1. Tranchant et al. [40] reported the signal-to-noise ratio to be < 1000 for the modulated beams intensity dose

measurement. It is clear from the evaluation obtained above that the microDiamond detector has low current leakage and is therefore suitable for therapeutic dosimetry.

3.4.2 Pre-irradiation (priming irradiation)

For the purpose of clinical measurement, it is a good practice to ensure that enough priming dose is applied on the detector until a stable reading output is obtained before any measurements are conducted [97]. This was done by delivering a total dose of 27 Gy on the detector in order to determine the minimum dose required by the detector to achieve a stable signal.

Figure 3.6 presents the pre-irradiation measurement results for the microDiamond detector. The initial response from the detector is attributed to the process of filling up the traps in the forbidden gap. As explained in section 3.3.4, when as the electrons acquire enough energy, they will be released from the traps . After a 500 cGy dose is delivered, the small increase in detector response may be attributed to the re-filling of shallow traps which has been emptied between the measurements before the detector reaches the plateau region or stable signal response. At this stage, there is only a small deviation in the subsequent dose measured.

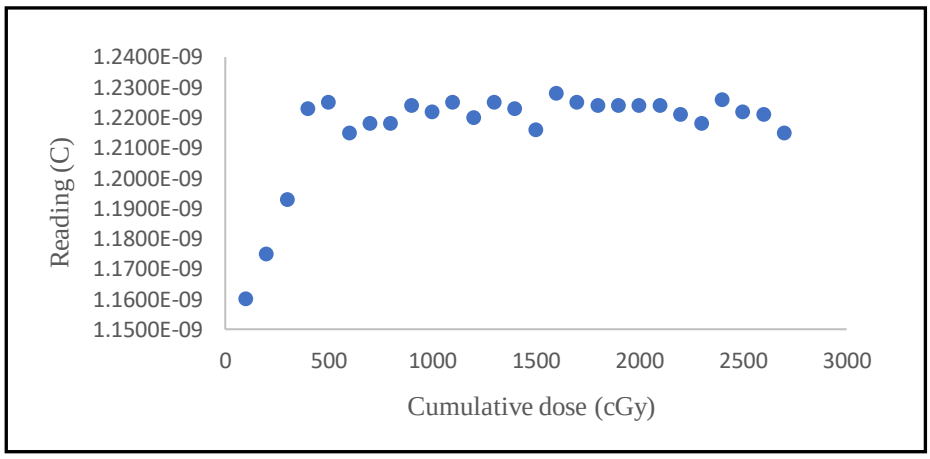

Figure 3.6: Pre-irradiation measurements for the microDiamond detector with a total dose of 2700 cGy being delivered at 419 MU/min measured at 1.5 cm depth of 6MV

Figure 3.7 presents the percentage difference in response of the detector with the cumulative dose delivered. The percentage deviation was determined by dividing the signals with the mean signal at the plateau region. The response of the initial irradiation was approximately 5 % lower than the value at the plateau region. A dose

range between 500 cGy to 1000 cGy is required for the detector to stabilize at the level of 0.5 % and 0.2 %, respectively. The result was in agreement with the findings of Ciancaglioni et al. [49], Yuich et al. [86], Manuel et al.[89] and Di Venanzio et al. [90] who all reported the required dose for pre-irradiation to be between 500-900 cGy for ± 0.5 % deviation and between 1000-1200 cGy to achieve within ± 0.2 % deviation. In contrast, Laub et al. [85] reported that without any pre-irradiation, the response of the microDiamond detector was within 0.5 % and suggested that 300 cGy of pre-irradiation is sufficient for the microDiamond detector. The results from the current study indicate that the microDiamond detector requires a pre-irradiation of at least 1000 cGy in order to achieve a deviation of within 0.2 %. If the detector is used daily, less priming dose will be required and a larger dose is needed if the detector had not been used for a long time.

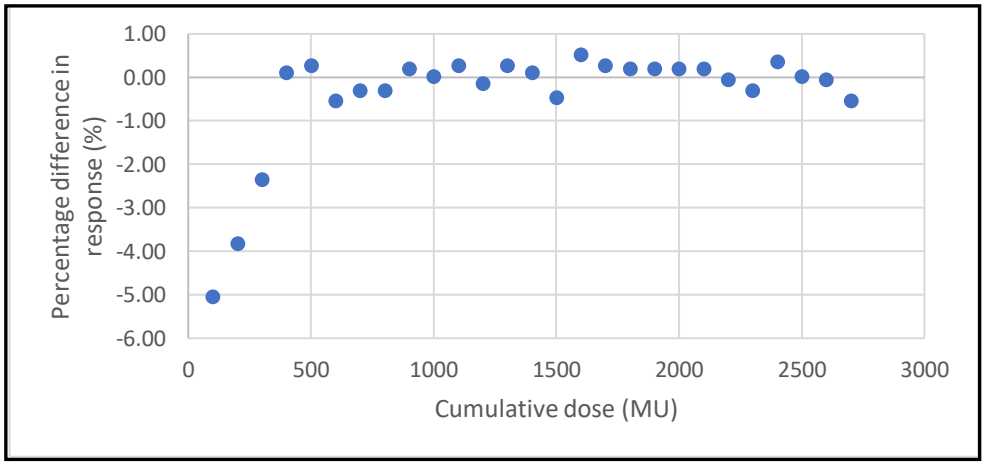

Figure 3.7: Percentage deviation on detector response against the cumulative dose delivered

3.4.3 Repeatability

Repeatability was evaluated at four different dose-rates for five consecutive measurements with 120 seconds time interval between the measurements. The reason for using longer time interval is to ensure that the dark charge has decreased before the next measurement is read. The results of the measurements are reported in Table 3.3. The delivery time of irradiation is calculated using the reciprocal of fixed MU over the respective dose-rate.

In general, it was found that the repeatability for the microDiamond detector is less than 0.2 % for the various dose-rates. The threshold recommended by the IAEA

[97] is for the repeatability value to be less than 0.5 %. In the study by Marsolat et al. [87], the repeatability for microDiamond detector was reported to be less than 0.1 % for proton beam source. No investigator has reported the repeatability for microDiamond detector with a photon beams source.

The results from Table 3.3 further show that the microDiamond detector has an excellent repeatability of less than 0.1 % for high dose-rate while the percentage of repeatability for low dose-rate is higher but still within the tolerance threshold. For low dose-rate, only 10 MU is delivered to ensure LINAC stability. The evaluation of results on the repeatability performance of the microDiamond detector in this study provides new insights as no other authors have reported any results for photon beams based on either high or low dose-rate. Interestingly, results from Table 3.3 indicate a difference of approximately 0.5 % in the charge measured at different dose-rates but fixed monitor unit (MU).

Dose-rate	**419 MU/min**	**207 MU/min**	**25 MU/min**	**5 MU/min**
MU	100	100	10	10
Delivery time (s)	14.32	28.99	24.00	120.00
Reading (nC)	1.245	1.239	0.126	0.128
	1.243	1.240	0.125	0.128
	1.245	1.239	0.125	0.128
	1.246	1.239	0.125	0.128
	1.243	1.239	0.125	0.128
Average(nC)	1.244	1.239	0.125	0.128
SD	0.001	0.001	0.000	0.000
%SD	0.11	0.04	0.18	0.15

Table 3.3: Evaluation of repeatability of microDiamond detector fixed at 100 MU (for 419 and 207 MU/min) and 10 MU (for 25 and 5 MU/min) measured for different dose-rates selected from the LINAC

3.4.4 Angular dependency

The results obtained on the angular dependency for microDiamond detector is shown in Table 3.4. The results from the output for different gantry angles were normalised with the output at gantry angle 0º. Figure 3.8 presents the percentage deviation of the

detector response against the gantry angle. The response from the detector up to ± 60° was approximately less than 1 %, and this is in agreement with the manufacturer's claim of up to ± 45° for detector directional dependency of less than 1 %. This is also in agreement with Larraga-Gutierrez et al. [89] who reported the deviation in respect to the response at 0° gantry angle to be within 1 % for gantry angle less than ± 40° and for a field-size of 3×3 cm^2. The higher deviation at gantry angle more than ± 60° is due to the attenuation of the water-equivalent multi-block phantom.

Gantry angle (degree)	Reading 1 (nC)	Reading 2 (nC)	Reading 3 (nC)	Mean (nC)	%SD	Normalised response (%)
0	1.244	1.242	1.242	1.243	0.12	0
15	1.245	1.246	1.246	1.246	0.06	0.24
30	1.249	1.248	1.248	1.248	0.06	0.46
45	1.248	1.249	1.248	1.248	0.06	0.46
60	1.229	1.229	1.229	1.229	0.00	-1.10
75	1.126	1.125	1.125	1.125	0.06	-9.44
90	0.839	0.839	0.839	0.839	0.00	-32.48
-15	1.247	1.246	1.247	1.247	0.06	0.32
-30	1.256	1.257	1.256	1.256	0.06	1.10
-45	1.249	1.249	1.249	1.249	0.00	0.51
-60	1.23	1.23	1.229	1.230	0.06	-1.05
-75	1.132	1.131	1.132	1.132	0.06	-8.93
-90	0.791	0.7925	0.7915	0.792	0.08	-36.29

Table 3.4: The charge measured from variable gantry angle were normalized to the charge measured at gantry angle 0^0 in determining angular dependency for microDiamond detector

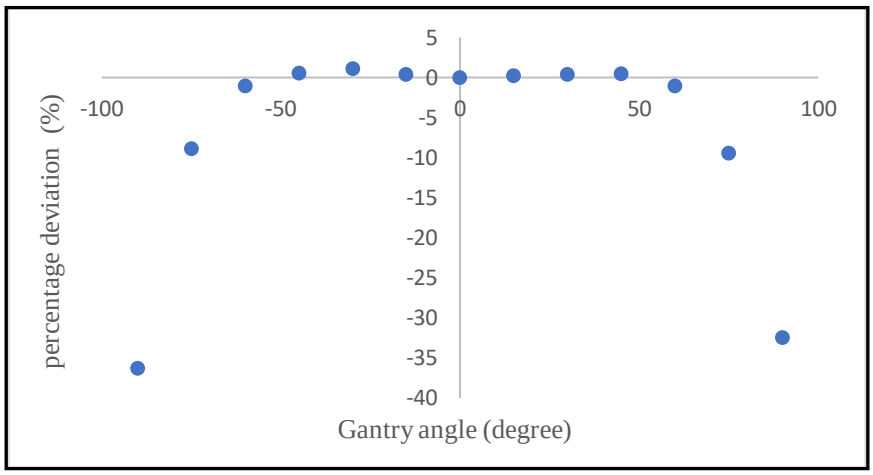

Figure 3.8: Percentage deviation on the response of microDiamond detector at various gantry angle and normalized at 0^0 gantry angle

A proper angular dependency evaluation is best done with a spherical phantom for complete gantry rotation angles that exactly matched the VMAT delivery.

3.4.5 Dose dependence

Table 3.5 presents the response of the microDiamond detector against the absorbed dose. The measurements were performed at the maximum available dose-rate (419 MU/min) at a depth of 1.5 cm, which is at the same depth for the LINAC absolute dose calibration that equates 1 MU to 0.01 Gy for 6 MV photon beam. During the measurements, all correction factors according to the calibration protocol from IAEA [97] are considered.

MU	D_w(Gy) (0.005)	Reading (nC)
1	0.01	0.012
5	0.05	0.063
10	0.1	0.125
50	0.5	0.622
100	1	1.244
300	3	3.703
700	7	8.695
1000	10	12.401

Table 3.5: Results of the dose response from the microDiamond detector against the monitor unit (MU) delivered

However, with this set up for the dose dependence is less accuracy since the tolerance for absolute dose calibration is within 2 % and the low number of monitor unit (MU) employed will worsen the accuracy.

Figure 3.9 presents the plot of the microDiamond detector response against the absorbed dose. The gradient of the plot provides the sensitivity of the microDiamond detector, which is 1.24 nC/Gy with 0.1 % uncertainty.

From equation 3.6, the theoretical calculated sensitivity of microDiamond detector is given as 1.1 nC/Gy while the value provided from the manufacturer's calibration certificate is 1.264 nC/Gy with 5 % uncertainty. Marsolat et al. [87] reported that the sensitivity of the microDiamond detector is between 0.667 to 1.018 nC/Gy with proton beam source. Larraga-Gutierrez et al. [89] and Di Venanzio et al. [91] reported the sensitivity of the microDiamond detector obtained as 1.080 ± 0.005 nC/Gy and 1.134 nC/Gy, respectively, for photon beams. The sensitivity value obtained in the present investigation is 2 % less than the calibration value from the manufacturer. The different nominal value may be attributed to the different radiation source and radiation dose-rate. The plot in Figure 3.9 indicates that the evaluated detector has excellent dose linearity with the sensitivity of the microDiamond detector as evidenced by the R^2 parameter with the best fit of 1.

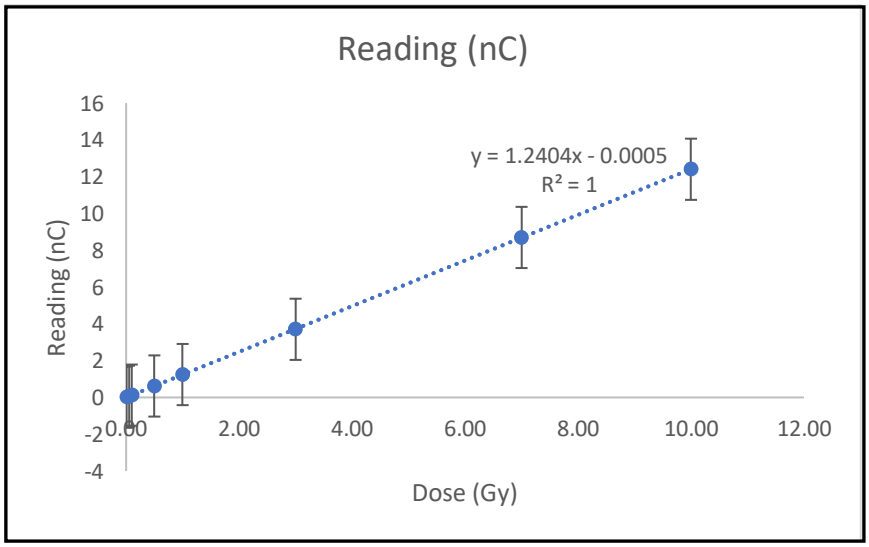

Figure 3.9: Plot for the linearity of microDiamond detector response with the absorbed dose. The line represents a linear fit with a linearity factor R=1 with a precision of 10^{-3}

Figure 3.10 presents the percentage deviations of measured charge per unit dose (C/Gy) normalised at 3 Gy. It can be seen that for a dose of more than 0.5 Gy (50 MU), the deviation level obtained was within 1.0 %, while for dose of less than 0.1 Gy (10 MU), the deviation is much higher. The reason for selecting 3 Gy was due to the nominal clinical dose delivery. Result of this investigation also reveals that the microDiamond detector loses sensitivity at low dose measurement. This is an important factor for VMAT dose delivery since the monitor unit employed might be less than 10 MU, and as such, the deviation can be expected to be more than 3 %.

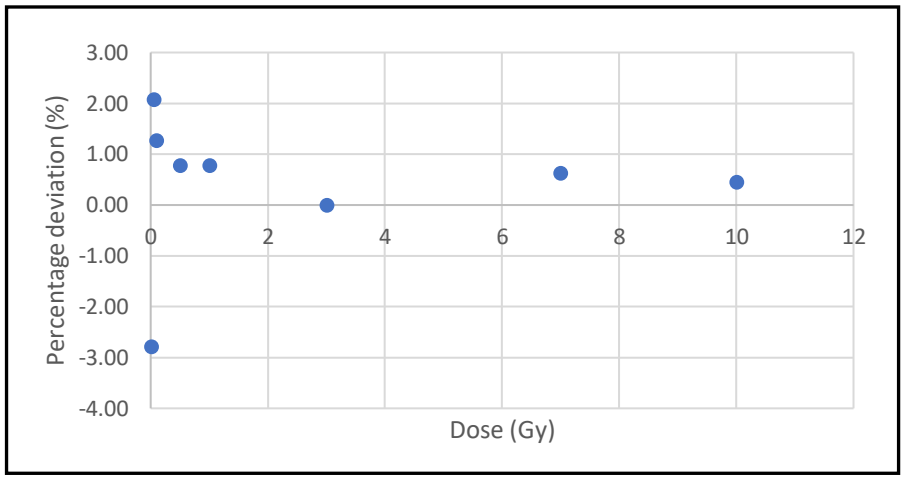

Figure 3.10: The percentage deviation of the measured charge per unit dose (C/Gy) with respect to the cumulative dose

3.5 *Conclusion*

Several studies have investigated the characteristics of the microDiamond detector (PTW 60019) on a small field either for photon, electron or proton. The detector in a metal/p/p^+ layered configuration was operated with zero bias voltage. The high density in diamond due to the number of carbon atoms per unit volume, allows it to have a small active volume for a high spatial resolution, which fits the criteria for measuring advanced techniques in therapeutic delivery. Throughout the investigations, only 6 MV photon energy was used with a PMMA cubic phantom surrounded with the multi-block solid water-equivalent phantom. The depth of measurement is at 1.5 cm (maximum depth dose). The results of the investigations on the dosimetry for the microDiamond detector for its leakage current measurement, pre-irradiation requirement, repeatability, angular dependency and dose linearity had been presented.

Leakage measurements, which indicate the dark current value in the absence of the radiation for the microDiamond detector is found to be 17.1 fA with 2 % of uncertainty. As shown in Table 3.1, the increase in dark current measurements is due to the deep traps being filled up which gradually increases the diamond detector's sensitivity until an equilibrium state is reached. This process is known as pumping. This is in agreement to the dark current value of $\pm < 20$ fA quoted in the manufacturer's certificate. The leakage charge measurement was in the absence of radiation for 60 seconds before irradiation and a further 60 seconds for 200 MU at 207 MU/min. Five consecutive measurements were made alternately with and without radiation. None of the previous researchers had reported in detail on the measurements for leakage charge for the microDiamond detector. The signal-to-noise ratio (S/N) for the microDiamond detector was found to be higher than the minimum recommended by the IAEA.

Results from the study suggested that the microDiamond detector requires a priming dose of between 0.5 to 1 Gy for the measurement deviation to be within 0.5 % and 0.2 %, respectively before it can reach stability. This was in agreement with the reported results by several researchers but contradicts that reported by Laub [85], who suggests that a priming dose of 250 cGy is sufficient to achieve 0.1 % deviation.

The microDiamond detector is also found to be reliable and stable for dosimetry as it shows good repeatability value of less than 0.15 %. This is similar to the manufacturer's quote on dose stability, which is less than 0.25 % even with different dose-rates. The current investigation is the first to look at the repeatability of the detector for different dose-rates.

The investigation on angular dependency for the microDiamond detector when positioned in vertical orientation up to $\pm$ 45° indicates the deviation to be within 0.5 % from gantry angle of 0° response. This was in agreement with the manufacturer's quotation for a directional response of less than 1 % for gantry angle less than $\pm$ 40°. As expected, the deviation was found to be more pronounced for larger gantry angle due to the setup geometry. The evaluation on the angular dependency is critical, especially for measurement with the VMAT technique, as it requires full gantry rotation during beam delivery. It is also desirable to have detectors being independent of the gantry angle.

The evaluation on the sensitivity of the microDiamond detector is found to be 1.24 nC/Gy with 0.1 % uncertainty while the manufacturer's calibration certificate quoted the detector's sensitivity as 1.26 nC/Gy with 5 % uncertainty for ^{60}Co gamma source. From the theoretical calculation, the sensitivity of microDiamond detector is given as 1.1 nC/Gy. The differences in the results on the sensitivity of the microDiamond detector may be attributed to the uncertainty on the precision of the sensitive area dimension due to the contact between the wire and the shape of the sensitive area. Results on dose dependence indicate that the microDiamond detector response has excellent linearity with the dose, with the deviation being less than ± 1 % down to the lowest delivered dose value of 0.5 Gy. The present investigation also revealed that the microDiamond detector lost its sensitivity at low dose delivery.

In general, the evaluations on the characteristics of microDiamond detector for the use in VMAT dose delivery measurements were satisfactory except for low dose delivery, where it seems to lose its sensitivity. This is based on the result of a sensitivity of 1.24 nC/Gy revealed in this study.

4

Dose-Rate Dependency of microDiamond and DD4 Detectors

4.1 *Introduction*

In solid-state physics of semiconductor, the mobile carriers (electrons and holes) are created and eliminated through the process known as carrier generation and carrier recombination, respectively. In order to create free electrons within a diamond, the carrier must be given energy that is at least equal to the energy in the bandgap (5.5 eV) in order to move an electron from the valence band to the conduction band.

At room temperature or thermal equilibrium, the generation and recombination rates are balanced and thus the net charge carrier density remains constant:

$$n_o = p_o \quad \ldots\ldots (4.1)$$

where n_o and p_o are densities of electrons and holes at thermal equilibrium, respectively. Therefore, the product of electrons and holes densities is constant,

$$n_o p_o = n_i^2 \quad \ldots\ldots (4.2)$$

where n_i^2 is the product of the electron and hole densities. In other words, the carrier recombination rate for a pure diamond is proportional to the square root of the carrier generation (electrons and holes) rate [32]. In the presence of impurities or defects in the diamond crystal, additional energy level will be introduced between the conduction band and valence band known as trap. During the recombination process, an electron can be captured in the trap. If the number of electrons in the trap is large, the recombination rate will be greater than the rate of the carrier generation, as follows:

$$n_o p_o << n_i^2 \quad \ldots\ldots (4.3)$$

Therefore, the recombination rate will be almost independent of the rate of ion-pairs production or be linear in the detector signal with the radiation dose-rate. For the diamond to be used in radiation dosimetry, a small amount of impurities or structural

defect will cause the signal in the detector to be linear with the dose-rate but excessive amount of impurities will cause the detector to be insensitive [32, 98, 102].

In the absence of radiation and at room temperature, the production of electrons and holes will be constantly generated from the thermal energy. The absorption of radiation will induce a temporary change in the electrical conductivity due to the production of the electrons and holes that have enough energy to be free to move through the diamond. This will also change the current flow within the crystal. The relationship between the current induced by the radiation and the radiation dose-rate for the diamond is given by Fowler [22] as follows,

$$I=R(\dot{D})^{\Delta} + I_{dark} \quad \text{..... (4.4)}$$

where I is the current measured by the detector, I_{dark} is the detector's leakage current, R is detector response characteristic, $\dot{D}$ is radiation source dose-rate and Δ is a non-linearity factor for diamond detector. The value of non-linearity factor varies between 0.5 and 1 depending on the distribution of the trapping centre in the crystal [22].

The attractive characteristics of diamond as discussed in Chapter 3, makes it a suitable element for therapeutic dosimetry. The only drawback of using diamond as a radiation detector is due to its dose-rate dependency as discussed above. In this chapter, an investigation was conducted on the characteristics of dose-rate dependence of microDiamond and synthetic diamond known as DD4 detectors. The evaluation of the two diamond detectors were based on Fowler's model where the diamonds are expected to have a non-linear relationship with the dose-rate [3,4]. In the present investigation, two methods were employed in varying the dose-rate of the radiation source. Besides the dose-rate response from both detectors, this investigation also attempted to demonstrate that the DD4 detector has the capability of measuring pulse-by-pulse dosimetry at the standard clinical pulse-rate with the support from an in-house customised, high count-rate system developed by a team of researchers from the University of Bristol, UK. The results of the investigation on the dose-rate dependency of the DD4 detector is important for the next chapter, where the dose for the VMAT technique delivery is measured at the pulse-rate using the DD4 detector.

The characteristics of DD4 detector have been investigated by Piliero [13] and thus will not be discussed at length in this chapter.

4.2 The Prototype CVD Single Crystal Diamond Detector

The prototype diamond detector purchased from the Diamond Detectors Ltd (Poole, UK) to be used in this investigation is a single-crystal (SC) fabricated through chemical vapour deposition (CVD) known as DD4 detector. Figure 4.1 presents the photograph of the detector (a) and the radiographic image of the encapsulated DD4 detector (b). The DD4 detector is a high purity single-crystal diamond which means it has less boron and nitrogen as impurities. According to the investigation by Piliero [13], the DD4 detector has a sensitive volume of $1 \times 1 \times 0.3$ mm^3 and fashioned into a cylindrical shape with a diameter of 7 mm [13]. However, other investigators [81,102] have reported the active sensitive volume to be 4.7×4.7 mm^2 and thickness of 500 μm from the same model and manufacturer. The large side of the sensitive volume faces upwards with a novel ohmic metallization of 3 mm in diameter at the top and bottom of the sensitive volume (Figure 4.1(b)). The electrical contact on the sensitive volume is made based on a proprietary metallization technique (DCL/Pt/Au).

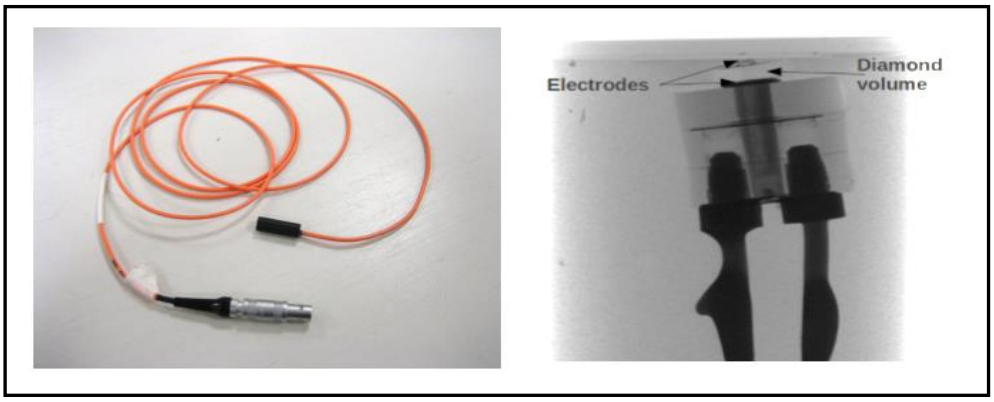

(a) **(b)**

Figure 4.1: Photographs of DD4 detector (a) and radiograph of the detector (b) [13]

The theoretical calculation for the DD4 detector's sensitivity using the method described in section (3.3.7) is given by 81 nC/Gy and 2.9 μC/Gy for other sizes of the detector [81, 102], assuming that no recombination event occurs. As reported by Piliero [13], the sensitivity of DD4 detector obtained is 180 nC/Gy with irradiation

source from the orthovoltage machine while Schirru et al. [102] and Galbiati et al. [81] reported the DD4's sensitivity based on their samples to be 510 $nCGy^{-1}$ and 1820 $nCGy^{-1}$ with photon beams, respectively. The different values of the sensitivity from the same model (DD4) and manufacturer may be attributed to the difference in the active volume of diamond material. Theoretically, the DD4 detector is found to be more sensitive compared to the microDiamond detector.

4.3 *Materials and Methods*

4.3.1 DD4 detector and electrometer

In order to investigate the suitability of the DD4 detector for use in high pulse-rate dosimetry, a customised front-end that focuses on a high count-rate with a low intensity signal was developed by a team in the School of Physics at the University of Bristol, UK. An analogue front-end is a charge-sensitive device and the shaping amplifier is used in creating signals from a solid-state detector that requires amplification and filtering before the signals can be digitised and processed [103]. The front-end was designed with the knowledge that the pulses generated from the LINAC is within a few microseconds (µs) with pulse repetition rate below 1kHz and pulse amplitude of 1mA. The developed front-end for the current investigation is an ac coupled preamplifier followed by a two-stage shaper that results in a semi-Gaussian voltage output. The schematic diagram of the front-end is illustrated in Figure 4.2 [23].

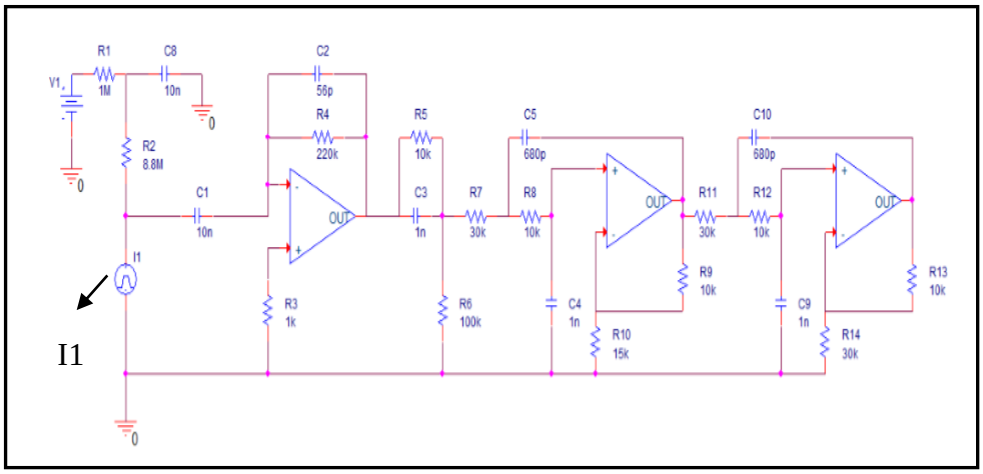

Figure 4.2: Schematic diagram of the front-end developed by a team from the University of Bristol, UK

The DD4 detector is presented by I1 in Figure 4.2. Since the prototype diamond detector is not a Schottky-diode type, it is supplied with 100 V for its operation. In Figure 4.2, the bias voltage for the detector comes from the high voltage (HV) source labelled as V1. Pulses from the LINAC will cause charges to flow onto the ac decoupling capacitor C1. Then the pulses will be amplified by the Texas Instruments TL082BCP, which is a pre-amplifier that has a fairly fast slew-rate, i.e. the speed of output signal transition will be at least equal to the minimum input rate. A summary of the property of the amplifier is provided in Table 4.1.

Property	Value
Bandwidth	3 MHz
Slew rate	13 $V\mu s^{-1}$
Maximum voltage supply	± 18 V
Operating temperature	0-70° Celsius

Table 4.1: The properties of TL082BCP from Texas Instruments as an amplifier [23]

The preamplifier that follows C1 is arranged as an operational integrator. The preamplifier output is first passed to a pole zero cancellation circuit in order to cancel the effect of the pole at $s = -R_4C_2$ and also to provide optimal baseline restoration. It will then pass through two Sallen-Key filters in a low pass configuration in order to filter out high frequency noises in the system and also to reshape the pulse for data acquisition. The output of this filter will produce a semi-Gaussian voltage pulse. The voltage output was measured between the circuit ground and the output of the amplifier used in the second stage of pulse shaping. The National Instruments PCI 6024E data acquisition (DAQ) was used to digitize the input signal to get a reading from the sensor. An analogue pulse generated during irradiation will be converted to digital signal (ADC) before it triggers the DAQ system to display the pulse measured using customised LabView software (National Instrument, Texas, USA). The DAQ system is operated at its maximum acquisition rate of 200 kilo-samples per second, resulting in a 5μs time base resolution. Then, the data sampled were analyzed offline using the "ROOT" package [104].

The findings from the investigations by Piliero [13] on the characteristics of the DD4 detector will not be presented here as the data acquisition system was different

from the current system used in this investigation. In Piliero's investigation, the charge generated in DD4 detector was acquired using the I-400 gated integrator electrometer which measures the average current over the integration time. The PSI Diagnostic Software was used to drive the electrometer and to save the data acquired. The A-300 loop controller acted as the interface between the electrometer and computer. Data acquisition using this system only allows a maximum sampling rate of 71 Hz. This means that some of the readings will be missed for integration periods of less than 14 ms since the nominal pulse from the LINAC is at 400 Hz. Therefore, a high count-rate device for measuring the pulse-rate from the LINAC is needed. This is the reason why the new high count-rate device was developed in order to accommodate the pulse-rate from the LINAC.

4.3.2 microDiamond detector and electrometer

The setup of the system here is the same as in Chapter 3. Therefore, this will not be discussed again here.

4.3.3 Dose-rate dependence

Given the new advanced techniques in radiotherapy beam delivery that has enabled employment of various dose-rates, it is thus vital to consider the dose-rate dependency of the detectors. This also applies for the new technique of LINAC delivery where flattening-filter-free (FFF) has been introduced in enabling dose-rate delivery capability of up to 1000 MU/min [105]. Since the advanced techniques involve very steep dose gradients, it is therefore desirable that the detector has a linear behaviour with the dose-rate.

An ideal detector to be used in therapeutic dosimetry should have a linear response with the dose-rate, $\Delta = 1$. If $\Delta < 1$, this implies that the response from the detector at a high dose-rate will be lower than the actual response. Here, the signal can be in the form of current, voltage or charge depending on the output device. Equation (4.4) is used to find the relationship between the signal measured by the detector as a function of dose-rate. By plotting the natural logarithm of the signal measured by the diamond detector against the natural logarithm of the dose-rate, an estimated value of Δ can be determined from a linear fit.

$$\log (I - I_{dark}) = \Delta \log (\dot{D}) + \log(R) \quad (4.5)$$

Several authors have specifically studied the dose-rate dependency of the microDiamond detector [106-107]. However, some authors only provide a comparison of the measurement results with other detectors or present the deviation from the normalised measurement obtained without indicating the value of Δ, which is the diamond detector's non-linearity constant. The detector response as a function of the dose-rate can be investigated by adopting two different methods: i) varying the nominal pulse repetition frequency (PRF), and ii) varying the distance between the radiation source and the detector (changing SSD).

The first approach in the evaluation of dose-rate dependency involves selecting the nominal pulse-rate available from the LINAC that will change the number of pulses generated. For the dose-rate dependency evaluation in this study, several dose-rates available from the LINAC were investigated as shown in Table 4.2. This method is adopted only for investigating the dose-rate dependency for the microDiamond.

Field size	10 x 10 cm^2
Depth	1.5 cm
Energy	6 MV
SSD	100 cm
Phantom	Cubic PMMA surrounded with multiblock solid water phantom
Detector orientation	Vertical
Dose rate	419, 207, 25 and 5 MU/min
MU	100
Detector	microDiamond

Table 4.2: The set-up for the measurements of different pulse-rates by varying the dose-rate available at the LINAC

In order to evaluate the response of the microDiamond detector with the dose-rate based on Fowler's proposal, the readout from the dosemeter which is in the form of charge (C) needs to be converted to current (I) by applying equation (4.6). By using PTW UNIDOS Universal dosemeter, leakage charge was eliminated from the reading since the leakage compensation button is available within the dosemeter. Five consecutive measurements for each selected dose-rate were conducted.

$$I_{measured} = \left(\frac{readout\ (C)}{time(s)}\right) \quad \text{..... (4.6)}$$

It is important to highlight that the assumption made is that by varying the PRF, the mean dose-rate will change but the dose per pulse will remain constant. This can be observed when the dose-rate displayed on the monitor fluctuates due to fine tuning of the optimum dose-rate. The time of delivery ($t_{delivery}$) for the fixed dose (100 MU) is calculated by the reciprocal of the selected dose-rate as in equation (4.7)

$$t_{delivery} = \left(\frac{100\ MU}{selected\ dose-rate}\right) \quad \text{.....(4.7)}$$

By applying equation (4.7), the estimated values of time delivery for 100 MU at different dose-rates are as presented in Table 4.3.

PRF (Hz)	Dose rate (MU/min)	Irradiation time (s)
400	419	14.32
200	207	28.99
50	25	240.00
6.25	5	1200.00

Table 4.3: The irradiation time for the dose delivery at different dose-rates for a fixed 100 MU using equation (4.7)

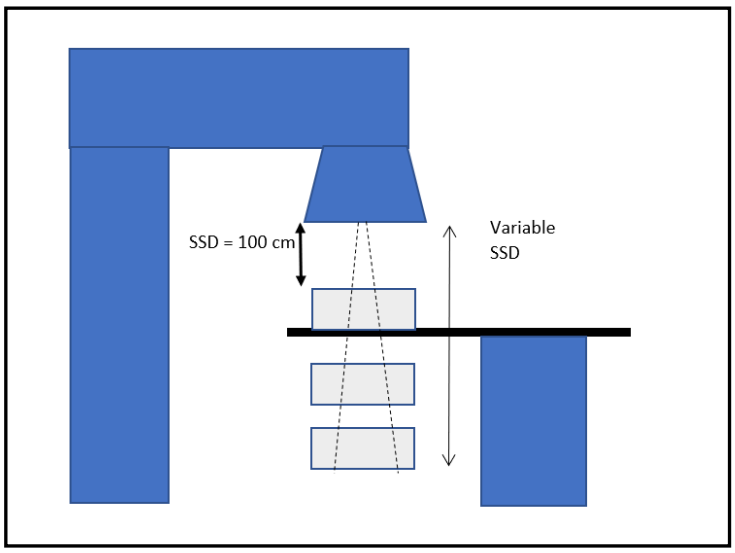

Figure 4.3: Schematic diagram showing the variation in dose-rate by varying the distance between the radiation source and the detector

The second approach in the evaluation of dose-rate dependency was by varying the distance between the radiation source and the detector. The distance from the radiation source to the detector can be varied by lifting the height of the treatment table up or down (see Figure 4.3). In order to reduce the uncertainty of the distance measured between the radiation source and the detector, the digital readout of the treatment table's height displayed on the monitor is used. Assuming that the source of radiation is a point source and ignoring the attenuation of the radiation in the air, the number of pulses per unit time or dose-rate ($\dot{D}$) crossing the field-size at a distance (d) is given by equation (4.8):

$$\dot{D} \propto \frac{1}{d^2} \quad \ldots\ldots\ldots\ldots\ldots\ldots\ldots\ldots\ldots\ldots\ldots\ldots\ldots\ldots\ldots \text{(4.8)}$$

Since varying the SSD is related to the difference in percentage depth dose (PDD), the Mayneord factor is introduced in the calculation of the relative dose-rate to ensure accuracy of the measurements. The Mayneord factor is an application of the inverse-square law which helps in calculating the percentage depth dose (PDD) when the photons are being delivered at a distance other than the standard reference conditions. Therefore, the relative dose-rate at a reference distance (SSD of 100 cm) measured at a depth of 1.5 cm towards the various distance measured ($\mathrm{d}_{\text{measured}}$), is given by

$$\dot{D}_{relative} = \left(\frac{\check{D}_v}{\check{D}_r}\right) = \left(\frac{\hat{d}_r}{\hat{d}_v}\right)^2 \quad \ldots\ldots (4.9)$$

where $\dot{D}_{relative}$ is a relative dose-rate, $\check{D}_v$ is dose-rate at respective distance measured at depth of 1.5 cm, $\check{D}_r$ is dose-rate at the reference distance measured at depth of 1.5 cm, $\hat{d}_r$ is the reference distance and $\hat{d}_v$ is the variable distance.

Since the reference dose-rate is at a distance of 100 cm SSD, hence equation (4.9) can be written as follows:

$$\dot{D}_{relative} = \left(\frac{\hat{d}_r}{\hat{d}_v}\right)^2 \quad \ldots\ldots (4.10)$$

Equation (4.9) is known as the inverse-square law and equation (4.10) is known as the Mayneord factor. An investigation for a fixed field-size of 10 × 10 cm^2 at SSD of 100 cm, 1.5 cm depth in the phantom and a fixed dose-rate from the LINAC was conducted to determine the relation for the dose-rate linearity. The investigation using this method was performed with both the microDiamond and DD4 detectors. The microDiamond detector was connected to the PTW UNIDOS Universal dosemeter which gives the output in charge (C). The DD4 detector was connected to the electronic system developed by the team at University of Bristol as explained in section 4.3.1 for measuring the total amplitude of the pulses generated during the dose delivery in volt (V). The set up for both detectors is presented in Table 4.4.

Field size	10 x 10 cm^2
Depth	1.5 cm
Energy	6 MV
SSD	55, 60, 65, 70, 75, 80, 90, 100, 110, 120 130 cm
Phantom	Cube PMMA surrounded with multiblock solid water phantom
Detector orientation	Vertical (parallel detector axis)
Dose rate (LINAC)	419 MU/min
MU	100
Dose meter	PTW UNIDOS/ in-house customised front-end
Time of delivery	14.32 s
Bias voltage	0 V/ 100 V

Table 4.4: The set-up parameters for varying the dose-rates by varying the distance between the radiation source and the detector

Hence, twelve different SSD positions i.e. 55, 60, 65, 70, 75, 80, 90, 100, 110, 120,130 and 140 cm, were set up with the time of delivery fixed at 14.32 s (fixed dose-rate). The closer the detector to the radiation source, the higher will be the dose-rate and the further the detector is from the radiation source, the lower will be the dose-rate. It is worth mentioning that the phantom for the measurements should be large enough to accommodate the increase in the field-size with SSD. As mention earlier, in order to reduce uncertainty and reproducibility of the distance measured between the radiation source and the detector, the digital readout of the height of the treatment table that is displayed on the monitor is used instead of measuring tape.

The plot for the calculation of the effective distance against the relative dose-rate is presented in Figure 4.4. It can be seen that the plots follow the inverse-square law. By applying equation (4.5), the non-linearity of the diamond detector's response to the relative dose-rate can be determined.

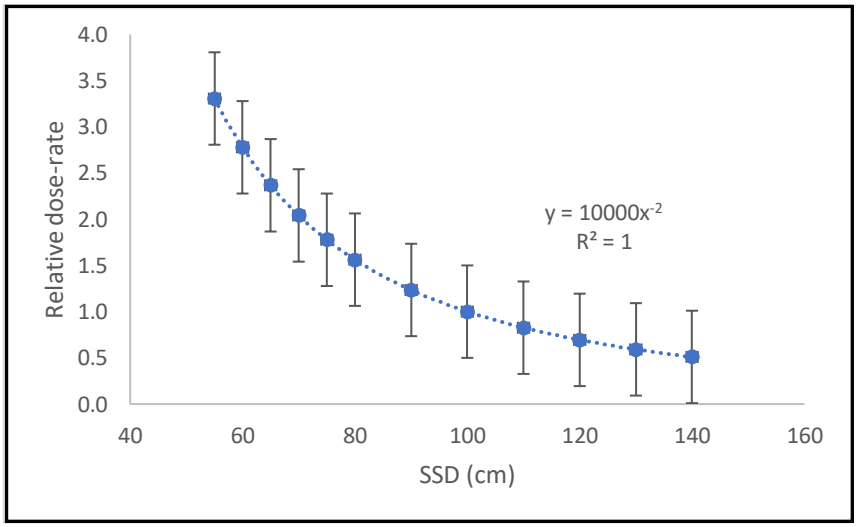

Figure 4.4: The relative dose-rate as a function of distance by applying the inverse-square law (Mayneord factor)

4.4 *Results*

4.4.1 Dose-rate dependency by varying the pulse-rate from LINAC

The evaluation for the dose-rate dependency of the microDiamond detector's response was conducted by changing the PRF of the LINAC. The total current was calculated using equation (4.6) where the time of measurement refers to the time to deliver

100 MU at the respective pulse-rate (equation 4.7). Table 4.6 presents the results for charge measurement by varying the pulse-rate for 10 × 10 cm^2, at 100 cm SSD and measured at 1.5 cm depth. The total monitor unit delivered was 100 MU. The deviation on the charge measured is within 0.5 %, since to deliver 100 MU at low pulse-rate takes longer time.

Dose-rate (MU/min)	Average charge (nC)	SD (%)	Time (s)
419	1.239	0.072	14.32
207	1.236	0.068	28.99
25	1.242	0.221	240.00
5	1.245	0.402	1200.00

Table 4.5: Results of the charge measurements with the microDiamond detector by varying the pulse-rates from the LINAC for a fixed 100 MU for five consecutive measurements

Based on Fowler's proposal (equation 4.5), an estimation of the value of Δ can be determined by plotting the natural logarithm of the signal measured by the microDiamond detector against the natural logarithm of the selected dose-rate. As mentioned earlier, Δ denotes the deviation from linearity for the diamond. The natural logarithms of the pulse-rate and current are presented in Table 4.7. The value of the dose-rate linearity obtained was 0.9985 ± 0.0005 (see Figure 4.5) while Brualla-Gonzalez et al. [105] reported the value obtained as 0.992 ± 0.001 with Varian Truebeam (Varian Medical Systems, Palo Alto) for FFF. The result obtained from the current evaluation provides evidence that the microDiamond detector has a good pulse-rate linearity and supports the claim by the manufacturer that it has very low dose-rate dependency.

Pulse-rate (MU/min)	log (pulse-rate)	I(pA)	log(I)
419	2.622	86.50	-10.06
207	2.316	42.64	-10.37
25	1.398	5.175	-11.29
5	0.699	1.038	-11.98

Table 4.6: Current (I) calculated as a function of dose-rate ($\dot{D}$) dependence for microDiamond

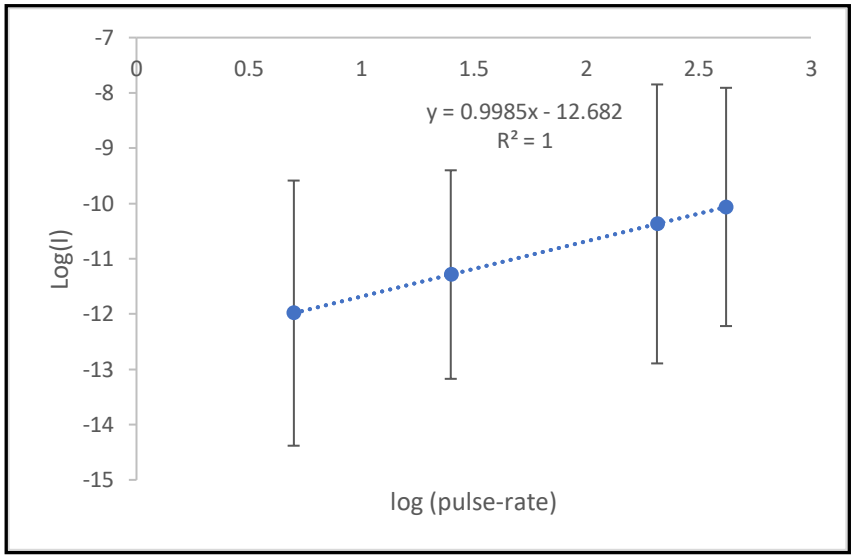

Figure 4.5: Plot of pulse-rate dependency of microDiamond detector shows good linearity measured at 100 cm SSD, 1.5 cm depth with 10 x 10 cm^2. The measurement was performed with cubical phantom

4.4.2 Varying the distance between the radiation source and the detector

Another method of evaluating dose-rate dependency is by varying the distance between the detector and the radiation source with a fixed pulse-rate. This can be done by changing the height of the treatment table. With the same method of calculation as in the previous section, the results are presented in Table 4.7 for the microDiamond detector. Again, leakage charge measurement is omitted by using the leakage compensation button. By plotting the natural logarithm for pulse-rate against the natural logarithm of the current (I) calculated, a Δ value of 1.004 ± 0.002 was obtained (see Figure 4.6) for the microDiamond detector. As far as the present evaluation is concerned, only several researchers have reported the value of Δ using the method of varying the distance between the source of the radiation and the detector [105].

Relative dose rate	Log(dose-rate)	Current(nA)	Log(I)
2.7238	0.4352	0.2374	-9.6245
2.0152	0.3043	0.1737	-9.7602
1.5510	0.1906	0.1348	-9.8702
1.2305	0.0901	0.1068	-9.9716
1.0000	0.0000	0.0864	-10.0636
0.8287	-0.0816	0.0717	-10.1446
0.6979	-0.1562	0.0603	-10.2199
0.5958	-0.2249	0.0515	-10.2883

Table 4.7: Results of the measurement of relative dose-rate dependency by varying the distance between the radiation source and the microDiamond detector

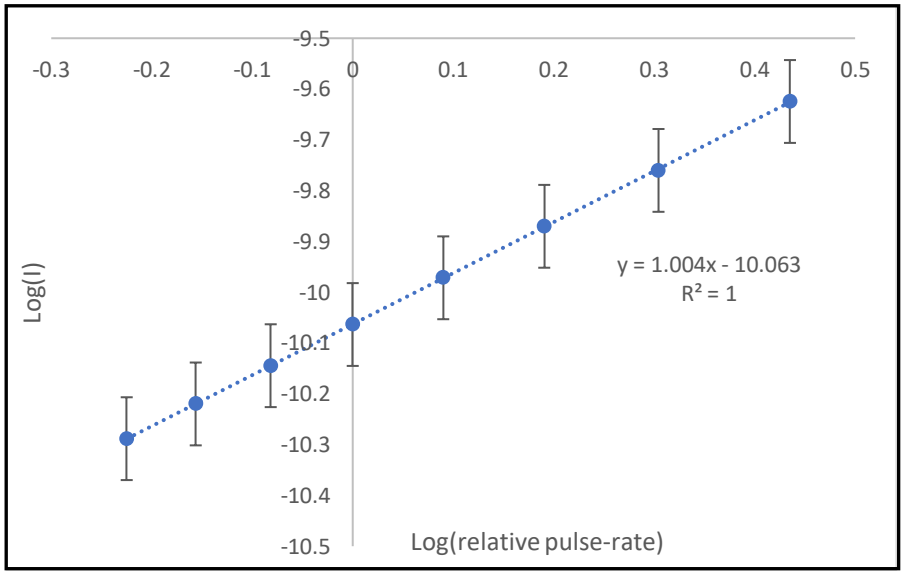

Figure 4.6: Plot of pulse-rate dependency for microDiamond detector by varying the SSD at 10 x 10 cm^2 and measured at 1.5 cm depth with cubical phantom

The energy absorbed by the microDiamond detector at the depth of maximum dose in the cubic PMMA phantom surrounded by the multi-block phantom is expected to closely follow the inverse-square law. Figure 4.7 shows the measured total charge as a function of the distance. The power value obtained is -2.008 which is close to -2 as given by inverse-square law. The deviation in the result may be attributed to attenuation of the photon in the air, as a result of scattering from the phantom and distance positioning. The deviation is within the limit of uncertainty.

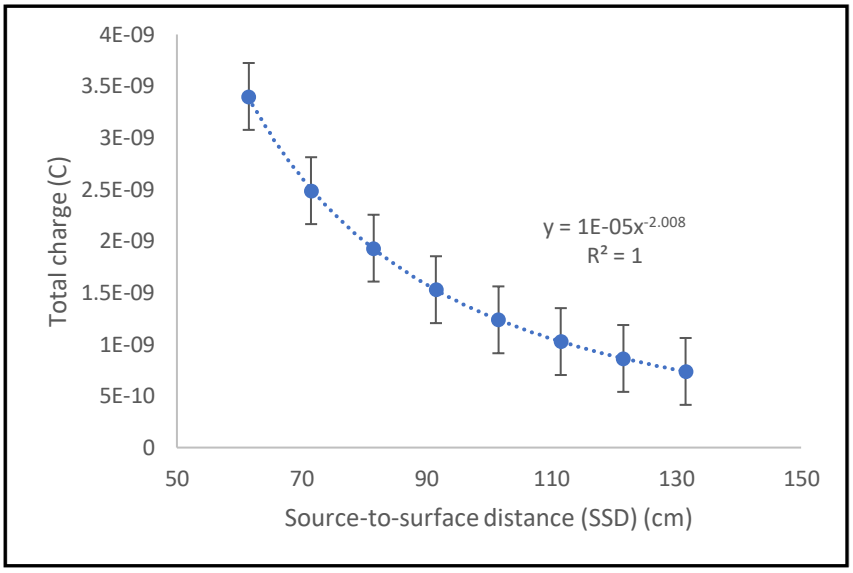

Figure 4.7: Plot of total charge measured by microDiamond as a function of the SSD with the cubical phantom at 10 x 10 cm^2 of field-size

The DD4 detector dependency on the pulse-rate was investigated using the same setup as the microDiamond detector except that the additional distance measurement is closer to the radiation source as presented in Table 4.8. The data were processed by T M Purves [23] using the ROOT package [104] that allows the pulse height which is a measure of the charge of the signal pulse and thus of the dose in patient per LINAC pulse, to be extracted.

Effective SSD (cm)	Relative Dose rate
55.0	3.3058
60.0	2.7778
65.0	2.3669
70.0	2.0408
75.0	1.7778
80.0	1.5625
90.0	1.2346
100.0	1.0000
110.0	0.8264
120.0	0.6944
130.0	0.5917
140.0	0.5102

Table 4.8: The relative dose-rate as a function of the distance between the radiation source and the DD4

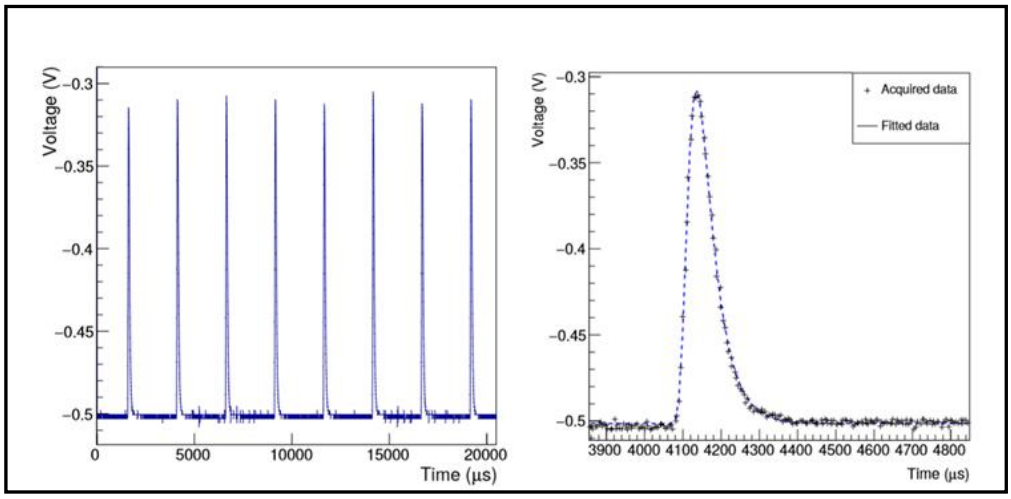

(a) **(b)**

Figure 4.8: An illustration of pulse measurements from the LINAC at a dose-rate of 419 MU/min (a) and measurement of a single pulse (b)[23]

Figure 4.8(a) presents an example of the DD4 detector's response to a series of LINAC pulses while Figure 4.8(b) present an example of a single pulse detected by the DD4 detector. The detector signal pulse displays the expected semi-Gaussian behaviour with a rapid rise and slower fall. It is worth mentioning that the displayed pulse is not the pulse generated from the LINAC.

One of the challenges in designing the front-end is that it must be fast enough so that the signal returns to the baseline before the next LINAC pulse is detected. If this does not occur, the pile-up of the signal will lead to an increased baseline for the subsequent measurements of the detector signal. In order to evaluate whether pile-up event occurs for the DD4 detector, the pulse signal duration is defined as the time the signal pulse exceeded a certain fraction of the pulse height and this was extracted from the data at 2 % and 5 % of the pulse height as a function of the SSD.

The illustration in Figure 4.9 indicates that the pulse duration does not depend on the dose-rate. Therefore, there is no problem with the pulse signal pile-up as long as the PRF is within 2734 Hz. As for the dose-rate dependency, the DD4 detector can be evaluated by varying the distance between the radiation source and the detector. The energy absorbed by the detector at the maximum depth (1.5 cm for 6 MV) is expected to closely follow the inverse-square law (see Figure 4.4).

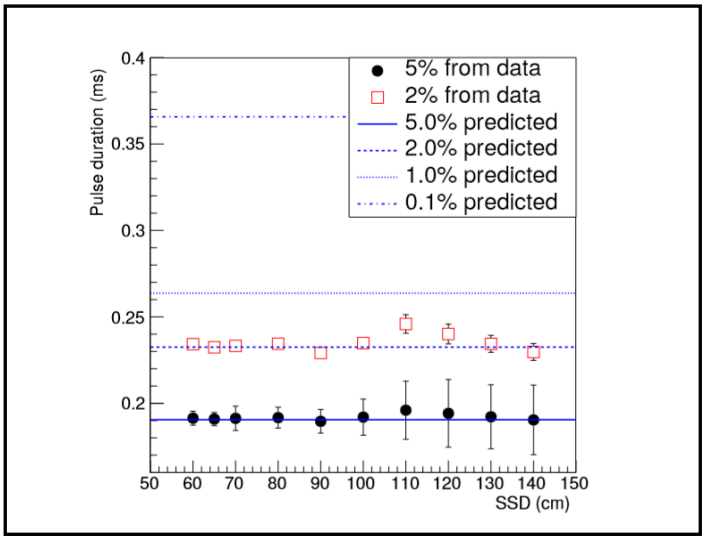

Figure 4.9: Illustration of pulse signal from the DD4 detector is defined as the time the pulse signal exceeded a certain fraction of the pulse height, measured for 2% and 5% of the pulse height as a function of the SSD

Figure 4.10(a) shows the variation of the pulse height (amplitude) of the charge per pulse as a function of the SSD. The variation in pulse height is due to the pulse-to-pulse intensity variation of the LINAC. The average charge per pulse as a function of SSD (Figure 4.10b) is achieved by using the inverse-square law.

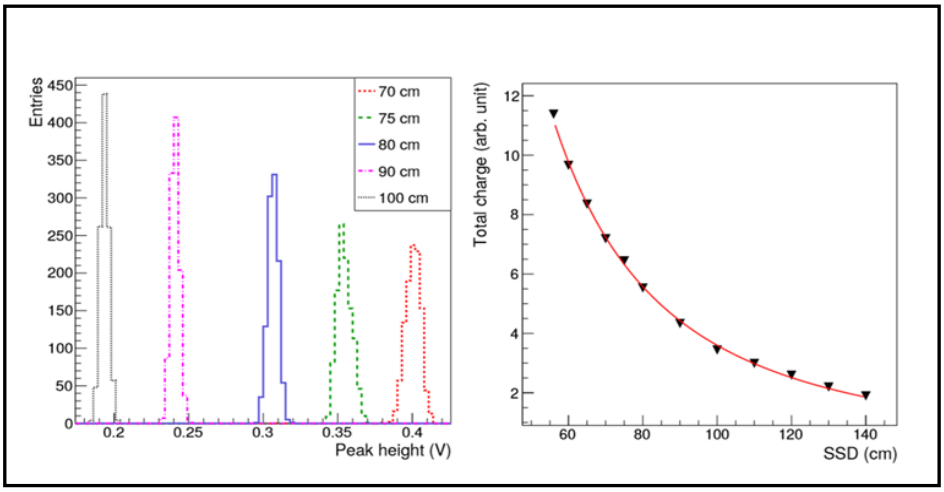

Figure 4.10: Illustration of the amplitude of the pulse as a function of the distance or dose-rate (a) and the average charge per pulse as a function of SSD (b). In Figure 4.10 (b), the error is comparable to the size of the symbol as explained in [26]

The Fowler factor (Δ) can be obtained by employing equation (4.5) and by plotting the natural logarithm of SSD (pulse-rate) against the natural logarithm of the average charge. The value of Fowler factor obtained for the DD4 detector is 0.996 ± 0.025 as presented in Figure 4.11. Piliero [13] reported the Δ value as 0.99 ± 0.03 for the DD4 detector. Galbiati et al. [81] reported the value of Δ as 1.011± 0.008 with ^{60}Co gamma irradiation while Schirru et al. [102] obtained the value of Δ as 1.020 ± 0.008 for 6 MV photon beam.

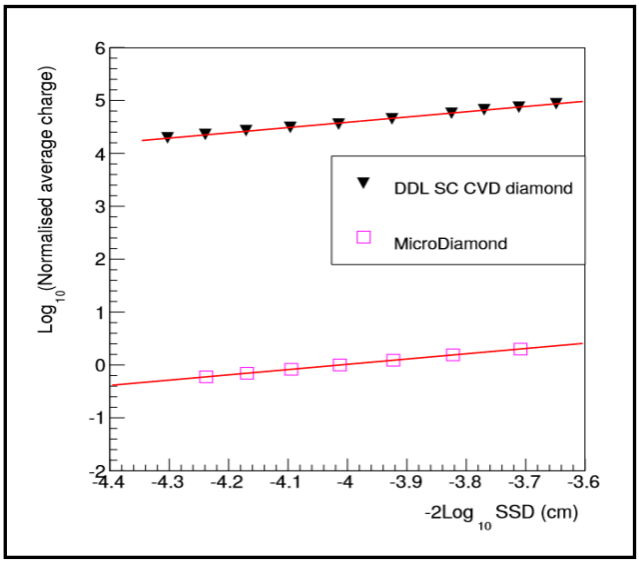

Figure 4.11: Illustration of the natural logarithm of the average charge per pulse for the DD4 detector and the microDiamond detector as a function of SSD. The error bar is comparable to the size of the symbol as explained in [26]

4.5 *Conclusion*

Dose-rate linearity is an important characteristic of a detector to be considered for use in the VMAT dosimetry, since variation pulse-rate were employed during the delivery. In this chapter, the response for the microDiamond and DD4 detectors on the pulse-rate were evaluated. The evaluation on the response of the detectors were based on the model proposed by Fowler, whereby the absorption of radiation will induce a temporary change in the electrical conductivity and the charge drift across the diamond will produce a signal that can be measured. The ideal detector for therapeutic dosimetry should have a value of $\Delta = 1$ and if $\Delta < 1$, then this implies that the response from the detector will be lower than the actual response when high dose-rate is

involved. The acceptable value of Δ varies between $0.5 < \Delta < 1$. For the microDiamond detector, the output measured is in terms of charge (C) and this requires a period of measurement in order to determine the current signal from the absorption of radiation. Meanwhile, for the DD4 detector, the output signal is in the pulse-counting mode.

Two methods of dose-rate dependency were applied on the detectors; one by utilizing the different pulse-rate available within the LINAC and the other by varying the distance between the radiation source and the detectors. The different pulse-rate available within the LINAC was investigated only on the microDiamond detector since Piliero has already investigated the pulse-rate dependency of the DD4 . On the other hand, varying the dose-rate based on the second method has been investigated for both detectors.

The active sensitive volume of the diamond as reported by Piliero is contradictory to that of other researchers even for the same model and manufacturer. Piliero [13] reported the DD4 to have a sensitive volume of $1 \times 1 \times 0.3$ mm^3 while Schirru et al. [102] and Galbiati et al. [81] reported the active sensitive volume for DD4 to be 4.7×4.7 mm^2 and thickness of 500 μm. The theoretical calculation on the sensitivity of the DD4 detector based on the size of diamond in DD4 as reported by Piliero is 81 nC/Gy while the sensitivity for the other size of diamond in DD4 is given by 2.9 μC/Gy. As for the evaluation of the microDiamond detector with different pulse-rates from the LINAC, the Δ value is found to be 0.9985 ± 0.0005 for Elekta Synergy 6 MV. Brualla-Gonzalez et al. [105] reported the value obtained as 0.992 ± 0.001 for Varian Truebeam (Varian Medical System, Palo Alto) with flattening filter free (FFF). The different in measurement results may be attributed to the calculation on the time of irradiation. In the current investigation, the time of irradiation was calculated from the reciprocal of the dose-rate with the fixed monitor unit (MU) which may not be a true reflection of the beam delivered.

Investigation on the dose-rate dependency of the diamond detectors using the second method involved varying the distance between the radiation source and the detector, which will in turn change the dose-rate according to the inverse-square law. The value of Δ obtained for the microDiamond detector is 1.0040 ± 0.0024 while for DD4 is 0.996 ± 0.025. Piliero [13] reported the value of Δ for DD4 as 0.99 ± 0.03 for pulse-rate variation method.

The investigations also successfully demonstrates in pulse-by-pulse dosimetry with the customised front-end system. The system has the capability to measure individual pulse up to the maximum pulse-rate of the LINAC. This investigation has also shown that the DD4 detector has the capability in measuring pulse-by-pulse during the dose delivery without pile-up issue which means the customised front-end has performed very well. The measured pulse height is proportional to the amount of charge induced by the radiation or to the total amount of charge measured. A comparison between the microDiamond and the DD4 detector shows similar results for dose-rate dependency. Both detectors have shown excellent dose-rate linearity compared to other conductivity detectors which are generally much poorer.

Knowledge of the deposited dose by pulses during the VMAT treatment will help in determining early on of any error during the dose delivery . Therefore, the high-count rate system developed has been successful in measuring pulse-by-pulse dosimetry and both detectors are shown to have excellent dose-rate linearity. The next chapter will investigate the performance of both detectors in measuring dose delivery with VMAT technique by utilizing various dose-rates.

5

Preliminary VMAT Dosimetry Analysis For Prostate Cancer Treatment

5.1 *Introduction*

In 2016, Cancer Research UK reported 47,700 new cases of prostate cancer in the United Kingdom, which reflects 1 in 6 of the male population in the country will be diagnosed with prostate cancer in their lifetime [108]. New prostate cancer cases are projected to rise by 12 % in the United Kingdom between 2014 and 2035. As a primary prostate cancer treatment, 15 % of the patients will undergo surgery to remove their tumour, 30 % will have radiotherapy and 5 % treated with chemotherapy. It is evident that the best method of cancer treatment is by using ionizing radiation. The main aim of radiotherapy is to deliver the maximum dose to the tumour and a minimum dose to the surrounding critical structures [109]. The techniques used in radiation therapy to treat cancer patients have been improving over the past few decades. Intensity-modulated radiation therapy (IMRT) and volumetric-modulated arc therapy (VMAT) are two typical more advanced and complex techniques used in external beam radiation therapy (EBRT) to treat cancer patients. Both techniques utilize LINAC with a dynamic multi-leaf collimator (MLC) to modulate or shape the radiation beams to deliver conformal and homogenous dose to the tumour [110], as presented in Figure 5.1. The difference between IMRT and VMAT is in the method of beams delivery. In IMRT, a specific number of beams will enter into the patient's body at certain gantry angle. On the other hand, in the VMAT method, the beams are delivered with the aperture changing continuously with gantry rotation by optimising the dose-rate, gantry speed and leaf position of dynamic MLC [111].

In both techniques, the beams are shaped by the dynamic MLC into a number of beam segments known as beamlets. Each beamlet has a different radiation intensity. The disadvantages of the IMRT technique is that it employs a high monitor unit (MU) and takes longer treatment time. The VMAT technique is more advanced than the IMRT in that as the radiation beams are continuously delivered while the gantry

rotates, resulting in less treatment time and lower MUs employed compared to the IMRT technique. The dose-rate used in the VMAT technique changes drastically and consequently, this creates a high dose gradient on every dose delivered. Hence, it is prone to errors and requires patient-specific quality assurance (QA) to be performed to verify that the actual dose delivered and the planned dose are correct [112-113].

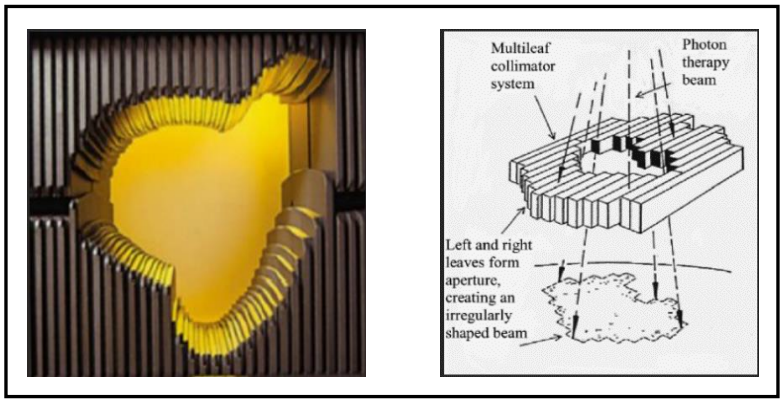

(a) **(b)**

Figure 5.1: Photograph of the multi-leaf collimator (a) [114] and the schematic diagram showing beams delivery with the use of MLC (b) [115]

Several authors have proposed various verification methods for quality assurance (QA) for VMAT technique. They recommended verification by mapping the total accumulated dose using film, arrays of ionization chambers, diodes and the latest being the electronic portal imaging device (EPID) [15,116 -117]. Depending on the device, the verification on the dose delivered can be based either on point dose (1D), planar (2D) or volumetric (3D). The accumulated dose calculated by the commercial treatment planning system (TPS) is based on a beam-by-beam or arc-by-arc calculation. Hence, the total dose delivered is a summation of a large number of static-gantry dynamic MLC fields called control points (CP). An experienced personnel can evaluate the cumulative dose measurement verification between the planned and dose delivered using quantitative method.

Since small fields are employed in the VMAT technique, it is essential to use an appropriate detector size in measuring the steep dose gradient; otherwise, the response from the detector will substantially differ from the absorbed dose [111]. Heydarian et al. [118] reported that the use of conventional ionization chamber for a steep dose gradient measurement is not valid as it requires a smaller sensitive volume

of the detector. Since diamonds can be fabricated in a small sensitive volume, this makes it suitable in measuring small-field dimensions of radiation beams. Due to its high-resolution characteristic, the diamond detector can also be used for real-time or time-resolved dosimetry in monitoring the dose delivered in radiotherapy. However, in practice, time-resolved dosimetry is seldom evaluated because the commercial QA tools are only able to measure the accumulated dose. Furthermore, the accumulated dose is customarily based on the TPS dose calculation which measures the total dose in a plane and as such, provides little information about on how the dose is being delivered during the treatment.

Errors due to patient positioning, the gantry angle position or the MLC position will result in poor analysis. With the time-resolved dosimetry, the causes of these errors can potentially be detected more efficiently during the dose delivery, e.g., by gantry angle or time basis [119]. Knowledge on how the dose is being deposited as a function of time or gantry angle can help in determining errors during the beam delivery, especially in measuring at steep dose gradient.

As explained in Chapter 3 and Chapter 4, both microDiamond and DD4 detectors have the potential in measuring the dose for small fields and high dose gradient. It has also been proven that the DD4 detector has the capability in measuring pulse-by-pulse dose delivered from the LINAC without any pile-up issue.

This chapter presents a preliminary evaluation of the DD4 detector for a point dose measurement as a function of time based on the VMAT technique delivery in prostate cancer treatment. An anonymised patient's treatment plan was created for prostate cancer treatment using commercial TPS with the VMAT technique. Once the plan was completed, it was then transferred to a record and verification system before having the beams delivered by the control console of the LINAC. The DD4 detector was employed to measure the dose at the sampling rate of 200 kHz. Therefore, this procedure will reveal the way the LINAC delivers the dose. During beam delivery, the MLC position and other machine parameters were logged by the LINAC but they can be retrieved later for analysis. The treatment delivery data was recorded at a sampling rate of 1 Hz on the LINAC control computer. The treatment parameters from the TPS were then saved and transferred to MatLab (MathWorks Inc, Natwick, MA, USA) in the DICOM RT standard.

As mentioned earlier, the cumulative dose calculated by the TPS at a preference or reference point set by the oncologist is based on the beam-by-beam summation dose calculation. However, data from the DICOM RT retrieved by MatLab only provides the calculated monitor unit per control point (MU/CP) or monitor unit per gantry angle (MU/degree) and not based on the dose. Hence, a model was reconstructed based on the information of the MLC position from the DICOM RT with an applied field-size correction factor. Cross-calibration between Farmer ionization chamber and the microDiamond and DD4 detectors were conducted in order to find the relationship between the dose and the pulse. The microDiamond detector has the conversion factor from charge (C) to dose (Gy) from the sensitivity certificate and the value is verified with the Farmer ionization chamber. The DD4 detector measures the pulse height in terms of voltage (V/pulse). From the cross-calibration between the microDiamond and DD4 detectors, the relationship between dose and pulse (Gy/pulse) can be obtained.

Cross-calibration	**Detector**	**Conversion**
Farmer ionization	microDiamond	charge/dose (nC/Gy)
microDiamond detector	DD4	dose/pulse (Gy/pulse)
Method	**Information**	
DD4 detector measurements	Provides the information of pulse-by-pulse dose deposition (time-resolved)	Gy/s
LINAC logfile	Provides the information of monitor unit delivered per control point or time	MU/CPs or MU/^{0}s
TPS	DICOM RT provides MLC position per control point or per gantry angle	MU/CP or MU/^{0}
Model reconstruction	Information from TPS on MLC position for dose contribution in the dose delivery together with the field-size correction factor (Gy/MU)	Gy/MU

Table 5.1: A summary of the conversion method used in the current investigation

Finally, the three cumulative dose deposition models of measurement, TPS and LINAC logfile are evaluated using gamma-like analysis. An essential feature of gamma analysis is the consideration of dose uncertainty against the second parameter, which is space. In gamma-like analysis, dose difference (ΔD) and the second parameter, either gantry angle or time (Δg or Δt), are evaluated simultaneously between the reference and evaluation. Gamma analysis was introduced by Low et al. [120] whereby they quantitatively compare between the reference (measurement) and evaluation dose distribution for each point of interest using preselected dose difference (ΔD) and distance-to-agreement (ΔDTA) criteria and then uses the value of gamma (γ) to determine the outcome of the comparison (pass-fail) [121]. In this chapter, a point dose measurement at 0.5 cm superior from the isocentre was measured for both the cumulative and instantaneous dose distributions. Then the gamma analysis was utilised for the purpose of quantitative analysis to verify if the reconstructed models are successful.

5.2 *Materials and Methods*

The measurements were performed with the Elekta Synergy LINAC (Elekta, Inc. Crawley, U.K.) which has an energy of 6MV with 40 pairs of MLC leaves (1 cm leaf width) located at the Singleton Hospital in Swansea. The LINAC was calibrated to deliver 1 cGy/MU (0.01 Gy/MU) at d_{max} (i.e., 1.5 cm depth for 6 MV) for a field-size of 10 × 10 cm^2 at 100 cm SSD. The irradiations for this study comprised only the dynamic delivery technique known as VMAT for a 6 MV photon beam. In this study, the measurements were conducted based on a cubical phantom surrounded with a solid water-equivalent multi-block phantom and an in-house customized spherical PMMA phantom to mount the detectors. The centre of the detector was aligned to the beam isocentre using in-room lasers. In cross-calibration measurements, irradiations were performed at 0° gantry angle and 0° collimator angle in order to get optimum reproducibility.

5.2.1 Detectors

A Farmer ionization chamber, a microDiamond (PTW) detector and a DD4 detector were used either for cross-calibration or for measuring the dose delivery for prostate cancer treatment with VMAT technique. The Farmer chamber has been described as a

reliable ionization chamber for the absolute dose measurements in radiotherapy [122]. A microDiamond detector is a commercially available diamond detector known for its suitability for small field measurements. Several publications have evaluated the characteristics and potential of the microDiamond detector in VMAT measurements, as explained in Chapter 3 and Chapter 4. The evaluation of the DD4 detector for measuring the pulses generated by the LINAC has been presented in Chapter 4. It is proven to have approximately a linear relationship with the dose-rate.

In this study, the microDiamond detector is first used for cross-calibration with the Farmer ionization chamber before it is used for cross-calibration with the DD4 detector.

5.2.2 Cross-calibration between Farmer chamber and microDiamond detector

The objective for performing cross-calibration between the Farmer ionization chamber and the microDiamond detector is to verify the sensitivity of the microDiamond detector obtained with the value provided by the manufacturer.

Farmer ionization chamber is a gas-filled radiation detector that has been used for decades and recognized as a stable and reliable radiation detector. It consists of two electrodes known as the anode and cathode. When the detector is exposed to the radiation, an ion-pair is created within the gas. The resultant positive ions will move to the cathode while the negative ions move to the anode under the influence of the electric field. This will generate an ionization current. When the detector is connected to the electrometer, it will count the cumulated charges (Q) and the proportional total charges to the number of ion-pairs created [122-123]. Figure 5.2 presents the schematic diagram of the cylindrical Farmer ionization chamber.

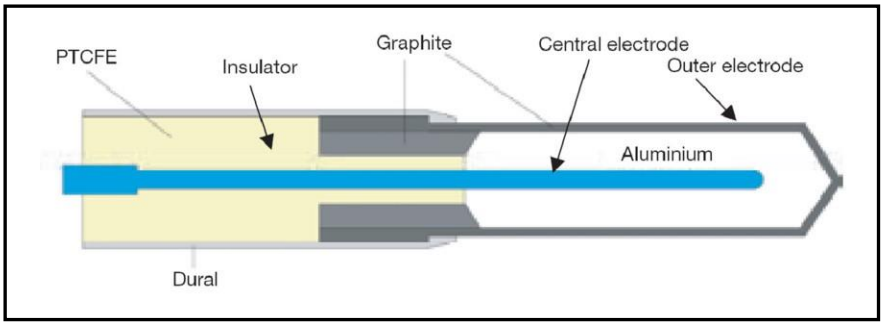

Figure 5.2: Schematic diagram of the Farmer ionization chamber [124]

The calculated monitor unit (MU) calibration on the LINAC in the water phantom at the reference point is a primary parameter in dose delivery, for both the conventional and modulated-beam. The accuracy of the dose delivery is still dependent on the traceability of the dose-to-water calibration factor on the ionization chamber, as provided by the accredited Secondary Standard Dosimetry Laboratories (SSDL) [125].

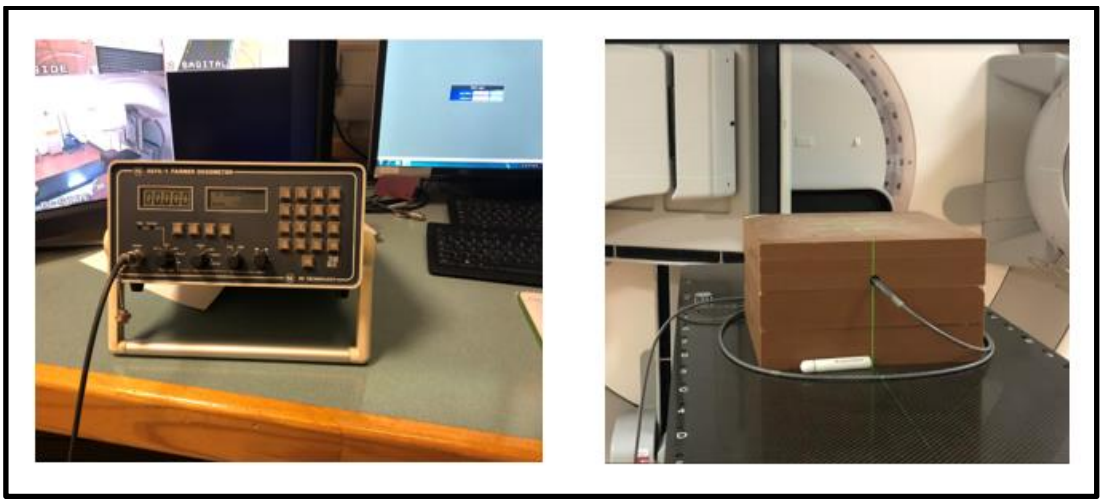

Figure 5.3: Photographs of the Farmer dosemeter (a) and set up of the Farmer chamber with the water-equivalent phantom measured at a depth of 5 cm (b)

Figure 5.3(a) presents the photograph of the 2570/1 Farmer dosemeter (Thermo Fisher Scientific Inc, Waltham, MA, USA). Figure 5.3 (b) shows the set up during the cross-calibration measurements with solid water-equivalence phantom. In this calibration, the dose was measured at a depth of 5 cm, for a field size of 10×10 cm^2 and a source-to-surface distance (SSD) of 100 cm with the LINAC set to deliver 400 monitor unit (MU) at 270 MU/min of the dose-rate. The depth of 5 cm for measurement is sufficient to produce full scatter condition of charge particle equilibrium instead of 10 cm depth in the LINAC calibration. The Farmer chamber was mounted in a solid water-equivalent phantom of $30 \times 30 \times 20$ cm^3. The detector was positioned in a horizontal orientation with the detector's main axis being perpendicular to the central beam axis (Figure 5.3b). The variable voltage from the dosemeter available are ± 250, ± 125, ± 62.5 and ± 30.8 V but only ± 250 V will be used in the investigation since this voltage was used during the LINAC calibration. The Farmer dosemeter output reading was selected to provide measurements in terms

of dose (Gy). The output readings from the dosimeter are uncorrected dose and will later be corrected during the absolute dose calculation.

The microDiamond detector was mounted in a customized 8 × 8 × 8 cm^3 PMMA cubic phantom surrounded with a solid water-equivalent multi-block to account for the effects of scattering (see Figure 5.4). The detector was positioned in a vertical orientation with the detector's main axis being parallel to the beam axis. The cubical phantom was placed on the solid water-equivalent phantom slab at a height of 5 cm above the treatment table. This is to avoid the measurement of the scatter dose from the table. The detector was connected to the PTW UNIDOS Universal dosemeter through the TNC cable. PTW UNIDOS Universal dosemeter provides the output in terms of cumulative charge (C). The result from this calibration will be compared with the value provided by the manufacturer. Table 5.2 presents the parameters for the cross-calibration set-up between the Farmer chamber and the microDiamond detector.

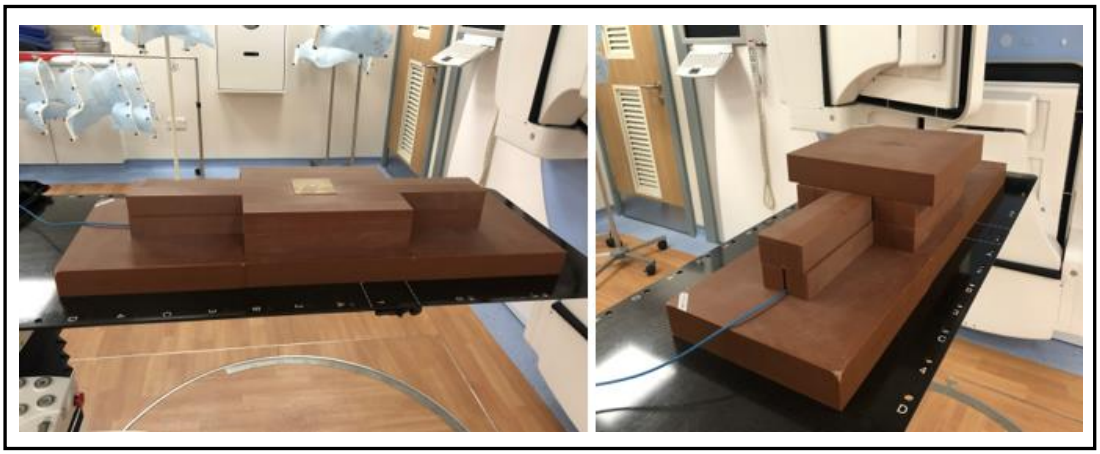

(a) **(b)**

Figure 5.4: Photographs of the set-up with the microDiamond detector for cross-calibration with the in-house customized PMMA cubical phantom (centre) surrounded with solid water phantom (a) and measurement of the detector at a depth of 5 cm (b)

Setup					
Linac		**Dosemeter**			
Field size	10 × 10 cm^2	**2570/1 Farmer**		**PTW UNIDOS**	
MU	400	Voltage	250 V	Voltage	0 V
Dose-rate	270 MU/min	Detector	Farmer	Detector	microDiamond
Depth	5 cm	Reading unit	**Gy**	Reading unit	**nC**
SSD	100 cm	Phantom	Solid water	Phantom	PMMA cubic + multiblock
Gantry	0°				

Table 5.2: The setup during cross-calibration between the Farmer chamber and the microDiamond detector

5.2.3 Cross-calibration between the microDiamond detector and the DD4 detector

Once the sensitivity of the microDiamond detector is verified as explained in the last section, the next step is to determine the conversion factor between the microDiamond detector and the DD4 detector in terms of dose per pulse (Gy/pulse).

In this cross-calibration, an in-house customized PMMA spherical phantom was used. The phantom is 6 cm in diameter with the detector's sensitivity volume located at the isocentre of the spherical phantom. Both detectors were positioned in the horizontal orientation, with the detector's main axis being perpendicular to the beam axis. As can be seen in Figure 5.5, the spherical phantom only measures the primary beams and not the scatter radiation from the floor or the treatment table. When setting the spherical phantom, extra caution was taken to ensure that there is enough height and space for the gantry rotation. This is to avoid collision between the LINAC head and the phantom.

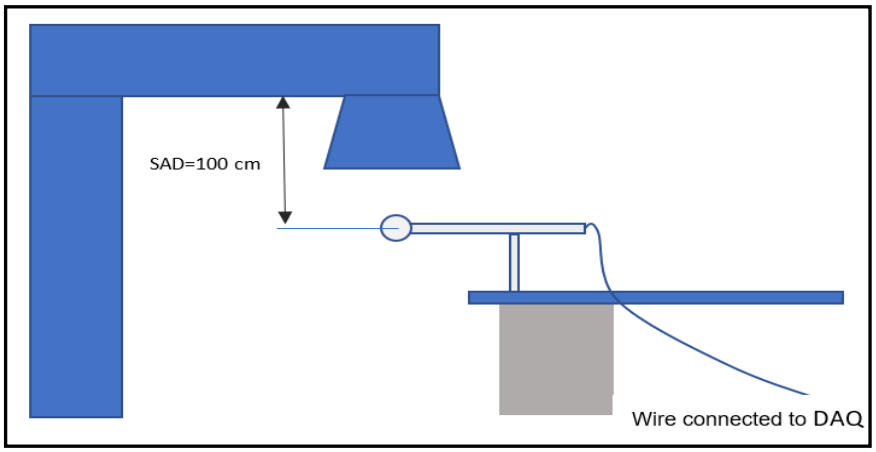

Figure 5.5: Schematic diagram of the cross-calibration between the microDiamond and the DD4 detectors using the spherical phantom

LINAC was operated under a VMATQA setup which is often used as a routine check by the in-house Medical Physicist. The field-size is 24 × 24 cm^2, the source-to-axis distance (SAD) is 100 cm, the gantry rotation follows clockwise (CW) direction from -180º until + 180º and a fixed dose-rate of 419 MU/min (the maximum dose-rate available for VMAT) delivering a total of 640 MU. Here, the microDiamond detector measures the dose in terms of the total charge (C) whereas the DD4 detector measures the dose in term of volt per pulse (V/pulse) during the beam delivery. The microDiamond detector was connected to the dosemeter (PTW UNIDOS Universal) without any voltage supplied (0 bias voltage). The DD4 detector was connected to the data acquisition (DQA) (as discussed in Chapter 4) and a host PC controlled the analogue front-end (AFE) by using the LabView software (National Instrument, TX, USA). The maximum data acquisition rate was 200 kilo-samples per second, giving a 5 microsecond (µs) resolution on time base. The data sampled were analyzed offline using the ROOT package [104]. Table 5.3 presents the parameters for the cross-calibration set-up between the microdiamond detector and the DD4 detector.

Setup					
Linac		**Dose meter**			
Field-size	24 x 24 cm^2	**PTW UNIDOS**		**Analogue Front End (AFE)**	
MU	640	Voltage	0 V	Voltage	100 V
Dose-rate	419 MU/min	Detector	microDiamond	Detector	DD4
Depth	3 cm	Reading	**nC**	Reading	**volt/pulse**
SAD	100 cm	Phantom	Spherical	Phantom	Spherical
Gantry rotation	Arc_CW				

Table 5.3: The setup details during the calibration between the microDiamond and the DD4 detectors

Here, the read out from the microDiamond detector is the total charge (C) measured based on the VMAT delivery with a fixed dose-rate measured at a depth of 3 cm. With the conversion of the sensitivity obtained in the last section, the total dose in gray (Gy) can be obtained. Then, the sampled data from the DD4 detector were analyzed offline using the ROOT package. The total number of pulses delivered is determined by selecting the highest pulse amplitude and considering the figure above a certain threshold as a pulse and below the threshold as a noise. Hence, in this way the DD4 conversion factor (Gy/pulse) can be determined.

5.3 Treatment Planning System (TPS) of VMAT technique for prostate cancer treatment

The prostate cancer treatment was created using the Nucletron Oncentra MasterPlan OTP V4.3.0.409 treatment planning system (TPS), developed by a previous postgraduate student [126]. The dose distribution calculated for the VMAT technique employs an inverse planning method where the planner must specify in advance the dose distribution that is desired. Then the TPS will calculate the dose distribution on the organ at risk (OAR) and target (tumor) based on the user-defined optimizing delivery parameters, such as the collimator angle, gantry angle for starting and ending, the clockwise or anti-clockwise direction of rotation, the gantry angle spacing between the control points, single or double number of arcs and the leaf speed. An understanding of the LINAC limitations, such as the number of monitor units per degree of gantry, the maximum gantry and leaf speed as well as the maximum dose

available, is essential in order to create an optimum plan for VMAT delivery. This includes the number of monitor units per degree of gantry angle (MU/^{o}), the maximum gantry and leaf speed, and the maximum dose-rate available. A single arc VMAT plan was created with D95 prescription (95% dose to PTV coverage) of 76 Gy in 37 fractions with a total monitor unit of 483 MU per fraction with a 4° gantry angle spacing starting from -178° to + 178° (clockwise rotation) and a fixed collimator angle at 45°. The treatment plan was discretized into 90 static beams known as control points (CP). Each CP contains details of the treatment parameters involved during beam delivery, such as the field-size, MLC positions, MU per CP (MU/CP) and gantry angle rotation.

LINAC used in these investigations takes into account the limitations of its parameters, such as the number of monitor units (MU) per degree of gantry rotation, i.e. 0.10 to 20.0 MU/^{0}, the maximum dose-rate available of 419 MU/min and maximum gantry and leaf speed of 6.0 ^{o}/s and 2.4 cm/s respectively. The current use of LINAC has seven fixed dose-rate levels in the binned dose-rate (BDR), with each being one half of the dose-rate of the next higher level [127]. Only five different dose-rates were allowed to be used for VMAT delivery using the current LINAC. Once the plan was completed, it was transferred to the MOSAIQ v1.6 (IMPAC Medical Systems, Sunnyvale, USA) which is a record and verification system. The beams were delivered by RT Desktop (Elekta), the control console for the LINAC. With the Synergy control system, the dynamic LINAC parameters of VMAT such as the MLC position, jaw, and gantry speed are servo controlled by the LINAC controller based on the cumulative MU [128].

In the VMAT plan printout, information regarding the gantry angle, monitor unit (MU), and the MLC position per control point (CP) are not available, but all the other essential information for the treatment delivery is contained in the DICOM RT format. By utilizing the MatLab tools, the information of the MLC positions can be retrieved from the DICOM RT file.

In general, the LINAC console controls the dose versus the gantry angle by varying the dose-rate and gantry speed as required to deliver the intended dose. The MLC's controller will control the leaf positions against the gantry angle. Therefore, the gantry angle plays a vital role in controlling the VMAT delivery [129]. The nominal

dose-rate set during the VMAT delivery was 419 MU/min, which may differ from the nominal dose-rate by ± 25 %, and the maximum leaf speed was 2.4 cm/s. Hence, the fastest combination of the dose-rate level, gantry rotation speed and leaf speed was selected automatically by the LINAC control system during the VMAT delivery.

When delivering the beams, LINAC control is dictated by the gantry speed. When less than approximately 2 MU/degree is required, then the gantry speed will move at its maximum speed with a low dose-rate level. When a higher MU/degree is required, a higher dose-rate level will be applied and the gantry speed slowed down [129]. The MLC speed will also vary to accommodate the gantry speed. If any leaf cannot reach their correct position during the delivery, then the beams' delivery will be stopped by the MLC interlock.

5.4 Measurement of VMAT prostate plan delivery

Once the treatment plan was created and approved, the VMAT plan is transferred to the LINAC control console for it to be ready to deliver the beams. For total dose measurement, the detectors were mounted in an in-house customized PMMA spherical phantom so that the distance between the detector and the gantry rotation axis will remain constant (100 cm) since the effective detector's point of measurement is set at the isocentre.

The DD4 detector was positioned at 0.5 cm superior from the LINAC isocentre in order to avoid the detector being placed in between the leaves of the MLC by moving the treatment table longitudinally (see Figure 5.6). DD4 detector measured the dose in terms of voltage per pulse (V/pulse).

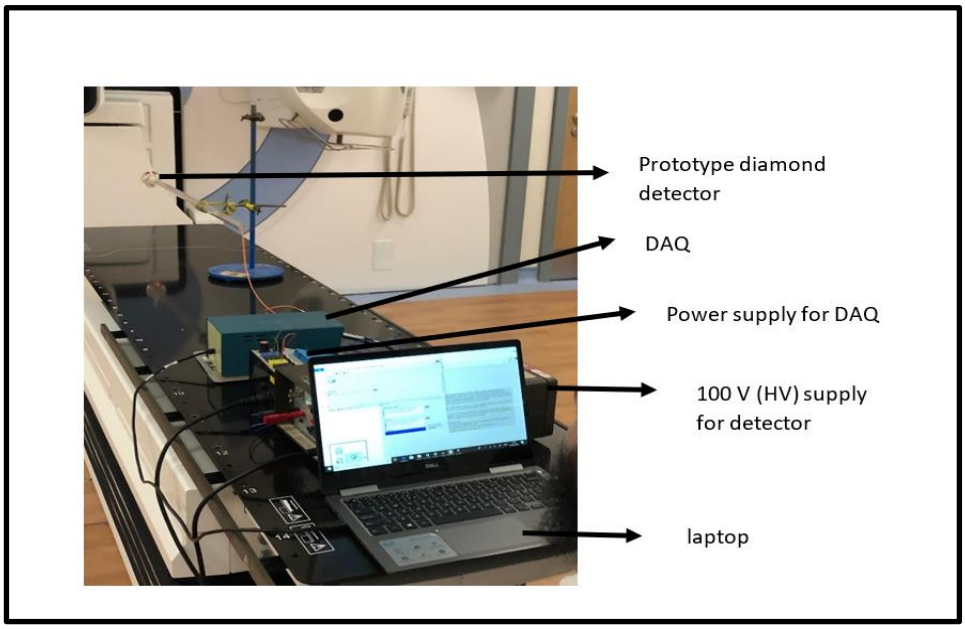

Figure 5.6: Photograph showing the setup during the VMAT measurement with DD4 detector

5.5 Data extracted from the LINAC logfile

During the measurement of the VMAT delivery, the LINAC control console concurrently logged all the LINAC parameters, such as the MLC positions, gantry position and MU for each CP, and saved the logged data after the treatment. The logfile can only be read after the beams have been delivered and they are recorded with a time resolution of 1s and stored in a file on the LINAC control console and the MLC workstation. The examination of LINAC logfile has been suggested as an alternative quality control (QC) method for IMRT or VMAT [130-131].

Generally, the data stored in the logfile are in binary format and this poses a challenge for the user when interpreting the data. Firstly, the user needs to know the exact time of the delivery and only a few items may be needed for the investigation. In the logfile, the first column is an item (every number refers to a specific item, e.g., gantry, field-size, MLC), the second column is part of the individual item, and the third column is the set of actual value delivered when the beams are on. LINAC's essential parameters in the current study are dose per CP, gantry starting and ending position, a few of the MLC positions near the isocentre and primary jaws. The LINAC parameters involved in the VMAT delivery are listed in Table 5.4.The logfile data from the LINAC was later used for the dose deposition model.

Item (1st column)	Description	Part (2nd column)	Actual value (3rd column)
35	Segment dose channel monitor (1)	4	Dose delivered in MU
36	Segment dose channel monitor (2)	4	Dose delivered in MU
70	Gantry starting position	4	Gantry angle in degree
71	Gantry stopping position	4	Gantry angle in degree
2080	1st MLC at the top on the left-hand side	129	Reading in the unit of mm
2099	20th MLC at the isocentre left-hand side	129	Reading in the unit of mm
2100	21st MLC at the isocentre left-hand side	129	Reading in the unit of mm
2119	40th MLC at last left-hand side	129	Reading in the unit of mm
2120	1st MLC at the top on the right-hand side	129	Reading in the unit of mm
2139	20th MLC at the isocentre right-hand side	129	Reading in the unit of mm
2140	21st MLC at the isocentre right-hand side	129	Reading in the unit of mm
2159	40th MLC at last right-hand side	129	Reading in the unit of mm
2060	Jaw X1 position	129	Reading in the unit of mm
2061	Jaw X2 position	129	Reading in the unit of mm
2062	Jaw Y1 position	129	Reading in the unit of mm
2063	Jaw Y2 position	129	Reading in the unit of mm

Table 5.4: The essential list of items for interpreting the LINAC logfile

5.6 Simple reconstructed model of point dose deposited for LINAC logfile and TPS during VMAT delivery

A simple model of dose deposited at the position of the DD4 detector was reconstructed for the TPS and LINAC logfile. With the understanding that dose deposition is associated with the MLC position against the detector during the beam delivery, three scenarios are expected to occur; a) the detector being totally exposed to the beam b) detector being totally blocked, and c) the detector being partially blocked (see Figure 5.7). With the knowledge that the diameter of the DD4 detector is

0.7 cm and the width of the leaf is 1.0 cm, and the response is influenced by the shape of the penumbra and partially volume effect, the partially blocked means that the detector being blocked to the maximum of MLC overtravel of 0.2 cm (crossing the detector).

The total dose $\{d_i\}$ at a particular point $\{i\}$ in a phantom can be determined by the summation of the dose contributions from each CP [132] and by considering a field-size correction factor during the VMAT delivery, given by

$$d_i = \sum_{s=1}^{S}\left(A_{i,s} \times MU_s \times CF_s\right) \quad \text{.....(5.1)}$$

where d_i is total dose (Gy) at point i, $A_{i,s}$ is dose contribution by the MLC position of the s^{th} CP at the point i, MU_s (MU/CP) is monitor unit delivered at the s^{th} CP and CF_s (Gy/MU) is a field-size correction factor. The dose contribution for each CP ($A_{i,s}$) is based on the three scenarios, $A_{i,s}$ = 1 if the detector is totally exposed to the radiation beam, $A_{i,s}$ = 0 if the detector is totally blocked to the radiation beam and $A_{i,s}$ = 0.5 if the detector is partially blocked by the MLC.

Only field-sizes of 3 × 3 cm^2 and 5 × 5 cm^2 were considered for the field-size correction factor since in VMAT delivery employed small field dimensions. The microDiamond detector was irradiated to the total monitor unit (MU) of 400 MU for the respective field-size and by applying the sensitivity conversion, the field-size correction factor is given by the unit of dose per monitor unit (Gy/MU).

As explained earlier, the MLC positions parameter for TPS can be retrieved from the DICOM RT through the MatLab tools while for LINAC logfile is extracted from the LINAC control console. From these, the models of dose deposition for the TPS and LINAC logfile were reconstructed based on the following assumptions: the MLC position being i) either totally exposed or totally blocked denoted as MLC1 and ii) either totally exposed, totally blocked or partially blocked denoted as MLC0.5 and field-size correction factor based on either 3 × 3 cm^2 or 5 × 5 cm^2. Hence, there will be a total of eight models of cumulative point dose deposited: LINAC logfile denoted as logfile5 × 5MLC1, logfile5 × 5MLC0.5, logfile3 × 3MLC1, logfile3 × 3MLC0.5

and for TPS denoted as TPS5 × 5MLC1, TPS5 × 5MLC0.5, TPS3 × 3MLC1 and TPS3 × 3MLC0.5.

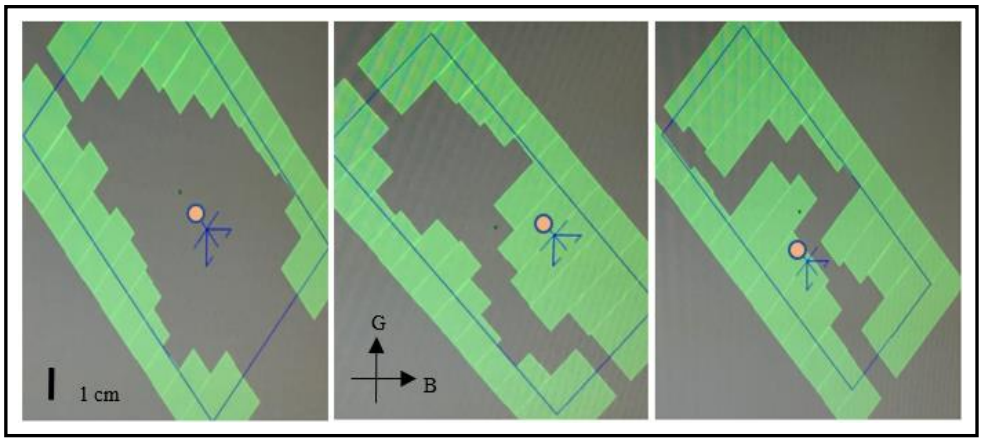

Figure 5.7: Illustration of the dose deposited against the MLC positioning during the beam delivery for three scenarios; totally exposed (left), totally blocked (middle) and partially blocked (right). As shown in the diagram, the position of the DD4 detector at 0.5 cm superior from the isocentre and the direction of the gun, target, A and B with the 45^0 of collimator angle

Table 5.5 presents the experimental setup for the field-size correction factor for the microDiamond detector. The detector was irradiated for 400 MU with the respective field-size at 100 cm SAD and 419 MU/min of dose-rate. Since the measurement for the microDiamond detector is based on unit of charge (C), and by using the sensitivity conversion, the field-size correction factor is given by the unit of the dose-per-monitor unit (Gy/MU).

Finally, the cumulative point dose deposition models for measurement, TPS and LINAC logfile were reconstructed. From the measurement approach, the only information available is the dose deposition (pulse height) as a function of time (V/s) while the VMAT delivery information from TPS only provides dose deposition (monitor unit) as a function of CP (MU/CP) without any information on the time basis. In contrast to the TPS, the LINAC logfile only provides information on dose deposition (monitor unit) as a function of time (MU/s). The interpolation method based on MatLab tools was used in order to have the same time stamp and also meeting the assumption that the gantry angle during the delivery is the same with the gantry angle in LINAC logfile. Such approach is essential to have an equal time stamp and gantry angle for the dose reconstruction.

Setup			
Linac		**Dosemeter**	
Field size	5 x 5 cm^2 and 3 x 3 cm^2	PTW UNIDOS	
MU	400	Voltage	0 V
Dose rate	419 MU/min	Chamber	microDiamond
Depth	3 cm	Reading	nC
SAD	97 cm	Phantom	Spherical
Gantry	0^0		

Table 5.5: The setup for field-size correction factor for the microDiamond detector with the spherical phantom

5.7 *Results*

5.7.1 Cross calibration between Farmer chamber and microDiamond detector

The percentage repetition measurement for the Farmer ionization chamber obtained is 0.217 % for five consecutive readings with a field-size of 10 × 10 cm^2, SSD of 100 cm, depth of measurement is 5 cm, and a total MU delivered of 400 for each reading (see Figure 5.6). This was agreeable as an in-house physicist recorded weekly calibration for the Farmer chamber with the same setup. The output reading from the Farmer dosemeter is the uncorrected dose. For the microDiamond detector, the background (BG) measurement was taken into consideration and this was subtracted to get the net reading. The corrected absorbed dose calculated for the Farmer chamber is given by:

$$\text{Dose} = (\text{Reading}) \times (N_{D,W}) \times (P_{ion}) \times (k_{T,P})$$

$$= (3.268\ \text{Gy}) \times (1.042) \times (1.0042) \times (1)$$

$$= 3.42\ \text{Gy with uncertainty of } 1.6\ \% \quad \ldots\ldots\ldots\ldots\ldots\ldots\ldots\ldots\ldots\ldots \quad (5.2)$$

where $N_{D,W}$ is a calibration coefficient in terms of absorbed dose-to-water for Farmer ionization chamber provided by SSDL, P_{ion} is the recombination factor for Farmer chamber and $k_{T,P}$ is the correction for air temperature and air pressure, which is given by

$$k_{T,P} = \frac{(273.2+T)}{(273.2+T_o)} \times \left(\frac{P_o}{P}\right)$$

The result obtained in equation (5.3) is for a 5 cm depth, which is 86.3 % from the percentage depth dose (PDD). The source of uncertainty from the measurement (0.07 %) and the $N_{D,W}$ is within 1.5 %.

Detector	Farmer (Gy)	microDiamond (nC)
	Reading	**Reading**
	3.266	4.327
	3.267	4.323
	3.267	4.324
	3.270	4.324
	3.270	4.324
Average	3.268	4.324
Standard deviation	0.002	0.002

Table 5.6: Results from cross-calibration between Farmer chamber and microdiamond detector

While for the measurement from the microDiamond detector is given by:

reading from microDiamond = 4.324 nC with the uncertainty of 0.05 % ……. (5.3)

Assuming that the dose measured under both conditions at a depth of 5 cm are the same, hence the dose measured by the Farmer ionization chamber is equal to the dose measured by microdiamond detector. Since 3.42 Gy is corresponds to the charge measured as 4.32 nC, therefore the sensitivity for the microDiamond detector is given by:

microDiamond sensitivity = (4.32 nC) / (3.42 Gy)

= 1.26 nC/Gy with 1.6 % uncertainty …… (5.4)

The value obtained is the same as quoted in the PTW certificate, which is 1.264 nC/Gy with 5 % uncertainty [133]. The sensitivity for the microDiamond detector was obtained from the cross-calibration with the Farmer chamber since the sensitivity factor provided by the manufacturer was from a different radiation source. The set up in this experiment may be less accurate since direct comparison is made with different phantoms during the measurement.

5.7.2 Cross-calibration of the mircoDiamond and DD4 detectors for VMATQA

The microDiamond detector was first used to measure the dose for a single-arc, which was set as a routine calibration for VMATQA delivery by the in-house medical physicist. The measured dose was calculated from the conversion of the microDiamond detector sensitivity, as shown in equation (5.5).

	Reading (nC)
	8.086
	8.086
	8.087
Average	8.09
SD	0.001

Table 5.7: The result for the microDiamond detector calibration with VMATQA at 3 cm depth measured with the spherical phantom

From the above measurement based on the microDiamond detector, the mean reading obtained was 8.09 nC with an uncertainty level of 0.1 % and the total dose delivered is given by;

$$\text{dose} = \text{Reading (nC)} \times 1/(\text{microDiamond sensitivity})$$

$$= 8.09(\text{nC}) \times \text{Gy}/1.264\ \text{nC}$$

$$= 6.40\ \text{Gy with 1.6 \% uncertainty} \quad \ldots\ldots (5.5)$$

The above result is the total dose measured at 100 cm of SAD for the spherical phantom with a field-size of $24 \times 24\ \text{cm}^2$, total monitor unit of 640 MU and at fixed dose-rate of 419 MU/min.

With the same set up as used for the microDiamond detector, the DD4 detector was used to measure pulse-by-pulse for VMATQA delivery. Figure 5.8(a) shows the processed measurement with DD4 detector. The threshold value was set at 0.04 V and any value below this was considered as noise. The threshold value was obtained after several attempts of measuring the pulse height and comparing them to the expected pulse height from the LINAC measured at 3 cm depth. Figure 5.8(b) shows the zoomed

plot of 5.8(a) at the startup region (ramp up). The pulse height increases rapidly until it stabilises in the plateau region. An example of single pulse from the LINAC was presented in Velthuis et al. [23] showing the signal displaying as expected a semi-Gaussian behavior with a rapid rise and slower fall off of approximately 60 µs and 160 µs, respectively. The reason for the plot pattern can be explained as follows: during the LINAC startup, a small number of electrons (minimum energy) are generated until they reached the target before the LINAC fine-tuned them till they reached the plateau region. At the startup, the photon (fluence) will have low energy level due to the low pulse height until it reaches a stable (desired dose-rate) pulse height. From Figure 5.8(a), the variation of the pulse height at the plateau region has a variation of within 2 %.This behavior is also in agreement with the result observed using organic scintillator for pulse-resolved measurement by Beierholm et al. [134].

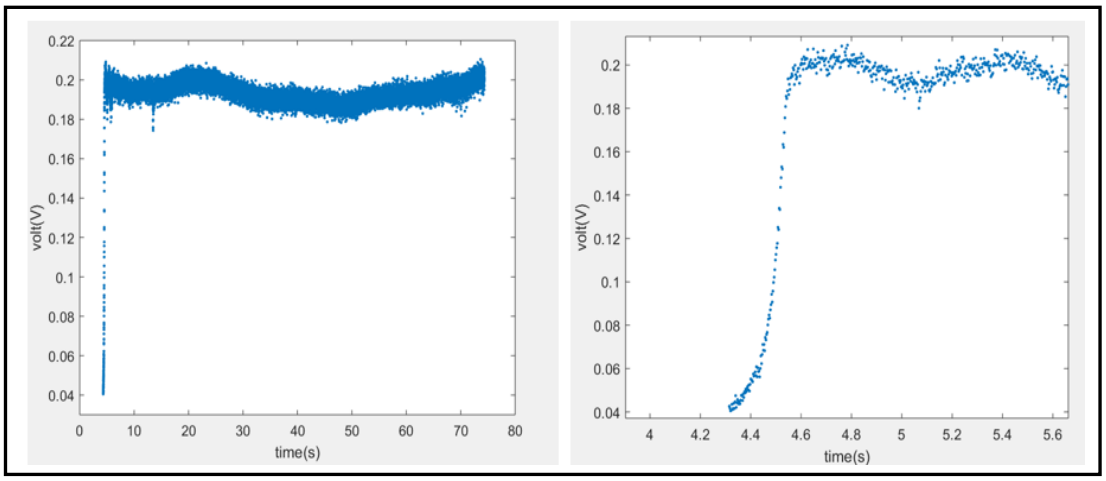

(a) **(b)**

Figure 5.8: Illustration of the response from the DD4 detector during the calibration under VMATQA protocol with spherical phantom at a fixed dose-rate of 419 MU/min

The average pulse height was calculated by the summation of the pulse height detected over the total number of pulses above the threshold.

From the data measurement for the spherical phantom calibration:

Total pulse height detected = 5381 V …… (5.6)

Total number of pulse = 27809 pulses …… (5.7)

Average pulse height = 0.1935 volt/pulse…… (5.8)

Therefore, the average height of the peak for every pulse is given by 0.1935 V/pulse with the statistical precision (1 s.d.) an of 2.4 %. From the measurement with the microDiamond detector, the dose delivered is given as 6.397 Gy, then, the correction factor for the DD4 detector in measuring the dose is given by;

Detector correction factor = (6.397 Gy) x (1/27809 pulse) x (pulse / 0.1935 volt)

= 0.0012 Gy/volt with 4 % uncertainty……... (5.9)

The dose per pulse is given by:

dose/pulse = pulse height (V/pulse) x 0.0012 (Gy/V) …….. (5.10)

5.7.3 The VMAT prostate plan delivery

Time-resolved point dose measurement at the centre of the spherical phantom for the VMAT beam delivery is presented in Figure 5.9. The fluctuations in the peak heights were due to the various dose-rates employed during the VMAT delivery. It is interesting to note that the dose measured as a function of pulse displayed different pulse height depending on the dose-rate employed during the irradiation.

Figure 5.9 (a) shows the pulse-by-pulse dosimetry with the VMAT technique delivery. Figure 5.9 (b) shows the zoomed in detail of the pulse height during the startup, which is similar as observed in Figure 5.8(b). This presents evidence that the behavior of the pulse height is not due to the electronic or detector but from the LINAC itself. The reason for the gaps at certain periods with no pulse detected (see Figure 5.9 5.9 (b: bottom left)) could be due to the MLC blocking the detector or that no dose is intended for that part of the delivery. Since a low pulse height (or volt) is expected for low dose-rate delivery, 0.018 V was set as the threshold value and this threshold is deemed appropriate based on the result of measurement of pulse at 3 cm depth. This value is comparable to Figure 5.8 where the threshold value is 0.04 V at 419 MU/min.

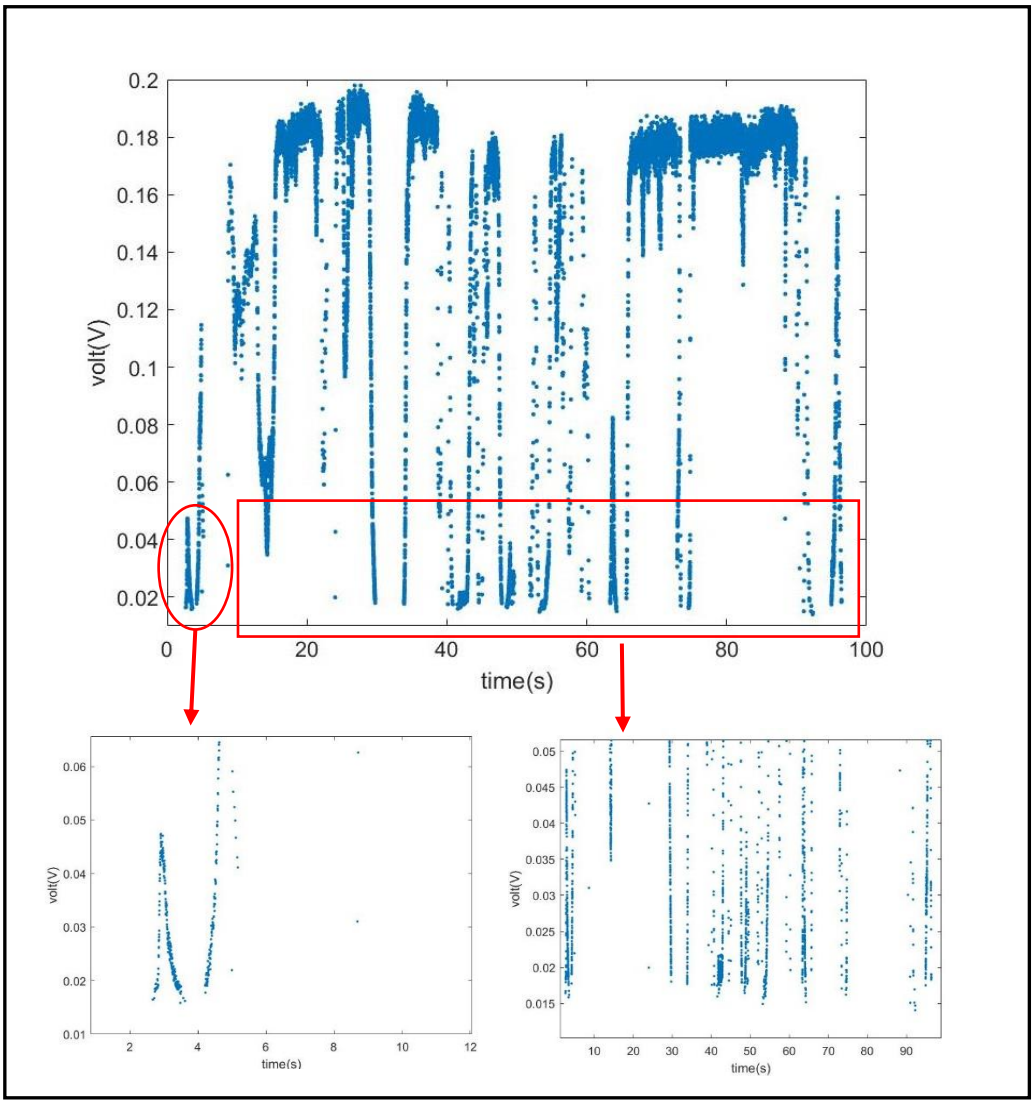

Figure 5.9: The DD4 diamond detector measurement for prostate with arc therapy delivery

Figure 5.10 presents the results for the multiplication of the conversion factor given in equation (5.11) with the data above. The DD4 detector has the capability of measuring the dose-per-pulse in the range of 0.05-0.25 mGy/pulse. The total dose measured at the 0.5 cm superior from the isocentre is given by the summation of the dose per pulse, which yields 3.2326 Gy.

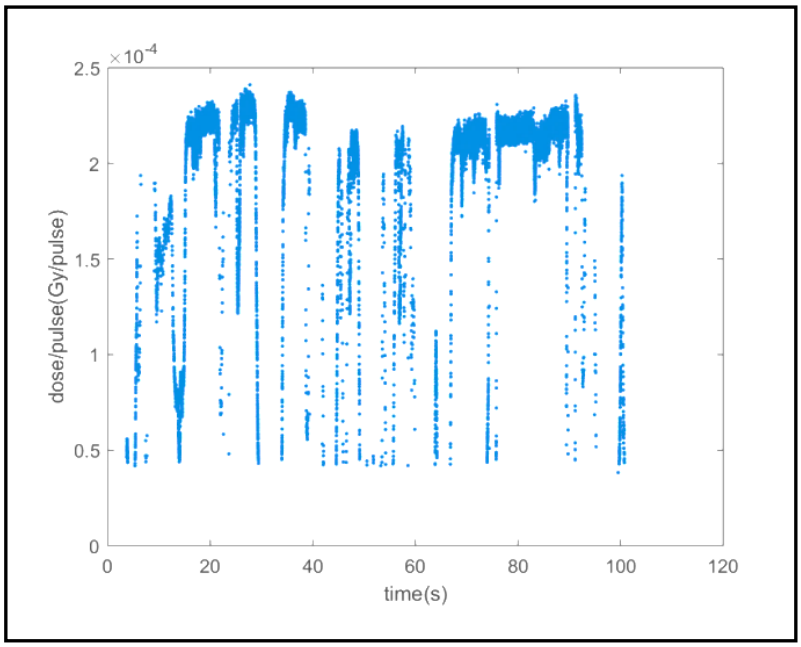

Figure 5.10: The dose per pulse (Gy/pulse) measurement after the conversion

5.8 The dose deposition model construction from TPS and LINAC logfile data during VMAT delivery.

The measurement of the beams output from the LINAC depends on the field-size used. Any increase in the field-size will increase the output due to collimator scattering added to the primary beam. Therefore, the field-size correction factor can be determined based on consideration of a field-size of 3×3 cm^2 and 5×5 cm^2 measured at SAD of 100 cm and total MU delivery of 400 MU (see Table 5.8). The conversion to dose is then calculated using the sensitivity factor of the microDiamond detector

Field size	5×5 cm^2	3×3 cm^2
	Reading (nC)	Reading (nC)
	4.730	4.586
	4.731	4.587
	4.730	4.586
	4.730	4.588
	4.731	4.587
Average	4.730	4.587
SD	0.0005	0.0008

Table 5.8: Field-size correction factor (CF) measured by the microDiamond detector with 400 MU at 100 cm SAD

By applying the charge (C) measured by the microDiamond detector and the sensitivity of the detector, the total dose in terms of dose (Gy) can be obtained. With the measurements provided from Table 5.8, the field-size correction factor (CF) can be converted from the charge (C) to the unit of dose (Gy), for the two different field-sizes:

For 5×5 cm^2,

dose = (reading) × (microDiamond sensitivity)

= (4.73 nC) × (Gy/1.26 nC)

= 3.74 Gy with the uncertainty of 1.6 %…….…..…… (5.11)

The field-size correction factor (CF) for the microDiamond detector as described in section 5.6 for 5×5 cm^2 and 3×3 cm^2 were irradiated for 400 MU, hence, the conversion factor for the dose per monitor unit (Gy/MU) can be determined. The total MU delivered is 400 MU, which gives

= (3.74 Gy) / (400 MU)

= 9.36 ± 0.15 mGy / MU ……..…… (5.12)

For 3×3 cm^2

dose = (4.59 nC) × (Gy / 1.26 nC)

= 3.63 Gy with the uncertainty of 1.6 % …..……...…..… (5.13)

likewise, for (5.13):

= (3.63 Gy) / (400 MU)

= 9.07 ± 0.15 mGy / MU ……..……. (5.14)

The construction of the cumulative dose deposition models from the LINAC logfiles and the TPS were done by analyzing both data with regards to the respective MLC position during the dose delivery, including the field-size correction factor (CF). From equation (5.1), the results for the eight models depending on the three scenarios are as follows:

Symbol	**Explanations**
$D_{LMLC1/5}$	Total dose model reconstructed from LINAC logfile for 5×5 cm^2 field-size correction factor with the assumption the detector either being totally exposed or totally blocked where CF = 0.00936 and $A_{i,s} = 1 \; or \; 0$
$D_{LMLC0.5/5}$	Total dose model reconstructed from LINAC logfile for 5×5 cm^2 field-size correction factor with the assumption the detector either being totally exposed, totally blocked or partially blocked where CF = 0.00936 and $A_{i,s} = 1, 0 \; or \; 0.5$
$D_{LMLC1/3}$	Total dose model reconstructed from LINAC logfile for 3×3 cm^2 field-size correction factor with the assumption the detector either being totally exposed or totally blocked where CF = 0.00907 and $A_{i,s} = 1 \; or \; 0$
$D_{LMLC0.5/3}$	Total dose model reconstructed from LINAC logfile for 3×3 cm^2 field-size correction factor with the assumption the detector either being totally exposed, totally blocked or partially blocked where CF = 0.00907 and $A_{i,s} = 1, 0 \; or \; 0.5$

$D_{TPSMLC1/5}$	Total dose model reconstructed from TPS for 5 × 5 cm^2 field-size correction factor with the assumption the detector either being totally exposed or totally blocked where CF = 0.00936 and $A_{i,s} = 1\ or\ 0$
$D_{TPSMLC0.5/5}$	Total dose model reconstructed from TPS for 5 × 5 cm^2 field-size correction factor with the assumption the detector either being totally exposed, totally blocked or partially blocked where CF = 0.00936 and $A_{i,s} = 1, 0\ or\ 0.5$
$D_{TPSMLC1/3}$	Total dose model reconstructed from TPS for 3 × 3 cm^2 field-size correction factor with the assumption the detector either being totally exposed or totally blocked where CF = 0.00907 and $A_{i,s} = 1\ or\ 0$
$D_{TPSMLC0.5/3}$	Total dose model reconstructed from TPS for 3 × 3 cm^2 field-size correction factor with the assumption the detector either being totally exposed, totally blocked or partially blocked where CF = 0.00907 and $A_{i,s} = 1, 0\ or\ 0.5$

Table 5.9: A summary of the dose model reconstructed based on the LINAC logfile and TPS

The cumulative dose deposition from the measurement is obtained via the summation of the total dose per pulse measured denoted as D_{Mea}. Another dose deposition model for the DD4 detector measurement is by the summation of the total average dose per pulse instead of considering the individual pulse height and this is denoted as $D_{AverMea}$.

The cumulative doses obtained were 3.1918, 3.2479, 3.0929, 3.1473, 3.1911, 3.2502, 3.0922, 3.1495, 3.2326 and 3.7996, for $D_{LMLC1/5}$, $D_{LMLC0.5/5}$, $D_{LMLC1/3}$, $D_{LMLC0.5/3}$, $D_{TPSMLC1/5}$, $D_{TPSMLC0.5/5}$, $D_{TPSMLC1/3}$, $D_{TPSMLC0.5/3}$, D_{Mea} and $D_{AverMea}$, respectively. Therefore, results indicate the assumption of the model construction based on $D_{LMLC0.5/5}$ and $D_{TPSMLC0.5/5}$ provided the closest total dose model to the measurement. Figure 5.11 shows the pattern based on the assumption of a constant average of dose per pulse in the VMAT delivery to be incorrect.

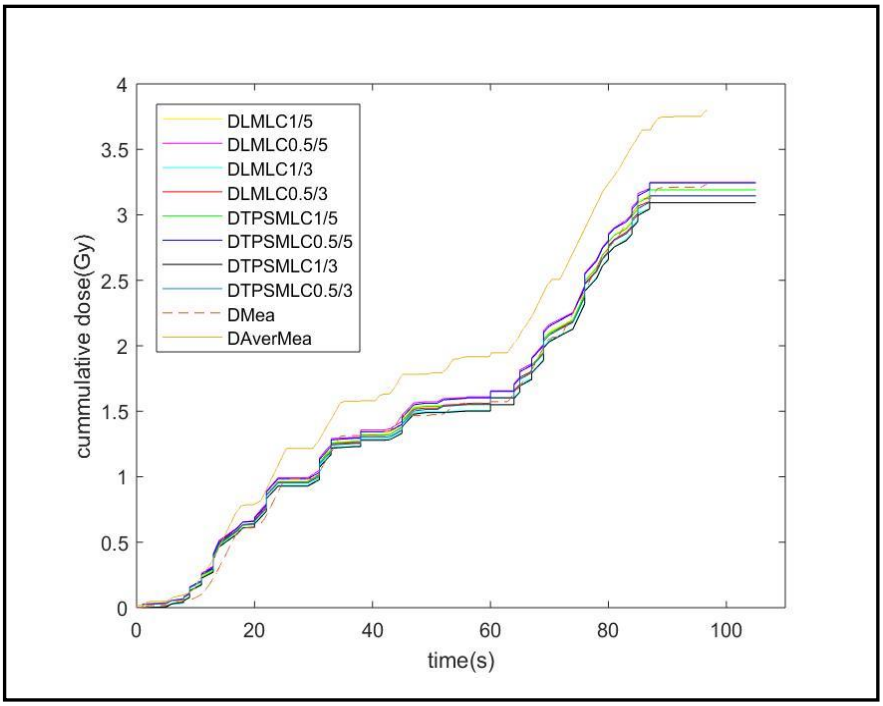

Figure 5.11: Illustration of the cumulative dose based on LINAC logfile data, TPS data, measurement and average pulse height

5.9 Point dose verification for VMAT delivery

Time-resolved dosimetry posed a new challenge for VMAT dose verification because measuring the integrated dose will provide little information about the dose deposited during the beam-on delivery. The advantage of time-resolved dosimetry over the integrated dose measurement is that errors due to either MLC positioning, gantry angle rotation or patient positioning, which will manifest in poor gamma evaluation, can be separated. Detectors with high temporal resolution are in demand, as has been discussed in Chapter 3.

Since the DD4 detector has shown excellent spatial resolution and a high degree of tissue-equivalent, it promises to be the right candidate for advance therapeutic dosimetry. Time-resolved dosimetry makes it possible to compare the planned dose and measurement dose at various time points. However, from the temporal measurement, one can also quantify the gantry angle position as a function of time. The success of dose verification for the VMAT delivery requires a quantitative evaluation method for the final decision-making and approval before executing it for

treatment. A gamma-like evaluation has been employed in this investigation to compare the cumulative and instantaneous dose with time. In this case, the LINAC logfile was used to determine the gantry angle but it could also be determined independently. The data were quantified using the gamma index (Low and Dempsey 2003) [135] as described in equation (5.15). This involves a combination of the dose difference (ΔD) and the distance-to-agreement (Δd) to calculate a dimensionless metric for each point in the evaluation distribution. The Δd presents the maximum accepted distance between a given point in the reference dose and a point in the evaluated dose distribution that receives the same dose, while ΔD is the dose difference criterion relative to a specific dose value.

$$\text{Gamma index } (\gamma) = \sqrt{\left(\frac{\Delta D}{dose\ criterion}\right)^2 + \left(\frac{\Delta d}{DTA\ criterion}\right)^2} \quad \text{.....(5.15)}$$

$$\text{Gamma passing rate (\%GP)} = \frac{(\sum(\gamma \leq 1\ and\ \gamma > 1)}{\sum \gamma > 0} \text{ x } 100\% \quad \text{.....(5.16)}$$

The reference dose distribution is generally taken from the measured dose distribution. The comparative evaluation involves the dose distribution calculated from the TPS or LINAC logfile. The gamma index (γ) is calculated based on the finding of the minimum time or gantry angle for each reference point (see Figure 5.12). The evaluation of the dose distribution at a particular point is considered passed if the gamma index is ≤ 1 and failed when the gamma index is > 1 (see Figure 5.12). In this study, the gamma index (γ) which combines dose difference and time/gantry-to-agreement difference are used to evaluate dose delivery in 1 D (point dose) where the $D_r(t_r), t_r$ is the reference point dose, $D_e(t_e), t_e$ and $D_{e\prime}(t_{e\prime})t_{e\prime}$ are two scenarios in the evaluation while ΔD and Δt/ Δg are the criteria for gamma evaluation. If the dose evaluated falls within the criteria set by the user, i.e., $D_{e\prime}(t_{e\prime})t_{e\prime}$, the dose difference at that particular time/gantry is considered passed, and if the evaluated dose falls outside the criteria, i.e., $D_e(t_e), t_e$, then it is considered as failed. The percentage gamma passing rate (%GP) was calculated by dividing the summation of each point less than the gamma index ($\gamma \leq 1$) with the total gamma index that is more than zero ($\gamma > 0$) as described in equation (5.16). The common gamma analysis criteria used is 3 %/3 mm as recommended by Low et al.

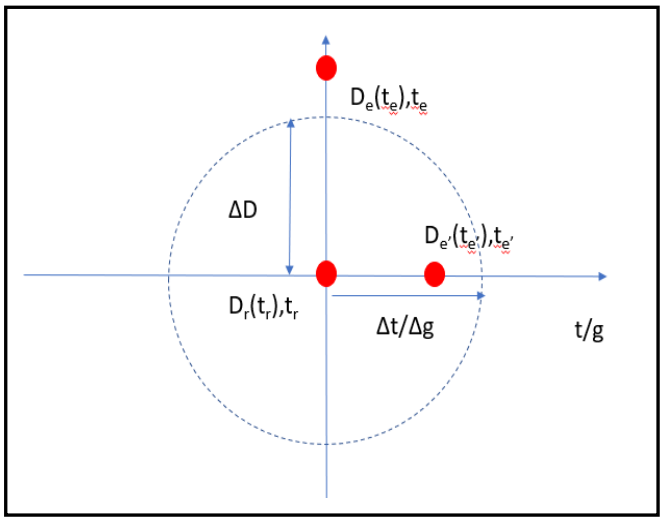

Figure 5.12: Schematic representation of the gamma index analysis in 1D. ΔD and Δt/Δg are the acceptance criteria. Using equation 5.15 and 5.16, $D_e(t_e), t_e$ would have γ value > 1 and $D_{e'}(t_{e'})t_{e'}$ would have γ value <1 but if the evaluated point is on the dotted line, the value is equal to 1

Besides dose difference (ΔD), two other parameters, i.e., time-to-agreement (Δt) and gantry angle-to-agreement (Δg), were selected for evaluation in the current study. The data from the measurements were considered as a “reference" while the data from the LINAC logfile and TPS were considered as the “evaluation”. For the dose-gantry angle differences, the evaluation was based on the assumption that the measurement is the same as the LINAC logfile gantry angle position. This evaluation can be made based on either the accumulated dose or the instantaneous dose depending on the user. AAPM TG 119 [136] recommended the use of 95 % gamma passing rate with criteria of 3%/3 mm in order to evaluate the accuracy of the comparisons and to eliminate dose out-of-target region. The task group also emphasised on the use of a low-dose threshold of 10 % in gamma analysis for 1 %/1mm acceptance criteria [137]. The low-dose threshold is a parameter used to exclude dose points below a selected threshold during the gamma index calculation. There is no consensus on the clinical criteria for gamma index evaluation and it is up to each individual centre to decide whether to use the criteria of 3 %/3 mm, 2 %/2 mm or 5 %/3 mm. The gamma evaluation was analysed offline using MatLab.

5.9.1 Gamma analysis for cumulative dose difference (ΔD) and time-to-agreement (Δt) parameters

An initial analysis of the cumulative dose as a function of time was evaluated. Figure 5.13 shows the cumulative dose comparison between the models constructed from the LINAC logfile, TPS and the measurement. For robust comparison, the interpolation method was applied with a timestamp of 0.005 seconds. Since the time data from the LINAC logfile sometimes has the same time value between CP, a small decimal point (maximum of 0.1 s) was added to the data in order to distinguish time points from one CP to the next. This adjustment is essential for the process of interpolation in MatLab but it does not affect the accuracy of the comparison. In general, the model for the LINAC logfile and TPS are in a good agreement since the time stamp for the TPS was taken from the LINAC logfile. It is important to note that the information available from the LINAC logfile is the cumulative dose delivered with the gantry position as a function of time (ΣMU/^{0}s), while information from the TPS is the cumulative dose planned as a function of control point (ΣMU/CP) and gantry position as a function of CP (^{0}/CP).

Meanwhile, the information available from the dose measurement is a cumulative dose measured as a function of time (Σ pulse height/time) without any details of the gantry angle position. Here, the assumption in using the interpolation method for the constructed models is to have an equal time stamp and dose resolution for comparison purposes. As can be seen in Figure 5.13, various dose-rates were employed in delivering the beams. When a high dose-rate is applied, the dose gradient is steep and when a low dose-rate is applied, the dose gradient is shallow.

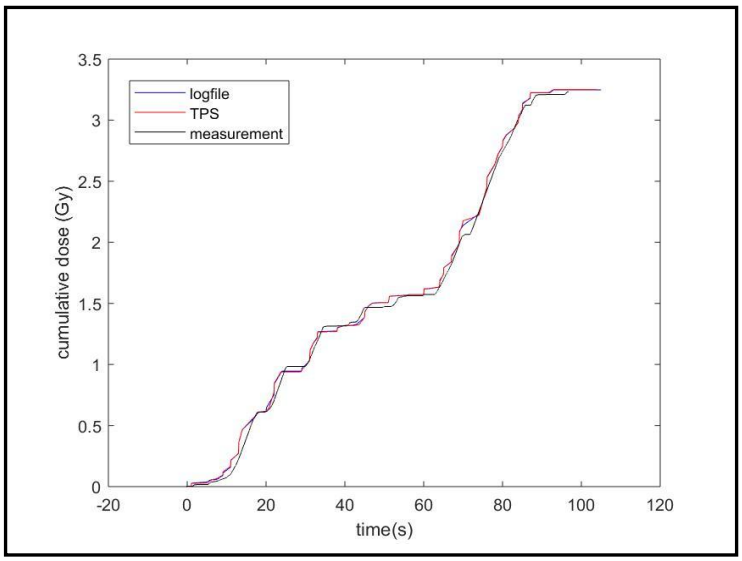

Figure 5.13: Plot of time against cumulative dose for LINAC logfile, TPS and measurement

With an in-house developed script using the MatLab for data analysis, gamma index (γ) and percentage gamma passing rate (%GP) can be obtained. The %GP can be determined using equation (5.17) based on the total cumulative dose of 3.23 Gy, the dose difference (ΔD) of 5 % and 1second of time-to-agreement (Δt), which is equivalent to 200 grid unit (time resolution is 0.005 second).

Figure 5.14 shows the gamma analysis evaluation with gamma criteria of 5 %/1 s and 3 %/1 s. The dose difference of 5 % and 3 % criteria in the gamma-analysis was based on the total cumulative dose planned. When applying the above criteria, the %GP with 5 %/1 s criterion was 100 % for both LINAC logfile and TPS reconstructed models. For the 3 %/1 s criterion, the %GP of 97.81 % and 96.70 % were obtained for the LINAC logfile and TPS, respectively, compared to the measurement. If a more relaxing criteria is imposed, for example, 2 seconds for time-to-agreement (Δt) instead of 1 second, as shown in Figure 5.15, the percentage gamma passing rate was found to be 100 % for both models at 5 % dose difference while at the 3 % dose difference, the results were 99.42 % for LINAC logfile and 98.72 % for TPS.

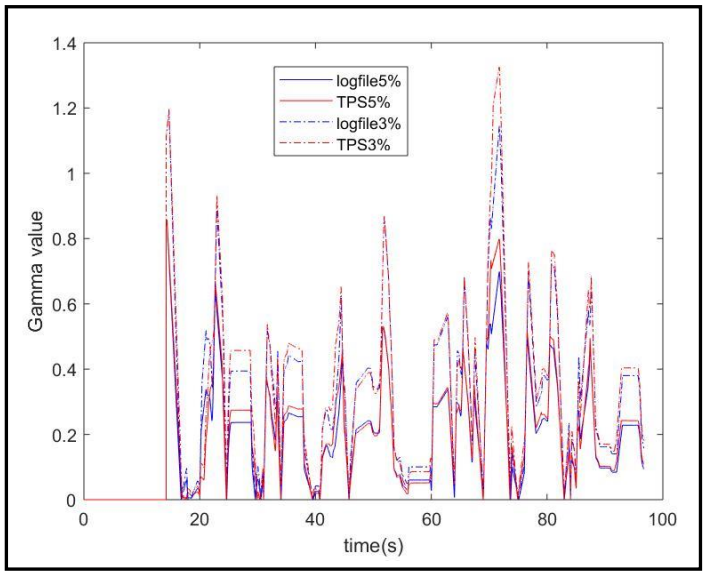

Figure 5.14: Gamma value analysis based on 5 %/1 s and 3 %/1 s showing %GP of 100 % for both models while above 96 % for the latter criteria

From the analysis as illustrated in Figure 5.14 and Figure 5.15 compared to Figure 5.13, it can be clearly seen that %GP is less when the LINAC delivered the dose at low dose rate (low gradient in cumulative dose plot).

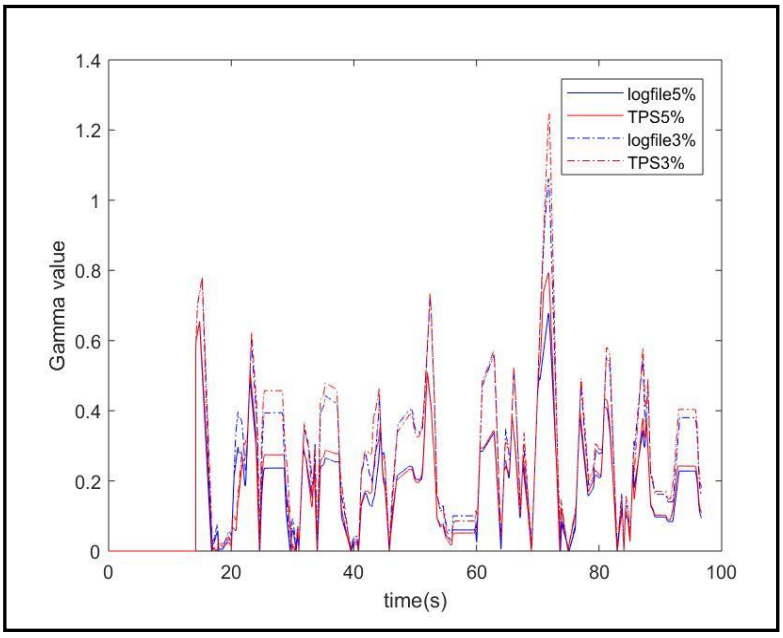

Figure 5.15: Gamma value analysis based on criteria of 5 %/2 s and 3 %/2 s showing %GP of 100 % for both models while more than 98 % for latter criteria

5.9.2 *Gamma analysis for dose difference (ΔD) and gantry angle-to-agreement (Δg) parameters*

Figure 5.16 shows the gantry angle against the cumulative dose for LINAC logfiles, TPS and measurement. As mentioned in the previous section, the interpolation method is used in determining the gantry position from the LINAC logfiles since there is no information available on the gantry position in the measurement data.

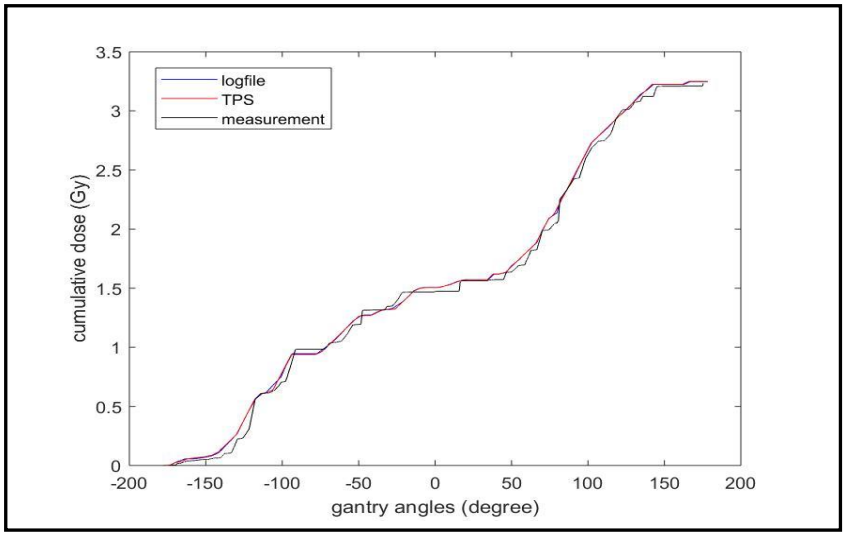

Figure 5.16: The gantry angles against cumulative dose for LINAC logfile, TPS and measurement

For gamma analysis, the interpolation from the LINAC logfile was applied since the measurement only provides the dose as a function of time. As in the last section, the %GP can be determined using equation (5.17) for dose difference (ΔD) of 5 % and gantry-to-agreement (Δg) of 4^o, which is equivalent to 214 of grid unit.

Figure 5.17 shows the two criteria of 5 %/4^o and 3 %/4^o for gamma evaluation. The percentage gamma passing rate are 100 % for the 5 %/4^o criterion for both the reconstructed models, while above 99 % for the 3 %/4^o criterion.

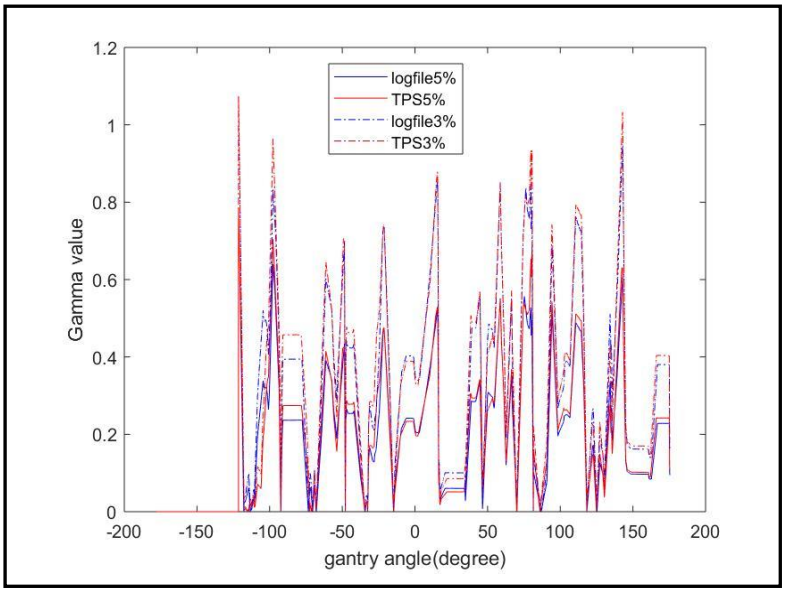

Figure 5.17: Comparison of gamma value based on 5 %/4^0 and 3 %/4^0 criteria showing %GP of 100 % for both models while more than 99 % for latter criterion

As expected, when a more relaxed criteria such as 6° gantry angle-to-agreement criterion was imposed on the evaluation, the percentage gamma passing rate of 100 % can be achieved for both the 5 % and 3 % dose difference (ΔD) criteria as shown in Figure 5.18.

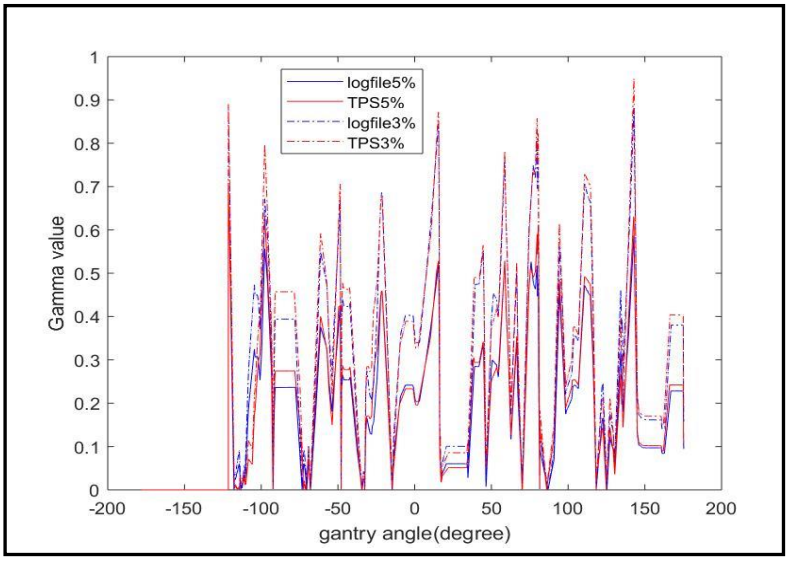

Figure 5.18: Comparison of gamma value based on 5 %/6^o and 3 %/6^o criteria showing %GP of 100 % for both models and criteria

The selection of a 4° gantry angle criterion was due to the gantry angle spacing planned in the TPS, while the 6° gantry angle criterion was selected due to the maximum gantry speed allowed by the IEC (International Electrotechnical Commission)[138]. This suggests that any errors during the dose delivery can be determined for every 4° gantry angle rotation as compared to the prediction dose.

5.9.3 Gamma analysis for instantaneous dose difference (ΔD) and time-to-agreement (Δt)

Figure 5.19 shows the instantaneous dose (Gy/s) against time. The instantaneous dose was produced using the gradient function in MatLab by dividing the cumulative dose with 0.005 seconds (time grid). The plots show spikes due to a 0.1 second adjustment in the data interpolation for the time in the LINAC logfile. However, the spikes will not affect gamma evaluation since the time adjustment is insignificant compared to the time stamp in gamma analysis.

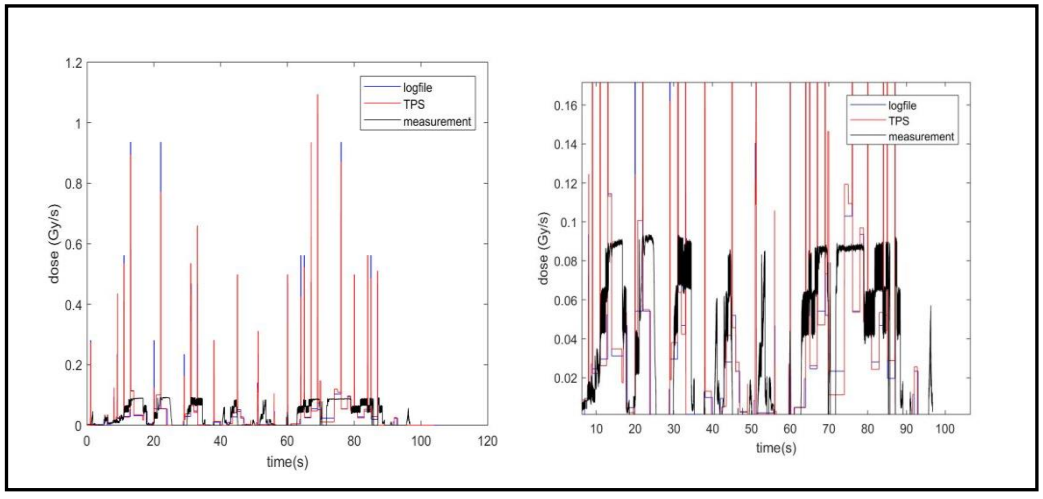

(a) **(b)**

Figure 5.19: The instantaneous-dose against time (a) and zoomed-in (b)

Figure 5.19(a) presents the instantaneous dose constructed for measurement, LINAC logfile and TPS. If the spike from the LINAC logfile and TPS were ignored, a pattern with a considerably small deviation from the measurement (see Figure 5.19(b)) can be observed. This can be explained as being due to either the effect of distortion or the effect of in distinguishability between pulses with the interpolation grid.

Figure 5.20 shows the gamma analysis with a 5 %/1 s criterion. The gamma passing rates were found to be 12.83 % for logfile and 28.76 % for TPS. Due to the significant percentage of gamma fail-rate for instantaneous dose evaluation, a more relaxed criterion was imposed for the evaluation. Figure 5.21 shows the gamma analysis with a criterion of 20 %/5 s. The %GP were now found to be 81.19 % for LINAC logfile and 97.35 % for TPS.

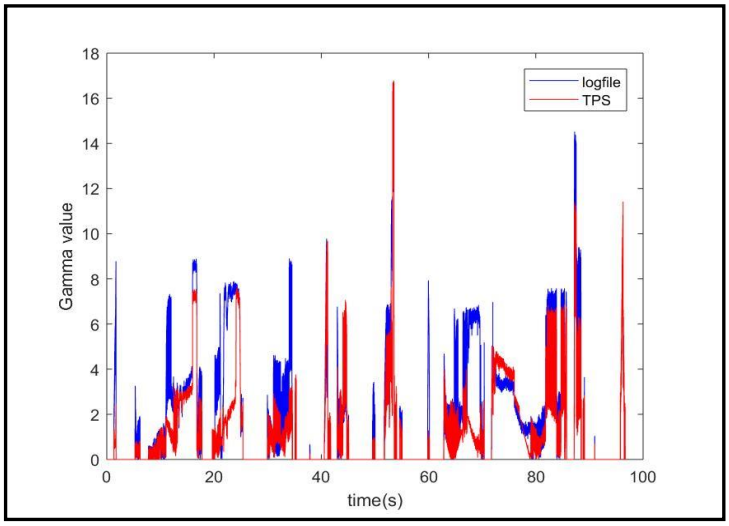

Figure 5.20: Plot of the gamma value for instantaneous-dose at the 5 %/1 s criterion

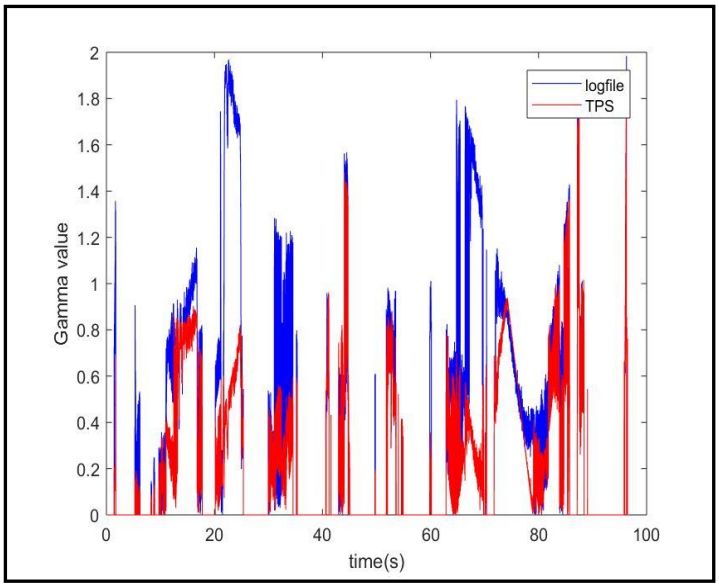

Figure 5.21: Plot of gamma value for instantaneous-dose at 20 %/5 s criterion

5.9.4 Gamma analysis for instantaneous dose difference (ΔD) and gantry angle-to-agreement (Δg)

Figure 5.22(a) shows the instantaneous dose method against the gantry angles, while Figure 5.22(b) shows the zoomed in detail results. As discussed previously, the few spikes seen are due to the interpolation method used in finding the relation between the gantry angle and time. Figure 5.23 shows the instantaneous dose difference with a maximum dose difference threshold of 0.04 Gy/s. Percentage gamma passing rate for the instantaneous dose evaluation against the gantry angles based on 5 %/4^0 criterion are 33.54 % and 25.94 % for LINAC logfile and TPS for the respective reconstructed model.

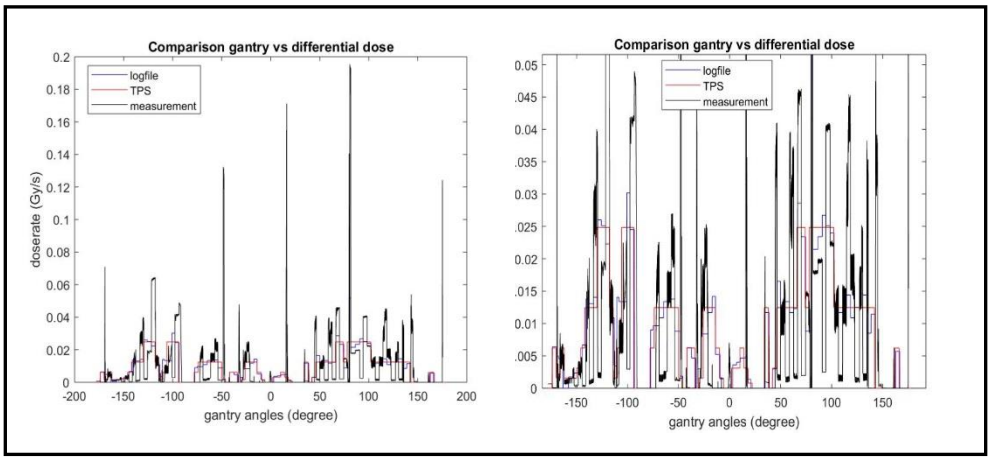

(a) **(b)**

Figure 5.22: The instantaneous-dose against the gantry angles (a) and zoom-in (b)

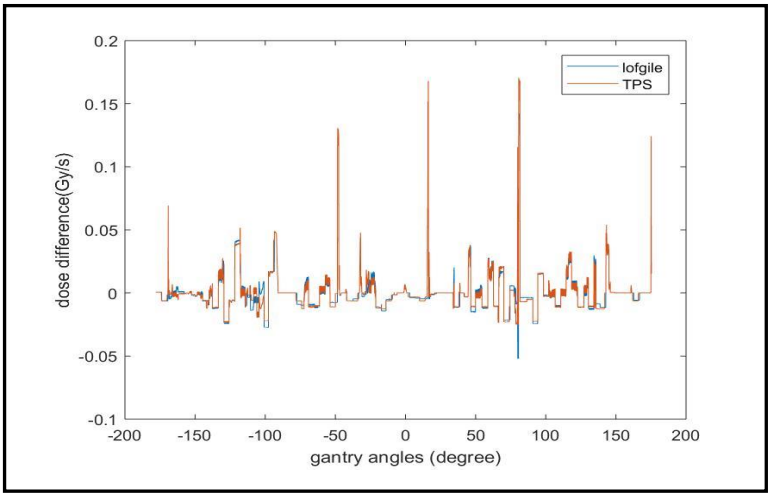

Figure 5.23: Comparison of instantaneous-dose difference for LINAC logfile and TPS measurement

Figure 5.24 (a) and (b) show the gamma value for the criteria of 5 %/4° and 10 %/4°, respectively. The %GP obtained are 33.53 % and 25.94 % for LINAC logfile and TPS, respectively based on the 5 %/4^0 criteria. The %GP based on the 10 %/4° criterion are 51.60 % and 40.89 % for LINAC logfile and TPS, respectively. Figure 5.25 shows the gamma value with a criterion of 10 %/6° and the percentage gamma passing rate obtained are 70.36 % and 69.93 % for the LINAC logfile and TPS constructed models.

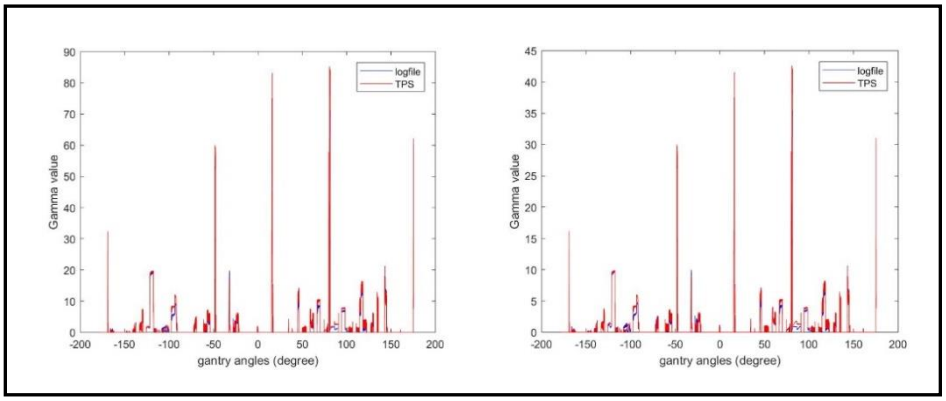

(a) **(b)**

Figure 5.24: Gamma value for the instantaneous-dose against the gantry angle with the criteria of 5 %/4° (a) and 10 %/4^0 (b), respectively

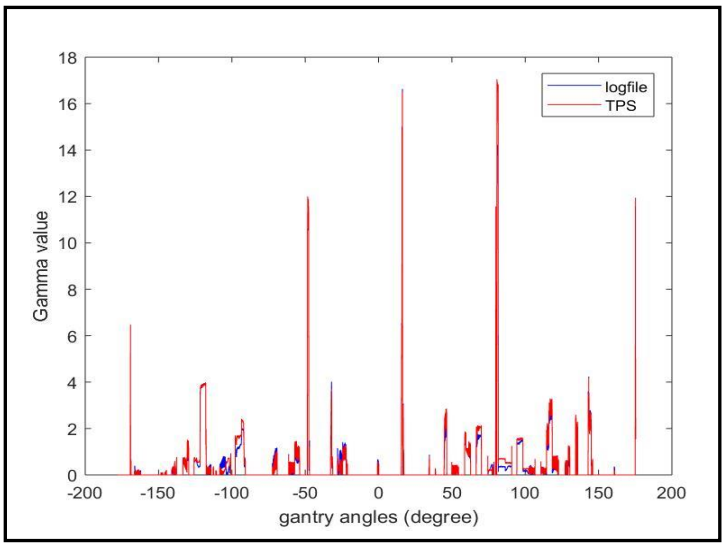

Figure 5.25: Gamma value for instantaneous-dose against gantry angle with more relaxed criteria of 10 %/6^0

5.10 Conclusion

The objective of the present chapter is to perform pulse-by-pulse dosimetry for VMAT dose delivery. It is known that during VMAT delivery, various parameters will need to be changed including the dose-rate. The expectation in the VMAT delivery measured by DD4 detector should therefore consist of various pulse height since various dose-rates were employed.

Before using the DD4 detector for the VMAT measurement, a cross-calibration between the Farmer chamber and microDiamond detector was conducted in order to verify the sensitivity of the microDiamond detector with the manufacturer's certificate. From this verification, it is found that the sensitivity of the microDamond detector is 1.26 nC/Gy with 0.15 % uncertainty while the manufacturer's calibration certificate state as 1.264 nC/Gy with 5 % uncertainty. The reason for conducting the verification is due to the sensitivity provided by the manufacturer is based on different radiation source. However, the result for this verification is less accurate due to differences set up during the measurement (phantom). The sensitivity of the microDiamond detector in the current chapter is also different from the sensitivity of 1.240 nC/Gy with 0.08 % uncertainty reported in Chapter 3. This was due to the different depth of measurement, whereby the depth of measurement in the current chapter is 5 cm while in the previous chapter it is 1.5 cm.

A cross-calibration between the microDiamond and DD4 detectors was also performed. The objective of this performance is to find the relationship between the dose and the pulse. The detector was irradiated with the set up for routine quality control by the in-house medical physicist known as VMATQA, which delivered total monitor unit (MU) of 640 MU at a fixed dose-rate of 419 MU/min. By applying the measured charge (C) and sensitivity for the microDiamond detector, the dose delivered in terms of gray (Gy) can be obtained. The VMATQA delivery measured by the microDiamond detector is given by 6.397 ± 0.103 Gy. With the same set up and delivery (VMATQA), the DD4 detector measured the dose in pulses (V/pulse). The total summation of pulse height (V/pulse) over the number of pulse detected provides the average pulse height (V/pulse). The DD4 detector correction factor is obtained by the multiplication of the dose measured by the microDiamond detector with the reciprocal number of pulses and average pulse height. Thus, the DD4 detector

correction factor is given as 0.0012 Gy/V with 4.044 % of uncertainty. The multiplication for every pulse measured by the DD4 detector correction factor during the VMAT delivery provided the dose measure per pulse (Gy/pulse). It is evident that the DD4 detector has the capability of measuring the dose per pulse in the range of 0.05-0.25 mGy/pulse.

As a preliminary VMAT dosimetry, an attempt was made to reconstruct a cumulative dose from the TPS and LINAC logfile models. From Figure 5.12, it is clear that there is a good agreement for TPS and LINAC logfile (with 5 x 5 cm^2 field-size correction) with the measurement. An important finding in this chapter is that it is wrong to assume that the average pulse height independent of the dose-rate.

microDiamond detector	
Investigation	**Manufacturer's calibration**
1.264 ± 0.002 nC/Gy	1.264 ± 0.063 nC/Gy
DD4 detector in measuring pulse-by-pulse	
Detector correction factor	0.0012 Gy/V
Dose per pulse	0.05 – 0.25 mGy/pulse
Field size correction factor	5 x 5 cm^2

Table 5.10: Comparison of sensitivity measurement for microDiamond detector and the manufacturer's calibration value and the value for DD4 detector based on correction factor calibration and dose per pulse measured during VMAT delivery

With the time-resolved dose measurement, two methods of dose delivery were evaluated; either based on the cumulative dose against time or against gantry angle, and instantaneous dose against time or gantry angle.

Using an appropriate gamma evaluation criteria, one can expect to get excellent gamma passing rates (more than 95 %) for cumulative dose evaluation. The gantry angle criterion is a more practical parameter compared to the time criterion for the evaluation of dose difference with the cumulative dose between planned delivery and the measurement. With the cumulative dose monitoring during the beam delivery, the error can be determined for every gantry angle spacing (4°) within the control point (CP) or 6° due to the maximum gantry angle speed (6°/s). The maximum dose difference between the planned and delivered dose should be within 10 % of the total delivered dose.

Gamma criteria; dose different (ΔD) with either time-to-agreement (Δt) or gantry angle-to-agreement (Δg)	Gamma passing rate (%) compared to the measurements	
	TPS	LINAC logfile
5 %/1 s	100 %	100 %
3 %/1 s	97 %	98 %
5 %/2 s	100 %	100 %
3 %/2 s	99 %	99 %
5 %/4°	100 %	100 %
3 %/4°	99 %	99 %
5 %/6°	100 %	100 %
3 %/6°	100 %	100 %

Table 5.11: Summary of gamma analysis based on various gamma criteria

This investigation also shows that the evaluation with an instantaneous dose is not practical for clinical application. This is because any deficiency in dose delivery for a small segment of the dose-rate will result in less dose being delivered. Even with more relaxed criteria imposed for evaluation, the gamma passing rate is still found to be below 95 %. In general, dose-rate evaluation with the gamma analysis is not essential in clinical criterion.

6

Improvement in VMAT dosimetry measurements with a DD4 detector

6.1 Introduction

In this chapter, real-time and pulse-by-pulse dosimetry measurements with the DD4 detector were comprehensively investigated. A newly purchased data acquisition (DAQ) system (USB-6210 from National Instruments) and a newly installed LINAC of Elekta Agility^{TM} (Elekta, Inc. Crawley, UK) with 160 MLC were used in the investigations. The new DAQ system provides a fast time settling of 4 μs (minimum) at a high sample-rate which is required in these investigations. With the on-board amplifier designed with this device, it is possible to acquire 200,000 samples per second which are sufficient time resolution to distinguish each pulse. A new prostate VMAT technique was also planned from a newly installed treatment planning system. For the data analysis, a new script was also developed with additional separation between the background and the pulse height measured. With the improved system, the reduced width of the MLC is expected to be more challenging on dosimetry measurements.

6.2 Experimental Setup

An improved customized analogue front-end (AFE) system was developed by the Physics team at the University of Bristol. The AFE is a classic design of an AC coupled pre-amplifier followed by a two-stage shaper design. As a result, it produces a semi-Gaussian voltage output. The National Instruments (NI USB-6210) data acquisition (DAQ) measurement hardware was used to digitize the input signal and readout from the detector. This differs from the last experiment where the DAQ system used was the National Instruments (NI 6025E). The DAQ was operated at its maximum acquisition rate of 200 kilo-samples per second (200 kHz), which is sufficient for time resolution to distinguish every pulse, especially for any pulse repetitions frequency (PRF) from the LINAC below 1 kHz. The NI USB-6210 card has a 91.6 μV sensitivity [139] on the voltage base. The DAQ hardware was connected to a laptop with

customized LabVIEW software installed to control the DAQ. The digital numeric values (in term of voltage) from the software were saved in a CSV extension file. Like in the previous chapter, the DD4 detector was supplied with 100 V as the bias voltage.

In the current study, a spherical phantom was used to mount the DD4 detector in order to evaluate the new DAQ system. All the measurements in this chapter were performed with the Elekta Agility (Elekta, Inc. Crawley, UK) with 160 interdigitating leaves that was recently installed at the Singleton Hospital in Swansea. Figure 6.1 shows the setup with the new system. The advantage of the recent version of VMAT is that it provides a larger range of dose-rate options [127]. The LINAC has the option of selecting from 255 bins of dose-rate from a continuously variable dose-rate (CVDR) compared to the previous version of VMAT that only allows 5 fixed dose-rates from the dose-rate bin (BDR).

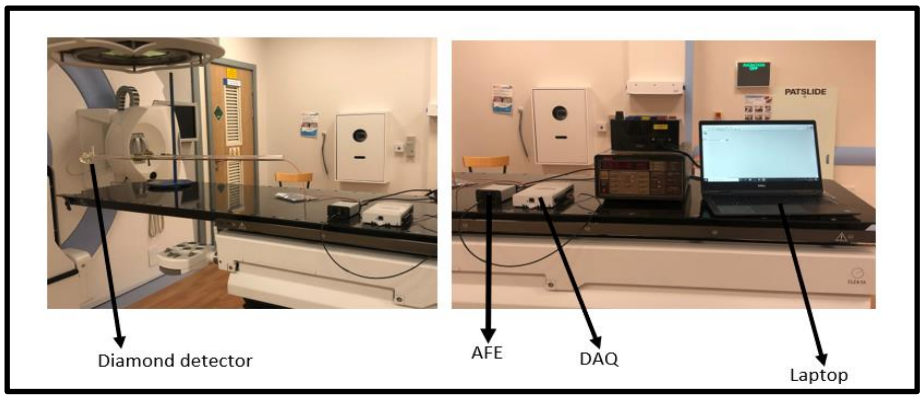

Figure 6.1: Photographs of the general set up for the measurements with the new improvement system

6.2.1 Pre-irradiation or priming the DD4detector

As a protocol recommended by the international dosimetry organization, radiation dosimeters used in therapeutic treatment need to be pre-irradiated until a stable readout is achieved [97].

Piliero [13] reported that the DD4 detector does not require any pre-irradiation dose to stabilize the readout. However, as part of the investigations, the detector was irradiated with a field-size of 10 × 10 cm^2, total monitor unit (MU) delivered for 2000 MU in 20 fractions at 522 MU/min from the LINAC known as LIN1 and at SAD of 100 cm as part of the routine before every measurement is taken. The DD4 detector

was mounted in a customised PMMA spherical phantom with a diameter of 6 cm. By using in-room lasers and isocentre of the field, the spherical phantom was set in such a position so that the centre of the detector was aligned with the centre of the beam during the irradiation. The detector was positioned in the horizontal orientation (the detector main axis is perpendicular to the beams axis, see Figure 6.1). Table 6.1 presents the setup for the priming dose study.

Parameter	Set up
Field size	10×10 cm^2
SAD	100 cm
MU	100 MU × 20
Dose rate	522 MU/min
Detector	DD4
Phantom	Spherical
LINAC	LIN 1
Energy	6 MV

Table 6.1: The setup parameters for the priming dose requirement for DD4 detector

The investigation on the reproducibility of the readout from the DD4 detector was also performed. The measurements were conducted in different weeks within the month.

6.2.2 Measurement of the optimum voltage supplied to AFE

It is essential to ensure that the optimum applied voltage to the AFE is within the limit. For the purpose of this investigation, the voltage supply to the AFE was in the range of ± 5 to ± 7 volt. The spherical phantom was used for the measurement at a fixed source to axis distance (SAD) of 100 cm with 100 MU at 522 MU/min of dose-rate. Table 6.2 presents the setup for the investigation on the optimum applied voltage to AFE. The aim of this investigation is to evaluate the response from the AFE on the variable applied voltages. The evaluations include the total pulse height, the number of pulses detected and the total BG detected.

Field-size	10 x 10 cm^2
SAD	100 cm
Dose rate	522 MU/min
MU	100
Linac	LIN 1
Detector	DD4
Phantom	Spherical
Energy	6 MV
Applied voltage	5,6 and 7 V

Table 6.2: Voltage applied to the setup of the AFE system to determine the optimum voltage

6.2.3 Dose-rate dependence with DD4 detector

In this chapter, the investigation on the DD4 detector for the respective dose-rate dependency was conducted again since the new LINAC and improved AFE system will be used in these investigations. The dose-rate dependency of DD4 detector was investigated with the use of an in-house customised PMMA spherical and cubical phantoms. As explained in Chapter 4, dose-rate dependency of the diamond detector was described by the Fowler model [22]:

$$I=I_{dark} + RD^{\Delta} \quad \ldots\ldots 6.1$$

where D is the dose-rate, I_{dark} is the dark current, with R and Δ as the fitting parameters.

It has been suggested that the dose-rate linearity of the diamond detector can be improved by increasing the bias voltage [11,140] but another researcher has reported only a slight decrease in dose-rate linearity with increase in bias voltage [141]. Similar to the microDiamond detector, the dose-rate dependency of DD4 detector was investigated using two methods: by changing the pulse-rate available from the LINAC dose-rate selection and by changing the SSD. The current investigation is different from previous investigation as the width of the MLC in the current study is 0.5 cm instead of 1 cm.

The DD4 detector was mounted in the spherical and cubical phantoms and it was irradiated to different selected dose-rates available from the Elekta Agility (LIN1) at the Singleton Hospital in Swansea. Although the LINAC used in this experiment

has a continuous dose-rate bin (CDRB), only dose-rates of 522, 260, 131, 65 and 32 MU/min were investigated. Table 6.3 and Table 6.4 show the setup for these experiments.

Set up	**Fixed SAD**
Field size	10 x 10 cm^2
SAD	100 cm
Dose rate (MU/min)	522, 261, 130, 65 and 32
MU	100 MU × 2
Linac	LIN 1
Detector	DD4
Phantom	Spherical

Table 6.3: The set up for the dose-rate dependency measurement at fixed SAD and variable pulse-rate from the LINAC with spherical phantom delivered for 100 MU

Set up	**Fixed SSD**
Field size	10 x 10 cm^2
SSD	100 cm
Dose rate (MU/min)	522, 261, 130, 65 and 32
MU	100 MU × 2
Linac	LIN 1
Detector	DD4
Phantom	Cubic and multi-block phantom
Depth	1.5 cm

Table 6.4: The set up for the dose-rate dependency measurement at fixed SSD and variable pulse-rate from the LINAC with cubic phantom delivered for 100 MU

In these investigations, two shapes of the in-house customised PMMA phantom were used; cubical and spherical. Surrounded by a multi-block water-equivalent PMMA cubic phantom, with a dimension of $8 \times 8 \times 8$ cm^3, the DD4 detector was positioned in the vertical orientation (parallel with the radiation beam) and the response from the detector was measured at a depth of 1.5 cm. On the other hand, the response of the detector was measured at the 3 cm depth with the spherical phantom.

6.2.3.1 Variable pulse-rate available from the LINAC

The investigation was conducted by varying the pulse-rate available within the LINAC using both shapes of the phantoms. Since the field-size of 10×10 cm^2 was used, the measurements based on the spherical phantom was not fully covered by the phantom. The phantom setup for both methods were the same as for the dose-rate dependency with the microDiamond detector in Chapter 4. Although the Elekta Agility has the option for various dose-rates, only 32, 65, 130, 261 and 522 MU/min of dose-rates were investigated. Those selected dose-rates reflect the change in the number of pulses generated or the pulse-rates, i.e., 25, 50, 100, 200 and 400 pulses per second.

The aim of this investigation is to evaluate the response from the DD4 detector with the variable pulse-rate from the LINAC being at a fixed distance between the radiation source and the detector. The relation between the induced charge flow through the detector and the dose-rate based on the Fowler's model can then be evaluated. The time of irradiation was calculated based on the selected dose-rate to deliver a fixed monitor unit of 100 MU. Using the same approach as in Chapter 4, the non-linearity value (Δ) for the DD4 detector can be obtained.

6.2.3.2 Variable SSD with fixed dose-rate

The second method in the evaluation of the dose-rate dependency on DD4 detector was conducted by varying the distance between the radiation source and the detector with a fixed dose-rate and measured with the cubical PMMA phantom surrounded with multi-block water-equivalent phantom. As explained in Chapter 4, the number of pulses per unit of time or dose-rate ($\dot{D}$) crossing the field-size at a distance (d) is given by equation (4.8) with consideration of the effect of the Mayneord factor. Adopting the same method, the relation between the number of pulses per unit of time and the current can be determined. Table 6.5 shows the setup used in this investigation.

Setup	
Field size	5 x 5 cm^2
SSD	70,80,90,100,110,120,130,140
Depth	1.5 cm
MU	100 MU × 2
Phantom	cubic + multiblock phantom
Threshold	0.007 V
Dose-rate	522 MU/min

Table 6.5: The set up for the dose-rate dependency measurement based on fixed dose-rate and variable SSD with cubic and multi-block phantom

6.2.4 Cross-calibration between microDiamond and DD4 detectors with spherical phantom

The cross-calibration between the microDiamond and DD4 detectors was conducted using the same method as in Chapter 5. An in-house customized 6 cm diameter spherical phantom measures the dose of 300 MU at 522 MU/min at 100 cm of SAD for a field-size of 10 x 10 cm^2. The detectors were positioned at the centre of the beams by utilizing the in-room lasers. The microDiamond detector was connected to the PTW UNIDOS Universal dosemeter which gives an output reading in cumulative charge (C). The DD4 detector was connected to the improved AFE system before it was connected to the laptop for the output via LabView software. The ADC measured the signal in terms of voltage and save it in CSV extension file. Similar to the previous chapter, the data acquisition rate was 200 kilo-samples per second, giving a 5 microsecond (μs) time resolution. The data were analyzed offline using MatLab. Table 6.6 presents the setup for cross-calibration for both detectors.

Setup					
LINAC		**Dose meter**			
Field size	10 x 10 cm^2	**PTW UNIDOS**		**Analogue Front End (AFE)**	
MU	300	Voltage	0 V	Voltage	100 V
Dose rate	522 MU/min	Chamber	microDiamond	Chamber	DD4
Depth	3 cm	Reading	**C**	Reading	**V/pulse**
SAD	100 cm	Phantom	Sphere	Phantom	Sphere
Gantry rotation	Arc_CW				
LINAC	LIN 1				

Table 6.6: The set up for cross-calibration measurement for the microDiamond and DD4 detectors

6.2.5 Treatment Planning System (TPS) for VMAT technique of prostate cancer treatment

The prostate cancer treatment planning was created using the Philips Pinnacle v.16.0 treatment planning system (TPS) based on an actual patient planning for the treatment. The prostate cancer patient was scanned on a Philips Brilliance 16-sclice CT (Philips Corporation, Ohio, USA) in a supine position according to the local standard protocol with 3 mm axial slice width. The organs at risk (OAR) were delineated (rectum, bladder, femoral heads, urethral bulb and bowel) and the target volumes followed the CHHIP (Conventional or Hypofractionated High dose Intensity) protocol [142]. The spherical phantom together with both detectors were also CT scanned with 3 mm axial slice width. Then the dose distribution was calculated for the VMAT technique by employing an inverse planning method with a collapsed-cone convolution/superposition (CCC) dose model algorithm. Based on the standard protocol used in the local department, gantry angle spacing for each control point (CP) is given within 4^o. The treatment was planned with the gantry angle starting at 140^0 and ending at -140^o. A fixed collimator angle of 0^o was set in order to avoid excessive inter-leaf leakage dose to the patient from the rotational delivery technique. The VMAT plan was set to have a total of 70 control points (CP). Once the treatment

planning was completed, it was transferred to a record and verification system, MOSAIQ v 1.6 (IMPACT Medical Systems, Sunnyvale, USA) before the beams were delivered by RT Desktop (Elekta) which is the control console for the LINAC.

International organizations have recommended that a second check on the dose calculated from the TPS should be applied before the beam delivery [143]. In this investigation, an independent dose calculation was applied using RadCalc version 6.3 (Austin, USA)[144] which uses pencil beam dose modelling for dose calculation. The Quality Assurance (QA) program in every radiotherapy department should include an independent dose calculation as a part of its Quality Control (QC) process [119]. The calculation on RadCalc was compared with the dose calculated with the TPS. This was different from the investigation in Chapter 5, where the details from the TPS and LINAC logfile were retrieved using MatLab and a dose deposition model was reconstructed based on the MLC position and MU delivered. Here, a comparison was made between the dose calculated by the TPS and RadCalc. Then gamma-like analysis was conducted to evaluate the performance of the DD4 detector.

6.2.6 Measurement with VMAT

The detectors were mounted in an in-house customized PMMA spherical phantom in a horizontal orientation. The centre of the detectors were positioned at the centre of the beam (isocentre) using the in-room lasers at 100 cm SAD. In this study, the focus is on evaluating a point dose measurement by the DD4 detector against the cumulative dose calculation by RadCalc using gamma analysis. The evaluation of the dose difference between these two methods against time was analysed based on several criteria. Gamma analysis evaluation was performed in the relative cumulative dose mode, with normalization to the maximum cumulative dose and a low-dose threshold of 10% for the clinically relevant evaluation.

6.3 Results

6.3.1 Pre-irradiation or priming the DD4 detector

Prior to the measurement, the DD4 detector was irradiated to a total monitor unit (MU) of 2000 MU in twenty fractions as a priming dose at a fixed dose-rate of 522 MU/min

from LIN1. The reason of the selection of 522 MU/min dose-rate for this investigation is that during the VMAT delivery mostly of dose delivery use maximum dose-rate. Figure 6.2 presents an example of the priming dose for 2000 MU in 20 fractions. This raw data clearly shows a change in the background (leakage) during the measurement and the noise contributed from the AFE. As explained in Chapter 4, the output reading from the ADC system, the signal is measured in terms of voltage and an in-house developed LabView software displayed the pulse height in voltage.

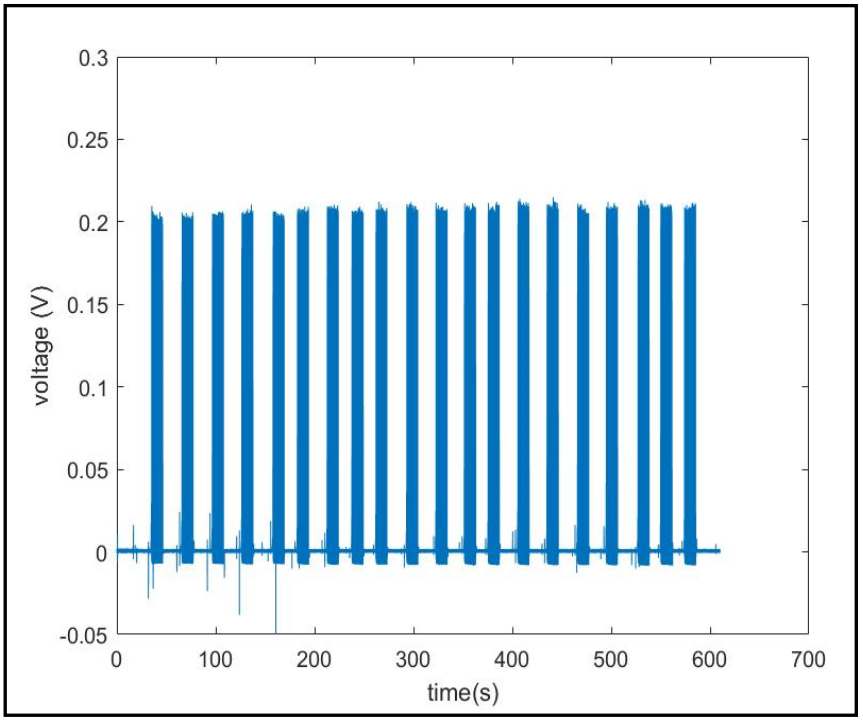

Figure 6.2: Illustration of the priming dose measurements with DD4 detector for 2000 MU without any smoothing process. The detector was mounted within the PMMA spherical phantom

Figure 6.3 shows the analogue voltage measurements after the Gaussian smoothing using MatLab tools. As for the data analysis, the distribution of the pulse height is considered to be within a Gaussian distribution (or Normal distribution with mean value is 0 and standard deviation (σ) of 5). Figure 6.4 presents the enlargement of the analogue measurement of the first fraction of the delivery. Here, the pulse height is found to be inversely proportional to the background, meaning the higher the pulse, the lower will be the background pulse height .

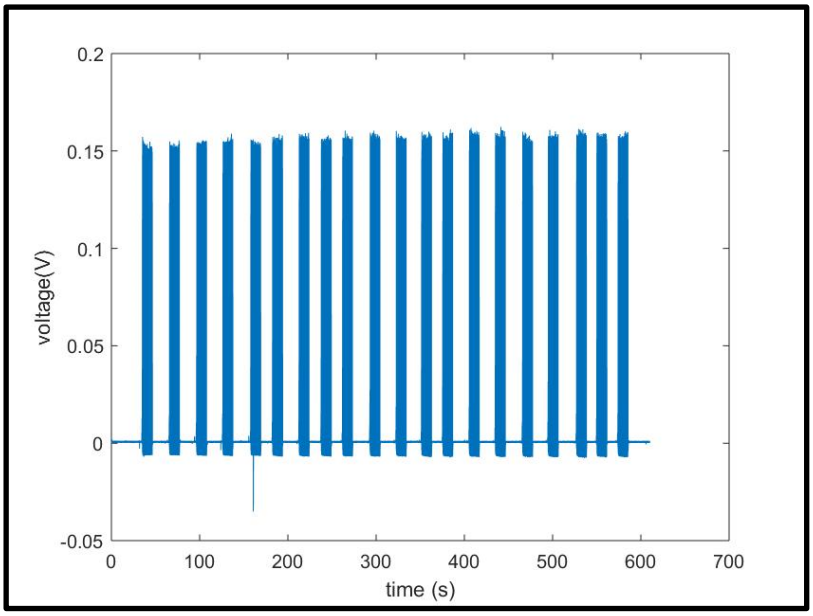

Figure 6.3: Illustration of the effect after the smoothing process, considering the distribution followed the Gaussian distribution with 5 % standard deviation

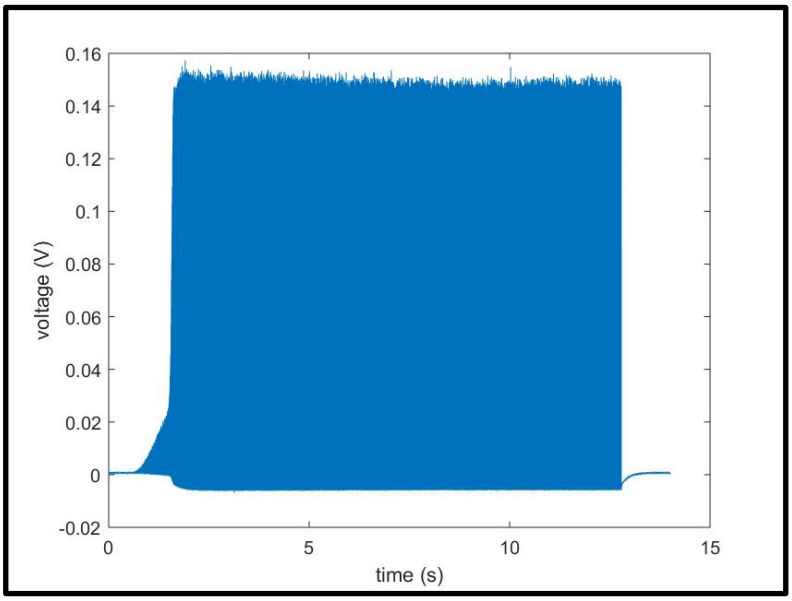

Figure 6.4: Illustration of the measurement of the first fraction of delivery measurement after smoothing using the convolution method

Figure 6.5 presents the analogue voltage for 40 pulses within 0.1 s. It clearly shows the pulse repetition frequency (PRF) is at 400 Hz and from the MatLab's tools, the time between pulses determined is 2.5 ms. The figure further shows variation in the pulse height even with the fixed dose-rate. The variation of the pulse height was approximately within 2 %.

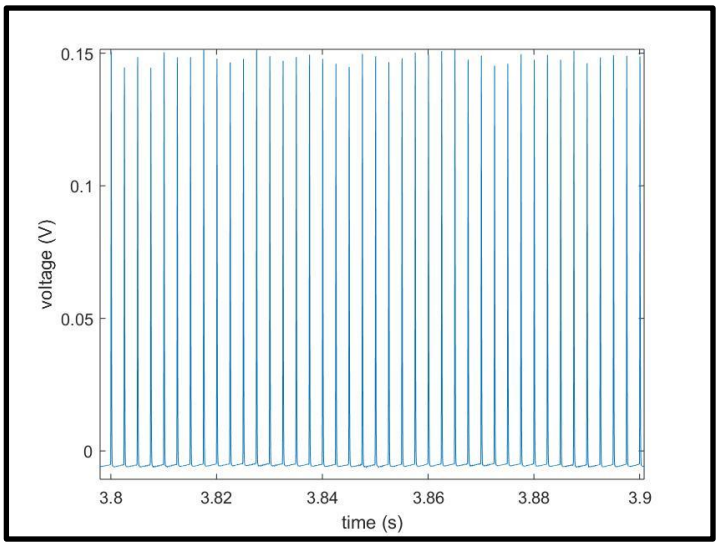

Figure 6.5: Illustration of the pulses from the LINAC during the beam delivery

Once the smoothing process was completed, an in-house MatLab script was developed to find the maximum peak for every pulse measured. Here, the maximum point was determined by fitting a quadratic equation with the knowledge that at the maximum peak, the gradient is zero. The maximum point was determined by comparing three points before and three points after the gradient. By applying a threshold condition, the pulses from the LINAC can be separated from the background measured by the DD4 detector. The threshold value is selected following several attempts during the data analysis stage to get to the lowest threshold level due to noise and leakage current. As for the priming dose evaluation, only pulses above 0.005 V (the threshold condition) were considered as they were pulses generated from the LINAC (from Figure 6.5 where the pulse height is above 0.05 V and it is reasonable to take tenth of the value). It is worth mentioning that within the MatLab tool there is a method of finding peaks from a pulse. The in-house written script was compared with the peak finding method in the MatLab's tools in order to find the best fit method of finding the maximum peak.

Figure 6.6 presents a comparison in finding the maximum peak and there seems to be good agreement for both methods. However, in Figure 6.7, the value of the maximum peak determined was different between the two methods. This indicates that the in-house written script was more convincing in finding the maximum value of the peak compared to the peak finding method with MatLab tools.

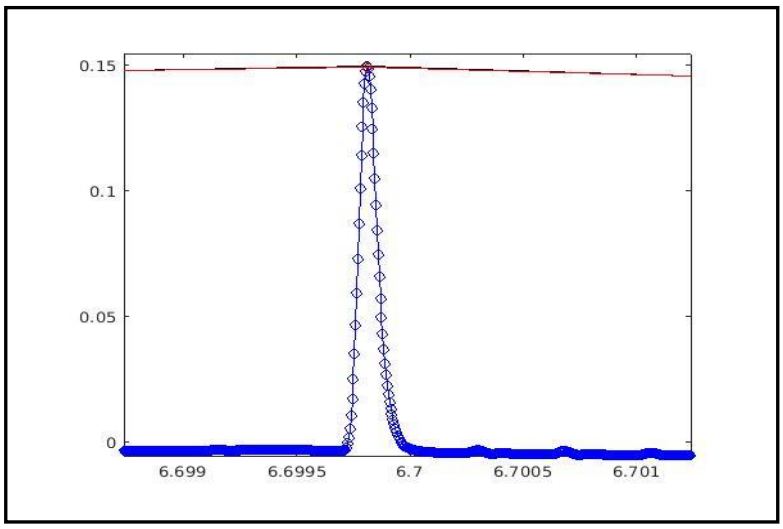

Figure 6.6: A comparison of two methods for finding the maximum peak. The blue circles show the original point against time. The red line indicates the maximum point determined in finding the peak using MatLab tools while the black circle indicates the method of finding the gradient at zero using an in-house script

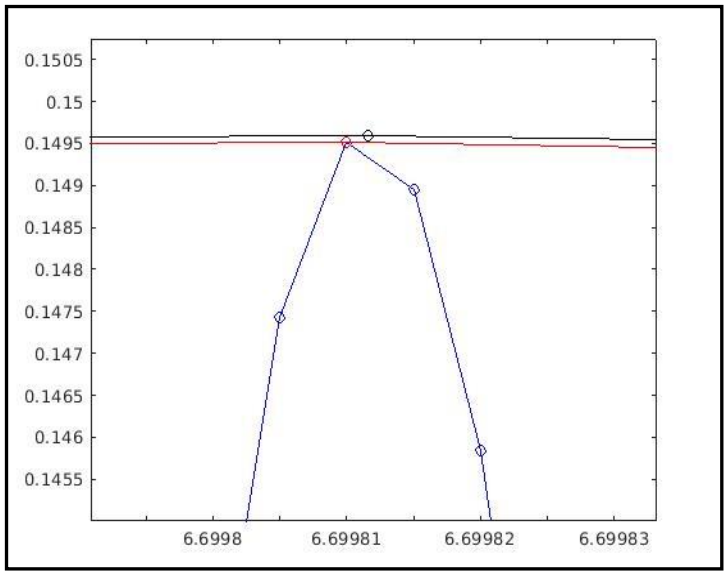

Figure 6.7: The enlargement at the peak is to show the difference from the maximum value of the peak

With the script written in MatLab, the peak of the pulses detected was plotted as a function of time. As illustrated in Figure 6.8, a peak height of 250 μs before the first detected peak is considered as the background (BG) and this is displayed together with the separation between the net pulse measurement and BG. As can be seen in the diagram, the pulse height increased at the startup (ramping up) before reaching the plateau region, as explained in the previous chapter.

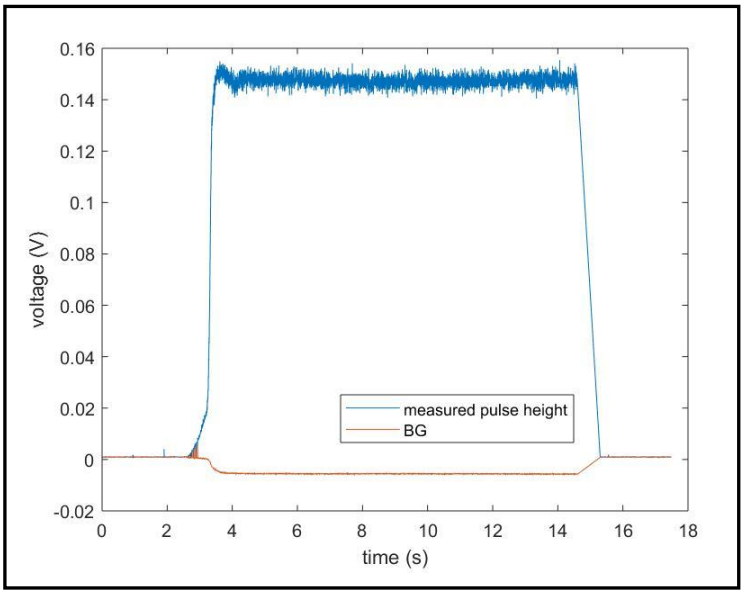

Figure 6.8: Illustration of the pulse peak measurement with the DD4 detector with 0.005 V selected as the threshold and any value below this is considered as BG. This processed illustration is drawn from the raw data in Figure 6.4 (for first fraction out of twenty fractions)

Figure 6.9 presents the pre-irradiation cumulative dose against the total pulse height in voltage. The total pulse height is calculated by the summation of each pulse height. Other fractions of the pre-irradiation were used in the same script in MatLab to analyse the measurements. By assuming that each pulse height is the amount of dose delivers by the LINAC, the total pulse height is equated to the total dose delivery. As the DD4 detector absorbed the dose, the electrons were realised from the traps as it acquires enough energy as explained in Chapter 3. After a 1000 MU of monitor unit (MU) is delivered, the small increase in DD4 detector response may be attributed to the re-filling of shallow traps which has been emptied between the measurements. It is evident that the DD4 detector requires a priming dose before it stabilises at a dose of least 1000 MU (10 Gy). In Figure 6.10 shows the deviation of the dose delivered from the average total pulse after 1000 MU delivered is less than 1 %, contradicting the results reported by Piliero [13] that DD4 detector do not required a priming dose.

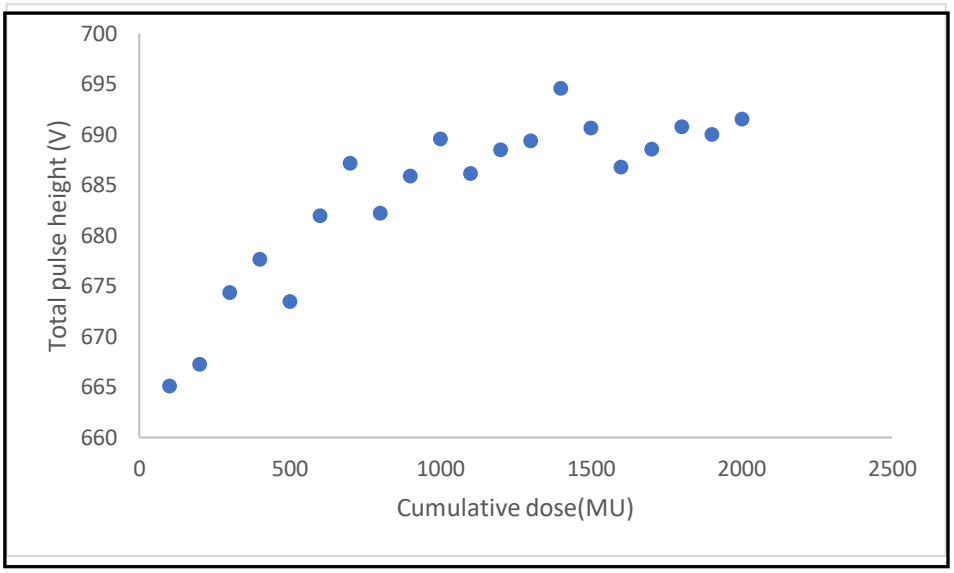

Figure 6.9: The result of the cumulative dose for DD4 detector with total monitor unit (MU) of 2000 in 20 fractions measured within the spherical phantom at 522 MU/min

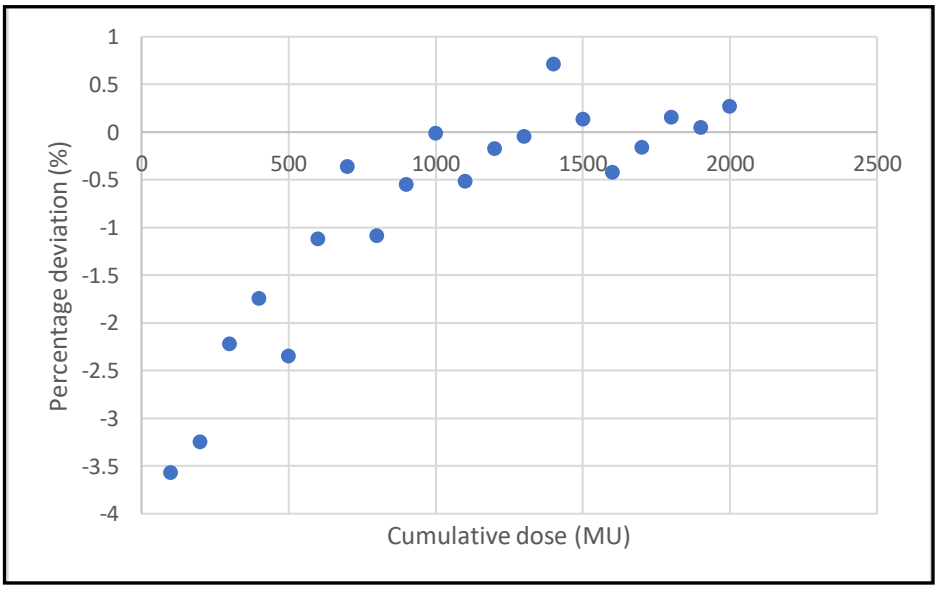

Figure 6.10: The percentage deviation from the average dose measured after the cumulative dose delivery of 1000 MU

After the analysis on the total pulse height relationship with the dose, it is interesting to analyse the relationship between the number of pulses with the dose. With the developed script written in MatLab, the number of pulses above the threshold can be counted. With the understanding that the total number of pulses detected by the detector should be reflected to the total dose delivered. The total monitor unit (MU) for each fraction is 100 MU, as expected the number of pulses detected should be the

same for each fraction. Figure 6.11 shows the number of pulses detected against the number of MU delivered. It is observed that the first fraction of the priming dose shows the number of pulses detected by DD4 detector was high. The second fraction onward present a small deviation of the number of pulses against the number of fractions.

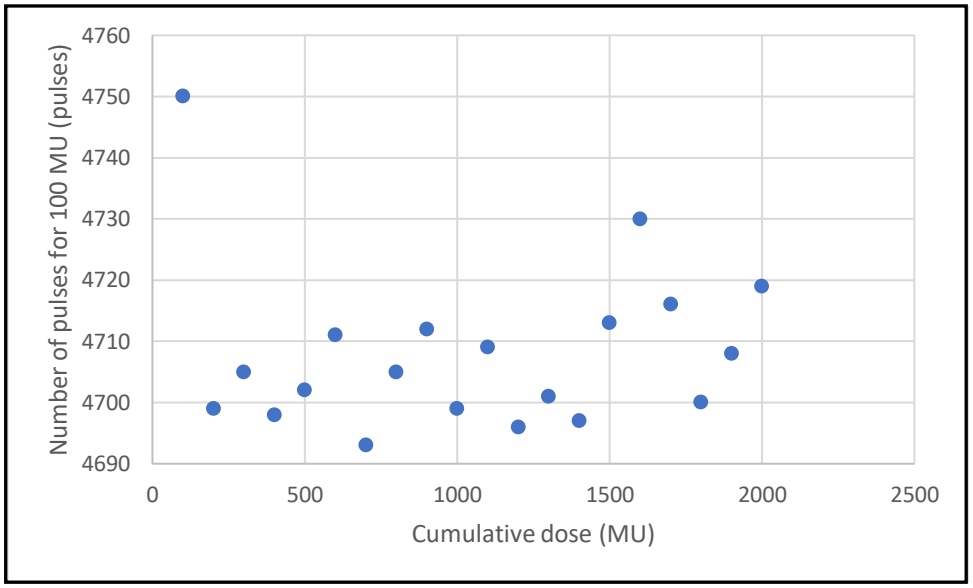

Figure 6.11: Plot showing the number of pulses detected by DD4 for 100 MU within the spherical phantom

The average number of pulses is given as 4714 pulses for 100 MU delivered. Figure 6.12 shows the percentage deviation of the number of pulses detected during the priming dose of 2000 MU in twenty fractions. It is interesting to discover that the number of pulses detected with the fixed monitor unit (MU) of 100 MU delivered is approximately constant with the deviation is approximately within 1 % from the average number of pulses detected. While the analysis for each fraction for the total pulse height has a deviation of 1 % from the average pulse height after the 1000 MU delivery (see Figure 6.10). As a conclusion from this analysis is that the total pulse height (V) and the number of pulses detected by DD4 detector are reflected to the dose delivered with the fixed of dose-rate.

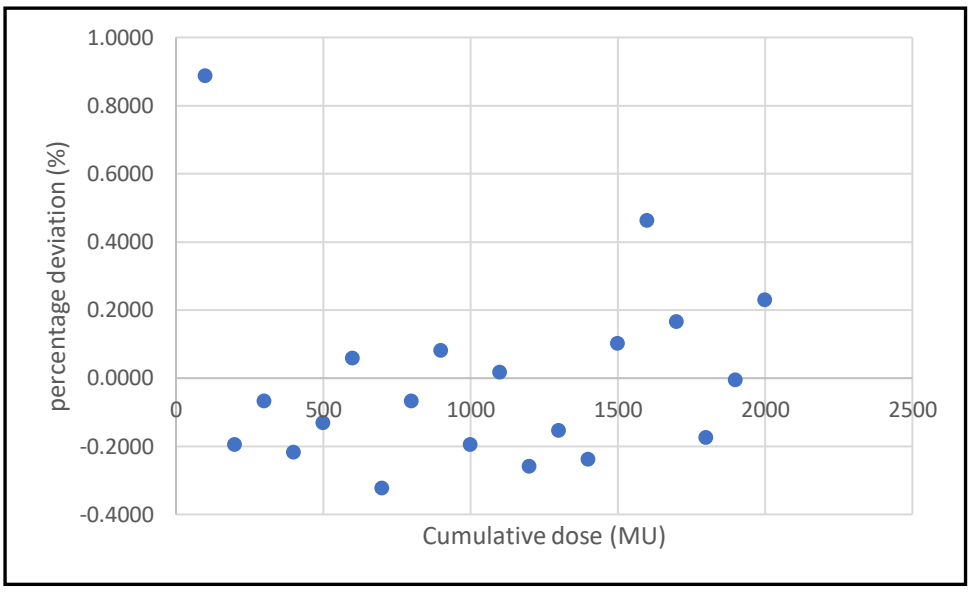

Figure 6.12: Plot showing the percentage deviation of the number of pulses against the cumulative dose

Figure 6.13 shows the total background (BG) for each fraction obtained from the written script in the MatLab. The error bar presents a standard deviation of 5 % from the average BG. The total BG calculated kept increasing before it reached the plateau region after 1000 MU cumulative dose delivered and this pattern is similar to the priming dose. The BG extracted was proportional to the pulse height detected as discussed earlier.

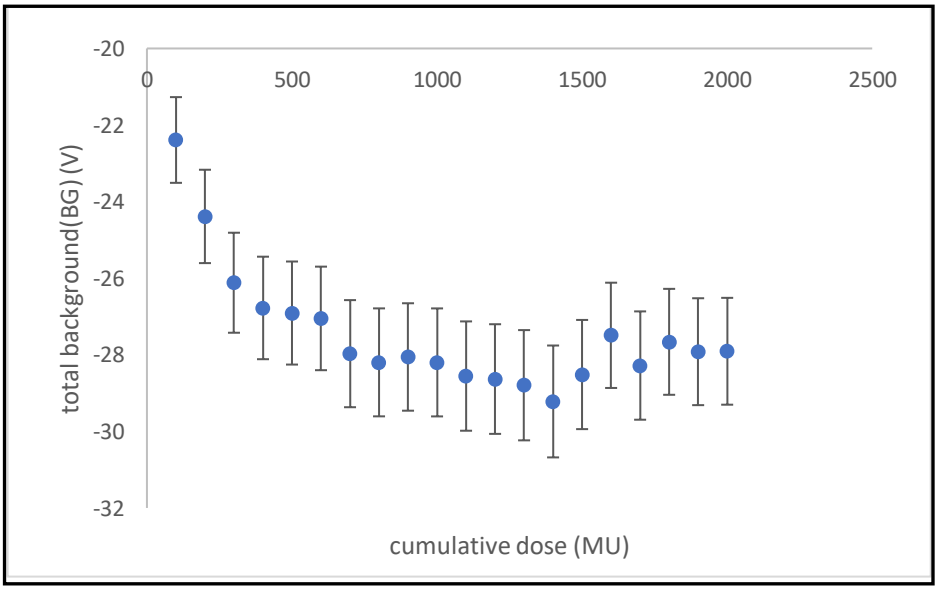

Figure 6.13: Plot of the measured background (BG) for DD4 during pre-irradiation

Figure 6.14 presents the results of reproducibility measurement for DD4 detector at different weeks within a month. The reproducibility of a detector refers to the closeness of the agreement of the measurements for the same quantity performed under the same radiation conditions. This is different from repeatability which refers to the closeness agreement between the consecutive measurements obtained under identical radiation condition. For the priming dose, the total number of monitor unit (MU) delivered was 2000 MU in 20 fractions. It is evident that the required priming dose for DD4 detector was in the range of 500 – 1000 MU. The recommendation for the reproducibility measurement was a few tenths of a percentage (<1 %) with 1SD [17]. From the investigation, the reproducibility of the DD4 detector obtained was within 2.2 % from the average total pulse height (V). From the Figure 6.14 also showing the similar pattern with Figure 6.9 and it is evident that the DD4 detector need the priming dose.

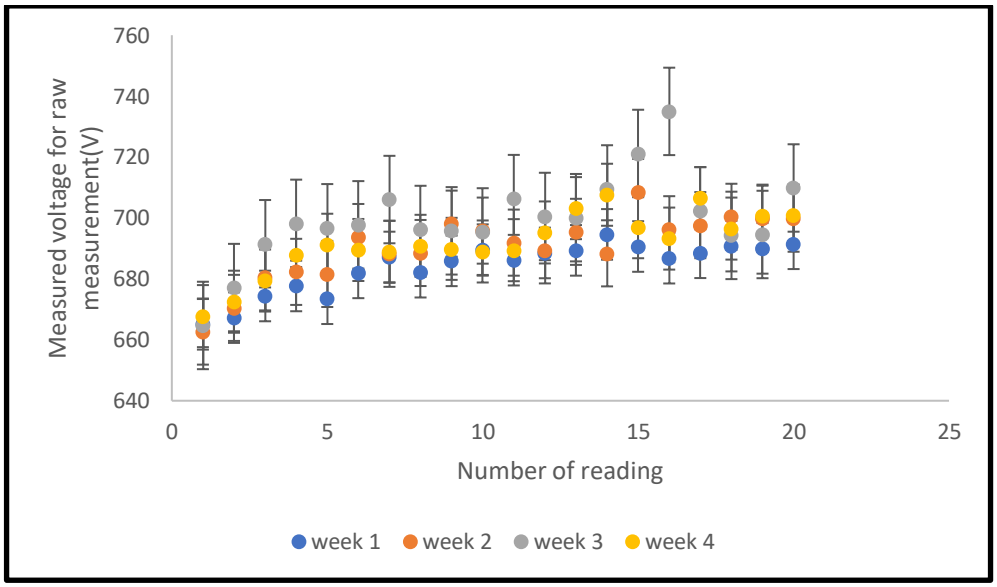

Figure 6.14: Illustration of the reproducibility measurements with the DD4 detector for different weeks based on the spherical phantom

6.3.2 Measurement of the optimum voltage supplied to AFE

Figure 6.15 presents the measurements of the net total pulse height with different voltage applied to the AFE system. The details for the measurement information are summarised in Table 6.7. As shown in the table, by changing the voltage applied to the AFE system, the deviation between the total pulse height and the average of the

three different applied voltage was within 0.1 %. Table 6.7 also indicates that the total BG calculated for the different applied voltages have a deviation within 1.6 % from the average BG calculated. It is worth noting that the analysed data only considered the pulses in the plateau region with the same threshold value of 0.001 V.

Voltage (V)	Total pulse height - BG (V)	Deviation	Average pulse height - BG (V)	Total BG (V)	Number of pulses
7	666.9459	-0.028669766	0.1368	-26.8698	4505
6	667.9489	0.121674128	0.1359	-27.1637	4524
5	666.5167	-0.093004362	0.1372	-27.7033	4496
Average	**667.1372**		**0.1366**	**-27.2456**	**4508**
SD	0.7350		0.0007	0.4427	14
%SD	0.1102		0.4873	1.5516	0.3171

Table 6.7: Result of the measurements for different voltage supply to the AFE system with 100 MU at 522 MU/min dose-rate. The script written in MatLab enabled the separation of the pulse height and the BG

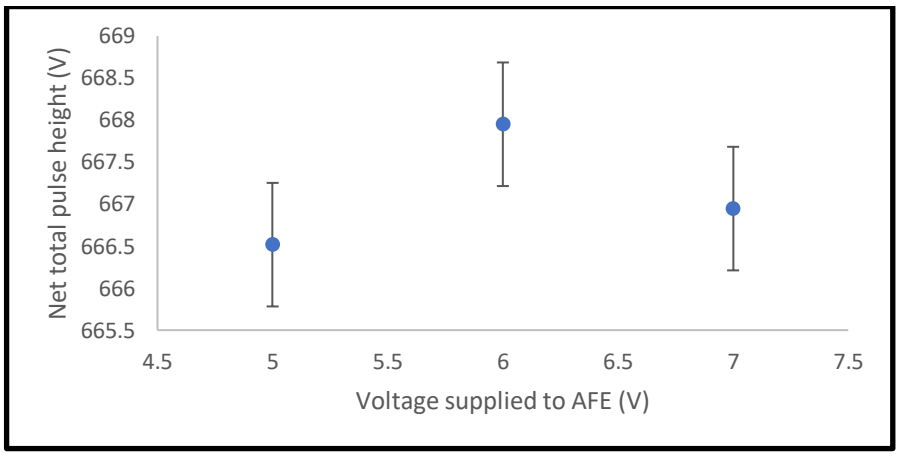

Figure 6.15: Illustration of the net pulse height calculation with different applied voltage to the AFE system. The deviation observed is approximately within 0.1 %

As expected, the pulses generated by the LINAC from the fixed dose-rate had identical pulse height. The deviation of the average pulse height for the different applied voltage in this investigation was found to be within 0.5 % as presented in Figure 6.16.

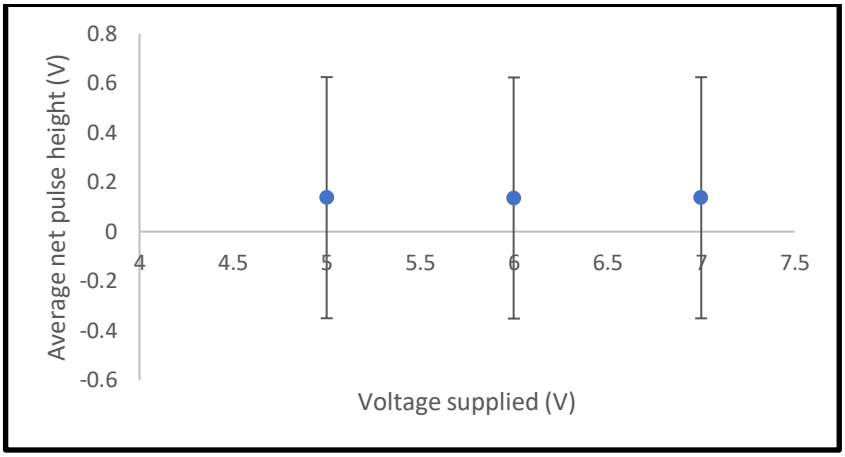

Figure 6.16: Plot of the average net pulse height (V) detected by DD4 for different voltage supply

Figure 6.17 shows the total number of pulses detected by the DD4 detector based on three different voltage supply. The highest number of pulses was observed when a voltage of 6 V is applied to the AFE system compared to the supply of other voltage values based on three measurements. Hence, 6 V was selected to be applied to the AFE system for further investigations with the DD4 detector since it has lower BG reading compared to the other voltages.

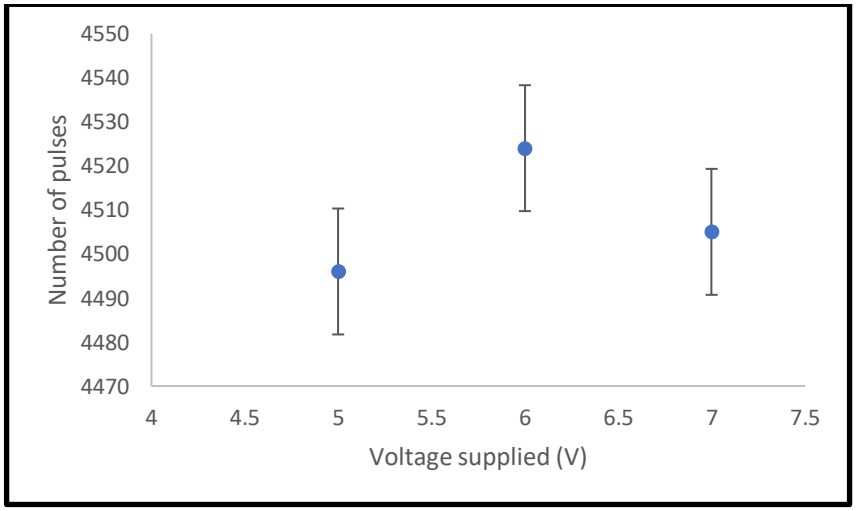

Figure 6.17: The net total number of pulses detected by the DD4 for different applied voltage

6.3.3 Dose-rate dependence with DD4 detector

6.3.3.1 Variable pulse-rate available from the LINAC

a) Measurement with spherical phantom

Table 6.8 presents the set of parameters extracted from the LINAC for offline analysis of the different dose-rates. Assuming that the pulse indicates that the dose has been delivered, then the total dose delivered (100 MU) would be equal to the total pulse height detected, regardless of the employed dose-rate. It can be seen in Table 6.8 that the total pulse height increases at higher dose-rate for the raw total pulse height and the net total pulse height (subtracted from the background). The deviation from the raw total pulse height is given as 1.1 % while for the net total pulse height is 2.6 %. The table further indicated that the total BG increased at higher dose-rate. The deviation obtained on the net total pulse is similar to the result in section 5.7.2 where the deviation on the pulse detected for the DD4 is given as 2.4 %.

For higher pulse-rate, the number of pulses detected is expected to increase due to shorter time of dose delivery. Table 6.8 presents the number of pulses detected increased for higher dose-rates as expected . But the average net pulse height seems to contradicting with the understanding that the average net pulse should be reduced with the larger number of pulses. The deviation is given as 0.81 % from the average net pulse height.

Dose-rate (MU/min)	Average total pulse height (V)	Average total BG (V)	Net total pulse height (V)	Net average pulse height (V)	Number of pulses
32	675.0744	2.2736	672.8008	0.1510	4456
65	677.7843	-0.0493	677.8336	0.1513	4481
130	683.8464	-2.1987	686.0451	0.1524	4502
260	692.8361	-9.0982	701.9343	0.1540	4557
522	690.8725	-24.4488	715.3213	0.1531	4671

Table 6.8: Results of the various parameters for different pulse-rates from the LINAC delivered at 100 MU. The magnitude of the BG increases with the pulse-rate

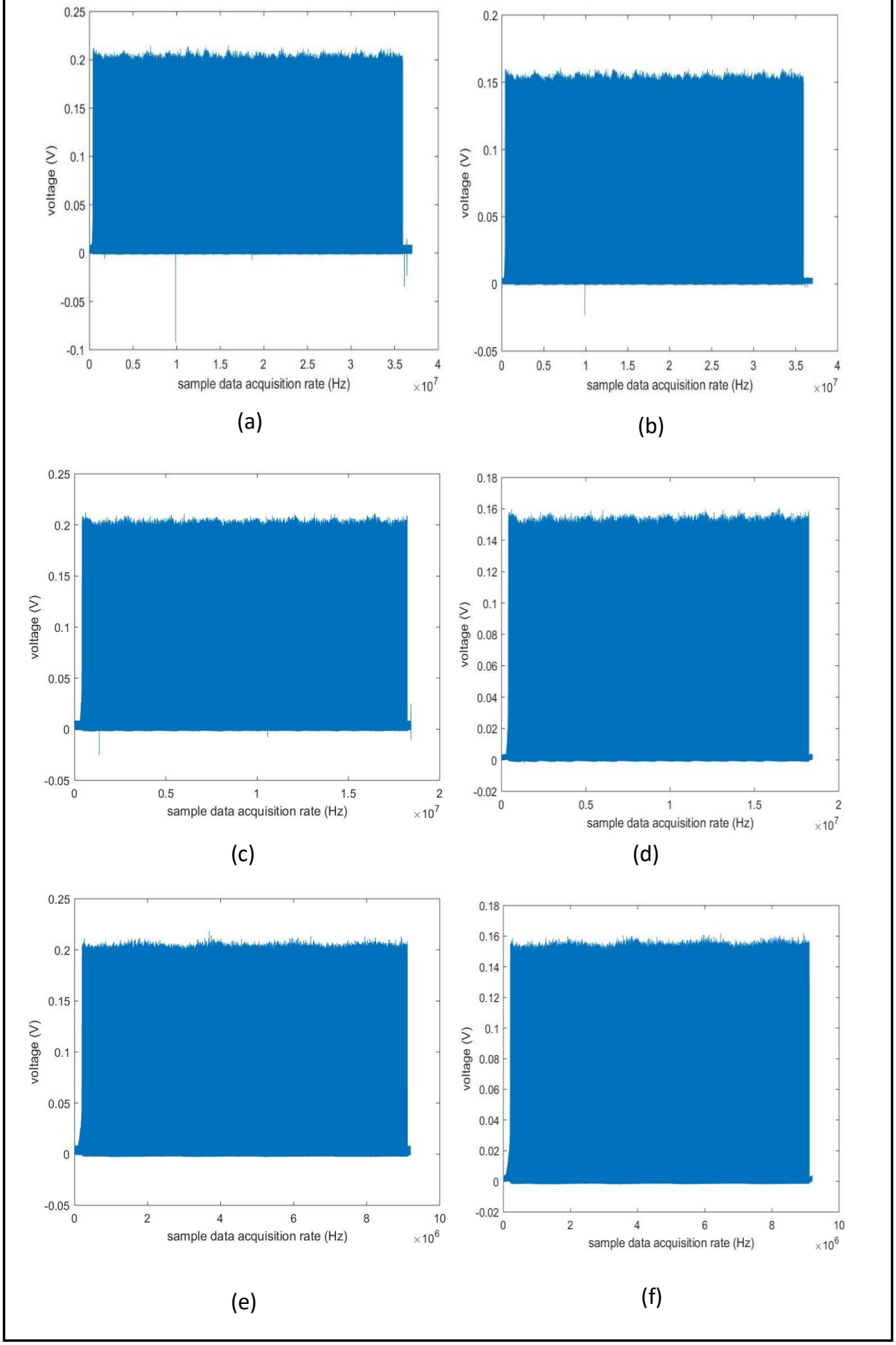
voltage (V)
sample data acquisition rate (Hz)
×10^7
(a)
(b)
(c)
(d)
×10^6
(e)
(f)

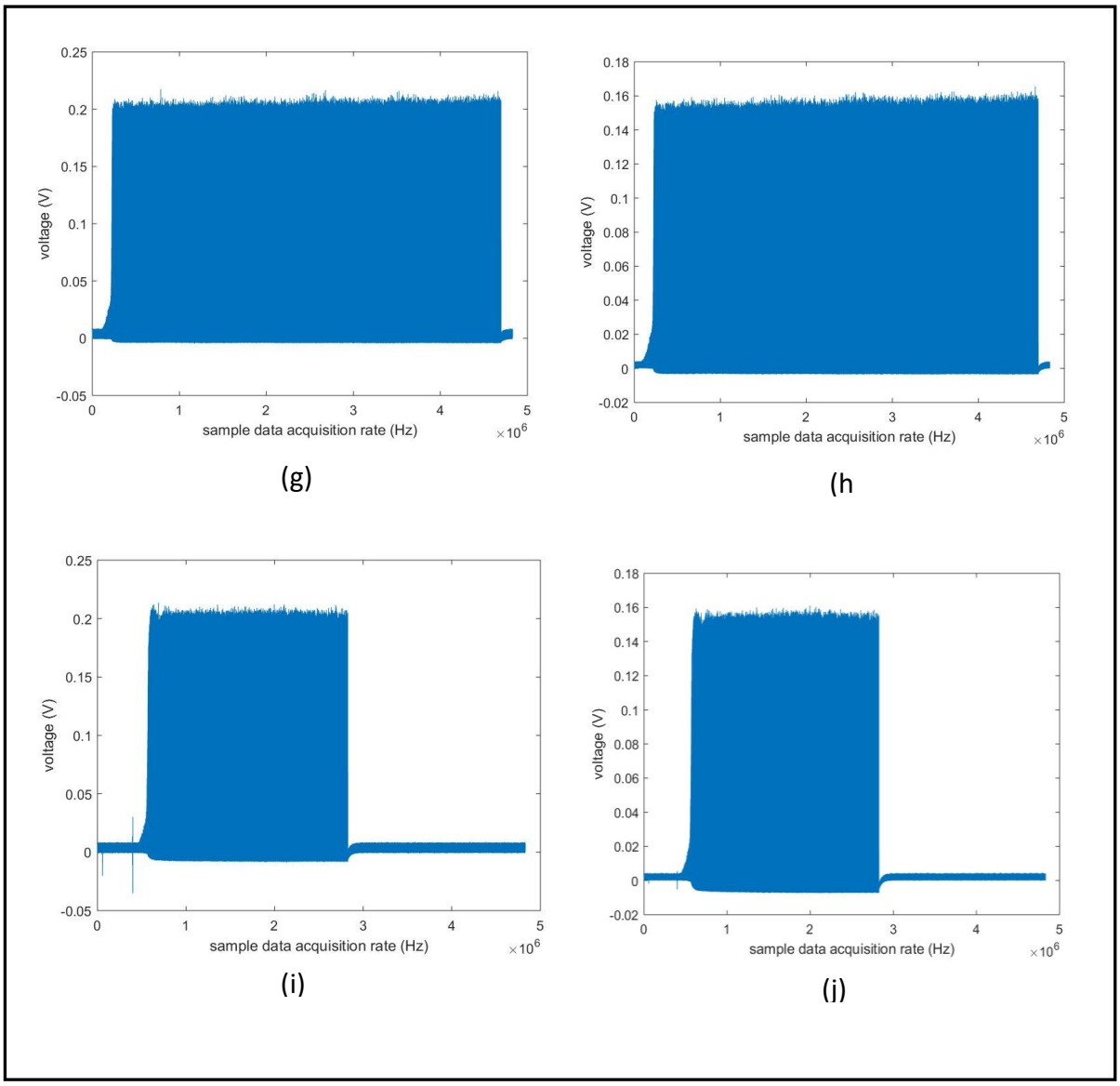

Figure 6.18 :Illustration of raw data acquisition (a, c, e, g, i) and after the smoothing process (b, d, f, h, j) for different pulse-rates from the LINAC (32, 65, 130, 260 and 522 MU/min), measured with spherical phantom delivered for 100 MU

Figure 6.18 presents the results of the comparison between the raw data acquisition from different dose-rates and the data after the smoothing process using the Gaussian convolution method. It can be seen that after the smoothing process, the pulse height reduced compared to the raw data.

Figure 6.19 presents the result of a single pulse detected by the DD4 detector after the smoothing process at 35 MU/min. It can be seen that the pulse displayed a

semi-Gaussian behavior which has a rapid rise and a slower fall which can be attributed to the effect of the two-stage shaper as described in Chapter 4. Therefore, the pulse displayed by the front-end system is a modified pulse shape.

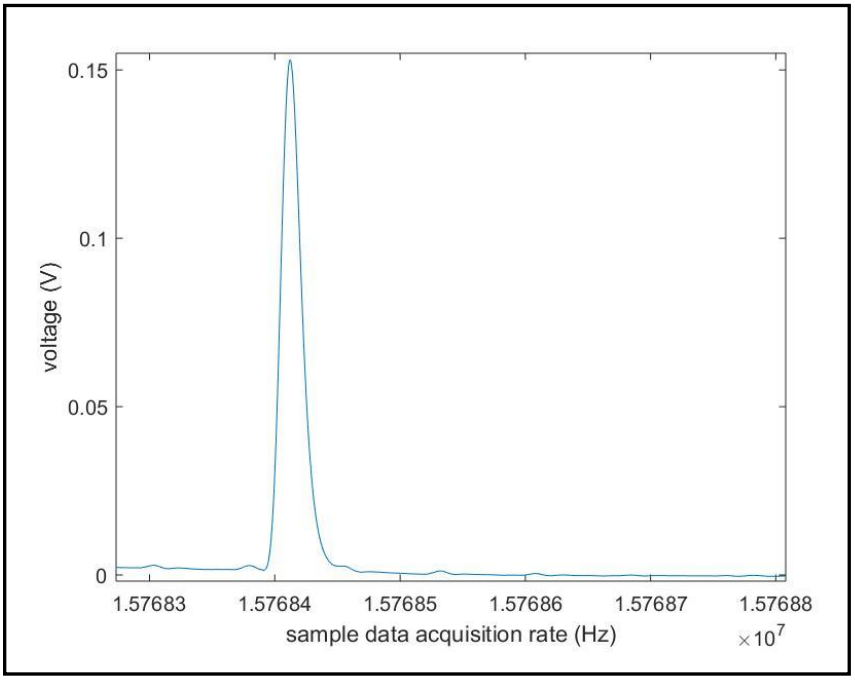

Figure 6.19: Illustration of a single pulse detected by DD4 detector after the smoothing process at 35 MU/min

Figure 6.20 presents the total number of pulses detected by the DD4 detector which reflects the time-resolved output of the LINAC over a period of 0.1 second. As expected, at a pulse-rate of 522 MU/min, the LINAC generated 400 pulses per second and 40 pulses were detected within 0.1 second, 20,10,5 and 2 number of pulses being detected within 0.1 s for 260 MU/min, 130 MU/min, 65 MU/min and 32 MU/min respectively.

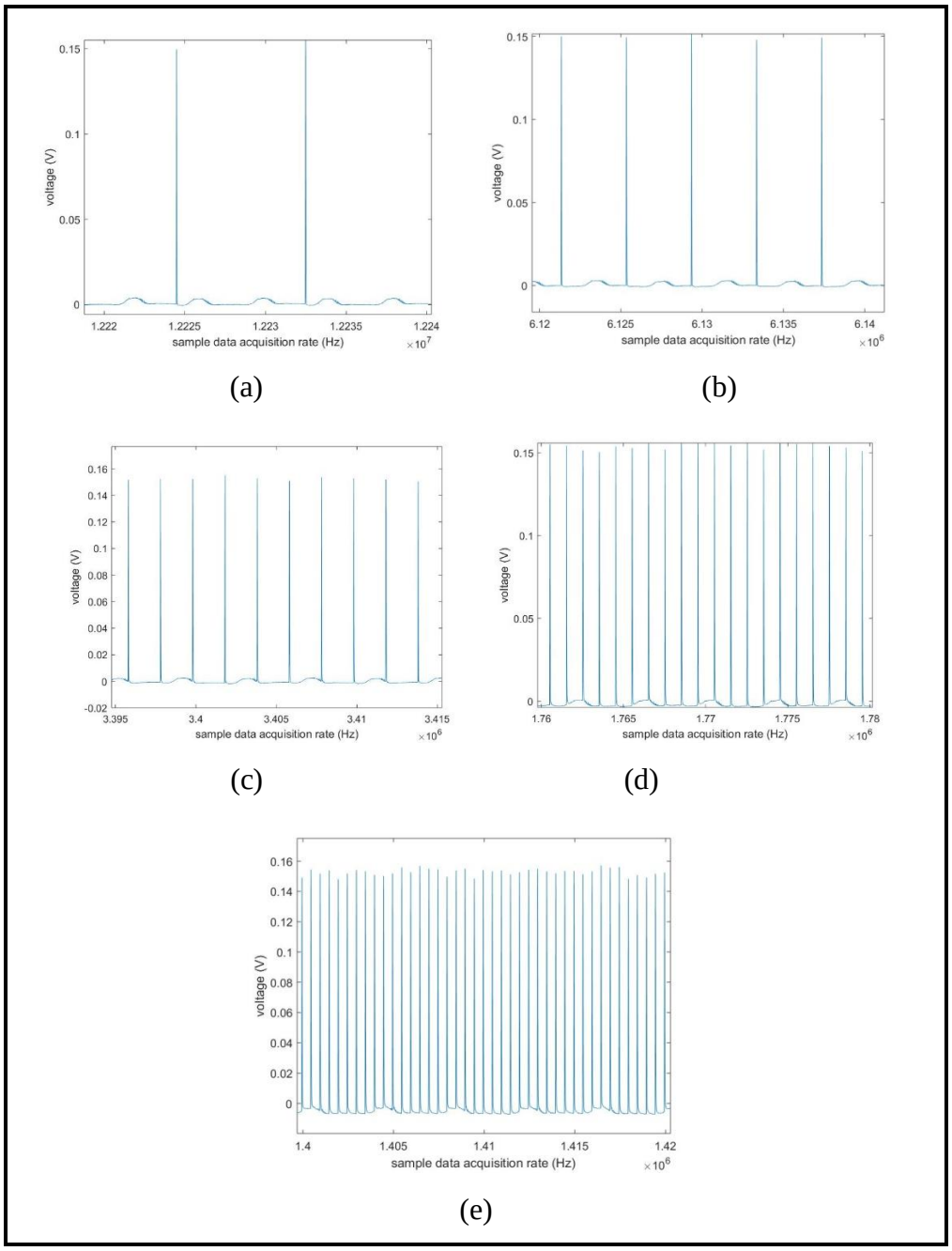

Figure 6.20: Illustration of the number of pulses detected by the DD4 detector for (a) 32, (b) 65, (c) 130, (d) 260, and (e) 522 MU/min for period of 0.1s before the subtraction of BG. The change in the periodic background might be due to the electronic component of the high-count system

Figure 6.21 presents the final plot after the offline analysis together with the separation of the BG. The threshold was set at 0.007 V and pulses below the threshold were considered as noise or BG. As shown in the figure, the BG increased when higher pulse-rates were employed. This effect might be due to the electronic component of

the high-count system and also possibly due to the characteristic of the diamond detector towards the higher pulse-rate.

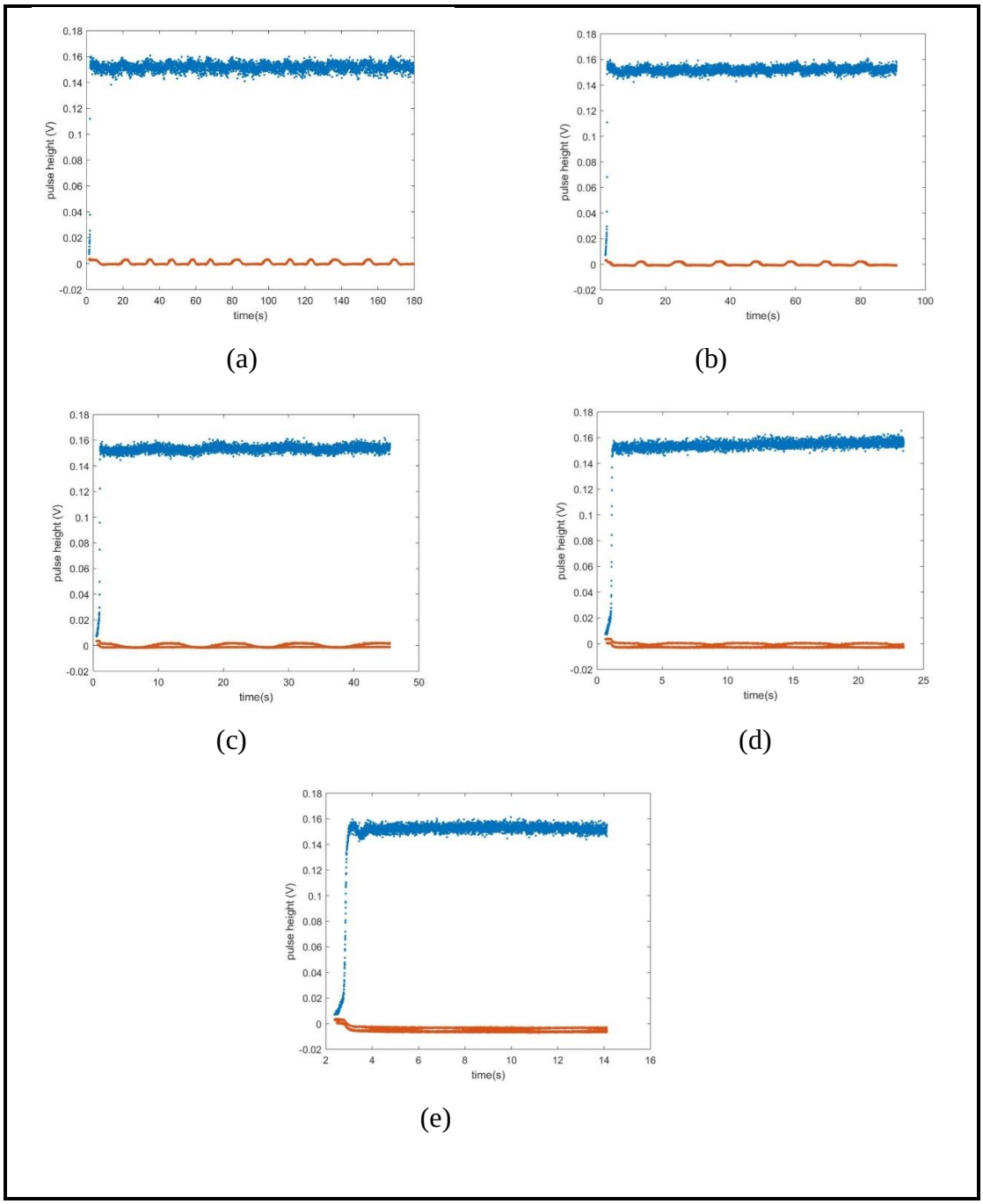

Figure 6.21: Illustration of the processed pulses separation with the BG at a threshold of 0.007V for the different pulse-rates from the LINAC (a: 32 MU/min, b: 65 MU/min, c: 130 MU/min, d: 260 MU/min and e: 522 MU/min)

Figure 6.22 presents the average pulse height for different pulse-rates from the LINAC. The average pulse height was found to increase with higher pulse-rates up to 260 MU/min. Piliero [13] reported that by changing the PRF, the current supplied to the electron gun will change as more electrons will be generated and this will in turn increase the number of pulses.

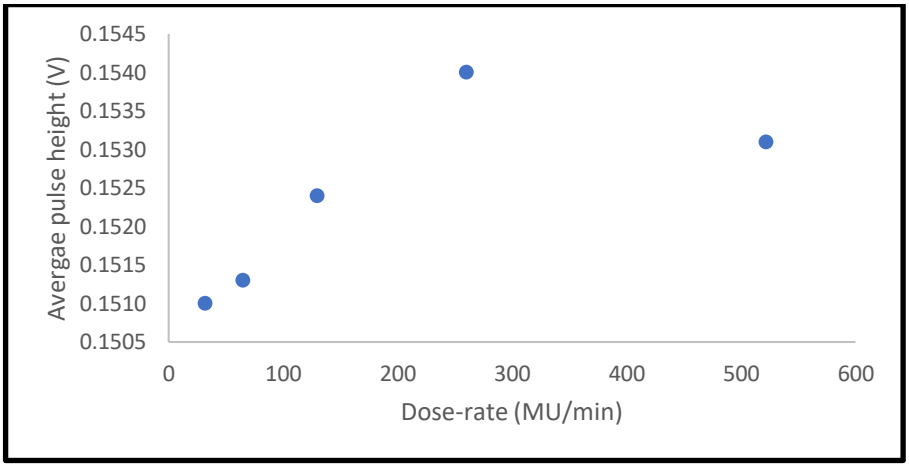

Figure 6.22: Plots of average pulse height for different pulse-rates from the LINAC measured by the D44 detector with the spherical phantom

The plots in Figure 6.23 supported Piliero's assertion as the number of pulses detected is found to increase with higher pulse-rates. However, based on the finding, the assumption that the product of the total number of pulses delivered with the average pulse height will determine the dose delivered does not hold. There are a number of possible reasons for this. Firstly, the total pulse height for different pulse-rates might be due to the different BG measured. Secondly, since the measurement was done with the spherical phantom and limiting the field-size employed to 10 x 10 cm^2, the effect of full scattering needs to be considered. Thirdly, the different number of pulses detected might also be due to the number of pulses detected at the start-up (ramping up) region which are above the threshold value.

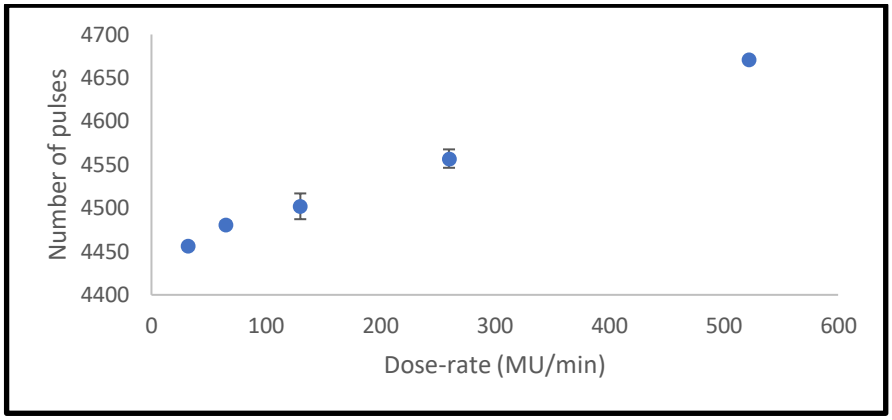

Figure 6.23: Plot of the number of pulses for different pulse-rates available from the LINAC

An evaluation was conducted to find the relationship between the detector's response and the pulse-rate based on Fowler's model. The calculation of the irradiation time are based on three methods; (i) irradiation time for 100 MU with respect to the pulse-rate on the LINAC, (ii) the irradiation time from the plot based on the first pulse until the last pulse detected, and (iii) the reciprocal of the PRF multiplied by the number of pulses detected.

For the first method in determining the irradiation time is based on the time required to deliver 100 MU with the respective dose-rate. By applying the Fowler's model of DD4 detector dependency on the pulse-rate as described in section 4.3.3, equation (4.5) and (4.7), the non-linearity factor (Δ) can be obtained. Table 6.9 present the respective parameters required in Fowler's model.

LINAC pulse-rate (MU/min)	Log (pulse-rate)	Total pulse height (V)	Irradiation time (s)	Log (total pulse height/irradiation time)
32	1.5051	672.8008	187.5	0.5560
65	1.8129	677.8336	92.3077	0.8681
130	2.1139	686.0451	46.1538	1.1750
260	2.4150	701.9343	23.0769	1.4844
522	2.7177	715.3213	11.4943	1.7955

Table 6.9: Result for irradiation time for delivery of 100 MU at respective pulse-rate available on the LINAC with spherical phantom. The irradiation time was calculated based on the time to deliver 100 MU for the respective pulse-rate

The second method is based on the plot where the irradiation time is obtained by the time duration from the first and the last pulse being detected. Table 6.10 present the required parameters in determining Δ value.

pulse-rate (MU/s) (100MU/irradiation time)	log(pulse-rate)	total pulse height (V)	irradiation time (s)	log(total pulse height/irradiation time)
0.5583	-0.2532	672.8008	179.1299	0.5747
1.1155	0.0475	677.8336	89.6482	0.8786
2.2137	0.3451	686.0451	45.17405	1.1815
4.3712	0.6406	701.9343	22.8770	1.4869
8.5045	0.9297	715.3213	11.7585	1.7841

Table 6.10: Result for irradiation time in delivering 100 MU at respective pulse-rate from the plot measured with the spherical phantom

The third method in determining the non-linearity for DD4 detector is based on the PRF instead of the LINAC pulse-rate. Table 6.11 present the parameters required for the Fowler's model. With the knowledge that LINAC will generate 400 pulses per second (pps) at 522 MU/min and given that the total number of pulses detected by the DD4 detector is 4671 pulses, therefore the irradiation time is determined as 11.675 seconds.

dose-rate (MU/s) (100MU/irradiation time)	log (pulse-rate)	total pulse number	irradiation time (s) (1/PRF*no of pulses)	log(total no pulse/irradiation time)
0.5617	-0.2505	4456	178.0400	1.3985
1.1152	0.0474	4481	89.6200	1.6987
2.2161	0.3456	4502	45.0200	1.9990
4.3816	0.6416	4557	22.7850	2.3003
8.5653	0.9327	4671	11.6775	2.6022

Table 6.11: Result for irradiation time for delivery of 100MU at the respective dose-rate from the PRF

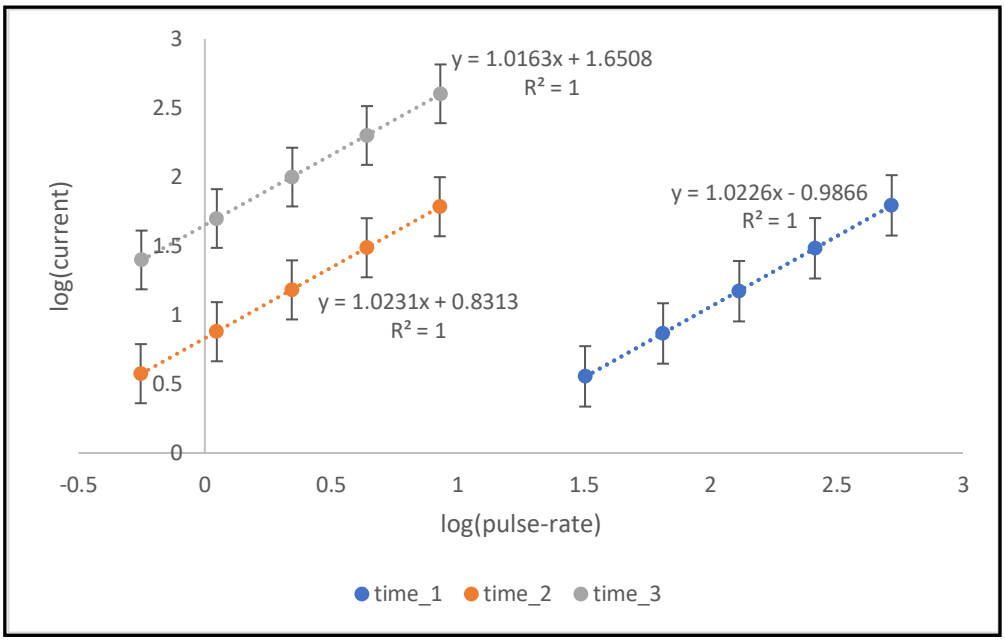

Figure 6.24: Illustration of the plot of log (pulse-rate) against the log(current) measured by the DD4 detector with the spherical phantom in order to determine the Δ value for the three methods. The first method of finding the irradiation time is represent by tme_1, second method is represent as time_2 and third method is represent as time_3

In Figure 6.24 presents the plot of the log (pulse-rate) against the log (total pulse/irradiation time) for all the three methods in order to find the Δ value measured by the DD4 detector. The value of Δ obtained is 1.0226 ± 0.0018 for the first method where the irradiation time is based on the time required to deliver 100 MU with the respective pulse-rate. The value of Δ for this method is presented as time_1.

The second method of the Δ value obtained is 1.0231 ± 0.0019 and represented as time_2 in Figure 6.24. In this approach, the pulse-rate was determined based on

delivery of 100 MU over the time of irradiation at the first and last pulses detected. It can be seen that there is a slight difference in the time irradiation between that based on the LINAC and the time calculated based on the pulses detected.

While the third method of finding the Δ value is given as 1.0167 ± 0.0029 as presented in Figure 6.24. In this approach, the dose-rate being considered is the dose of 100 MU over the time of irradiation. There is a slight difference on the time of irradiation between that based on the LINAC and the time calculated based on the pulses detected.

b) Measurement with cubical phantom

With the field-size of 10 x 10 cm^2, 100 cm SSD, measured at 1.5 cm depth and 100 MU monitor unit(MU) with cubical and multi-block phantoms was setup for this investigation. Table 6.12 presents the result of relevant parameters extracted from the offline analysis. With the same method as in the last section, 0.007 V was set as the threshold value to ensure evaluation consistency. Similar to the last section, the average raw pulse height and average net pulse height was found to increase with higher pulse-rate. As expected, the higher value for both pulse heights is due to the measurement at 3 cm depth for the spherical phantom. From Table 6.12, the deviation on the average raw total pulse height and the average net total pulse height are approximately 1.42 % and 2.95 % from the average, respectively.

As explained earlier, the total BG pulse calculated is proportionate to the LINAC pulse, with the higher pulse-rate being observed as contributing to the increased in the total BG pulse height. This was also observed in the last section.

The average net pulse height is calculated from the summation of pulse height over the number of pulses detected. From Table 6.12, the average pulse height is seen to increase with higher pulse-rate. This was similar with the result obtained with the spherical phantom. The number of pulses detected increased with higher pulse-rate, as predicted. Surprisingly, the number of pulses detected is approximately the same even with different phantom and depth of measurement (see Table 6.8 and Table 6.12). This is contrary to our expectation for the number of pulses detected to vary due to the different depth and scattering effects.

Pulse-rate (MU/min)	Average raw total pulse height (V)	Total BG (V)	Average net total pulse height (V)	Average net pulse height (V)	Number of pulses
32	766.0037	1.7983	764.2054	0.1714	4458
65	779.2748	3.1684	776.1064	0.1727	4495
130	784.9703	-1.6870	786.6573	0.1736	4531
261	789.7238	-10.1027	799.8265	0.1746	4580
522	794.9170	-29.7538	824.6708	0.1756	4694

Table 6.12: The result of parameters detected from the DD4 detector with cubic and multi-block phantom for different pulse-rate of the LINAC delivered for 100 MU

Dose-rate dependency for the DD4 detector with the cubical and multi-block phantom was evaluated using Fowler's model, similar as in the previous section. Again, three method of determining of irradiation time were employed.

Table 6.13 shows the time of irradiation calculation based on the fixed 100 MU delivered with selected pulse-rate. Figure 6.25 presents the plot of the log (pulse-rate) against log (total pulse/irradiation time). From the Figure 6.25, the non-linearity (Δ) value obtained is 0.9968 ± 0.0039 which indicating the DD4 detector has approximately linear to the LINAC pulse-rate.

LINAC pulse-rate (MU/min)	log (pulse-rate)	Total pulse height (V)	Irradiation time (s)	log(total pulse height/irradiation time)
32	1.5051	0.1714	187.5000	-3.0371
65	1.8129	0.1727	92.3077	-2.7266
130	2.1139	0.1736	46.1538	-2.4244
261	2.4166	0.1746	22.9885	-2.1226
522	2.7177	0.1756	11.4943	-1.8296

Table 6.13: Result for irradiation time for delivery of 100MU at the respective pulse-rate available on the LINAC with the cubical phantom

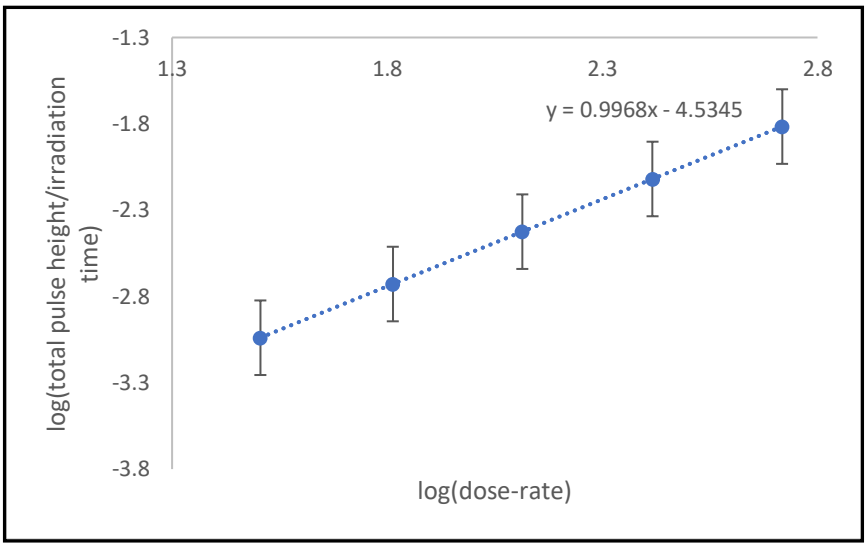

Figure 6.25: The value of Δ for DD4 detector with cubical phantom where the irradiation time calculation is based on the pulse-rate of the LINAC

Then, with the second method in determining irradiation time which based on the time duration from the first and the last pulse being detected. From the plot in Figure 6.26, the non-linearity (Δ) factor obtained is given as 1.0268 ± 0.0029. The result is approximately similar with the result obtained (1.0231 ± 0.0019) with the spherical phantom for the same method of irradiation time determination.

Dose-rate (MU/s) (100MU/irradiation time)	Log (dose-rate)	Total pulse height	Irradiation time	Log(total pulse height/irradiation time)
0.5604	-0.2515	765.8236	178.4364	0.6326
1.1114	0.0459	776.94205	89.9782	0.9363
2.2046	0.3433	788.9526	45.3591	1.2404
4.3655	0.6400	805.1160	22.9071	1.5459
8.4497	0.9268	830.0218	11.8348	1.8459

Table 6.14: Result for irradiation time on delivery of 100 MU at the respective pulse-rate from the plot with cubical phantom

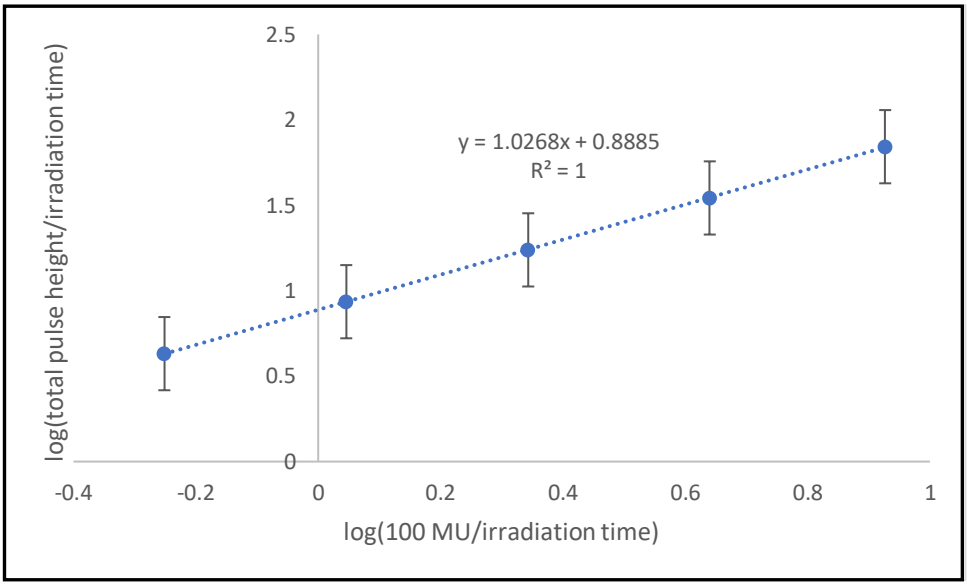

Figure 6.26: Value of Δ for DD4 with cubical phantom with irradiation time obtained from the plot

Finally, the third method for irradiation time determination is based on the multiplication of the reciprocal of PRF and the number of pulses detected The third method in finding the irradiation time is by considering changing the PRF. Table 6.15 presents the relevant parameters for Fowler's model in determining the non-linearity factor. The plot of the log(pulse-rate) against the log(total pulse height/ irradiation time) is presented in Figure 6. 27. The non-linearity factor for DD4 detector against the pulse-rate is given by 1.0199 ± 0.0043. The result is also similar with the Δ value obtained in the last section with the spherical phantom.

pulse-rate (MU/min) (100MU/irradiation time)	log (pulse-rate)	total pulse number	irradiation time (1/PRF*no of pulses)	log(total no pulse/irradiation time)
0.5601	-0.2517	4458	178.5400	1.3979
1.1110	0.0457	4495	90.0100	1.6989
2.2056	0.3435	4531	45.3400	2
4.3655	0.6400	4580	22.9325	2.3010
8.4497	0.9268	4694	11.7475	2.6021

Table 6.15: Result for irradiation time for delivery of 100 MU at the respective dose-rate from the PRF

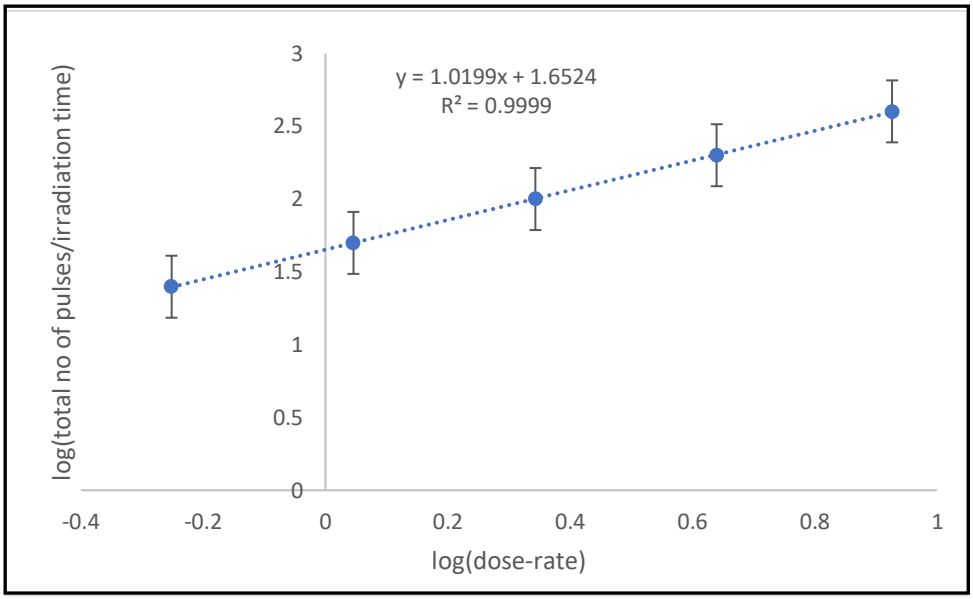

Figure 6.27: Value of Δ for DD4 detector with cubical phantom where the irradiation time obtained are the inverse of PRF multiply with the number of pulses detected

Figure 6.28 presents the total number of pulses detected by the DD4 for different dose-rates with the cubical phantom and for variable pulse-rates from the LINAC (from Table 6.12). As expected, the number of pulses was found to increase with higher pulse-rates.

Figure 6.29 shows the average of the total pulse height with variable pulse-rates measured by the DD4 detector. The plot shows an increase in the pulse height with higher pulse-rates. The finding contradicts the assumption that the average pulse height generated by the LINAC should be less with the higher pulse-rate. The assumption is based on the understanding that if the number of pulses increases with the dose-rate, the pulse height for higher dose-rate should therefore be less in order to deliver the same amount of dose.

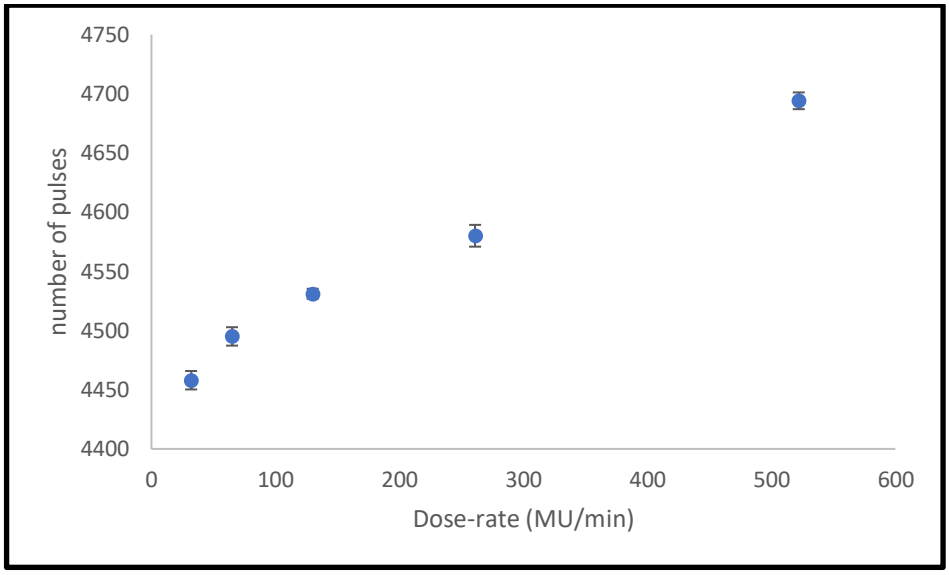

Figure 6.28: Plot of the number of pulses detected against different pulse-rates from the LINAC measured with cubical phantom at 1.5 cm depth

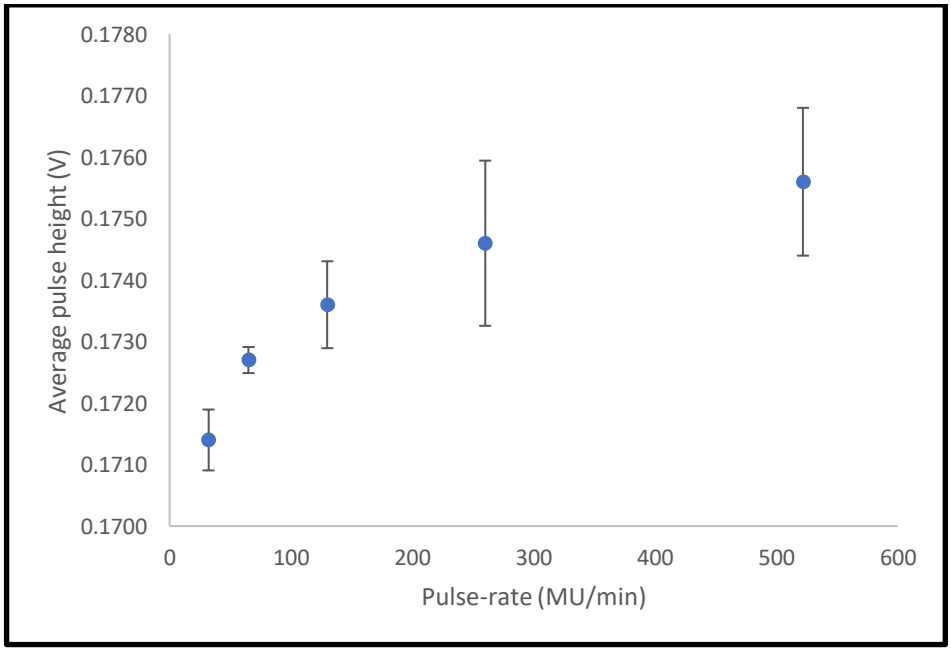

Figure 6.29: Plot of the average pulse height for different pulse-rates from the LINAC measured with cubical phantom at 1.5cm depth

6.3.3.2 Fixed dose-rate and variable SSD

Another method of evaluating dose-rate dependency is by varying the distance between the detector and the radiation source with a fixed dose-rate from the LINAC. The distance of the measurement can be varied by changing the height of the treatment table.

Table 6.16 shows the results of the relevant parameters after the offline data analysis. As expected, the total pulse height and the number of pulses detected nearer to the radiation source have higher values compared to those that were of further distance from the radiation source. BG measurement was also found to be higher when it was nearer to the radiation source. The plots of the total pulse height against the SSD as presented in Figure 6.30 show a slight diversion from the inverse-square law. Irradiation time obtained in this investigation was based on the time of delivery of fixed 100 MU at 522 MU/min from the LINAC. Another method of measuring irradiation time is by subtracting the time of the last pulse detected from the time of the first pulse detected. To be consistent with the time measured during pulse delivery, the irradiation time is calculated based on the fixed 100 MU delivery at 522 MU/min. From Table 6.16, at the effective distance of 101.5 cm, the average total pulse height and average net pulse height are similar to the one obtained in Table 6.12. The deviation is due to the field dimension and setup. The number of pulses detected is similar with the number of pulses as in the Table 6.12.

Effective SSD (cm)	Average total pulse height (V)	BG (V)	Net pulse height (V)	Average net pulse height (V)	No of pulses
71.5	1556.150	-62.3445	1618.4945	0.3427	4724
81.5	1185.500	-45.8870	1231.3870	0.2616	4706
91.5	942.495	-36.0093	978.5043	0.2084	4695
101.5	761.7862	-27.6422	789.4283	0.1686	4683
111.5	641.5119	-22.3864	663.8982	0.1422	4666
121.5	538.4491	-17.4710	555.9201	0.1198	4648
131.5	456.4485	-13.6180	470.0665	0.1014	4641
141.5	395.0145	-10.9878	406.0023	0.0881	4634

Table 6.16: Results for cubic and multi-block phantom at fixed dose-rate with variable SSD at 1.5 cm depth for 5 x 5 cm^2 field-size

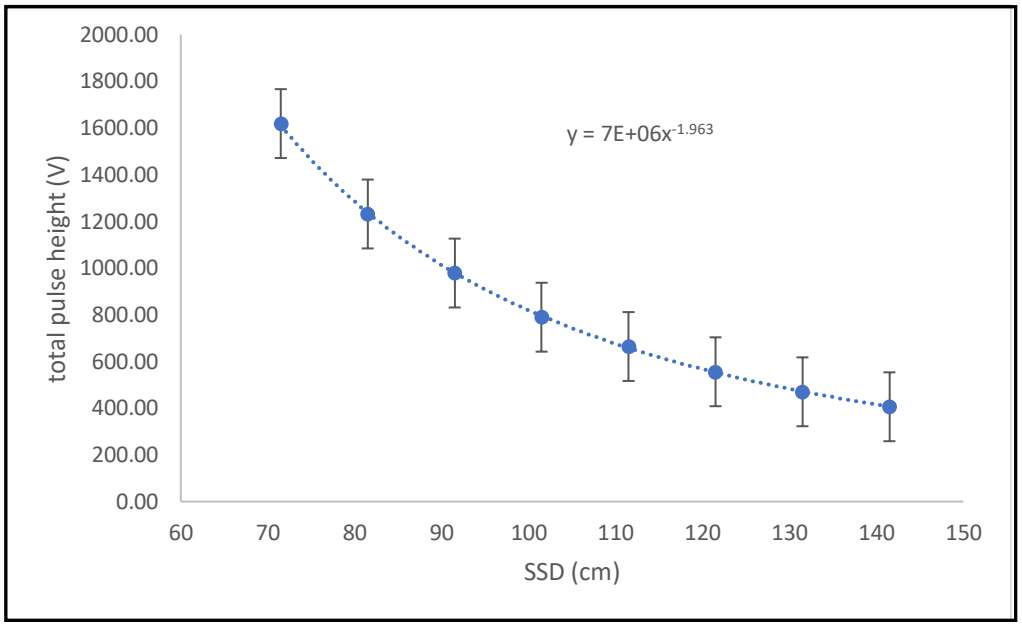

Figure 6.30: Plot of response of the DD4 detector on the total pulse height with SSD utilizing cubic phantom at 1.5 cm depth

Dose-rate dependency of DD4 detector using the Fowler's model by variable SSD investigation is presented in Table 6.17. Here, the irradiation time was calculated based on the time required to deliver 100 MU at 522 MU/min which is 11.4943 s (similar to the first method). From the Figure 6.31, the non-linearity factor (Δ) for DD4 detector is given as 1.0083 ± 0.0129, which indicated through this method (varying SSD) the DD4 detector is approximately linear to the dose-rate.

Effective SSD	relative dose-rate	Log (dose-rate)	average total pulse height (V)	irradiation time (s)	log(total pulse height/time)
71.5	2.0408	0.3098	1618.4945	11.4943	2.1486
81.5	1.5625	0.1938	1231.3870		2.0134
91.5	1.2346	0.0915	978.5043		1.9301
101.5	1	0	789.4283		1.8368
111.5	0.8264	-0.0828	663.8982		1.7616
121.5	0.6944	-0.1583	555.9201		1.6845
131.5	0.5917	-0.2278	470.0665		1.6117
141.5	0.5102	-0.2923	406.0023		1.5481

Table 6.17: The result for irradiation time for delivery of 100MU at 522MU/min measured by DD4 detector with cubical phantom at 1.5 cm depth for 5 x 5 cm^2 field-size

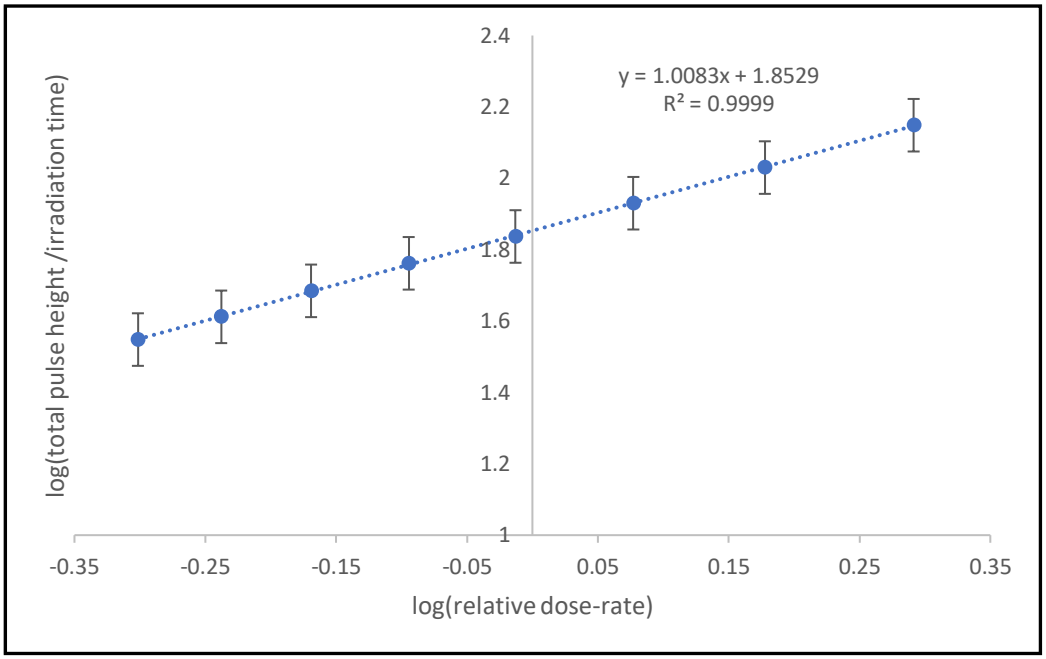

Figure 6.31: The value of Δ for DD4 detector with cubical phantom at 1.5 cm depth, field-size of 5 x 5 cm^2 for relative dose-rate and variable SSD

6.3.4 Cross-calibration between the microDiamond and DD4 detectors

Five consecutive measurements, as shown in Table 6.18, was conducted with the microDiamond detector in order to evaluate the repeatability percentage of 0.2 % for a 10 x 10 cm^2 field-size at SAD of 100 cm and 522 MU/min of dose-rate. From Chapter 5, the sensitivity of the microDiamond detector obtained was 1.264 ± 0.020 nC/Gy. Based on the sensitivity factor of the microDiamond detector, the dose measured with the microDiamond detector for 300 MU at 3 cm depth of spherical phantom is given by 2.901 Gy with the uncertainty is 1.6 %.

Reading (nC)	
3.665	
3.668	
3.665	
3.668	
3.668	
Average	3.667 nC
SD	0.002

Table 6.18: Results of repeatability measurement for microDiamond detector with the spherical phantom for field-size of 10 x 10 cm^2 and at 3 cm depth

Figure 6.32(a) presents the raw data measured by the DD4 detector and Figure 6.32(b) shows the pulses detected with the BG separation after the processed analysis. The value used for the threshold is set at 0.007 V for the consistency evaluation.

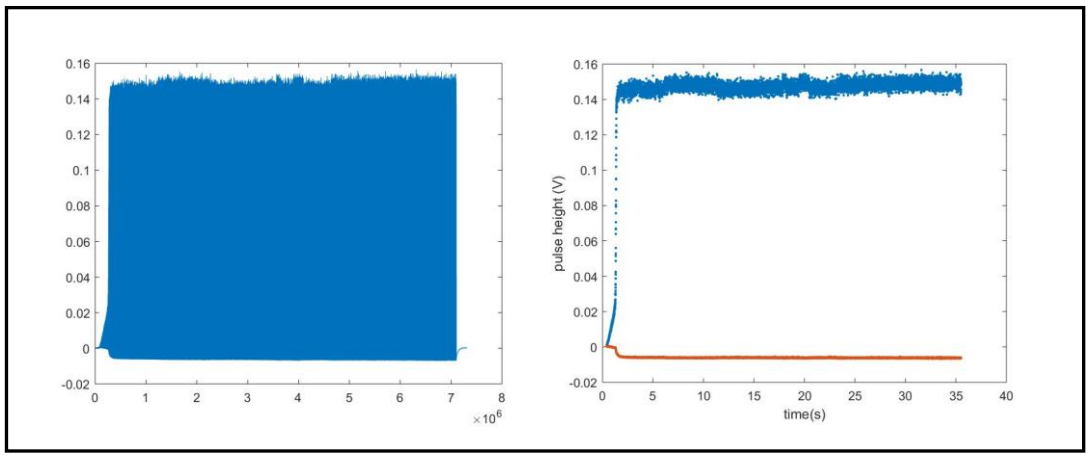

(a) (b)

Figure 6.32: The response from the DD4 detector during cross-calibration at 100 cm SAD, field-size of 10 x 10 cm^2 at 522 MU/min and 300 MU with the spherical phantom

Table 6.19 shows the parameters extracted from the plot. The total pulse height was calculated by summing the pulse height detected by the DD4 detector.

Total BG (V)	-83.3778
Total pulse height (V)	2020.3
Average pulse height (V)	0.1451
Average BG (V)	-0.0060
No of pulses	13920
Net pulse height (V)	2103.6778
Net average pulse (V/pulse)	0.1511

Table 6.19: Result of the measurements with DD4 detector with the spherical phantom for field-size of 10 x 10 cm^2 at 100 cm SSD for 300 MU

From the data in Table 6.19,

Total number of pulses = 13920 pulses ……..…….. (6.2)

Average pulse height = 0.1511 V/pulse ……...……...…… (6.3)

Dose/volt $= (2.901\ Gy) \times \left(\frac{1}{13920\ pulse}\right) \times \left(\frac{pulse}{0.1511\ volt}\right)$

= 1.38 mGy/volt ……...… (6.4)

Equation (6.4) is the dose per volt measured with the spherical phantom at 3 cm depth. This correction factor was used for the conversion from the pulse to dose during the VMAT delivery. From Table 6.19, the total pulses detected with the total monitor unit of 300 MU was delivered with spherical phantom was 13920 pulses while the number of pulses detected with the same dose-rate of 522 MU/min for 100 MU delivered as shown in Table 6.8, was 4671 pulses. This was in agreement with the number of pulses for 300 MU with the same dose-rate which should be 14013 pulses while from Table 6.19 the number of pulses detected was 13920 pulses and the deviation was within 0.7 %. The average net pulse height obtained from this section was 0.1511 V/pulse with an uncertainty limit of 4.1 %.

6.3.5 VMAT measurements

Point dose measurements at the isocentre of the spherical phantom for the VMAT delivery for prostate cancer treatment is presented in Figure 6.35. The pulse height

fluctuates as various dose-rates are being employed during the beams delivery. The pulse height presents the dose-rate employed during the delivery especially with the Elekta Agility which has 255 continuous variable dose-rate (CVDR) bin. This was different from Chapter 5, where there were only 5 options of dose-rates allowed with the Elekta Synergy. Figure 6.33 shows a dip in the pulse heights. The script written in MatLab successfully separate the pulse and the BG as shown in Figure 6.35.

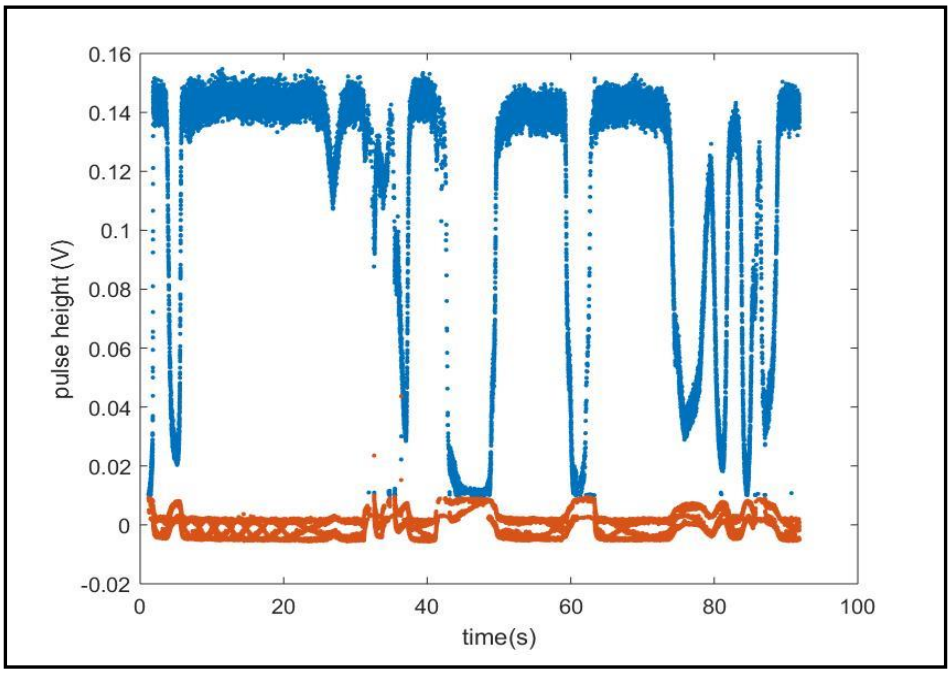

Figure 6.33: Measurement of VMAT beams delivery on pulse-by-pulse dosimetry for the DD4 detector at 100 cm SSD with the spherical phantom

Figure 6.34 presents the result for dose per pulse after the multiplication with the conversion factor in equation (6.4). The DD4 detector has the capability in measuring the dose-per-pulse in the range of 0.05-0.23 mGy/pulse. The total dose measured at the isocentre with the VMAT delivery at 3 cm depth by the DD4 detector is 5.3061 ± 0.2168 Gy where the error from the conversion factor.

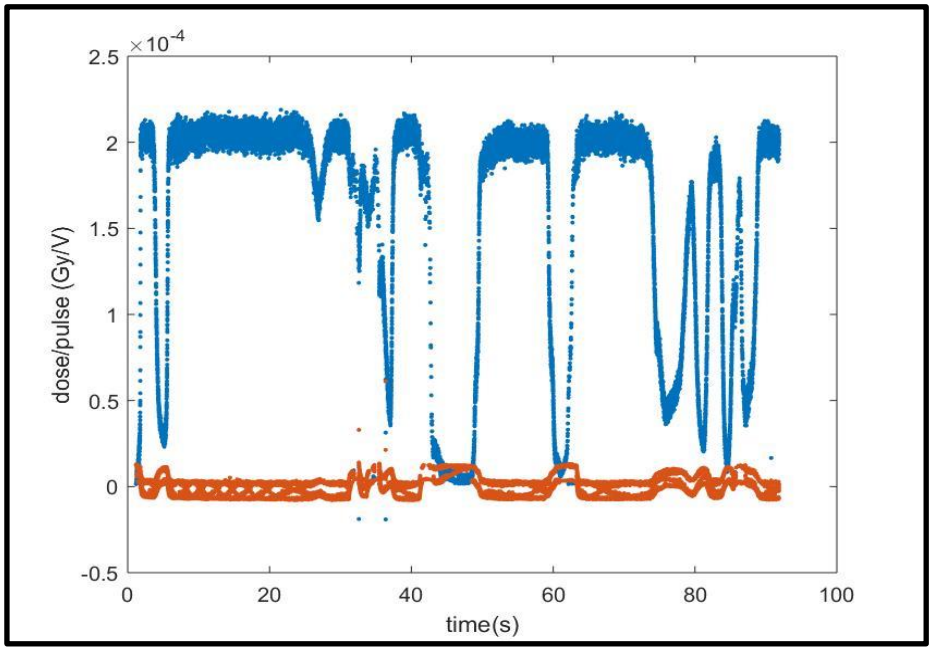

Figure 6.34: The dose per pulse measured by DD4 with the spherical phantom after applying the detector's correction factor

For comparison with the DD4 detector, the same setup was employed for the VMAT delivery measured with the microDiamond detector as presented in Table 6.20. The average reading obtained was 6.744 ± 0.026 nC. Based on the microDiamond sensitivity of 1.264 ± 0.020 nC/Gy calculated in Chapter 5, the total dose measured for VMAT is given by 5.335 ± 0.106 Gy. As mentioned early, both detectors were CT scanned and transferred to the TPS for the calculation of the dose point. Based on the TPS calculations for the two different detectors placed in the spherical phantom, the doses calculated were 5.344 Gy and 5.346 Gy for the microDiamond and DD4 detectors, respectively. The deviations in the measurement based on the TPS calculation for the microDiamond detector and the DD4 detector were 0.17 % and 0.75 %, respectively. The figures for both detectors are within the uncertainty limit.

The same treatment planning was calculated with an independent commercial software known as RadCalc[144]. The software has the capability of providing the dose per control point (Gy/CP) calculated independently based on the parameters of details provided from the TPS. The cumulative dose calculated by the RadCalc was 5.7055 Gy. The different cumulative dose reported by the RadCalc was due to the different dose algorithm calculation used.

Reading	Measured (nC)
1	6.718
2	6.743
3	6.771
Average	6.744

Table 6.20: Measurement of VMAT delivery for the microDiamond detector with the spherical phantom

By using the interpolation method with MatLab, the cumulative dose as a function of time was reconstructed for the measurement with DD4 detector and RadCalc. Figure 6.35 presents the normalised cumulative dose between the measurement and calculated by the RadCalc. Both methods are normalised to its respective maximum total dose.

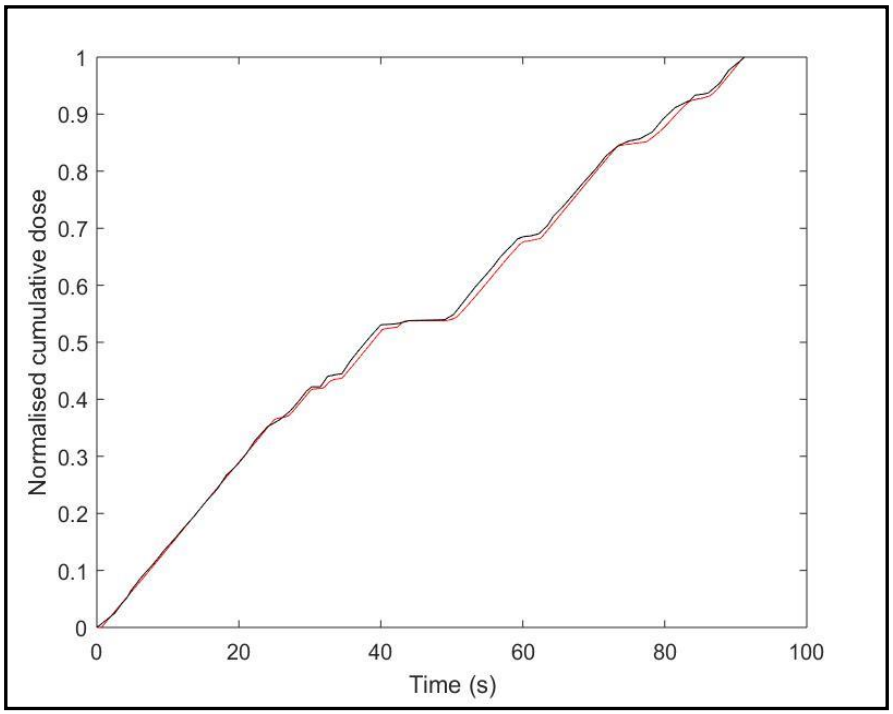

Figure 6.35: Comparison of VMAT delivery method based on normalised cumulative dose and RADCALC normalised at the total maximum dose

6.3.6 Gamma analysis

Pulse-resolved dosimetry posed a new challenge for dose verification since the integrated dose provides little information on how the dose is deposited during delivery. As discussed in the last chapter, the advantage of pulse dosimetry is its ability to detect errors early on before the completion of the treatment. In this study, the dose verification with gamma-like analysis will focus on the cumulative dose since instantaneous dose is unimportant in clinical use. For a robust comparison, the interpolation method has been applied with a timestamp of 0.005 seconds. With the developed in-house programme for data analysis with MatLab, the gamma index (γ) and percentage gamma passing rate (%GP) can be obtained. For gamma analysis evaluation, the measurement data will be referred to as a reference while RadCalc calculation will be referred as evaluated. The criteria of the evaluation will be based on the following: dose difference (ΔD) of 5 %, 3 % and 1% from the total cumulative dose while time-to-agreement (Δt) is for 2 seconds.

Figure 6.36 presents the result of gamma analysis between the RadCalc and the measurement. Based on the criteria of 5 %/2 s and 3 %/2 s, the gamma passing rate obtained was 100 %. With a tighter criterion imposed at 1 %/2 s, the gamma passing rate still remained as 100 %.

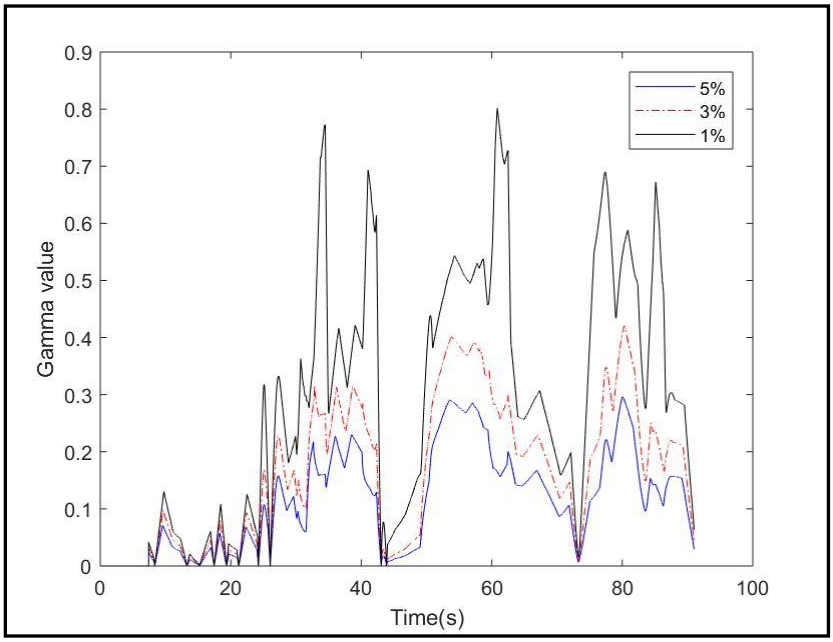

Figure 6.36: Gamma analysis for 5 %/2 s, 3 %/2 s and 1 %/2 s

6.4 Discussion

In this chapter, a comprehensive investigation on the performance of the DD4 detector for use in pulse-by-pulse dosimetry has been conducted. The newly installed Elekta Agility and improvement on the high-count rate system have given rise to new challenges for the DD4 detector in detecting the pulse from the LINAC which has a continuous variable dose-rate (CVDR). A treatment plan for a prostate cancer patient with Pinancle v16.0 for VMAT technique delivery has been created. The microDiamond and the DD4 detectors were mounted in the spherical phantom and had been scanned with CT scanner in order to get more accurate dose calculation with the TPS.

The first investigation was to evaluate the priming dose requirement of the DD4 detector. From the investigation, it is evident that the DD4 detector requires a priming dose of at least 1000 MU which contradicts Piliero's [13] finding that it does not require any priming dose. The in-house written script developed using MatLab has allowed for more comprehensive offline data analysis to determine the highest pulse height compared to the tools available in MatLab. With the knowledge that the gradient should be zero at the maximum pulse height, therefore the maximum pulse can be determined by solving the quadratic equation. In the script, a pulse height of 50 µs before the first pulse is detected is considered as pulse for the BG. In addition, the developed script has made it possible to separate between the pulse from the LINAC above the threshold set and the pulse from the BG. The offline data analysis revealed the pulse height of the BG to be proportionate to the pulse height from the LINAC. The BG extracted from the data also showed similar behavior, i.e., the BG kept increasing until it reached the plateau region. The total pulse height which reflects the dose measured after a minimum priming dose, is found to be less than 1 % (Figure 6.10). However, the number of pulses detected is within 0.5 % regardless of the priming dose. This can be attributed to the delivery of a number of electrons with lower energy at the LINAC startup till it reached the optimum dose-rate (plateau region). As can be seen in Figure 6.8, the number of pulses delivered is still the same. Then, the investigation turned to determine the reproducibility of the DD4 detector. The measurements performed during different weeks within a month with the same setup and radiation conditions revealed the reproducibility of the DD4 detector to be 1.4 %.

Due to the new high-count system, an investigation on the optimum applied voltage on the system was conducted. The DD4 detector was mounted on the spherical phantom for a field-size of 10 x 10 cm^2 and was setup for the maximum dose-rate available (522 MU/min) at 100 cm SAD. The response from the DD4 detector for applied voltages of 5, 6 and 7 V to the AFE system was evaluated. The results show that the variation on the applied voltage did not affect the response from the DD4 detector. The total pulse height, total BG and the number of pulses detected only show small deviation but since the number of pulses detected with 6 V is the highest, it was decided that this voltage will be used in further investigations.

The evaluation on the dose-rate dependency of the DD4 detector was conducted using the developed script and setting a threshold of 0.007 V in determining the pulse height. The reason for choosing this threshold is because it represents the pulse generated from the LINAC and anything below the threshold is considered as BG. Two methods of varying the dose-rate were adopted in the investigation: by varying the pulse-rate available from the LINAC and the other was by varying the distance between the radiation source and the detector (variable SSD).

The response from the DD4 detector based on the former method was evaluated with the spherical and cubical phantoms at 10 x 10 cm^2 of field-size and delivery of 100 MU. With the spherical phantom, the pulse was measured at 100 cm of SAD while for the cubical phantom at 100 cm SSD and depth of 1.5 cm. Since a field-size of 10 x 10 cm^2 was used for the spherical phantom, it failed to fulfil the scatter condition since the phantom is smaller than the field-size used.

With the spherical phantom, the DD4 detector was irradiated at different pulse-rates from the LINAC at fixed 100 MU. The analysis revealed that the average net pulse height, average total BG and the number of pulses detected increased with higher pulse-rate. The deviation between the average net total pulse height against the maximum average net pulse height is 6 %. The average total pulse height as reflected to the dose measured by the DD4 detector is contrary to expectation for the dose measured to be the same. The average pulse height was also found to increase with higher pulse-rate, which again is contrary to expectation. However, the number of pulses was found to increase for higher pulse-rate and this is not surprising as the shorter the time of dose delivery (higher pulse-rate), the higher will be the number of

pulses. As a verification on the written script, Figure 6.20 presents the number of pulses detected with the different pulse-rate at 0.1 s.

Another aspect considered in this study is the pulse-rate dependency of DD4 detector following Fowler's model. Three methods of calculating the irradiation time were adopted in the evaluation of the response against the pulse-rate from the DD4 detector. The first method of calculating the irradiation time is by dividing the fixed 100 MU with the selected pulse-rates from the LINAC. The second method of calculating irradiation time is by subtracting the time of the last pulse from the first pulse detected. The last method is by multiplying the known selected PRF generated from the LINAC with the total number of pulses detected. From the plots, the non-linearity factor (Δ) for the DD4 detector can be determined.

The measurements with the cubical phantom followed the same setup. Analysis of the results revealed the average net pulse height, average total BG and the number of pulses detected to increase with higher pulse-rate for the cubical phantom. The deviation between the average net total pulse height against the maximum average net pulse height is 7 %. Again, the average total pulse height, as reflected by the dose measured by the DD4 detector, is contradictory to the expectation for the dose measured to be the same. The average pulse height was found to increase with higher pulse-rate while the expectation is for it to be lower, a result which is contrary to expectation. Similarly, although the average net pulse is expected to be less for higher pulse-rate, results indicate the number of pulses to increase for higher pulse-rate. The explanation for this is that dose delivery at shorter time (higher pulse-rate) requires the number of pulses to be higher. Similar results were obtained with the spherical phantom. Interestingly, both phantoms have shown the number of pulses detected for the same field dimension and number of monitor unit (MU) delivered with the deviation to be within 0.5 %.

Similar to the method of obtaining the irradiation time and the response from the DD4 detector, the cubical phantom was evaluated by varying the pulse-rates from the LINAC. Table 6.21 shows the value of Δ determined with different phantom shape and different methods of calculating irradiation time.

Phantom	Method 1	Method 2	Method 3
spherical	1.0226 ± 0.0018	1.0231 ± 0.0019	1.0167 ± 0.0029
cubical	0.9968 ± 0.0039	1.0289 ± 0.0029	1.0199 ± 0.0043

Table 6.21: The value of Δ determined by different calculation methods of irradiation time with spherical and cubical phantoms for DD4 detector

The response of the DD4 detector was also evaluated by varying the distance between the radiation source and the detector at the fixed dose-rate from the LINAC. Based on the same threshold as set in the previous method, the response of the DD4 detector with the cubical phantom was evaluated. The irradiation time calculated for the variable SSD was the reciprocal of the 100 MU of 522 MU/min dose-rate of the LINAC which is similar to the first method in variable pulse-rates investigation. In this investigation, the average net total pulse height, average net pulse and number of pulses detected were conducted on a field-size of 5 x 5 cm^2 and depth of 1.5 cm, . A comparison of the results from varying the pulse-rate with spherical and cubical phantom and from varying the SSD with the cubical phantom, revealed the number of pulses detected to be the same. This indicates that the number of pulses detected is the same regardless of the method with 2.44 % deviation for the DD4 detector correction factor as discussed in section 5.9.

With the Fowler's model, the Δ value for varying the SSD for the DD4 detector is given as 1.0083 ± 0.0129 which indicates that the DD4 detector is nearly linear to the dose-rate.

Treatment plan for prostate cancer with VMAT technique delivery was also created. As a local practice, the result of dose calculation from the RadCalc software was compared to that by the TPS. The details on the related parameters are transferred to the RadCalc for dose calculation which may be in the form of either the cumulative dose per control point (Gy/CP) or instantaneous dose per control point (Gy/CPs), depending on the license purchased. In this evaluation, only the cumulative dose per control point (Gy/CP) was used.

From the cross-calibration between the microDiamond and DD4 detectors irradiated for field size 10 x 10 cm^2 and delivered for 300 MU at 522 MU/min, the number of pulses detected was 13920 pulses. This was three fold the number of pulses detected in previous investigation. This indicates that the number of pulses detected

by the DD4 detector is consistent when comparing the number of pulses detected with varying the pulse-rate with spherical or cubical phantoms and varying the dose-rate with cubical phantom for 522 MU/min of dose-rate.

The VMAT planned was transferred for delivery to be measured by the DD4 detector. The DD4 detector has the capability in measuring the dose per pulse in the range of 0.05 – 0.23 mGy/pulse. The total dose measured by the DD4 detector at the isocentre is 5.3061 Gy at 3 cm depth of spherical phantom. As a comparison with the microDiamond detector, the total dose obtained is 5.335 Gy. Results of dose calculations from the TPS for the microDiamond and DD4 detectors were 5.344 Gy and 5.346 Gy, respectively. As for the independent dose calculation by RadCal, the total dose plan is given as 5.7055 Gy.

The final evaluation on the total dose measured by the DD4 detector and the dose calculated by the RadCalc was conducted using gamma analysis. Only the dose-different (ΔD) and time-to-agreement (Δt) were evaluated. Verification on the dose delivered was successful in demonstrating that by utilizing the gamma-like analysis with the cumulative dose difference (ΔD) and time-to-agreement (Δt) criteria of 1 %/2 s, 3 %/2 s and 5 %/2 s, a 100 % gamma passing rate was obtained.

7

Conclusions and Future Work

7.1 *Conclusions*

The main objective of this thesis is to address a gap in the literature and contribute new knowledge by investigating the suitability of the prototype diamond detector for pulse-by-pulse dosimetry for use in VMAT technique delivery. The commercial diamond detector known as DD4 detector was purchased from Diamond Detectors Ltd (Poole, UK) for the investigation. Although the characteristics of the DD4 detector has been investigated by a previous PhD student, the data acquisition (DAQ) system used was different from the current DAQ system. The characteristics of the commercial microDiamond detector has also been investigated in the current study to complement the study on dose-rate delivery method and also for measurement verification.

Throughout the study, two models of LINAC were used as the radiation source; Synergy with a 1 cm leaf width and Agility with a 0.5 cm leaf width, both from Elekta. Each LINAC has different dose-rate method of delivery. The treatment planning system (TPS) for the calculation of dose distributions used different algorithms as they are from different suppliers, Synergy with Nucletron Oncentra MasterPlan v.4.3.0.409 while Agility with Philips Pinnacle v.16.0.

As explained in Chapter 3, the characteristics of the commercial microDiamond detector specifically studied in this thesis are the level of leakage, priming dose requirement, repeatability, angular and dose dependency. These characteristics are the basic requirements in determining the suitability of a detector to be used in therapeutic dosimetry as recommended by the International Atomic Energy Agency (IAEA). The results of the current investigations have successfully demonstrated that the microDiamond detector has low leakage or dark current and has high signal-to-noise ratio (S/N). The detector to be used in measuring the VMAT technique should have high S/N value, hence microDiamond detector fits the criteria. With regards to priming dose requirement, the microDiamond detector studied

indicates that it needs a priming dose as recommended by the manufacturer which contradicts the report by other investigators that the microDiamond detector does not require any priming dose. Repeatability characteristic of the microDiamond detector was conducted based on different dose-rates available from the Synergy LINAC, an aspect that has not been reported in prior study. The current study found the microDiamond detector to show variation on the output readings and its repeatability was found to be below the minimum recommended by the IAEA. Angular dependency is another important aspect in the VMAT technique as gantry rotates during beam delivery. The results of the investigation on the angular dependency of the microDiamond detector concur with the manufacturer's specification and as reported by other investigators. It is worth highlighting that the current study used the PMMA cubical phantom surrounded by multi-block phantom to mount on the microDiamond detector in a vertical orientation.

The results of the investigation on dose-rate dependency of the diamond detector are presented in Chapter 4. Fowler suggested the limited use of the diamond detector to be due to non-linearity of the dose-rate. Hence, the current study sought to better understand dose distribution by specifically investigating the dose per pulse generated by LINAC using a newly developed front-end. Two methods were adopted in examining the dose-rate responses of the detectors; by varying the pulse-rate available within the LINAC and by varying the distance between the radiation source and the detector. The dose-rate response based on the former method was investigated only for the microDiamond detector while the second method was adopted for investigating both the microDiamond and DD4 detectors. The value of Δ for the microDiamond detector is found to be 0.9985 ± 0.0005, thus clearly demonstrating the microDiamond detector has excellent dose-rate independency. Based on the second method, the value of Δ for the microDiamond detector and DD4 detector was 0.9870 ± 0.0024 and 0.996 ± 0.025, respectively. The result for the DD4 detector in the current investigation is in agreement with that reported by Piliero on the value of non-linearity (Δ). In short, the study has successfully demonstrated that the developed front-end has the capability of measuring the dose per pulse generated by the LINAC. This is a new dimension in looking at the dose distribution being delivered by dynamic therapeutic.

In Chapter 5, the preliminary result for the VMAT technique delivery was achieved with the DD4 detector using pulse-by-pulse dosimetry. In this investigation, a customised PMMA spherical phantom was used to mount the detector. Cross-calibration between the microDiamond and DD4 detectors aided in finding the conversion factor for dose per pulse (Gy/pulse). The written script in MatLab and offline analysis revealed how the LINAC delivered the pulse which thus reflects the dose delivery. The low pulse height at the start-up of pulse delivery from LINAC indicates that the number of electrons emitted by the filament is initially low until the pulse height is stabilised (plateau region). The fluctuations in the plateau region represents the adjustment of the LINAC to achieve an optimum selected dose-rate. A model was reconstructed based on dose delivered from the TPS and the LINAC logfile. With the knowledge that dose measurement is dependent on the field dimension, a field-size correction factor for 3 x 3 cm^2 and 5 x 5 cm^2 were measured. Finally, the point cumulative dose model from the DD4 measurement, TPS and LINAC logfile were reconstructed. From the model, it is observed that the cumulative dose with 5 x 5 cm^2 field-size from the TPS and LINAC logfile was close to the measurement by DD4 detector. For the quantitative evaluation, the models were reconstructed utilizing gamma-analysis. The measurement data was used as the reference while the TPS and LINAC logfile data were evaluation. A new dimension of the gamma analysis was introduced based on with the dose difference (ΔD) compared with the time-to-agreement (Δt) or gantry angle-to-agreement (Δg). The evaluation of dose delivery with the DD4 detector based either the cumulative dose against time or cumulative dose against gantry angle was performed. Limits of 5 % and 3 % of dose-difference criteria were used for the gamma-analysis. The results of the investigations also indicated that instantaneous dose analysis is not applicable for clinical practice.

In Chapter 6, the measurement of pulse-by-pulse dosimetry based on VMAT technique delivery was successful performed with the use of the newly installed LINAC Agility from the Elekta with 0.5cm leaf width. This provides more challenges to the DD4 detector since the width of the leaf is less compared to the previous chapter and more variable dose-rate delivery with the new LINAC. Improvements on the AFE system and the in-house developed script in MatLab for analysis were also introduced. The investigation revealed that the DD4 detector requires a priming dose of at least 1000 MU. The newly written script developed is also better in determining the peak of

the pulse compared to the tool of detecting pulse peak available in MatLab. In addition, the script has enabled the separation of the pulse height from the LINAC with the pulse from the background reading. The investigation on the variable pulse-rate based on the spherical and cubical phantoms confirmed that the number of pulses detected increases with higher pulse-rate. However, the average pulse height revealed contradicting result, i.e., the average pulse height increased with higher pulse-rate. The investigation on dose-rate dependency by varying the SSD revealed the number of pulses detected to be similar to the previous method. This indicates that in evaluating the dose measured by the DD4 detector, it is important to consider the number of pulse instead of the total pulse height and this finding contributes to new knowledge on how the LINAC delivers the dose. The verification of dose delivery measured by the DD4 and commercial microDiamond detectors was conducted using the same VMAT plan. The verification based on the measurement for both detectors and that calculated by the TPS shows good agreement. For comparison, an independent dose calculation software known as RadCalc was used to calculate the dose with the same VMAT plan. A quantitative evaluation on the performance of the DD4 detector in measuring pulse-by-pulse dosimetry was compared with the result from RadCalc. Both results are normalised at its maximum dose before employing the gamma analysis for evaluation. In the gamma analysis, the DD4 detector measurement was used as reference while the dose calculated by RadCalc was used for evaluation. Based on the 5 %/2 s, 3 %/2 s and 1 %/2 s evaluation criteria, results indicate an excellent gamma passing rate of 100 % for 1 %/2 s criterion. This explained that even with the 5 % of dose difference in every 2 second, the dose measurement is in a good agreement with the expected dose planned.

7.2 *Future Work*

The results in Chapter 6, contributes to new knowledge as they revealed how the LINAC delivers the dose in pulses. From the investigations, the number of pulses detected by DD4 detector seems consistent regardless of the dose-rate, field-size and phantom. In future, an investigation on the relationship between the total pulse height and the number of pulses with different dose-rates from LINAC can be conducted. This includes closer analysis in determining whether the increase in the pulse height

at the startup till the plateau region is due to the characteristics of the LINAC or to the diamond detector.

Another issue that can be investigated is the measurement system in order to improve the background reading which is proportionate to the pulse from the LINAC. As a result, the dose-rate dependency of the diamond detector which follows the Fowler's model has taken into consideration the effect of the BG.

Appendix A

Matlab code in Chapter 5

A) VMAT measurement

```
[A,B,AB]=xlsread('CSVPeakdata_7VMAT21.xls');
time=A(:,1);
dose=A(:,2);
Dose=dose.*(1);
plot(time,Dose,'.')
%figure1
xlabel('time(s)')
ylabel('volt(V)')
%xlabel('time(s)')
%ylabel('dose/pulse(Gy/pulse)')
axis([0 95 0.02 0.25])
```

B) Gamma analysis

```
%%%%%%%%%%%%%%%%%Logfile5x5MLC1%%%%%%%%%%%
%
        %%%%%%%cumulative dose analysis%%%%%%%
[a,b,ab]=xlsread('VMATplanningprostate_original_logfile_5x5MLC_05.xlsx'
);
cumdoselog=a(:,13);
timelog=a(:,15);
gantrylog=a(:,1);
timeinter= 0:0.005:105;
gantryinter=-178:0.016970621:178.4;
gantrylogtime=interp1(timelog,gantrylog,timeinter);
timeloggantry=interp1(gantrylog,timelog,gantryinter);
cumdoselogtime=interp1(timelog,cumdoselog,timeinter);
cumdoseloggantry=interp1(gantrylogtime,cumdoselogtime,gantryinter);
diffdoselogtime=gradient(cumdoselogtime)/0.005;
diffdoseloggantry=gradient(cumdoseloggantry)/0.016970621;

% % %%%%%%%TPS:5x5MLC1%%%%%%%%%%%%%%%%%%

        %%%%%%%%% cumulative dose analysis for TPS
%%%%%%%%%%

[c,d,cd]=xlsread('VMATplanningprostate_original_TPS_5x5MLC_05.xlsx');
cumdoseTPS=c(:,17);
gantryTPS=c(:,2);
diffdoseTPS=gradient(cumdoseTPS);
cumdoseTPSgantry=interp1(gantryTPS,cumdoseTPS,gantryinter);
cumdoseTPStime=interp1(timeloggantry,cumdoseTPSgantry,timeinter);
```

```
diffdoseTPSgantry=gradient(cumdoseTPSgantry)/0.016970621;
diffdoseTPStime=gradient(cumdoseTPStime)/0.005;

% % %%%%%%%Measurement%%%%%%%%%%%%%%%%%%
          %%%%%% cumulative dose analysis for measurement
%%%%%%%%%%%
[e,f,ef]=xlsread('VMATplanningprostate_original_measurementVMAT_test3
.xlsx');
t=e(:,2);
r=e(:,5);
cumdosereftime=interp1(t,r,timeinter);
cumdoserefgantry=interp1(gantrylogtime,cumdosereftime,gantryinter);
diffdosereftime=gradient(cumdosereftime)/0.005;
diffdoserefgantry=gradient(cumdoserefgantry)/0.016970621;

%%%%%%%%%%%%%%comparison data
analysis%%%%%%%%%%%%%%%%%%
          %%%cumulative dose comparison%%%%%%

figure(1)
plot(timelog,cumdoselog,'b',timeinter,cumdoseTPStime,'r',t,r,'k');
xlabel('time(s)')
ylabel('cumulative dose (Gy)')
%title('Comparison time vs cumulative dose')
legend('logfile','TPS','measurement')

    %%%gantry vs cumulative dose %%%

 figure(2)
plot(gantrylog,cumdoselog,'b',gantryTPS,cumdoseTPS,'r',gantryinter,cumdos
erefgantry,'k')
 xlabel('gantry angles (degree)')
 ylabel('cumulative dose (Gy)')
 %title('Comparison gantry vs cumulative dose')
 legend('logfile','TPS','measurement')

          %%% differential dose comparison %%%

figure(3)
plot(timeinter,diffdoselogtime,'b',timeinter,diffdoseTPStime,'r',timeinter,diffd
osereftime,'k');
xlabel('time(s)')
ylabel('dose (Gy/s)')
%title('Comparison time vs diffrential dose')
legend('logfile','TPS','measurement')
figure(4)
dose_diff_time_log=(diffdosereftime)-(diffdoselogtime);
dose_diff_time_TPS=(diffdosereftime)-(diffdoseTPStime);
plot(timeinter,dose_diff_time_log);
hold on
```

```
plot(timeinter,dose_diff_time_TPS)
xlabel('time(s)')
ylabel('dose difference(Gy/s)')
legend('lofgile','TPS')
hold off

    %%%gantry vs diffential dose%%%%%%%%%%

figure(5)
plot(gantryinter,diffdoseloggantry,'b',gantryinter,diffdoseTPSgantry,'r',gantryi
nter,diffdoserefgantry,'k')
xlabel('gantry angles (degree)')
ylabel('doserate (Gy/s)')
title('Comparison gantry vs differential dose')
legend('logfile','TPS','measurement')
figure(6)
dose_diff_gantry_log=(diffdoserefgantry)-(diffdoseloggantry);
dose_diff_gantry_TPS=(diffdoserefgantry)-(diffdoseTPSgantry);
plot(gantryinter,dose_diff_gantry_log);
hold on
plot(gantryinter,dose_diff_gantry_TPS)
xlabel('gantry angles (degree)')
ylabel('dose difference(Gy/s)')
legend('lofgile','TPS')
hold off

%%%%%%%%%%%%%%%%%%%%gamma analysis%%%%%%%%%

%global gammaM
%%%%% 5% criteria time vs cumulative dose %%%%%%%%%%%
%gammaM=gammaDose1d(cumdosereftime,cumdoselogtime,[1 1
1],0.162395,200,400,0.32479);
gammaM=gammaDose1d(cumdosereftime,cumdoselogtime,[1 1
1],0.162395,400,800,0.32479);%%% 5% 2s 10% threshold criteria
%figure(411)
figure(5)
plot((timeinter),gammaM,'b')
xlabel('time(s)')
ylabel('Gamma value')
%title('Gamma analysis for 5%/1s and 3%/1s cumulative dose')
gamma_A=(sum(gammaM<=1&gammaM>0)/sum(gammaM>0))*100;
%%% excluding point below the threshold %%%%%
hold on
%gammaM=gammaDose1d(cumdosereftime,cumdoseTPStime,[1 1
1],0.16251,200,400,0.32502);  %%%% 5% 1s  10% threshold criteria
gammaM=gammaDose1d(cumdosereftime,cumdoseTPStime,[1 1
1],0.16251,400,800,0.32502);   %%% 5% 2s 10% threshold criteria
plot((timeinter),gammaM,'r')
%legend('logfile5%','TPS5%')
```

```
gamma_B=(sum(gammaM<=1&gammaM>0)/sum(gammaM>0))*100;
%%%% excluding points below threshold %%%%
hold on
%gammaM=gammaDose1d(cumdosereftime,cumdoselogtime,[1 1
1],0.097437,200,400,0.32479); %%% 3% 1s  10% threshold criteria
gammaM=gammaDose1d(cumdosereftime,cumdoselogtime,[1 1
1],0.097437,400,800,0.32479); %%% 3% 2s 10% threshold criteria
plot((timeinter),gammaM,'-.b')
xlabel('time(s)')
ylabel('Gamma value')
%title('Gamma analysis for 3% DD and 10% threshold')
gamma_C=(sum(gammaM<=1&gammaM>0)/sum(gammaM>0))*100;
%%%% excluding points below threshold %%%%
hold on
%gammaM=gammaDose1d(cumdosereftime,cumdoseTPStime,[1 1
1],0.097506,200,400,0.32502);  %%% 3% 1s criteria
gammaM=gammaDose1d(cumdosereftime,cumdoseTPStime,[1 1
1],0.097506,400,800,0.32502); %%% 3% 2s criteria
plot((timeinter),gammaM,'-.r')
legend('logfile5%','TPS5%','logfile3%','TPS3%')
gamma_D=(sum(gammaM<=1&gammaM>0)/sum(gammaM>0))*100;
%%%% excluding points below threshold %%%%
hold off

%       %%%%%%%% gantry vs cum dose %%%%%%%%
%  %%%% 5% dose difference %%%%% 5%=0.1624Gy with
10%threshold=0.32326Gy.4degree=214pixel.

%gammaM=gammaDose1d(cumdoserefgantry,cumdoseloggantry,[1 1
1],0.162395,236,472,0.32479);  %%%% 4degree criteria
gammaM=gammaDose1d(cumdoserefgantry,cumdoseloggantry,[1 1
1],0.162395,325,650,0.32479);  %%%% 6 degree criteria
figure(6)
%figure(4142)
%figure(4143)
plot((gantryinter),gammaM,'b')
xlabel('gantry angle(degree)')
ylabel('Gamma value')
%title('Gamma analysis 5%/4degree and 3%/4degree cumulative dose')
gamma_E=(sum(gammaM<=1&gammaM>0)/sum(gammaM>0))*100;
%%%% excluding points below threshold %%%%
hold on
%gammaM=gammaDose1d(cumdoserefgantry,cumdoseTPSgantry,[1 1
1],0.16251,236,472,0.32502);   %%%% 4degree criteria
gammaM=gammaDose1d(cumdoserefgantry,cumdoseTPSgantry,[1 1
1],0.16251,325,650,0.32502);   %%%% 6 degree criteria
plot((gantryinter),gammaM,'r')
legend('logfile','TPS')
gamma_F=(sum(gammaM<=1&gammaM>0)/sum(gammaM>0))*100;
%hold off
```

```
% %%%% 3% dose difference %%%%%

%gammaM=gammaDose1d(cumdoserefgantry,cumdoseloggantry,[1 1
1],0.097437,236,472,0.32479);    %%%% 4degree criteria
gammaM=gammaDose1d(cumdoserefgantry,cumdoseloggantry,[1 1
1],0.097437,325,650,0.32479);    %%%% 6 degree criteria
plot((gantryinter),gammaM,'-.b')
gamma_G=(sum(gammaM<=1&gammaM>0)/sum(gammaM>0))*100;
%%%% excluding points below threshold %%%%
hold on
%gammaM=gammaDose1d(cumdoserefgantry,cumdoseTPSgantry,[1
1,1],0.097506,236,472,0.32502);   %%%% 4degree criteria
gammaM=gammaDose1d(cumdoserefgantry,cumdoseTPSgantry,[1
1,1],0.097506,325,650,0.32502);   %%%% 6 degree criteria
gamma_H=(sum(gammaM<=1&gammaM>0)/sum(gammaM>0))*100;
%%%% excluding points below threshold %%%%
plot((gantryinter),gammaM,'-.r')
legend('logfile5%','TPS5%','logfile3%','TPS3%')
hold off
%
%      %%%%%% Diffential dose %%%%%%%
%      %%%%%%%%%%%%%%%%%%%%%%%%%%%%%
%
%      %%%% time vs diff dose %%%%%%%
%
% %  %%%% 5 % DD %%%%%%
% max dose difference = 0.09 Gy/s
gammaM=gammaDose1d(diffdosereftime,diffdoselogtime,[1 1
1],0.005,200,400,0.01);  %%% 5% 1s 10% threshold criteria
%gammaM=gammaDose1d(diffdosereftime,diffdoselogtime,[1 1
1],0.005,400,800,0.01); %%% 5% 2s 10% threshold criteria
%gammaM=gammaDose1d(diffdosereftime,diffdoselogtime,[1 1
1],0.01,400,800,0.02); %%% 10% 2s 20% threshold criteria
%gammaM=gammaDose1d(diffdosereftime,diffdoselogtime,[1 1
1],0.02,1000,2000,0.02); %%% 20% 2s 20% threshold criteria
figure(7)
% %figure(4172)
% %figure(4173)
plot((timeinter),gammaM,'b')
xlabel('time(s)')
ylabel('Gamma value')
%title('Gamma analysis 5%/1s and 3%/1s cumulative dose')
gamma_I=(sum(gammaM<=1&gammaM>0)/sum(gammaM>0))*100;
%%%% excluding points below threshold %%%%
hold on
gammaM=gammaDose1d(diffdosereftime,diffdoseTPStime,[1 1
1],0.005,200,400,0.01); %%% 5% 1s 10% threshold criteria
%gammaM=gammaDose1d(diffdosereftime,diffdoseTPStime,[1 1
1],0.005,400,800,0.01); %%% 5% 2s 10% threshold criteria
```

```
%gammaM=gammaDose1d(diffdoseref,diffdoseTPStar,[1 1
1],0.01,400,800,0.02); %%% 10% 2s 10% threshold criteria
%gammaM=gammaDose1d(diffdosereftime,diffdoseTPStime,[1 1
1],0.02,1000,2000,0.02); %%% 20% 2s 10% threshold criteria
plot((timeinter),gammaM,'r')
legend('logfile','TPS')
gamma_J=(sum(gammaM<=1&gammaM>0)/sum(gammaM>0))*100;
%%%% excluding points below threshold %%%%
hold off
%hold on
% %
% %   %%%% 3% DD %%%%%%%%
% %
% gammaM=gammaDose1d(diffdosereftime,diffdoselogtime,[1 1
1],0.003,200,400,0.01);  %%% 3% 1s 10% threshold criteria
% %gammaM=gammaDose1d(diffdosereftime,diffdoselogtar,[1 1
1],0.003,400,800,0.01); %%% 3% 2s 10% threshold criteria
% plot((timeinter),gammaM,'-.b')
% xlabel('time(s)')
% ylabel('Gamma value')
% gamma_K=(sum(gammaM<=1&gammaM>0)/sum(gammaM>0))*100;
%%%% excluding points below threshold %%%%
% hold on
% gammaM=gammaDose1d(diffdosereftime,diffdoseTPStime,[1 1
1],0.003,200,400,0.01); %%% 3% 1s 10% threshold criteria
% %gammaM=gammaDose1d(diffdosereftime,diffdoseTPStime,[1 1
1],0.003,400,800,0.01); %%% 3% 2s 10% threshold criteria
% plot((timeinter),gammaM,'-.r')
% gamma_L=(sum(gammaM<=1&gammaM>0)/sum(gammaM>0))*100;
%%%% excluding points below threshold %%%%
% legend('logfile5%','TPS5%','logfile3%','TPS3%')
% hold off
% %
% %      %%%%%% gantry vs diff dose %%%%%%
% %
% %   %%% 5% DD %%%%%%%
%max instantaneous dose difference
%gammaM=gammaDose1d(diffdoserefgantry,diffdoseloggantry,[1 1
1],0.002,236,472,0.004);  %%%% 5% 4degree 10% threshold criteria
%gammaM=gammaDose1d(diffdoserefgantry,diffdoseloggantry,[1 1
1],0.002,325,650,0.004);   %%%% 5% 6degree 10% threshold criteria
gammaM=gammaDose1d(diffdoserefgantry,diffdoseloggantry,[1 1
1],0.004,236,472,0.004);    %%%% 10% 4degree 10% threshold criteria
%gammaM=gammaDose1d(diffdoserefgantry,diffdoseloggantry,[1 1
1],0.01,354,708,0.004);     %%%% 10% 6degree 10% threshold criteria
figure(8)
% %figure(4202)
% %figure(4203)
plot((gantryinter),gammaM,'b')
xlabel('gantry angles (degree)')
```

```
ylabel('Gamma value')
%title('Gamma analysis 5%/1s and 3%/1s cumulative dose')
gamma_M=(sum(gammaM<=1&gammaM>0)/sum(gammaM>0))*100;
hold on
gammaM=gammaDose1d(diffdoserefgantry,diffdoseTPSgantry,[1 1
1],0.002,236,472,0.004);    %%%% 5% 4degree 10% threshold criteria
%gammaM=gammaDose1d(diffdoserefgantry,diffdoseTPSgantry,[1 1
1],0.002,325,650,0.004);    %%%% 5% 6degree 10% threshold criteria
gammaM=gammaDose1d(diffdoserefgantry,diffdoseTPSgantry,[1 1
1],0.004,236,472,0.004);     %%%% 10% 4degree 10% threshold criteria
%gammaM=gammaDose1d(diffdoserefgantry,diffdoseTPSgantry,[1 1
1],0.004,354,708,0.004);
%gammaM=gammaDose1d(diffdoserefgantry,diffdoseTPSgantry,[1 1
1],0.01,354,708,0.004);
%%%% 10% 6degree 10% threshold criteria
plot((gantryinter),gammaM,'r')
legend('logfile','TPS')
gamma_N=(sum(gammaM<=1&gammaM>0)/sum(gammaM>0))*100;
hold off
%
% %   %%% 3% DD %%%%%%
% gammaM=gammaDose1d(diffdoserefgantry,diffdoseloggantry,[1 1
1],0.009,236,472,0.003); %%% 3% 4degree 10% threshold criteria
% %gammaM=gammaDose1d(diffdoserefgantry,diffdoseloggantry,[1 1
1],0.009,325,650,0.003);%%% 3% 6degree 10% threshold criteria
% plot((gantryinter),gammaM,'-.b')
% xlabel('gantry (degree)')
% ylabel('Gamma value')
% gamma_O=(sum(gammaM<=1&gammaM>0)/sum(gammaM>0))*100;
% hold on
% gammaM=gammaDose1d(diffdoserefgantry,diffdoseTPSgantry,[1 1
1],0.009,216,432,0.003); %% 3% 4degree 10%threshold criteria
% %gammaM=gammaDose1d(diffdoserefgantry,diffdoseTPSgantry,[1 1
1],0.009,325,650,0.003); %% 3% 6degree 10%threshold criteria
% plot((gantryinter),gammaM,'-.r')
% legend('logfile5%','TPS5%','logfile3%','TPS3%')
% gamma_P=(sum(gammaM<=1&gammaM>0)/sum(gammaM>0))*100;
% hold off
```

Appendix B

Matlab code in Chapter 6

A) Warm up

```
A=csvread('test090419_preirradiation_1.csv');
figure(1)
tA=(1:122000000)';
plot(tA/200000,A)
xlabel('time(s)')
ylabel('voltage (V)')
axis([0 700 -0.05 0.3])
B=conv(A,normpdf(-10:10,0,5));
tB=(1:126400020)';
figure(2)
plot(tB/200000,B)
xlabel('time (s)')
ylabel('pulse height (V)')

C=A(6.7e6:9.5e6);
% figure(3)
% plot(tB/200000,C)
BC=conv(C,normpdf(-10:10,0,5));
t=(1:2800021)';
figure(3)
plot(t/200000,BC)
xlabel('time (s)')
ylabel('pulse height (V)')
Ct1=BC(1:2800020);
Ct2=BC(2:2800021);
Cdt1=gradient(Ct1);
Cdt2=gradient(Ct2);
Cdtdt=Cdt1.*Cdt2;
Cxt=(1:2800020)';
Cxtzd=Cxt(Cdtdt<0&Ct1>0.001);
Ctzd=Ct2(Cdtdt<0&Ct1>0.001);
Cqtrs=zeros(length(Cxtzd),3);
for i=1:length(Cxtzd)
Cxtrs=(Cxtzd(i)-3):(Cxtzd(i)+3);
Ctrs=Ct1(Cxtrs)'/1e8;
Cqfit=polyfit(Cxtrs-Cxtzd(i),Ctrs,2);
Cqtrs(i,:)=Cqfit;
End
```

B) Voltage 5 V

```
A=csvread('t211218_Voltage_5.csv');
%figure(1)
plot(A)
t=(1:8277000)';
v1=A(1:8276999);
v2=A(2:8277000);
dv1=gradient(v1);
dv2=gradient(v2);
dvdv=dv1.*dv2;
xt=t(dvdv<0&v1>0.01);
qtrs=zeros(length(xt),3);
for i=1:length(xt)
xtr=(xt(i)-3):(xt(i)+3);
vr=v1(xtr)';
qfit=polyfit(xtr-xt(i),vr,2);
qtrs(i,:)=qfit;
end
a=qtrs(:,1);
b=qtrs(:,2);
c=qtrs(:,3);
vq1=c-b.^2./4.*a;
tq1=xt-b./a.*2;
ave_peakheight=mean(vq1);
tq=(tq1./200000)-29.50;
plot(tq,vq1)
xlabel('time(s)');
ylabel('reading');
```

C) Variable pulse-rate with spherical phantom

```
A=csvread('test250419_SAD_doserate_32_sphere_1.csv');
% tA=(89000000);
figure(1)
plot(A)
A1=A(7.0e6:4.4e7);
figure(2)
plot(A1)
xlabel('sample data acquisition rate (Hz)');
ylabel('voltage (V)');
B1=conv(A1,normpdf(-10:10,0,5));
tB1=(36000021);
figure(3)
plot(B1)
xlabel('sample data acquisition rate (Hz)');
ylabel('voltage (V)');
At1=B1(1:37000020);
At2=B1(2:37000021);
```

```
Adt1=gradient(At1);
Adt2=gradient(At2);
Adtdt=Adt1.*Adt2;
Axt=(1:37000020)';
Axtzd=Axt(Adtdt<0&At1>0.007);
Atzd=At2(Adtdt<0&At1>0.007);
Aqtrs=zeros(length(Axtzd),3);
for i1=1:length(Axtzd)
Axtrs=(Axtzd(i1)-3):(Axtzd(i1)+3);
Atrs=At1(Axtrs)'/1e8;
Aqfit=polyfit(Axtrs-Axtzd(i1),Atrs,2);
Aqtrs(i1,:)=Aqfit;
end
a=Aqtrs(:,1);
b=Aqtrs(:,2);
c=Aqtrs(:,3);
dose_A=c*1e8-b.^2./a/4*1e8;
time_A=Axtzd-b./a/2;
BG_A=B1(uint32(time_A+250));
figure(4)
plot(time_A/200000,dose_A)
hold on
plot(time_A/200000,BG_A)
hold off
xlabel('time(s)');
ylabel('voltage (V)');
cumpulseheight_1=sum(dose_A);
average_pulse_height_1=mean(dose_A);
cum_BG_A=sum(BG_A);
average_BG_pulse_height_A=mean(BG_A);
irradiation_A=(time_A/200000)
```

D) Variable pulse-rate with cubical phantom

```
A=csvread('test250419_SAD_doserate_32_cube_1.csv');    %%%%%%%
raw data with noise %%%%%%%%%%
figure (1)
plot(A)
% B=conv(A,normpdf(-10:10,0,5));
% plot(B)
% tB=(1:66600020)';
% figure(2)
% plot(tB/200000,B)
% xlabel('time (s)')
% ylabel('pulse height (V)')

C=A(9.6e6:4.59e7);
figure(2)
plot(C)
```

```
BC=conv(C,normpdf(-10:10,0,5));
% t=(1:2800021)';
% figure(3)
% plot(t,BC)
% xlabel('time (s)')
% ylabel('pulse height (V)')
Ct1=BC(1:36300020);
Ct2=BC(2:36300021);
Cdt1=gradient(Ct1);
Cdt2=gradient(Ct2);
Cdtdt=Cdt1.*Cdt2;
Cxt=(1:36300020)';
Cxtzd=Cxt(Cdtdt<0&Ct1>0.007);
Ctzd=Ct2(Cdtdt<0&Ct1>0.007);
Cqtrs=zeros(length(Cxtzd),3);
for iC=1:length(Cxtzd)
Cxtrs=(Cxtzd(iC)-3):(Cxtzd(iC)+3);
Ctrs=Ct1(Cxtrs)'/1e8;
Cqfit=polyfit(Cxtrs-Cxtzd(iC),Ctrs,2);
Cqtrs(iC,:)=Cqfit;
end
a=Cqtrs(:,1);
b=Cqtrs(:,2);
c=Cqtrs(:,3);
Ctq=c*1e8-b.^2./a/4*1e8;
Cxq=Cxtzd-b./a/2;
CBG=Ct1(uint32(Cxq+250));
Ctqr=Ctq./gradient(Cxq)*500;
figure(4)
plot(Cxq/200000,Ctq)
hold on
plot(Cxq/200000,CBG)
hold off
xlabel('time (s)')
ylabel('pulse height (V)')
legend('measured pulse height','BG');
pulse_averageC=mean(Ctq);
cumdpulseheightC=sum(Ctq);
cumCBG=sum(CBG);
average_CBG_pulse_height=mean(CBG);
%total_timeC=Cxq(4468-1)/200000;
timeC=max(Cxq)-Cxq(1);
total_irradiationC=timeC/200000;
```

E) Cross-calibration between the microDiamond and DD4

```
A=csvread('t211218_1_MU300.csv');
figure(1)
plot(A)
A1=A(9.7e6:1.7e7);
B1=conv(A1,normpdf(-10:10,0,5));
figure(2)
plot(B1)
At1=B1(1:7300020);
At2=B1(2:7300021);
Adt1=gradient(At1);
Adt2=gradient(At2);
Adtdt=Adt1.*Adt2;
Axt=(1:7300020)';
Axtzd=Axt(Adtdt<0&At1>0.001);
Atzd=At2(Adtdt<0&At1>0.001);
Aqtrs=zeros(length(Axtzd),3);
for i=1:length(Axtzd)
Axtrs=(Axtzd(i)-3):(Axtzd(i)+3);
Atrs=At1(Axtrs)'/1e8;
Aqfit=polyfit(Axtrs-Axtzd(i),Atrs,2);
Aqtrs(i,:)=Aqfit;
end
a=Aqtrs(:,1);
b=Aqtrs(:,2);
c=Aqtrs(:,3);
dose_A=c*1e8-b.^2./a/4*1e8;
time_A=Axtzd-b./a/2;
BG_A=B1(uint32(time_A+250));
figure(3)
plot(time_A/200000,dose_A)
hold on
plot(time_A/200000,BG_A)
hold off
xlabel('time(s)');
ylabel('pulse height (V)');
cumpulseheight_1=sum(dose_A);
average_pulse_height_1=mean(dose_A);
cum_BG_A=sum(BG_A);
average_BG_pulse_height_A=mean(BG_A);
```

F) VMAT measurement

```
A=csvread('t271118_15.csv');
%figure(1)
plot(A)
t=(1:33000000)';
v1=A(1:32999999);
v2=A(2:33000000);
dv1=gradient(v1);
dv2=gradient(v2);
dvdv=dv1.*dv2;
xt=t(dvdv<0&v1>0.01);
qtrs=zeros(length(xt),3);
for i=1:length(xt)
xtr=(xt(i)-3):(xt(i)+3);
vr=v1(xtr)';
qfit=polyfit(xtr-xt(i),vr,2);
qtrs(i,:)=qfit;
end
a=qtrs(:,1);
b=qtrs(:,2);
c=qtrs(:,3);
vq1=c-b.^2./4.*a;
tq1=xt-b./a.*2;
mean(vq1);
plot(tq1/200000,vq1)
vq=vq1.*0.0010920;
tq=(tq1./200000)-45.26;
plot(tq,vq)
xlabel('time(s)');
ylabel('dose/pulse');
cumdose=cumsum(vq);
```

G) Gamma analysis (1D)

```
%%%% RadCal %%%%%%%%%

[e,f,ef]=xlsread('cumulative_dose_RadCal.xlsx');
time_Rad=e(:,4);
cumdose_Rad=e(:,2)/max(e(:,2));
gantry_Rad=e(:,6);
timeinter=0:0.005:91;
gantryinter=-140:0.0153838:140;
gantry_Rad_time=interp1(time_Rad,gantry_Rad,timeinter);
time_Rad_gantry=interp1(gantry_Rad,time_Rad,gantryinter);
cumdose_Rad_time=interp1(time_Rad,cumdose_Rad,timeinter);
cumdose_Rad_gantry=interp1(gantry_Rad_time,cumdose_Rad_time,gantryin
ter);
```

```
% plot(time_Rad,cumdose_Rad,timeinter,cumdose_Rad_time)
% plot(gantry_Rad,cumdose_Rad,'k',gantryinter,cumdose_Rad_gantry,'r')

%%%%%%% measurements %%%%%%
[a,b,ab]=xlsread('cumulative_dose_measurement.xlsx');
time_measured=a(:,1);
cumdose_measured=a(:,3)/max(a(:,3));
cumdose_measured_time=interp1(time_measured,cumdose_measured,timeint
er);
%
cumdose_measured_gantry=interp1(gantry_Rad_time,cumdose_measured_ti
me,gantryinter);
plot(timeinter,cumdose_Rad_time,timeinter,cumdose_measured_time)
xlabel('Time(s)')
ylabel('Normalised cumulative dose (Gy)')
% plot(gantryinter,cumdose_measured_gantry,'k',gantryinter,cumdose_Rad-
gantry,'r')
% xlabel('Gantry angle(degree)')
% ylabel('Normalised cumulative dose (Gy)')
% legend('measured','RadCal')


%global gammaM
%%%%% 5% criteria time vs cumulative dose %%%%%%%%%%%
gammaM=gammaDose1d(cumdose_measured_time,cumdose_Rad_time,[1 1
1],0.05,400,800,0.1);%%% 5% 2s 10% threshold criteria
figure(5)
plot((timeinter),gammaM,'b')
xlabel('Time(s)')
ylabel('Gamma value')
%title('Gamma analysis for 5%/1s and 3%/1s cumulative dose')
gamma_A=(sum(gammaM<=1&gammaM>0)/sum(gammaM>0))*100;
%%% excluding point below the threshold %%%%%
hold on
gammaM=gammaDose1d(cumdose_measured_time,cumdose_Rad_time,[1 1
1],0.03,400,800,0.1); %%% 3% 2s criteria
plot((timeinter),gammaM,'-.r')
xlabel('Time(s)')
ylabel('Gamma value')
hold on
gammaM=gammaDose1d(cumdose_measured_time,cumdose_Rad_time,[1 1
1],0.01,400,800,0.1);%%% 5% 2s 10% threshold criteria
figure(5)
plot((timeinter),gammaM,'k')
xlabel('Time(s)')
ylabel('Gamma value')
legend('5%','3%','1%')
hold off
```

BIBLIOGRAPHY

1. https://www.cancerhealth.com/article/world-health-organization-releases-global-cancer-data

2. M. Aspradakis, J. Byrne, H. Palmans, J. Conway, K. Rosser, J. Warrington and S. Dvane, “Small field MV photon dosimetry”, IPEM Report No 103 (Institute of Physics and Engineering in Medicine, York, 2010.

3. De Angelis, C. Bucciolini, M. Casati, M. Lovik, I. Bruzzi, M. Lagomarsino, S. Sciortino, S. Onori. S, “Improvement in CVD diamond properties for radiotherapy dosimetry," Radiation Protection Dosimetry,vol. 120, pp. 38-42, 2006.

4. Planskoy. B, “Evaluation of diamond radiation dosemeters," Physics in Medicine and Biology, vol. 3, 1980.

5. M.J. Guerrero, D. Tromson, M. Rebisz, C. Mer, B. Bazin, and P. Bergonzo, "Requirements for synthetic diamond devices for radiotherapy dosimetry applications," Diamond and Related Materials, vol. 13(11), pp. 2046-2051, 2004.

6. Cotty. WF, “Diamond as a Pinpoint Radiation Counter," Nature, vol 177, no. 4519, pp. 1075-1076 , 1956.

7. E.A. Burgemeister, "Dosimetry with a diamond operating as a resistor," Physics in Medicine and Biology, vol. 26(2), pp. 269, 1981.

8. B. Gorka, B. Nilsson, J. Fernandez-Varea, R. Svensson, and A. Brahme, "Influence of electrodes on the photon energy deposition in CVD-diamond dosimeters studied with the Monte Carlo code PENELOPE," Physics in Medicine and Biology, vol. 51(15), pp. 3607- , 2006.

9. A. Fidanzio, L. Azario, P. Viola, P. Ascarelli, E. Cappelli, G. Conte, and A. Piermattei, “Photon and electron beam dosimetry with a CVD diamond detector", Nuclear Instruments and Methods in Physics Research Section A: Accelerators, Spectrometers, Detectors and Associated Equipment, 524(1), pp. 115-123, 2004.

10. C. Butter, J. Conway, R. Meyfarth, G. Scarsbrook, P.J. Sellin and A. Whitehead", CVD diamond detectors as dosimeters for radiotherapy," Nuclear Instruments and Methods in Physics Research Section A: Accelerators, Spectrometers, Detectors, and Associated Equipment, vol 392(1), pp. 281-284, 1997.

11. A.Fidanzio, L. Azario, R. Kalish, Y. Avigal, G. Conte, P. Ascarelli, and A. Piermattei, “ A preliminary dosimetric characterization of chemical vapor deposition diamond detector prototypes in photon and electron radiotherapy beams," Medical Physics, vol. 32(2), pp. 389-395, 2005.

12. A. Lohstroh, "Temperature dependent charge transport studies in polycrystalline and single crystal CVD diamond detectors," Ph.D. Thesis, University of Surrey, U.K., 2006.

13. Maria Antonietta Piliero, “ Modelling and development of tissue-equivalent dosimeters for small field radiotherapy," Ph.D. Thesis, Swansea University, U.K., 2013.

14. Stefano Peca and Derek W. Brown, “Two-dimensional in vivo dose verification using portal imaging and correlation ratios," Journal of Applied Clinical Medical Physics, vol. 15, no 4, 2014.

15. Zeina Al Kattar Elbalaa, Jean Noel Fouquier, Alaxendre Orthuon, Hanna Elbalaa, and Emmanuel Touboul, “ Role of “the frame cycle time” in portal dose imaging using an aS500-II EPID”, Physica Medica, vol 25, pp. 148-153, 2009.

16. Henry C. Woodruff, Todsaporn Fuangrod, Eric Van Uytven, Boyd M.C. McCurdy, Timothy van Beek, Shashank Bhatia, and Peter B. Greer, “First Experience With Real-Time EPID-Based Delivery Verification During IMRT and VMAT Sessions," International Journal of Radiation Oncology Biology Physics, vol. 93(3), pp. 516-522, 2015.

17. Clinical 3D Dosimetry in Modern Radiation Therapy, by Ben Mijnheer, CRC Press, 2019.

18. Greer PB, “Correction of pixel sensitivity variation and off-axis response for amorphous silicon EPID dosimetry”, Medical Physics, vol.32, pp.3558-3568,2005.

19. Greer PB, “ 3D EPID based dosimetry for pre-treatment verification of VMAT-methods and challenges”, Journal Physics Conf. Ser, 444:012010, 2013.

20. McCowan PM, “ Gantry angle correction methods for EPID images acquired in cine-mode”, Journal Application Clinical Medical Physics, vol.15, pp.187-201, 2014.

21. Siewerdsen JH and Jaffray DA, " A ghost story: Spatio-temporal response characteristics of an indirect-detection flat-panel imager", Medical Physics, vol.26, pp.1624-1641, 1999.

22. Fowler J.F, "Radiation-induced conductivity in the solid state and other applications," Physics in Medicine and Biology, vol. 3, pp. 395-410, 1959.

23. Velthuis J.J, R.F. Page, T. M. Purves, L. Beck, M.A.M.Hanifa and R.P.Hugtenburg, "Toward Pulse by Pulse Dosimetry Using an SC CVD Diamond Detector", IEEE Transactions on Radiation And Plasma Medical Sciences, vol 1, issue 6, pp. 527-533, 2017.

24. Sarah Aldridge, PhD Thesis, Swansea University,U.K. 2020.

25. Gavin Morgan, "Development of Diamond Dosimeters for Real-time Dosimetry", MSc Dissertation, Swansea University, U.K., 2019.

26. Hanifa. A, Hugtenburg R, and Velthuis .J, "Pulse-by-pulse dosimetry of intensity modulated radiotherapy with a CVD diamond detector", 3rd International Conference on Dosimetry and its Applications, Lisbon, 2019.

27. http://www.stevesque.com/diamond/structure/

28. D.R.Kania, M.I.Landstrass, M.A.Plano, L.S.Pan and S.Han, "Diamond radiation detectors," Diamond and Related Materials, vol 2, pp. 1012-1019, 1993.

29. Chris J.H.Wart and Richard S. Balmer, "Diamond as an electronic material" Material Today, vol 11, Number 1-2, Jan-Feb 2008.

30. Alison Mainwood, "Recent developments of diamond detectors for particles and UV radiation", Semiconductor Science and Technology , vol 15, no 9, pp. R55-R63,2000.

31. Walker J, "Optical absorption and luminescence in diamond," Reports on Progress in Physics, vol 42, pp. 1605-1654, 1979.

32. P W Hoban, M Heydarian, W A Beckham and A H Beddoe, " Dose rate dependence of a PTW diamond detector in the dosimetry of a 6 MV photon beam" Physics in Medicine and Biology, vol 39, pp. 1219-1229, 1994.

33. Vatnitsky S and Jarvinent H, "Application of a natural diamond detector for the measurement of relative dose distributions in radiotherapy," Physics in Medicine and Biology, vol 38, pp. 73-184, 1993.

34. D.Tromson, M. Rebisz-Pomorska, N. Tranchant, A. Isambert, F. Moigrau, A. Moussier, B. Marczewska, and P. Bergonzo, "Single crystal CVD diamond detector for high resolution dose measurement for IMRT and novel radiation therapy needs," Diamond & Related Materials, vol 19, pp.1012-1016, 2010.

35. F.P.Bundy, H.T.Hall,H.M.Strong and R.H.Wentorf, "nature: Man-made diamond", International Journal of Science,1955.

36. Betzel GT, "Development of a prototype synthetic diamond detector for radiotherapy dosimetry, Ph.D. Thesis, University of Canterbury, N.Z., 2010.

37. Butler JE, Cheesman. A and Ashfold MNR, "Recent Progress in the Understanding of CVD Growth of Diamond," CVD Diamond for Electronic Devices and Sensors, pp. 103-24, 2009.

38. Butler JE, Mankelevich YA, Cheesman A, Jie M, and Ashfold MNR, "Understanding the chemical vapor deposition of diamond recent progress," Journal of Physics: Condensed Matter, vol 21, pp. 1-20,2009.

39. https://www.rough-polished.com/upload/medialibrary/c01/analyt_06032017_1_eng.jpg

40. N. Tranchant, D. Tromson, C. Descamps, A. Isambert, H. Hamrita, P. Bergonzo, and M. Nesladek, "High mobility single crystal diamond detectors for dosimetry: Application to radiotherapy," Diamond & Related Materials, vol 17, pp. 1297-1301, 2008.

41. http://slideplayer.com/slide/3818567/13/images/11/Chemical+Vapor+Deposition+of+Diamond.jpg

42. Fox B.A, M.L. Hartsell, D.M. Malta, H.A. Wynands, C.-T. Kao, L.S. Plano, G.J. Tessmer, R.B. Henard, J.S. Holmes, A.J. Tessmer, D.L. Dreifus, "Diamond devices and electrical properties," Diamond, and Related Materials, vol 4, pp. 622-627, 1995.

43. Laub. Wolfram U, Theodor W. Kaulich and FridtjofNusslin, "A diamond detector in the dosimetry of high-energy electron and photon beams," Physics in Medicine and Biology, vol 44, pp. 2183-2192, 1999.

44. Laub. Wolfram U and Tony Wong, "The volume effect of detectors in the dosimetry of small fields used in IMRT," Medical Physics, vol 30,no 3, 2003.

45. P. Bergonzo, D. Tromson, C. Descamps, H. Hamrita, C. Mer, N. Tranchant, M. Nesladek, “Improving diamond detectors: A device case," Diamond & Related Materials., vol 16, pp. 1038-1043, 2007.

46. Kagan K, "Recent advances in diamond detector development," Nuclear Instruments & Methods in Physics Research A, vol 541, issues 1-2, pp. 221-227, 2005.

47. Almaviva S, Ciancaglioni I, Consorti R, De Notaristefani F, Manfredotti C, Marco Marinelli, Milani E, Petrucci A, Prestopino G, Verona C and Verona-Rinati G, "Synthetic single crystal diamond dosimeters for Intensity Modulated Radiation Therapy applications", Nuclear Instruments & Methods in Physics Research A, vol 608, issue 1,pp.191-194, 2009.

48. Marco M, Prestopino G, Verona C, and Verona-Rinati G, “Experimental determination of the PTW 60019 microDiamond dosimeter active area and volume”, Medical Physics, vol 43, issue 9, pp. 5205-5212,2016.

49. Ciancaglioni I, Marco M, Milani E, Prestopino G, Verona C, Verona-Rinati G, Consorti R, Petrucci A, and De Notaristefani F, “Dosimetric characterization of a synthetic single crystal diamond detector in clinical radiation therapy small photon beams," Medical Physics, vol 39, issue 7(Part 1), pp. 4493-4501,2012.

50. Marsolat F, L De Marzi, A Patriarca and C Nauraye, C Moignier, M Pomorski, F Moignau, S Heinrich, D Tromson and A Mazal, "Dosimetric characteristics of four PTW microDiamond detectors in high-energy proton beams," Physics in Medicine and Biology, vol 61, pp. 6413-6429, 2016.

51. A.R.Beierholm, C.E.Anderson, L.R.Lindvold, and M.C. Aznar, "Investigation of linear accelerator pulse delivery using fast organic scintillator measurements," Radiation Measurements, vol 45, issues 3-6, pp. 668-670, 2010.

52. https://image.slidesharecdn.com/linearaccelerators-151109075843-lva1-app6892/95/linear-accelerators-8-638.jpg?cb=1466403973

53. Robertson JM, Kessler ML, Lawrence TS, “Clinical results of three-dimensional conformal irradiation," Journal of the National Cancer Institute, vol 86, issue 13, pp.968-974, 1994.

54. David A. Palma, Wilko F.A.R. Verbakel, Karl Otto, and Suresh Senan, "New development in arc radiation therapy: A review," Cancer Treatment Review, vol 36, pp.393-399, 2010.

55. https://www.bing.com/images/search?view=detailV2&id=3CE76692EF512CF63838204AB5F9F7D61D944F9B&thid=OIP.V0C_8Tc86JfFQctempY5_wHaFj&mediaurl=https%3A%2F%2Fimage.slidesharecdn.com%2Fradiationtherapyinprostatecancer2014-141001084406-phpapp01%2F95%2Fradiation-therapy-in-prostate-cancer-60-638.jpg%3Fcb%3D1412154310&exph=479&expw=638&q=2d+radiotherapy+prostate+planning&selectedindex=0&ajaxhist=0&vt=0&eim=1,2,6

56. https://www.bing.com/images/search?view=detailV2&id=AF8C0B7551BB0B0523C85943519190EF2BA26BBA&thid=OIP.QbfEfEjK_RKu9-At3gmUCgHaFj&mediaurl=http%3A%2F%2Fslideplayer.com%2F5677283%2F18%2Fimages%2F59%2FProstate%2B3D%2BPlanning.jpg&exph=720&expw=960&q=3d+radiotherapy+&selectedindex=182&ajaxhist=0&vt=0&eim=1,2,6

57. https://www.bing.com/images/search?view=detailV2&id=730512CCBD9A3DF2D48DD9EE06DCB7FE9BDF962F&thid=OIP.zXw6pj6vhKV63OGkN_HEwwHaHT&mediaurl=http%3A%2F%2F1.bp.blogspot.com%2F_679PUGcPS6g%2FR8CczLQaGpI%2FAAAAAAAABmw%2F4MmGXbvuw4s%2Fs400%2Fimrt-example-enlg.jpg&exph=271&expw=275&q=imrt+radiotherapy+images&selectedindex=2&ajaxhist=0&vt=0&eim=1,2,6

58. Suresh Rana, "Intensity modulated radiation therapy versus volumetric intensity modulated arc therapy," Journal of Medical Radiation Sciences, vol 60, pp. 81-83, 2013.

59. Wang JZ, Li XA, D'Souza WD, and Stewart RD, "Impact of prolonged fraction delivery times on tumor control: a note of caution for intensity-modulated radiation therapy (IMRT)," International Journal Radiation Oncology Biology Physics, vol 57, issue 2, pp.543-552, 2003.

60. Cedric X Yu, "Intensity-modulated arc therapy with dynamic multileaf collimation: an alternative to tomotherapy," Physics in Medicine and Biology, vol 40, pp. 1435-1449, 1995.

61. Webb S, "Tomotherapy and beamweight stratification," Proc XIth Int. Conf on the Use of Computers in Radiation Therapy(Manchester 1994)

62. Otto K, "Volumetric modulated arc therapy: IMRT in a single gantry arc," Medical Physics, vol 35, pp. 310-317, 2008.

63. https://www.bing.com/images/search?view=detailV2&id=4AF6A5D98DF0E6C00541EF1DA987424CD9A0FE3B&thid=OIP.eAP_3kg2SU-TY6La6kLq7QHaFe&mediaurl=http%3A%2F%2Fwww.vims.ac.in%2Fhealthcare%2Fimages%2Frapid%2FRectal.jpg&exph=222&expw=300&q=vmat+radiotherapy+images&selectedindex=25&ajaxhist=0&vt=0&eim=1,2,6

64. Hoogeman MS, Nuyttens JJ, Levendag PC, Heijmen BJM," Time dependence of intrafraction patient motion assessed by repeat stereoscopic imaging," International Journal Radiation Oncology Biology Physics, vol 70, issue 2, pp. 609-618, 2008.

65. W. P. M. Mayles, "The Glasgow incident – a physicist's reflections," Clinical Oncology, vol 19, pp. 4-7, 2007.

66. C. Marajh, "Anatomy of an error: Cancer treatment radiation overdose," Trinidad Express Newspapers, July 20, 2011.
(availableURL: http://www.trinidadexpress.com/news/Anatomy_of_an_error-125929808.html)

67. Eric C. Ford, Suzanne B. Evans, "Incident learning in radiation oncology: A review," Medical Physics, vol 45, no 5, pp. , 2018.

68. O. Holmberg, M. Coffey, T. Knoos and J. Cunningham, "Sportlight on in-vivo dosimetry," ROSIS Newsletter, March 2, 2006.
(available URL: http://www.rosis.info/docs/sportlight_case2.pdf)

69. Ben Mijnheer, Sam Beddar, Joanna Izewska, and Chester Reft, "In vivo dosimetry in external beam radiotherapy," Medical Physics, vol .40, no 7, 2013.

70. S.M.J.J.G. Nijsten, W.J.C. van Elmpt, M. Jacobs, B.J.Mijnheer, A.L.A.J. Dekker, P. Lambin and A.W.H. Minken, "A global calibration model for a-Si EPIDs used for transit dosimetry," Medical Physics, vol .34, pp. 3872-3884, 2007.

71. IAEA (International Atomic Energy Agency), “Dosimetry of small fields used in External Beam Radiotherapy: An International Code of Practice for Reference and Relative Dose Determination,” Technical Report Series No 483 (TRS 483) (IAEA, Vienna, 2017).

72. C.M. Buttar, R. Airey, J. Conway, S. Ramkumar, G. Scarsbrook, R.S. Sussmann, S. Walker, and A. Whitehead, "A study of radiotherapy dosimeters based on diamond grown by chemical vapour deposition," Diamond and Related Materials, vol 9, issue 3-6, pp. 965-969, 2000.

73. M. Rebisz-Pomorska, D. Tromson, A. Isambert, B. Marczewska, and P. Bergonzo, "Single crystal chemical vapor deposited diamond detectors for intensity-modulated radiation therapy applications," Journal of Applied Physics vol. 106, pp. 084509: 1-4, 2009.

74. G.T.Betzel, S.P.Lansley, D.McKay and J.Meyer, “Reproducibility of CVD diamond detectors for radiotherapy dosimetry," Nuclear Instruments and Method in Physics Research A, vol 691, pp. 34-38, 2012.

75. S. Almaviva, I. Ciancaglioni, R. Consorti, F. De Notaristefani, C. Manfredotti, Marco Marinelli, E. Milani, A. Petrucci, G. Prestopino, C. Verona and G. Verona-Rinati, “Synthetic single crystal diamond dosimeters for conformal radiation therapy application”, Diamond & Related Materials, vol 19, pp. 217-220, 2010.

76. M. Bruzzi, M. Bucciolini, G.A.P. Cirrone, G. Cuttone, S. Mazzocchi, S. Pirollo and S. Sciortino, “Characterisation of CVD diamond dosimeters in on-line configuration”, Nuclear Instruments and Methods in Physics Research A, vol 454, pp. 142-146, 2000.

77. B. Gorka, B. Nilsson, R. Svensson, A. Brahme, P. Ascarelli, D.M. Trucchi, G. Conte, and R. Kalish, " Design and characterization of a tissue-equivalent CVD-diamond detector for clinical dosimetry in high-energy photon beams," Physica Medica, vol 24, pp. 159-168, 2008.

78. S. Spadaro, D.M. Trucchi, G. Conte, M. Pimpinella, A.S. Guerra, and R.F. Laitano, “ Dynamic response of diamond sensors to ionizing radiation beams," Sensors and Actuators A: Physical, vol 171, pp. 43-47, 2011.

79. F. Marsolat, D. Tromson, N. Tranchant, M. Pomorski, D. Lazaro-Ponthus, C. Bassinet, C. Huet, S. Derreumaux, M. Chea, J. Alvarez, and P. Bergonzo, " Diamond dosimeter for small beam stereotactic radiotherapy," Diamond & Related Material, vol 33, pp. 63-70, 2013.

80. P. Bergonzo, A. Brambilla, D. Tromson, C. Mer, B. Guizard, F. Foulon and V. Amosov, “ CVD diamond for radiation detection devices”, Diamond & Related Materials, vol 10, pp. 631-638, 2001.

81. A. Galbiati, S. Lynn, K. Oliver, F. Schirru, T. Nowak, B. Marczewska, J.A. Duenas, R. Berjillos, I. Martel and L. Lavergne, “Performance of Monocrystalline Diamond Radiation Detectors Fabricated Using TiW, Cr/Au and a Novel Ohmic DLC/Pt/Au Electrical Contact”, IEEE Transactions on Nuclear Science, vol 56,no 4, pp. 1863-1874, 2009.

82. Marczewska B, Nowak T, Olko P, Nesladek M, Waligorski MPR, “Studies on the application of CVD diamonds as active detectors of ionizing radiation. Physica B: Condensed Matter, vol 308-310, pp. 1213-1216, 2001.

83. S. Almaviva, Marco Marinelli, E. Milani, A. Tucciarone, G. Verona-Rinati, R. Consorti, A. Petrucci, F. De Notaristefani, and I. Ciancaglioni, “Synthetic single crystal diamond diodes for radiotherapy dosimetry”, Nuclear Instruments and Method in Physics Research A, vol 594, pp. 273-277, 2008.

84. A Chalkey and G Heyes, “ Evaluation of a synthetic single-crystal diamond detector for relative dosimetry measurements on a CyberKnife," The British Institute of Radiology, vol 87, issue 1035, 2014.

85. Wolfram U. Laub and Richard Crilly, " Clinical radiation therapy measurements with a new commercial synthetic single crystal diamond detector," Journal of Applied Clinical Medical Physics, vol 15, no 6, pp. 92-102, 2014.

86. Yuichi Akino, Archana Gautam, Len Coutinho, Jan Wurfel, and Indra J. Das, "Characterization of new commercial single crystal diamond detector for photon- and proton-beam dosimetry," Journal of Radiation Research, vol 56, no.6, pp. 912-918, 2015.

87. F Marsolat, L De Marzi, A Patriarca, C Nauraye, C Moignier, M Pomorski, F Moignau, S Heinrich, D Tromson, and A Mazal, " Dosimetric characteristics of four PTW microDiamond detectors in high-energy proton beams," Physics in Medicine and Biology, vol 61, pp. 6413-6429, 2016.

88. Ramamoorthy Ravichandran, John Pichy Binukumar, Iqbal Al Amri, and Cheriyathmanjiyil Antony Davis, "Diamond detector in absorbed dose measurements in high-energy accelerator photon and electron beams," Journal of Applied Clinical Physics, vol 17, no 2, 2016.

89. Jose Manuel Larraga-Gutierrez, Paola Ballesteros-Zebadua, Miguel Rodriguez-Ponce, Olivia Amanda Garcia-Garduno, and Olga Olinca Galvan de la Cruz, “Properties of a commercial PTW-60019 synthetic diamond detector for the dosimetry of small radiotherapy beams”, Physics in Medicine and Biology, vol 60, pp. 905-924, 2015.

90. C. Di Venanzio, Marco Marinelli, E. Milani, G. Prestopino, C. Verona, G. Verona-Rinati, M.D. Falco, P. Bagala, R. Santoni and M. Pimpinella, “Characterization of a synthetic single crystal diamond Schottky diode for radiotherapy electron beam dosimetry”, Medical Physics, vol 40, issue 2, 2013.

91. C. Di Venanzio, Marco Marinelli, A. Tonnetti, G. Verona-Rinati, M.D. Falco, M. Pimpinella, A. Ciccotelli, S. De Stefano, G. Felici, F. Marangoni, “Characterization of microdiamond detector in high-dose-per-pulse electron beams for intra operative radiation therapy”, Physica Medica, vol 31, pp. 897-902, 2015.

92. http://www.electricalbasicprojects.com/difference-between-schottky-diode-and-pn-junct

93. PTW microDiamond brochure.

94. PTW Ionizing Radiation Catalogue 2019/2020

95. PTW UNIDOS Universal Dosemeter brochure.

96. Precise Treatment Clinical Mode , User’s Manual, R50 System 2003.

97. IAEA (International Atomic Energy Agency), “Calibration of Dosimeters Used in Radiotherapy,” Technical Report Series No 374 (IAEA, Vienna, 1994).

98. Cirrone G.A.P, G. Cuttone, S. Lo Nigro, V. Mongelli, L. Raffaele and M. G. Sabini, “ Dosimetric characterization of CVD diamonds in photon, electron and proton beams”, Nuclear Physics B (Proc. Suppl), pp. 330-333, 2006.

99. IAEA (International Atomic Energy Agency), “Absorbed dose determination in external beam radiotherapy: An international code of practice for dosimetry based on standards of absorbed dose to water,” Technical Report Series No 398 (IAEA, Vienna, 2000).

100. Ramamoorthy Ravichandran, John Pichy Binukumar, Iqbal Al Amri and Cheriyathmanjiyil Antony Davis, “Diamond detector in absorbed dose measurements in high-energy accelerator phantom and electron beams”, Journal of Applied Clinical Medical Physics, vol 17, Number 2, 2016.

101. S J Woodings, J W H Wolthaus, B van Asselen, J H W de Vries, J G M Kok, J J W Lagendijk and B W Raaymakers, “Performance of a PTW 60019 microDiamond detector in a 1.5 T MRI-linac”, Physics in Medicine and Biology, vol 63**,** issue 5, pp. **,** 2018.

102. F Schirru, K Kisielewicz, T Nowak and B Marczewska, “Single crystal diamond detector for radiotherapy”, Journal of Physics D : Applied Physics, vol 43, no 26, 2010.

103. Merlin Fisher-Levine, Jaap Velthuis, David Cussans and Steve Nash, “A Fast Analogue Front End for a Diamond Radiation Spectrometer”, IEEE Transactions on Nuclear Science, vol 60, issue 5, pp. 3990-3994, 2013.

104. ROOT Data Analysis Framework. Accessed:Sep.28,2017.[Online]. Avaiable: http://root.cern.ch

105. Luis Brualla-Gonzalez, Faustino Gomez, Miguel Pombar and Pardo-Montero, “ Dose rate dependence of the PTW 60019 microDiamond detector in high dose-per-pulse pulsed beams ”, Physics in Medicine and Biology, vol 61, no 1, 2016.

106. D. Tromson, C. Descamps, N. Tranchant, P. Bergonzo, M. Nesladek and A. Isambert, “ Investigations of high mobility single crystal chemical vapor deposition diamond for radiotherapy photon beam monitoring”, Journal of Applied Physics, vol 103, issue 5, 2008.

107. J.H. Kaneko, T. Tanaka, T. Imai, Y. Tanimura, M. Katagiri, T. Nishitani, H. Takeuchi, T. Sawamura and T. Iida, “Radiation detector made of 28a diamond single crystal grown by a chemical vapor deposition method”, Nuclear Instruments & Methods in Physics Research A, vol 505, issues 1-2, pp. 187-190, 2003.

108. CANCER RESEARCH UK (https://www.cancerresearchuk.org).

109. Ramachandran Prabhakar and Goura K. Rath, “A simple plan evaluation index based on the dose to critical structures in radiotherapy”, Journal of Medical Physics, vol 36, no 4, pp. 192-197, 2011.

110. Erin Barnett, Marc MacKanzie and B. Gino Fallone, “ IMRT point dose measurements with a diamond detector”, Radiology and Oncology, vol 39, issue 1, pp 71-78, 2005.

111. A Manikandan, B Sarkar, R Holla, T R Vivek, and N Sujatha, " Quality assurance of dynamic parameters in volumetric modulated arc therapy", The British Institute of Radiology, vol 85, issue 1015, pp. 1002-1010, 2012.

112. N S Midi and Hafiz M Zain, "Feasibility of using the linac real-time log data for VMAT treatment verification", Journal of Physics: Conference Series, vol 851, conference 1, 2017.

113. Craig A. Elith, Shane E. Dempsey, Fred Cao, Afrooz Farshadi, and Helen M. Warren-Forward, "The quality assurance of volumetric modulated arc therapy (VMAT) plans for early stage prostate cancer: a technical note" Journal of Medical Radiation Sciences, vol 61, issue 4, pp. 261-266, 2014.

114. http://advuro.myonlineweb.net/main/wp-content/uploads/2015/06/Multileaf-collimator.jpg

115. https://www.researchgate.net/profile/H_Romeijn/publication/220133319/figure/fig2/AS:277519820443654@1443177289871/A-multileaf-collimator-MLC-system.png

116. Krzysztof Slosarek, Marta Szlag, Barbara Bekman, and Aleksandra Grzadziel, "EPID in vivo dosimetry in RapidArc technique", Reports of Practical Oncology And Radiotherapy, vol 15, issue 1, pp. 8-14, 2010.

117. M Bakhtiari, L Kumarasamy, D.W. Bailey, S de Boer, H.K. Malholtra, M.B. Podgorsak, " Using an EPID for patient-specific VMAT quality assurance", Medical Physics, vol 38, issue 3, pp. 1366-1373, 2011.

118. M Heydarian, P W Hoban and A H Beddoe, "A comparison of dosimetry techniques in stereotactic radiosurgery", Physics in Medicine and Biology, vol 41, pp. 93-110, 1996.

119. A.R. Beierholm, C.F. Behrens and C.E. Andersen, "Studying the potential of point detectors in time-resolved dose verification of dynamic radiotherapy", Radiation Measurements, vol 82, pp. 129-137, 2015.

120. Low DA, Harms WB, Mutic S, and Purdy JA, "A technique for the quantitative evaluation of dose distribution", Medical Physics, vol 25, issue 5, pp. 656-661, 1998.

121. Heng Li, Lei Dong, Lifei Zhang, James N. Yang, Micheal T. Gillin, and X. Ronald Zhu, "Toward a better understanding of the gamma index: Investigation

of parameters with a surface-based distance method", Medical Physics, vol 38, issue 12, pp. 6730-6741, 2011.

122. Sathiyan Saminathan, Henry Finlay Godson, Retna Ponmalar, Ravikumar Manickam, James Mazarello BE, and Rahul Fernandes, "Dosimetric performance of newly developed Farmer-type ionization chamber in radiotherapy practice", Technology in Cancer Research & Treatment, vol 15, issue 6, 2016.

123. Radiation Therapy Physics by William R. Hendee, Geoffrey S. Ibbott, and Eric G. Hendee, Third Edition, John Wiley & Son, Inc Publication(2005).

124. https://www.bing.com/images/search?view=detailV2&id=642D6D1E7A56F15E0DE5B3864A6BA9526A286EE0&thid=OIP.oCOyfgOhVV84

125. Ramamoorthy Ravichandran, Johnson Pichy Binukumar and Cheriyathmanjiyil Antony Davis, "Estimation of absorbed dose in clinical radiotherapy linear accelerator beams: Effect of ion chamber calibration and long-term stability", Medical Physics, vol 38, issue 4, pp. 205-209, 2013.

126. Alper Mehmed Ahmed. Monte Carlo Dose Verification of Prostate Patient Treated With VMAT. M.Sc. Thesis, Swansea University, U.K. 2015.

127. Christopher Boylan, Alan McWilliam, Emily Johnstone, and Carl Rowbottom,"The impact of continuously-variable dose rate VMAT on beam stability, MLC positioning, and overall plan dosimetry", Journal of Applied Clinical Medical Physics, Vol 13, Number 6,2012.

128. Akihiro Haga, Akira Sakumi, Yukari Okano, Saori Itoh, Naoya Saotome, Satoshi Kida, Hiroshi Igaki, Kenshiro Shiraishi, Hideomi Yamashita, Kuni Ohtomo and Keiichi Nakagawa, "Dose verification of volumetric modulated arc therapy (VMAT) by use of in-treatment linac parameters", Radiological Physics and Technology, vol 6, issue 2, pp. 335-342, 2013.

129. C J Boylan, C Golby and C G Rowbottom, " A VMAT planning solution for prostate patients using a commercial treatment planning system", Physics in Medicine and Biology, vol 55, no 14, 2010.

130. Baozhou Sun, Dharanipathy Rangaraj, Sunita Boddu, Murty Goddu, Deshan Yang, Geethpriya Palaniswaamy, Sridhar Yaddanapudi, Omar Wooten and Sasa Mutic,"Evaluation of the efficiency and effectiveness of independent dose calculation followed by machine log file analysis against conventional

measurement based IMRT QA", Journal of Applied Clinical Medical Physics, vol 13, no 5, 2012.

131. Litzenberg DW, Moran JM, and Fraass BA."Verification of dynamic and segmental IMRT delivery by dynamic log file analysis". Journal of Applied Clinical Medical Physics, vol 3, issue 2, pp. 63-72, 2002.

132. Xin Chen, Karl Bush, Aiping Ding, and Lei Xing. Independent calculation of monitor units for VMAT and SPORT. Medical Physics, vol 42, issue 2, pp. 918-924,2015.

133. PTW calibration certificate.

134. Ander R Beierholm, Rickard O Ottossom, Lars R Lindvold, Claus F Behrens and Claus E. Andersen, " Characterizing a pulse-resolved dosimetry system for complex radiotherapy beams using organic scintillators", Physics in Medicine and Biology, vol 56, no 10, 2011.

135. Daniel A. Low and James F. Dempsey. "Evaluation of the gamma dose distribution comparison method", Medical Physics, vol 30, issue 9, pp. 2455-2464, 2003.

136. IMRT commissioning: Multiple institution planning and dosimetry comparisons, a report from AAPM Task Group 119; Medical Physics, vol 36, issue 11, pp. 5359-5373, 2009.

137. Ji-Hye Song, Min-Joo Kim, So-Hyun Park, Seu-Ran Lee, Min-Young Lee, Dong Soo Lee, and Tae Suk Suh, "Gamma analysis dependence on specified low-dose thresholds for VMAT QA", Journal of Applied Clinical Medical Physics, vol 16, no 6, pp. 263-272, 2015.

138. International Electrotechnical Commission (IEC);61217:2011.

139. National Instruments (NI) specifications for USB-6210 manual.

140. De Angelis C, Casati M, Bruzzi M, Onori S, Bucciolini M, "Present limitations of CVD diamond detectors for IMRT applications", Nuclear Instruments Methods Physics Research Section A, vol 583, issue 1, pp. 195-203, 2007.

141. Betzel G, Lansley S, Baluti F, Reinisch L, Meyer J, "Operating parameters of CVD diamond detectors for radiation dosimetry", Nuclear Instruments Methods Physics Research Section A, vol 614, issue 1, pp. 130-136, 2010.

142. Dearnaley D, Syndikus I, Mossop H, Khoo V, Birtle A, Bloomfield D, Graham J, Kirkbride P, Logue J, Malik Z, Money-Kyrle J, O'Sullivan JM, Panades M, Parker P, Patterson H, Scrase C, Staffurth J, Stockdale A, Tremlett J, Bidmead M, Mayles H, Naismith O, South C, Gao A, Cruickshank C, Hassan S, Pugh J, Griffin C and Hall E, "Conventional versus hypofractionated high-dose intensity-modulated radiotherapy for prostate cancer: 5-year outcomes of the randomised, non-inferiority ,phase 3 CHHiP trail", Lancet Oncol 2016. Betzel G, Lansley S, Baluti F, Reinisch L, Meyer J, "Operating parameters of CVD diamond detectors for radiation dosimetry", Nuclear Instruments Methods Physics Research Section A, vol 614, issue 1, pp. 130-136, 2010.

143. Ezzell G.A, Galvin J.M, Low D, Palta J.R, Rosen I, Sharpe M.B, Xia P, Xiao Y, Xing L and Yu C. X, "Guidance document on delivery, treatment planning and clinical implementation of IMRT: report of the IMRT Subcommittee of the AAPM radiation therapy committee", Medical Physisc, vol 30, pp. 2089-2115,2003.

144. RadCalc: QA Software for Secondary Check, LifeLine Software, Inc,2407,Pemberton Place, Austin, TX 78703,USA.